MULTIPHYSICS MODELING OF THE STEEL CONTINUOUS CASTING PROCESS

BY

LANCE C. HIBBELER

DISSERTATION

Submitted in partial fulfillment of the requirements
for the degree of Doctor of Philosophy in Mechanical Engineering
in the Graduate College of the
University of Illinois at Urbana–Champaign, 2014

Urbana, Illinois

Doctoral Committee:

Professor Brian G. Thomas, Chair and Director of Research
Professor Armand J. Beaudoin
Professor Jonathan A. Dantzig
Professor Alan W. Cramb, Illinois Institute of Technology

Abstract

This work develops a macroscale, multiphysics model of the continuous casting of steel. The complete model accounts for the turbulent flow and nonuniform distribution of superheat in the molten steel, the elastic-viscoplastic thermal shrinkage of the solidifying shell, the heat transfer through the shell-mold interface with variable gap size, and the thermal distortion of the mold. These models are coupled together with carefully constructed boundary conditions with the aid of reduced-order models into a single tool to investigate behavior in the mold region, for practical applications such as predicting ideal tapers for a beam-blank mold.

The thermal and mechanical behaviors of the mold are explored as part of the overall modeling effort, for funnel molds and for beam-blank molds. These models include high geometric detail and reveal temperature variations on the mold-shell interface that may be responsible for cracks in the shell. Specifically, the funnel mold has a column of mold bolts in the middle of the inside-curve region of the funnel that disturbs the uniformity of the hot face temperatures, which combined with the bending effect of the mold on the shell, can lead to longitudinal facial cracks. The shoulder region of the beam-blank mold shows a local hot spot that can be reduced with additional cooling in this region. The distorted shape of the funnel mold narrow face is validated with recent inclinometer measurements from an operating caster. The calculated hot face temperatures and distorted shapes of the mold are transferred into the multiphysics model of the solidifying shell.

The boundary conditions for the first iteration of the multiphysics model come from reduced-order models of the process; one such model is derived in this work for mold heat transfer. The reduced-order model relies on the physics of the solution to the one-dimensional heat-conduction equation to maintain the relationships between inputs and outputs of the model. The geometric parameters in the model are calibrated such that the reduced-order model temperatures match a small, periodic subdomain of the mold. These parameters are demonstrated to be insensitive to the calibration conditions. The thermal behavior of the detailed, three-dimensional mold models used in this work can be approximated closely with a few arithmetic calculations after calibrating the reduced-order model of mold heat transfer.

The example application of the model includes the effects of the molten steel jet on the solidification front and the ferrostatic pressure. The model is demonstrated to match measurements of mold heat removal and the thickness of a breakout shell all the way around the perimeter of the mold, and gives insight to the cause of breakouts in a beam-blank caster. This multiphysics modeling approach redefines the state of the art of process modeling for continuous casting, and can be used in future work to explore the formation and prevention of defects and other practical issues.

This work also explores the eigen-problem for an arbitrary 3x3 matrix. An explicit, algebraic formula for the eigenvectors is presented.

to the radiant C. T.,

may you find the answers to all of your questions

Acknowledgments

Table of Contents

List of Figures

List of Tables

CHAPTER 1
Introduction

Steel is both literally and figuratively the backbone of the industrialized world. No other material has comparable specific strength or specific stiffness at so low a price. It is steel that enables structures to reach nearly hundreds of meters into the sky and bridges to cross great expanses. Continuous casting is the process responsible for more than 95% of the 1.4 billion tonnes of steel produced annually around the world [91], with mind-blowing efficency: production rates are now measured in man-minutes per tonne, whereas not 30 years ago the average production rate was around 10 man-hours per tonne.

A schematic of the continuous casting process is given in Figure 1.1. Molten steel flows under gravity from a ladle into a vessel called the tundish and then into a bottomless, water-cooled copper mold, where the steel begins to solidify. The main purpose of the tundish is to act as a buffer between ladle changes so that the process is continuous. The solidifying "strand" is withdrawn from the bottom of the mold at a rate called the "casting speed," which matches the rate at which new metal solidifies. Below the mold, the strand is sprayed with water to finish the solidification of the steel. Variants of this basic process are used for casting alloys of aluminium, copper, and magnesium. Further downstream these cast slabs are rolled down into a desired shape, and later into anything from wide-flanged beams to thin sheets used in automotive, food, or other consumer applications.

The copper mold in continuous casting extracts heat from the molten steel by means of cooling water flowing through rectangular and/or circular channels, and also supports the solidifying shell to determine its shape. The mold assembly consists of two wide faces (WFs), two narrow faces (NFs), and their respective waterboxes. The steel waterboxes, either machined single-piece slabs or built up from several slabs, serve to circulate the cooling water in the mold, and also increase the rigidity of the assembly to control the thermal distortion of the mold when it heats up to operating temperature.

Near-net shape continuous casting offers efficient alternatives to the traditional slabs, blooms, and billets. The conventional 250 mm-thick slabs have been replaced by thinner sections in the range of 50 mm–90 mm, starting with the thin-slab caster in the late 1980s. Similarly, blooms have been replaced by a dogbone-shaped "beam-blank" section, which was developed in the late 1960s. Casting these near-net shapes saves on rolling costs, but also
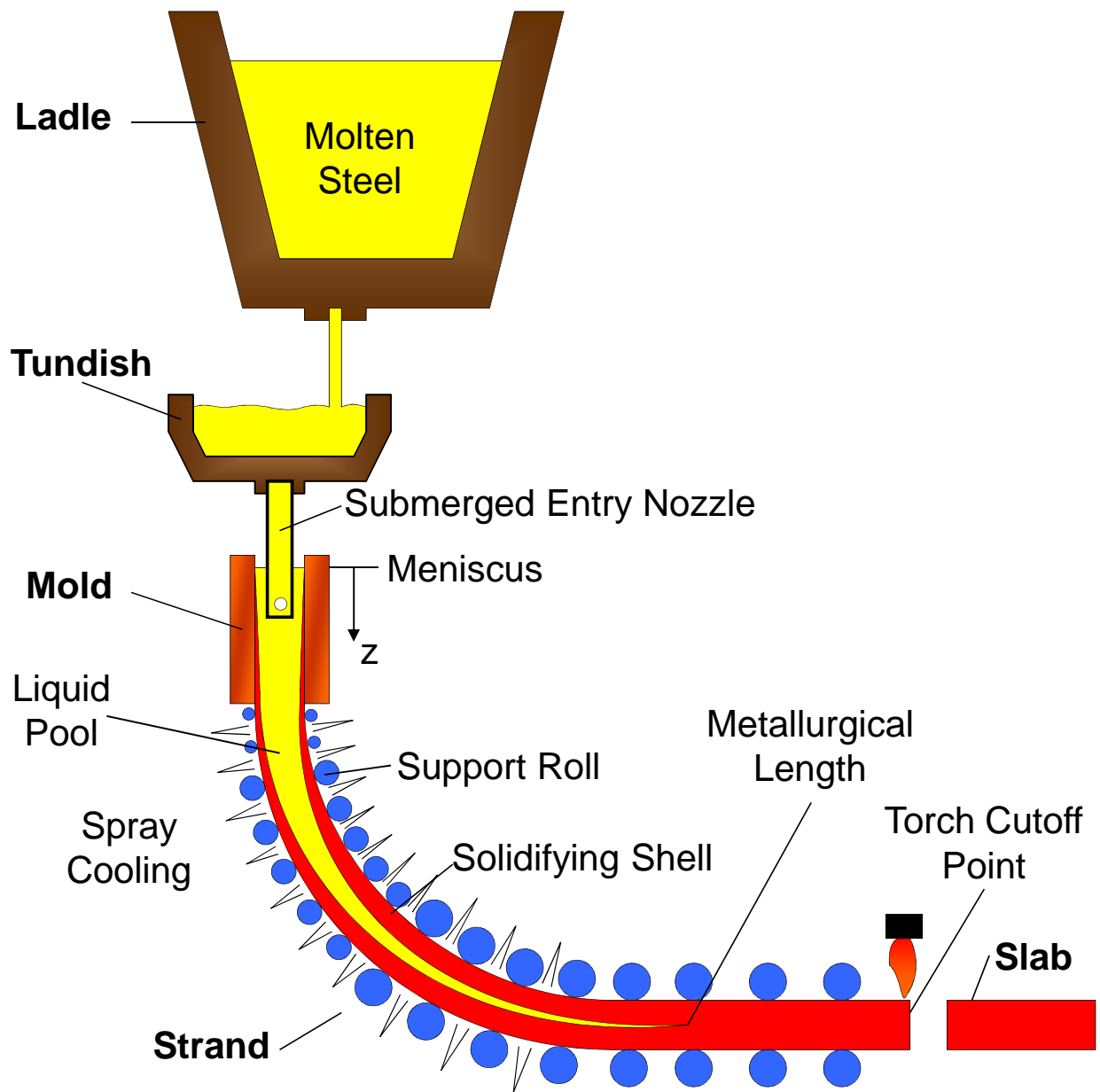
Figure 1.1 Schematic of the steel continuous casting process

offers higher productivity and improved energy efficiency.

A slight taper is applied to the mold pieces to accommodate the solidification shrinkage of the solid steel. Too little taper causes defects in the solidifying steel, because of the reduction in heat flux from the solidifying steel. Locally hot and thin spots of the shell will accumulate strain and eventually the strand will tear open, a defect called a breakout. Conversely, too much taper can lead to excessive wearing of the mold and/or strand, or buckling of the shell and again leading to a breakout.

The efficiency and quality of continuously-cast steel constantly is improving, owing to increased automation and other technological improvements over time. However, as profit margins decrease and energy costs increase, technology growth by empirical methods alone is inefficient and costly; computational modeling is one tool that can help offset the cost of developing the various steel manufacturing processes. A practical application of computational models is the design of the mold geometry, to control the mold temperatures and ultimately avoid crack formation in the solidifying steel shell and the mold itself. The development of mold tapers to match the shrinkage of the solidifying shell is an ongoing challenge that must be met for each cast section and each steel grade. There exists a strong incentive to develop quantitative computational models that can predict the thermo-mechanical behavior of the solidifying steel shell, to improve casting speed or product quality, and reduce the occurrence of defects.

The proliferation of fast computers offers the opportunity to do more with and to learn more about the continuous casting process. Computational process models now are being used in addition to sensors in real-time caster control systems [72]. The complexity of offline models has grown to the point that multiple interacting, coupled fields can be combined and paint an accurate and realistic picture of the continuous casting process, which is the subject of this work. The thermal and mechanical behavior of a beam-blank and funnel mold are explored in Chapters 2 and 4. The mechanical behavior of the funnel mold is validated in this work with new measurements of the orientation of the mold. As fast and as complicated as process models can be, there remains a need for simple-but-accurate models of aspects of the process to use in more-complicated models; Chapter 3 presents a reduced-order model of mold heat transfer that accurately models the three-dimensional mold presented in Chapter 2 with a small fraction of the computational effort. Having a model such as the one presented in Chapter 3 is useful for more complicated models of aspects of the process like the mechanical behavior of the solidifying strand, or of the turbulent flow of the molten steel, where the models already are challenging enough that quite often the mold is assumed down to something inaccurate at best and unrealistic at worst.

Many manufacturing processes besides continuous casting, such as foundry casting, and welding, are governed by multiple coupled phenomena that include turbulent fluid flow, heat transfer, solidification, and mechanical distortion. The difficulty of experiments under such harsh operating conditions makes computational modeling an important tool in the design and improvement of these processes. Continuous casting is particularly difficult to model because of the nature of the process: everything affects everything else. The transport of superheat in the molten steel affects how the steel solidifies, and where the solidified steel is affects how the molten steel flows. The mold removes heat from the steel, which causes thermal contraction of the steel, which changes the amount of heat flowing into the mold. As the mold comes to operating temperature its shape changes, which also changes the heat removal from the steel. The interface between the mold and the steel is sensitive to the size of the gap between them, the material in the gap, and the temperature on both sides of the gap. Each of these issues – and more – are different for each grade of steel. Coupling together the different models of the different phenomena to make accurate predictions of these processes remains a challenge. Chapter 5 presents a multi-physics, multi-field, multi-domain model of the continuous casting process that accounts for all of these phenomena.

A serendipitous (re)discovery of the author was an explicit algebraic formula for the eigenvectors of a 3×3 matrix. Appendix B discusses this eigenproblem, which appears all throughout mechanics.

CHAPTER 2
Steady-State Thermal Behavior of the Mold[1]

2.1 Introduction

This chapter investigates the thermal behavior of a beam-blank and a funnel continuous casting mold at steady casting conditions. Mold heat transfer is an important and widely-researched topic, because the mold governs the initial solidification and surface quality of the final product. The results from this chapter are used in Chapter 4 to investigate the thermal distortion of the molds, and the thermal and mechanical results together are a part of the multiphysics simulations presented in Chapter 5.

The continuous casting literature has several examples of mold heat transfer models. Some of these models investigate only phenomena related to mold heat transfer [11, 81], like cooling-channel design [55, 95, 97, 110], or the effect of mold thickness on various process variables [84]. Some analyses are a part of an inverse model to calculate information about the heat extraction from the strand [18, 19, 22, 54, 74, 102, 108, 111, 112], but these models without exception simplify the mold geometry to a rectangle or slab. Most of the previous work on mold heat transfer has simplified the geometry of the mold in the interest of computational efficiency, and this work seeks to explore mold heat transfer with an accurate description of the geometry, as well as using boundary conditions from other models of continuous casting that have been calibrated with plant measurements.

2.2 Model Description

The temperature field $T(\boldsymbol{x})$ within the mold is governed by the conservation of energy,

$$0 = \nabla \cdot (\boldsymbol{K} \cdot \nabla T),\qquad(2.1)$$

where $\boldsymbol{K}$ is the thermal conductivity tensor. The mold is composed of isotropic polycrystalline copper, so the thermal conductivity tensor is

$$\boldsymbol{K} = k\boldsymbol{I},\qquad(2.2)$$

---

[1]Much of the work presented in this chapter has been published by the author, for beam-blank molds [35] and for funnel molds [33]. Beyond the content of these articles, this chapter contains an updated literature review and some details that were not included in the original publications. The measurements presented in this chapter were provided by C. Spangler at Steel Dynamics, and G. Abbel and R. Schimmel at Tata Steel.

where k is the isotropic thermal conductivity and I is the second-rank identity tensor. The temperature dependence of the thermal conductivity of mold copper alloys has a negligible effect on the calculated temperature field [81], so the governing equation simplifies to

$$0 = \nabla^2 T. \tag{2.3}$$

The hot face of the mold is supplied a heat flux,

$$-k\nabla T \cdot \boldsymbol{n} = q_{\text{hot}}, \tag{2.4}$$

where $q_{\text{hot}}(\boldsymbol{x})$ is the heat flux from the solidifying strand and $\boldsymbol{n}$ is the unit normal vector of the surface. This heat load is applied only on the "active" hot face in contact with the solidifying strand, from the meniscus to mold exit and in between the mold pieces. The surfaces of the water channels are supplied a convection condition,

$$-k\nabla T \cdot \boldsymbol{n} = h_{\text{water}} \left(T - \bar{T}_{\text{water}} \right), \tag{2.5}$$

where $h_{\text{water}}(\boldsymbol{x})$ and $T_{\text{water}}(\boldsymbol{x})$ are the heat transfer coefficient and bulk temperature of the cooling water. All other faces of the mold are insulated,

$$-k\nabla T \cdot \boldsymbol{n} = 0, \tag{2.6}$$

because of symmetry or by assuming that all heat input to the mold from the steel is removed by the cooling water. This assumption on the heat removal allows the waterbox to not be included in the thermal analysis.

For all simulations, the water convection coefficient h_{water} is calculated with a forced-internal-flow empirical correlation. The Sleicher and Rouse [89] model,

$$\text{Nu} = 5 + 0.015\,\text{Re}^{a_1}\,\text{Pr}^{a_2}, \tag{2.7}$$

where

$$a_1 = 0.88 - \frac{0.24}{4 + \text{Pr}}, \tag{2.8}$$

$$a_2 = \frac{1}{3} + 0.5\exp(-0.6\,\text{Pr}), \tag{2.9}$$

is used in this work because of its accurate fit, on average about 7% error [89], with measurements. The Nusselt number,

$$\text{Nu} = \frac{h_{\text{water}} D_{\text{h,c}}}{k_{\text{water}}}, \tag{2.10}$$

from which the water convection coefficient h_{water} is calculated, is evaluated at the bulk temperature of the water, $\bar{T}_{\text{water}}$. The Prandtl number,

$$\text{Pr} = \frac{\mu_{\text{water}} c_{p,\text{water}}}{k_{\text{water}}}, \tag{2.11}$$

is evaluated at perimeter-average temperature of the water channel surface, T_{c}, and is valid for $10^{-1} \le \text{Pr} \le 10^5$. The Reynolds number,

$$\text{Re} = \frac{\rho_{\text{water}} \bar{v}_{\text{water}} D_{\text{h,c}}}{\mu_{\text{water}}}, \tag{2.12}$$

is evaluated at the "film" temperature $T_{\text{film}} = \frac{1}{2}\left(\bar{T}_{\text{water}} + T_{\text{c}}\right)$, and is valid for $10^4 \le \text{Re} \le 10^6$. The hydraulic diameter $D_{\text{h,c}}$ of the water channel is defined as four times the cross-sectional area divided by the perimeter length. The average speed of the water in the channel,

$$\bar{v}_{\text{water}} = \frac{Q_{\text{water}}}{A_{\text{c,total}}}, \tag{2.13}$$

is calculated from the total volumetric flow rate of the cooling water Q_{water} measured in the plant and the total cross-sectional area $A_{\text{c,total}}$ of all water channels in the mold. The water properties vary with temperature T in °C according to

$$k_{\text{water}}(T) = 0.59 + 0.001\,T, \tag{2.14}$$

$$\rho_{\text{water}}(T) = 1000.3 - 0.040\,286\,T - 0.003\,977\,9\,T^2, \tag{2.15}$$

$$c_{p,\text{water}}(T) = 4215.0 - 1.5594\,T + 0.015\,234\,T^2, \tag{2.16}$$

$$\mu_{\text{water}}(T) = 2.062 \times 10^{-9}\rho_{\text{water}}10^{\frac{792.42}{T+273.15}}, \tag{2.17}$$

with thermal conductivity k_{water} in W/(m·K), mass density ρ_{water} in kg/m^3, isobaric specific heat capacity $c_{p,\text{water}}$ in J/(kg·K), and dynamic shear viscosity μ_{water} in Pa·s. For conditions typical of continuous casting, $\text{Pr} \approx 4$ and $\text{Re} \approx 1.5 \times 10^5$, so Equation (2.7) is used safely. Equation (2.7) also assumes that the flow in the channel is fully developed, which for continuous casting requires that the position of the meniscus of the liquid steel occurs lower in the mold than the entry length of the channel, or with the usual liberal estimate that $z_{\text{men}}/D_{\text{h,c}} > 10$.

Continuous casting molds are designed and operated such that almost all heat is removed by the water in the cooling channels; this observation allows many simplifications to be made in the modeling of the thermal distortion of the mold. The waterbox is taken as thermally inert, which simplifies the coupling between the thermal and mechanical fields; the thermal expansion drives the distortion of the mold, but the distortion does not affect the temperature field in the mold.

The finite-element method is employed to solve this thermal boundary-value problem, using the commercial software ABAQUS [1]. The molds are modeled with complete geometric detail, including the mold plates, water channels, and bolt holes, as discussed in Sections A.2 and A.1. The domains are discretized with a mix of "fully-integrated" linear 4-node tetra-hedral, 6-node wedge, and 8-node hexahedral elements (ABAQUS diffusion-controlled heat-transfer elements DC3D4, DC3D6, and DC3D8). Numerical experiments with these elements in similar thermal problems [1] has shown them quite capable of matching analytical solutions, so numerical artifacts are of little concern. The hot face heat load is applied with the user subroutine DFLUX. The convection boundary condition given in Equation (2.7) is implemented with the user subroutine FILM.

2.3 Beam-Blank Mold

2.3.1 Model Details

The geometry of the beam-blank mold and waterbox analyzed in this work is presented in Section A.2. The mold has a constant thermal conductivity $k_{\mathrm{mold}} = 370 \, \mathrm{W/(m \cdot K)}$. For the beam-blank mold considered in this work, the shell-mold heat flux profile was calculated with a two-dimensional Lagrangian analysis of the solidifying steel shell, which is discussed further in Chapter 5. The specific grade of steel considered in this work is a 0.071% wt. C low-carbon A992 structural steel, cast at 0.899 m/min. This Si- and Mn-killed steel was open-poured from two ceramic funnels located in the center of the flanges, shown in Figure A.6. The wide face convection condition is $h_{\mathrm{water}} = 45 \, \mathrm{kW/(m^2 \cdot K)}$ and $T_{\mathrm{water}} = 33.35 \, {}^\circ\mathrm{C}$. The narrow face convection condtion is $h_{\mathrm{water}} = 34 \, \mathrm{kW/(m^2 \cdot K)}$ and $T_{\mathrm{water}} = 34.48 \, {}^\circ\mathrm{C}$.

2.3.2 Heat Input to the Mold

The heat flux from the shell is presented in Figure 2.1 around the perimeter of the mold at multiple locations down the mold, and in Figure 2.2 down the mold at multiple locations around the perimeter. This heat flux field inputs to the water the energies listed in Table 2.1, which match well with values measured in the plant, based of the temperature change of the mold water, which is discussed in Section 3.3.3. This model over-predicts the WF heat removal but underpredicts the NF heat removal, for a total overprediction of about 4%. Matching the heat flux measurements is a difficult task because the interfacial gaps are not known *a priori*; this agreement was acheived by iteration with the parameters in the interfacial gap

Table 2.1   Beam-blank mold measured and predicted heat removal

	Measurement (kW)	Model (kW)	Error (%)
Wide face	1112.4	1204.7	+8.30
Narrow face	651.4	634.2	−2.64
Total	1763.8	1838.9	+4.26

model described in Section 5.6.

2.3.3   Thermocouple Temperature Validation

The mold considered in this work was specially instrumented with 47 thermocouples, shown in Figures 2.3 and A.7. The thermocouple temperatures resented in Figures 2.4 and 2.5 were averaged over 30 min of steady casting. These thermocouple temperatures are adjusted to account for the heat lost along the thermocouple wire, as discussed in Section 3.4.3. The chromel-slumel thermocouples used in this work with wire diameter $D_{TC} = 3.175\,\text{mm}$ and thermal conductivity $k_{TC} = 19.2\,\text{W/(m}\cdot\text{K)}$ are adjusted with Equation (3.45) for a gap between the mold and thermocouple of size $d_{gap} = 0.01\,\text{mm}$ and thermal conductivity $k_{gap} = 0.026\,\text{W/(m}\cdot\text{K)}$, since no thermal paste was used in the plant. The wire convection coefficient h_{wire} is taken as $3\,\text{kW/(m}^2\cdot\text{K)}$ if the thermocouple passes through water, or as $0.06\,\text{kW/(m}^2\cdot\text{K)}$ if the thermocouple is only in ambient air. The ambient temperature is taken as $25\,°\text{C}$, regardless of the medium. The shoulder thermocouple passes through water; all others pass through air. All thermocouples give low values before adjustment; the air gap significantly changes the thermocouple temperatures.
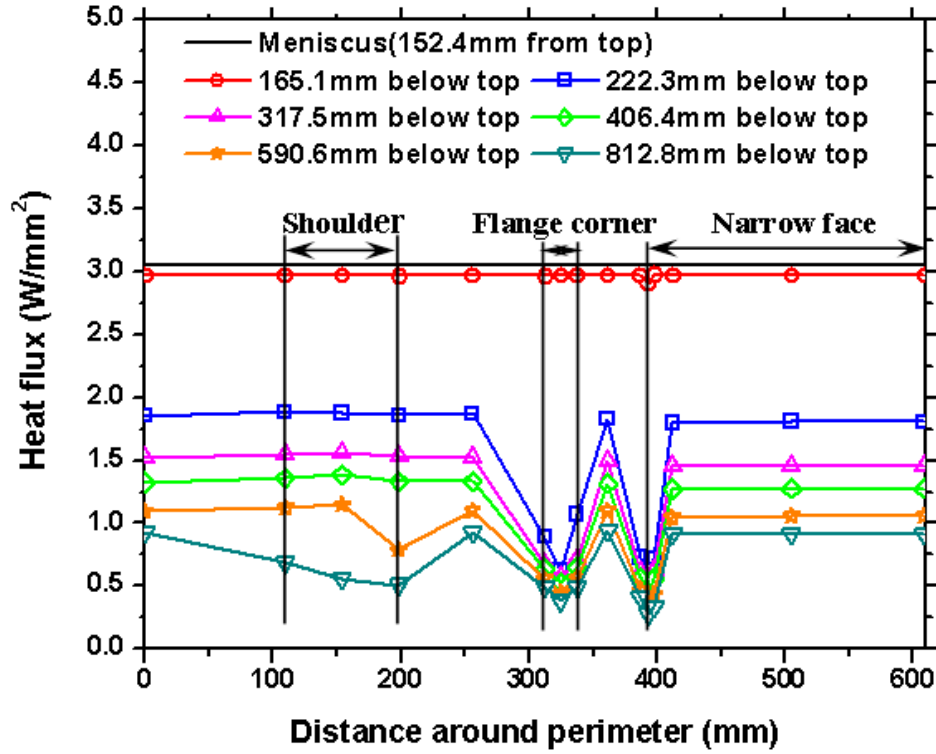
Figure 2.1 Beam-blank mold applied heat flux around the mold perimeter
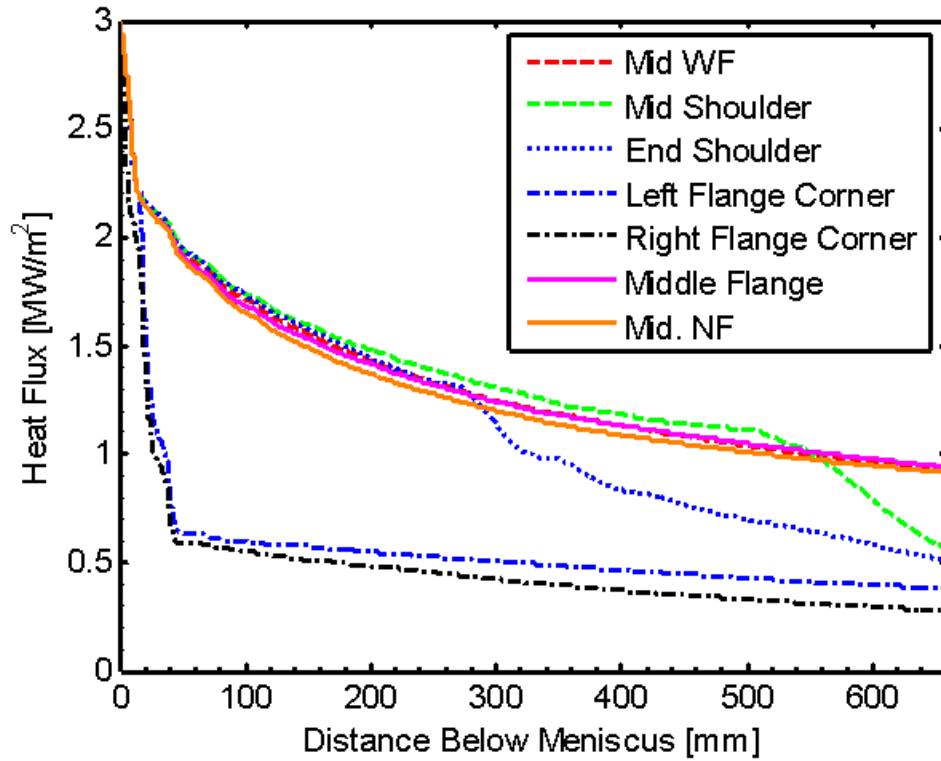
Figure 2.2 Beam-blank mold applied heat flux down the length of the mold

Figure 2.3 Back of the beam-blank mold instrumented with 47 thermocouples
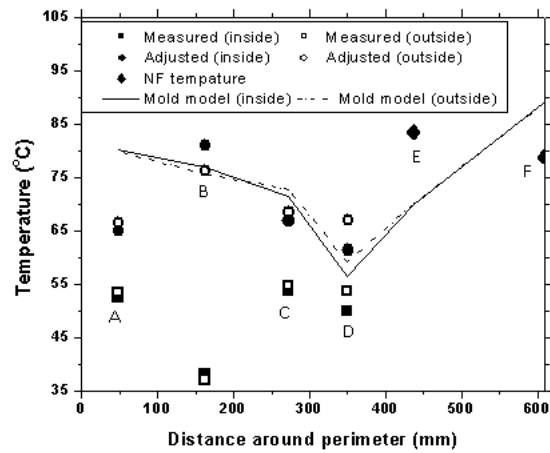
Figure 2.4 Beam-blank mold thermocouple temperatures around the mold perimeter
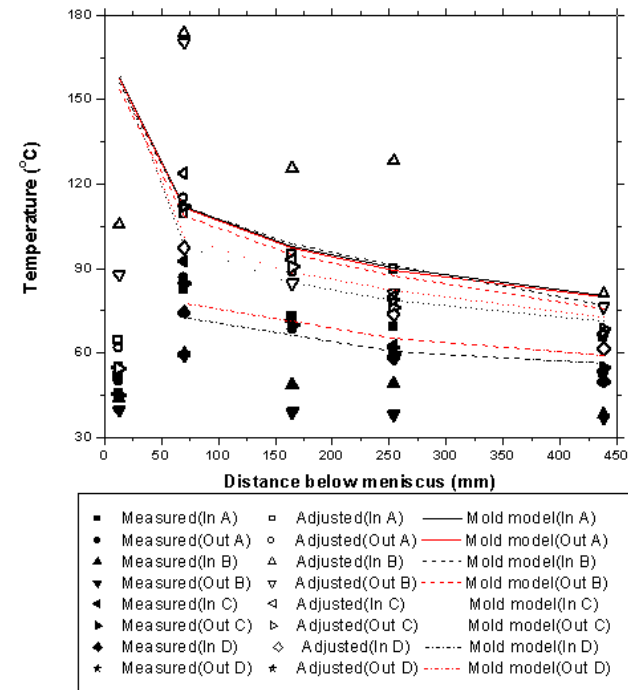
Figure 2.5 Beam-blank mold thermocouple temperatures down the length of the mold

2.3.4   Mold Heat Transfer

The calculated mold temperatures are shown in Figures 2.6 through 2.10. The hot face on both the outer radius and the inner radius molds show a substantial hot spot just below the meniscus at the shoulder, as shown in Figure 2.7 and 2.8. The hot spot is caused by a combination of converging heat flow at the shoulder of the mold, and insufficient cooling to remove this locally higher heat load. Mold cracks have been observed [95] in the region of the hot spot, as shown in Figure 2.11 for a mold with a chromium coating layer. This delamination failure was reduced by adding a small cooling channel in the shoulder and reducing the temperature of the hot face [95]. This variation in hot face temperature around the perimeter of the mold also can affect the behavior of the solidifying steel, which is discussed further in Chapter 5. The higher hot face temperature indicates that the heat locally is not extracted as efficiently as neighboring regions of the hot face, which indicates that the shell has locally higher temperatures, and generally means weaker steel. Thus, the shoulder region is the most likely region for problems in the solidifying shell. As seen in Figures 2.6 through 2.10, the hot face temperatures increase by about 30 °C near mold exit because the cooling channels turn 90° to exit out of the back of the mold; this higher temperature, and again a local hot spot at the shoulder, at mold exit, can be harmful to the shell, as discussed above.

The narrow face also has hot spots near the meniscus because of the variable distance from the water channels to the edges of the mold; as shown in Figure 2.9, the outer-radius edge of the NF mold has higher temperatures in the middle of the mold, and the inner-radius edge has higher temperatures near the meniscus. These temperature patterns can cause variations in the amount of edge-crushing in the NF–WF contact, perhaps leading to "fin defects" as described in previous work [98].
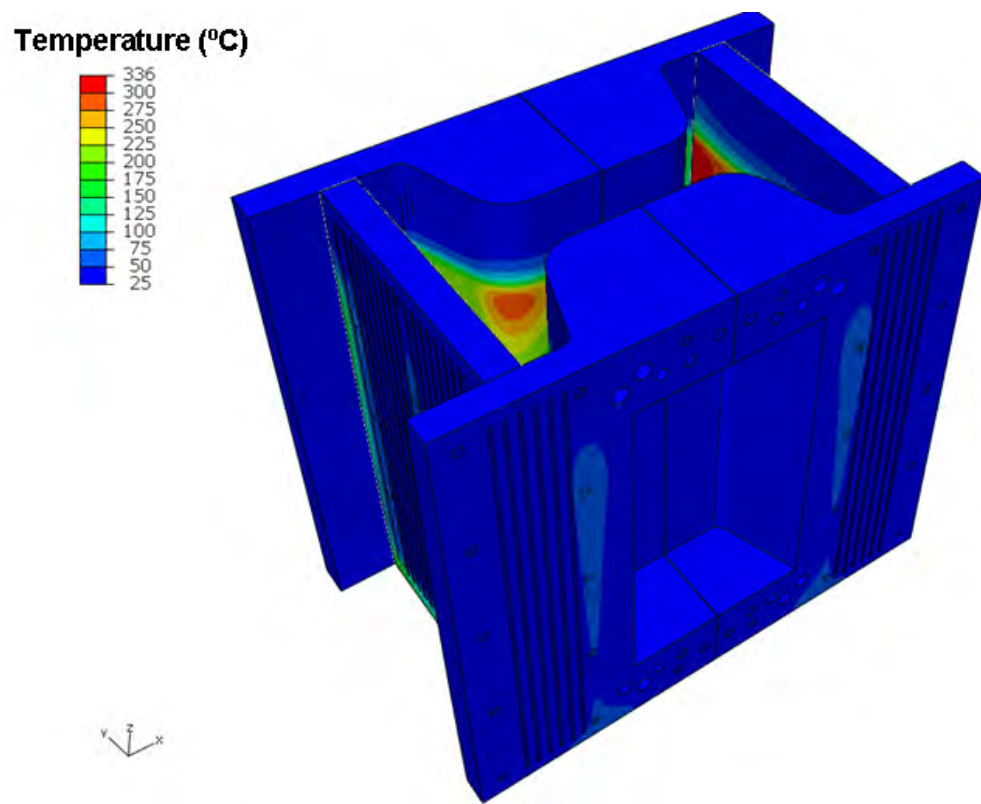
Figure 2.6   Beam-blank mold calculated temperatures
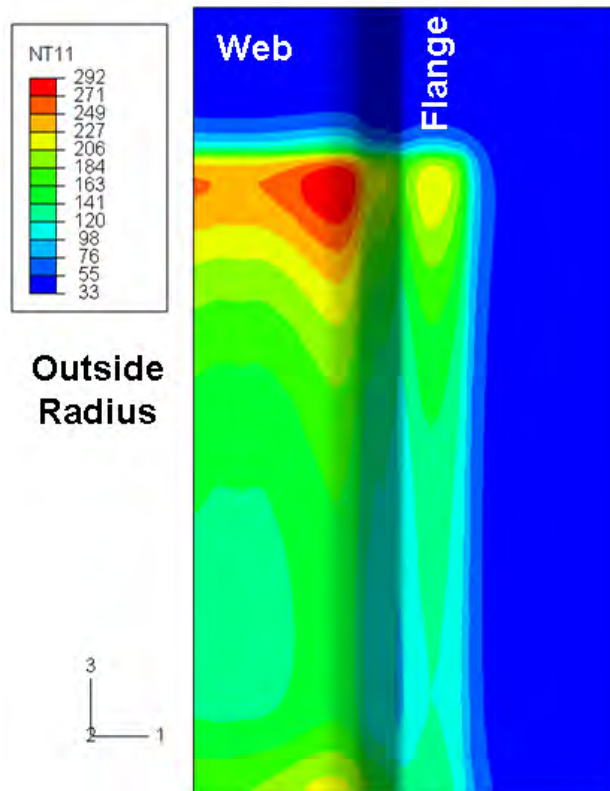
Figure 2.7 Beam-blank mold hot-face temperatures on the outer radius wide face (temperature in °C)
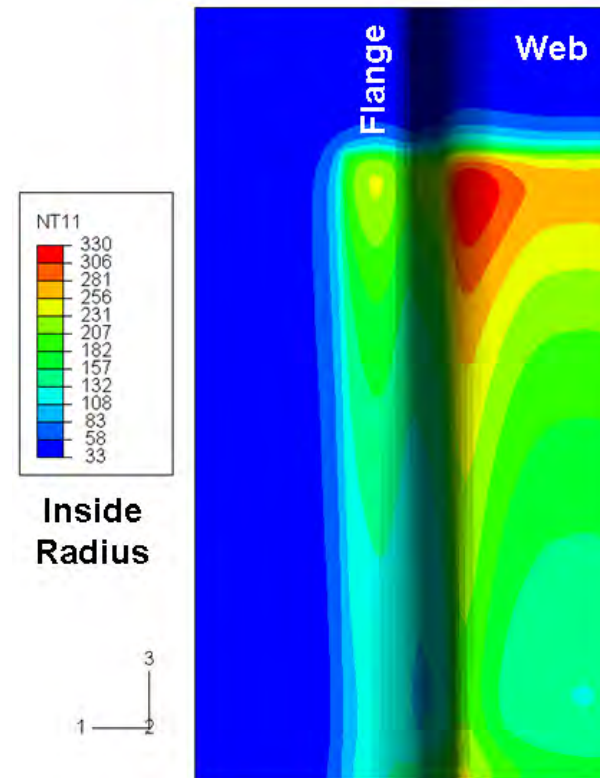
Figure 2.8 Beam-blank mold hot-face temperatures on the inner radius wide face (temperature in °C)
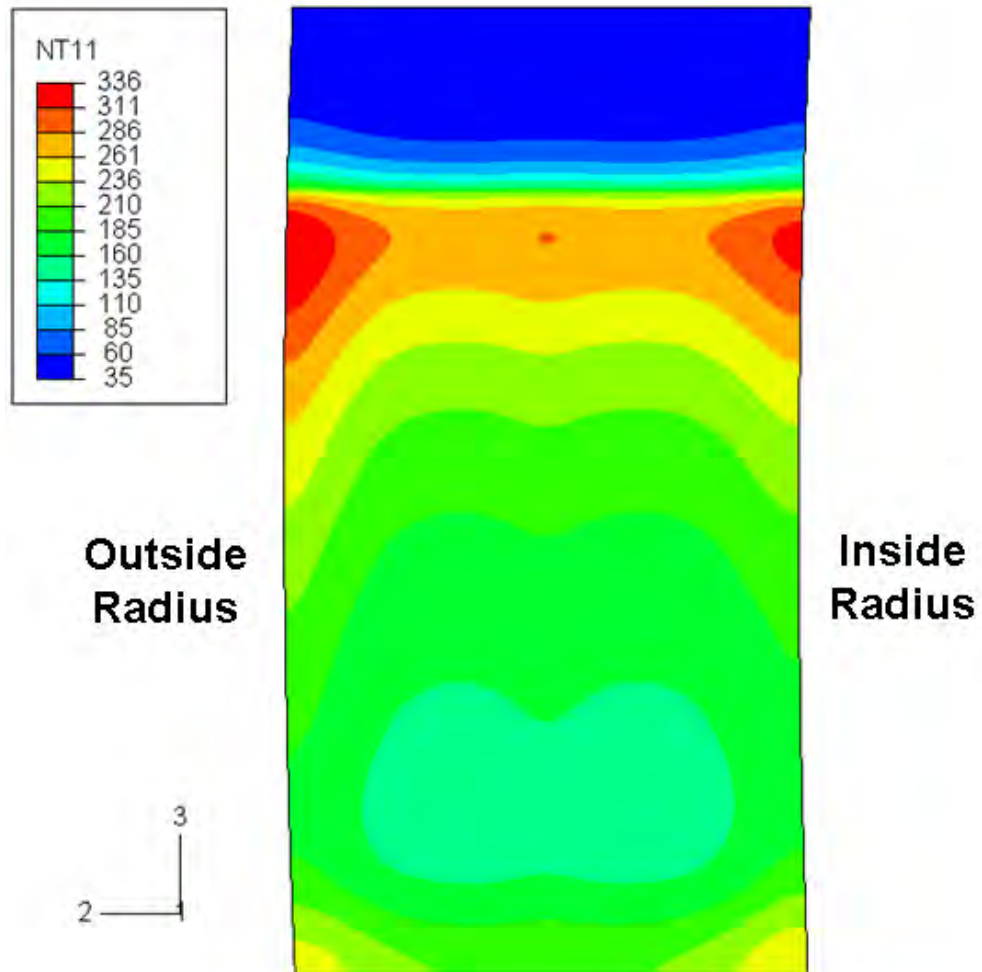
Figure 2.9   Beam-blank mold NF temperatures
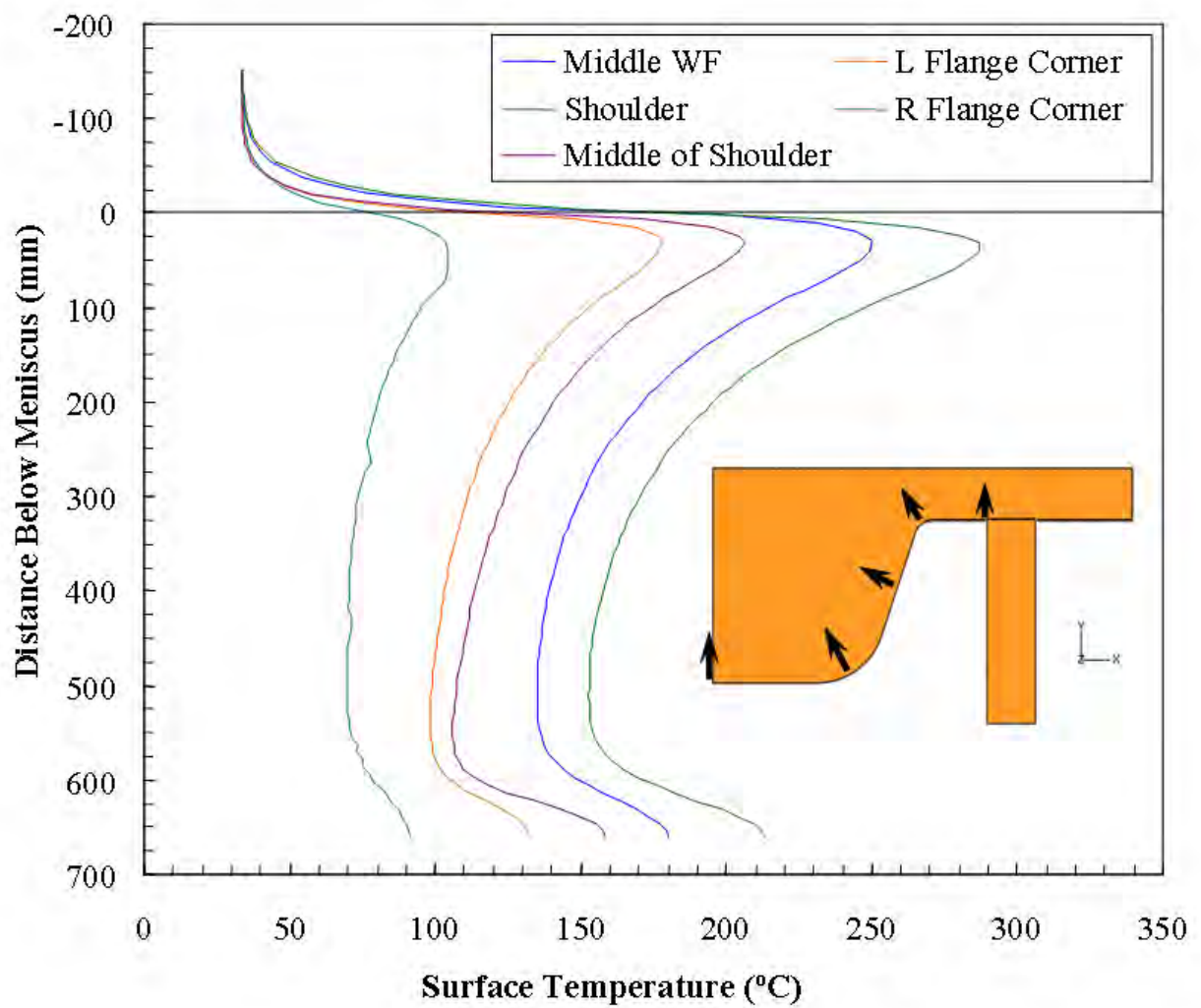
Figure 2.10 Beam-blank mold WF hot face temperatures
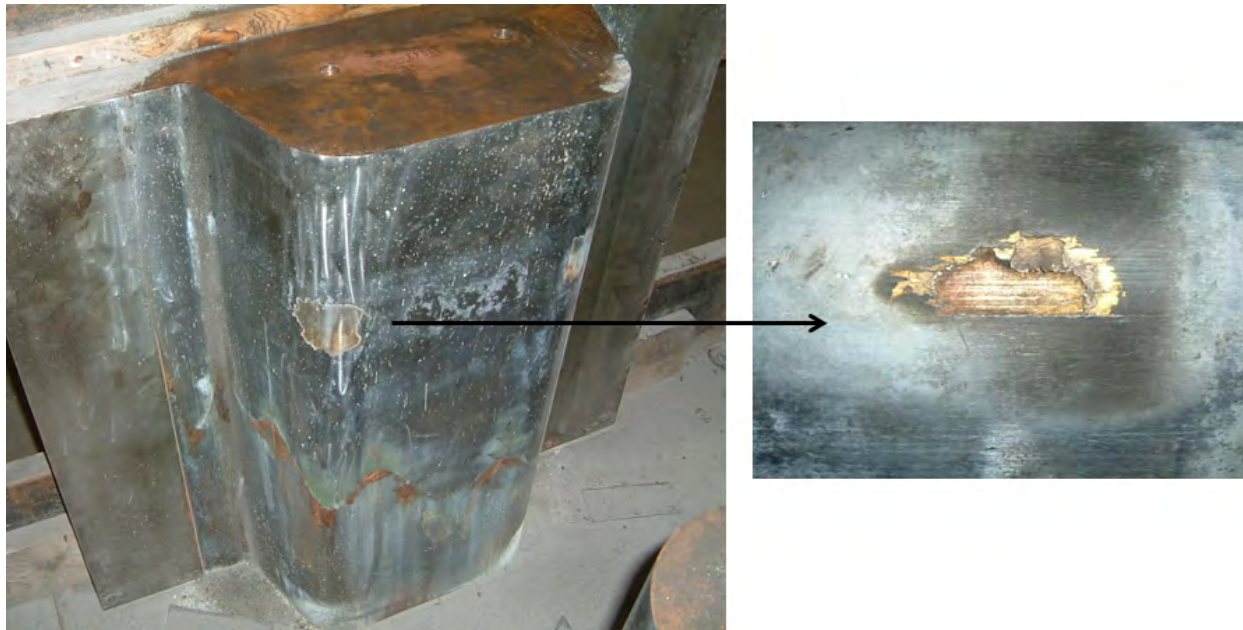
Figure 2.11 Beam-blank mold failure of hot-face coating layer, coincident with hot spot predicted by numerical model [97]

2.4   Funnel Mold

2.4.1   Model Details

The geometry of the funnel mold and waterbox analyzed in this work is presented in Section A.1. For the funnel mold considered in this work, the shell-mold heat flux profile, average water channel convection coefficient, and bulk water temperature varied with position down the mold as calculated by the continuous casting process model CON1D [56] that was calibrated in previous work [84]. The values of these three quantities are shown in Figure 2.12 for each mold piece. Specifically, the heat flux profile in Figure 2.12 represents an average heat removal of $2.7 \, \mathrm{MW/m^2}$, which is close to the $2.8 \, \mathrm{MW/m^2}$ measured during typical casting of a 0.045% wt. C low-carbon, 90 mm-by-1200 mm Al-killed and Ca-treated steel slab cast at 5.5 m/min, with 14 °C superheat and 8.5 m/s water velocity. The mold material is CuCrZr alloy with a constant thermal conductivity $k_{\mathrm{mold}} = 350 \, \mathrm{W/(m \cdot K)}$. With 1 089 166 total degrees of freedom, this linear heat-conduction problem requires about 12 min to solve on an 8-core 2.66 GHz workstation with 8 GB of RAM.
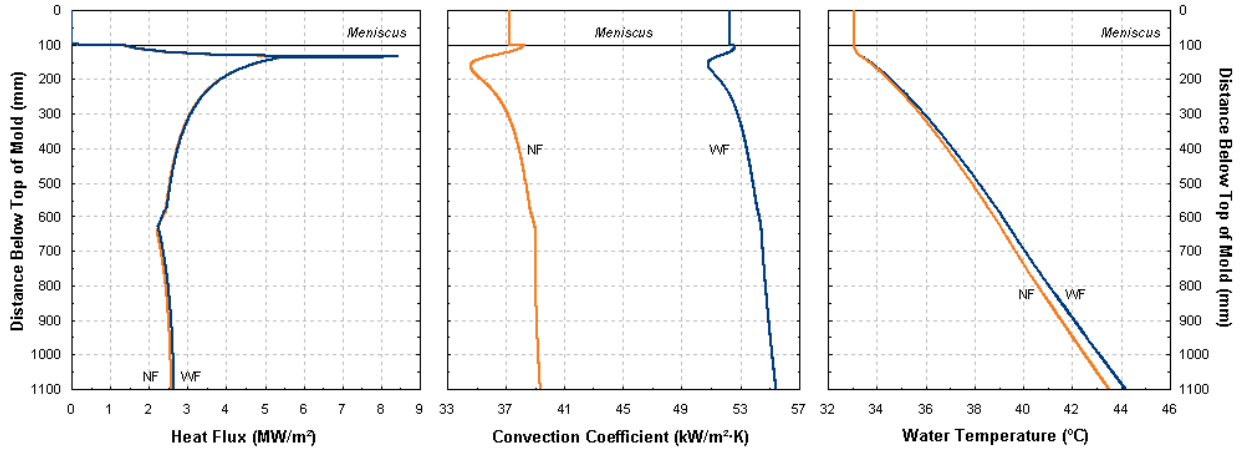
Figure 2.12   Funnel mold steady-state heat flux and water channel convection coefficient and bulk temperature

2.4.2   Mold Heat Transfer

The calculated surface temperatures of the wide-face and narrow-face mold pieces are shown in Figures 2.13 and 2.14. The field is clearly three-dimensional and is affected by both the cooling channels and the funnel geometry. Hot-face temperature profiles around the WF mold perimeter are shown in Figure 2.15 at various distances down the length of the mold. The hot
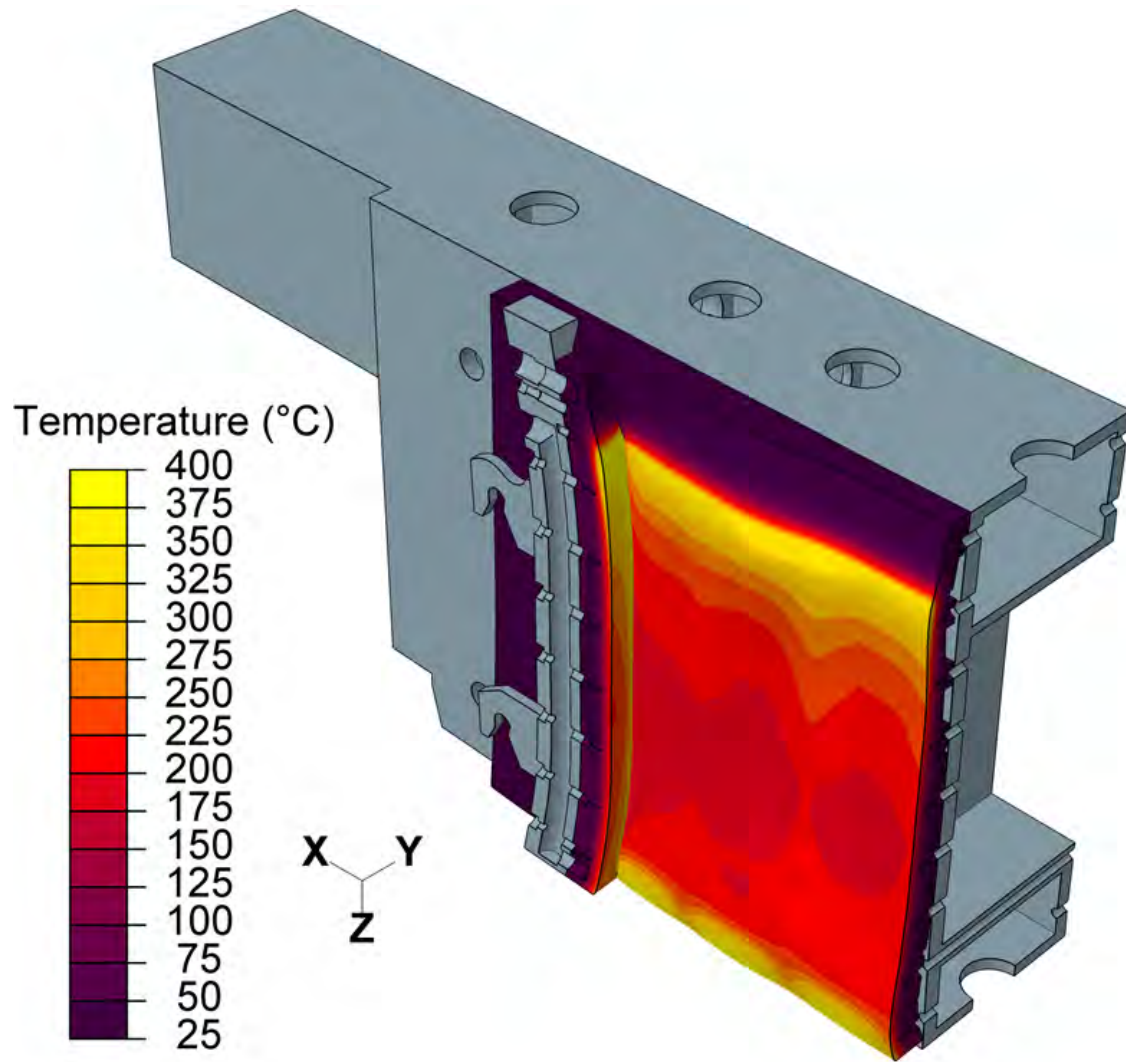
Figure 2.13   Calculated funnel mold temperature field (50 times scaled distortion)

face of the wide face shows temperature variations around its perimeter mainly because the vertical water tubes near the bolts are further from the hot face, and thus extract heat less efficiently than the channels. This effect causes regions beneath the bolt holes to be hotter locally by about 15 °C over most of the length of the mold. The wider channel cut for the mold level sensor also disturbs the uniformity of the surface temperatures, but this effect is much smaller than the change in cooling around the bolt columns.
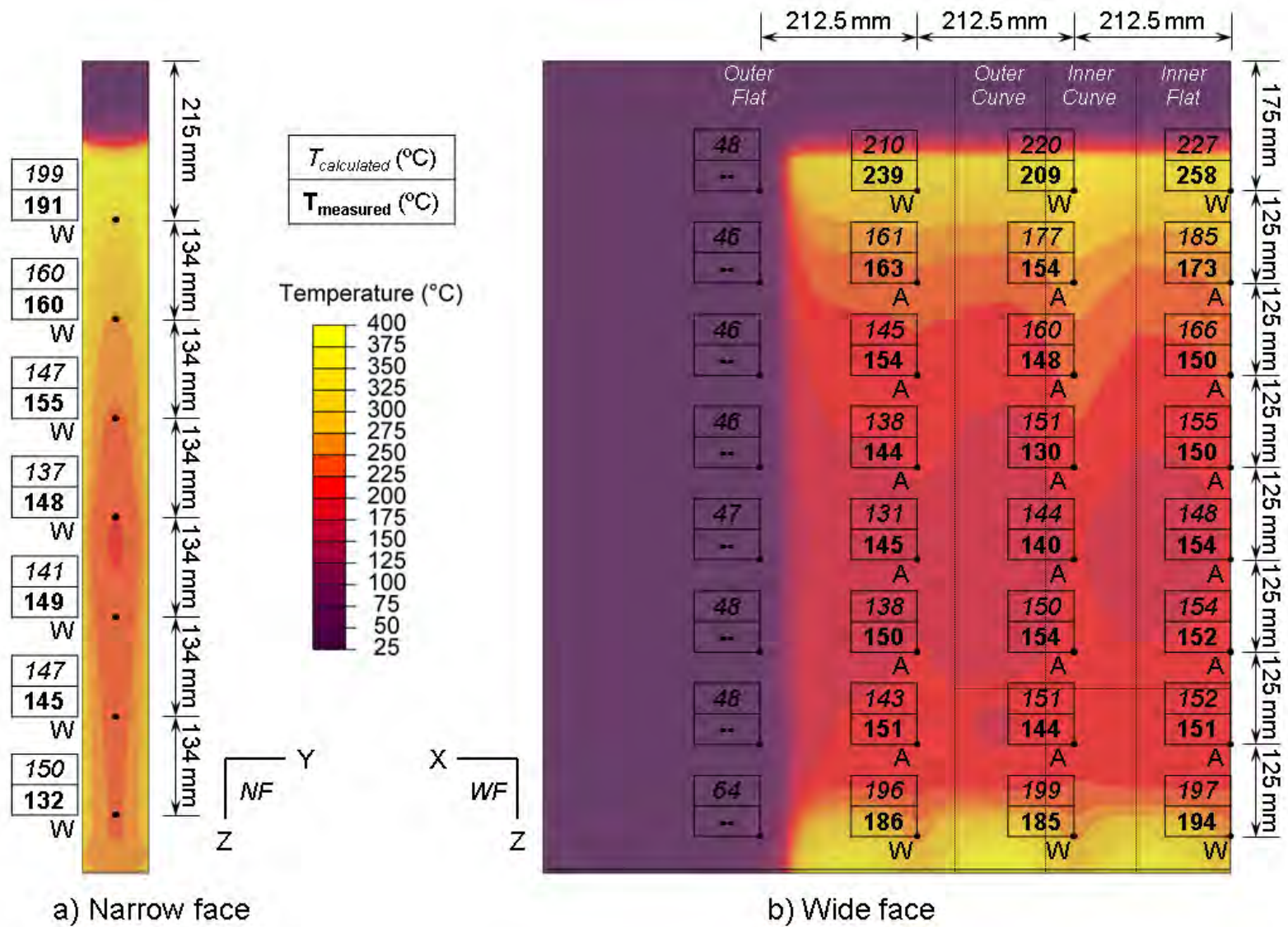
Figure 2.14 Calculated funnel mold hot face (contours) and thermocouple (boxes) temperatures for the (a) narrow face and (b) wide face

21

The funnel geometry adds a very small two-dimensional effect to the heat extraction. The "inside-curve" region of the funnel surface, discussed in Section A.1, extracts slightly *more* heat than the flat regions, resulting in a cooler shell and warmer mold by about 2 °C (diverging heat flow). The "outside-curve" region of the funnel surface extracts slightly *less* heat, resulting in a warmer shell and a cooler mold (converging heat flow). The column of bolts in the middle of the inside-curve region perhaps may contribute to the increased number of longitudinal cracks observed in that region in the shell [30]. The funnel shape appears to have no other effect on heat transfer, owing to the constant distance of the cooling channel roots from the hot face, even though the channels are cut perpendicular to the back face and not to the funnel itself.

The bottom portion of the mold shows much larger surface temperature variation, by more than 120 °C, because the cooling channels cannot extend to the bottom of the mold, as pictured in Figure 2.16. This causes increasing temperature towards the mold bottom at the water channels, with peak temperatures of almost 350 °C, which is similar to the region of peak heat flux near the meniscus. This effect is less near the water tubes because they extend further down the mold than the curving water channels.

The surface temperature of the mold is higher locally by 10 °C–25 °C near the center of the inside-curve region of the funnel for most of the length of the mold. This higher mold temperature, and resulting change in heat transfer across the shell-mold gap, especially near the meniscus, can lead to longitudinal facial cracks (LFCs) in the shell. The temperature and heat-flux variations around the perimeter cause corresponding variations in the temperature and thickness of the solidifying steel shell, causing strain concentration and hot tears at the liquid films between the largest, weakest grain boundaries. Previous work [30, 32] found more depression-style LFCs in this region due to shell bending caused by the funnel. The higher mold surface temperature of this region may exacerbate the problem. This important cracking mechanism deserves further study.

The temperature profile down the length of the narrow face mold at the centerline is shown in Figure 2.17. The narrow face exhibits less variation of surface temperature around the perimeter because the cooling channel design is more uniform and the mold is relatively narrow. Due to the concave shape of the narrow face hot face, the extra copper between the water and the hot face serves to increase the mold hot face temperature slightly towards the slab corners. This effect could contribute to "finning" defects and sticker breakouts due to inelastic squeezing of the narrow-face edges, according to the mechanism described in previous work [98].
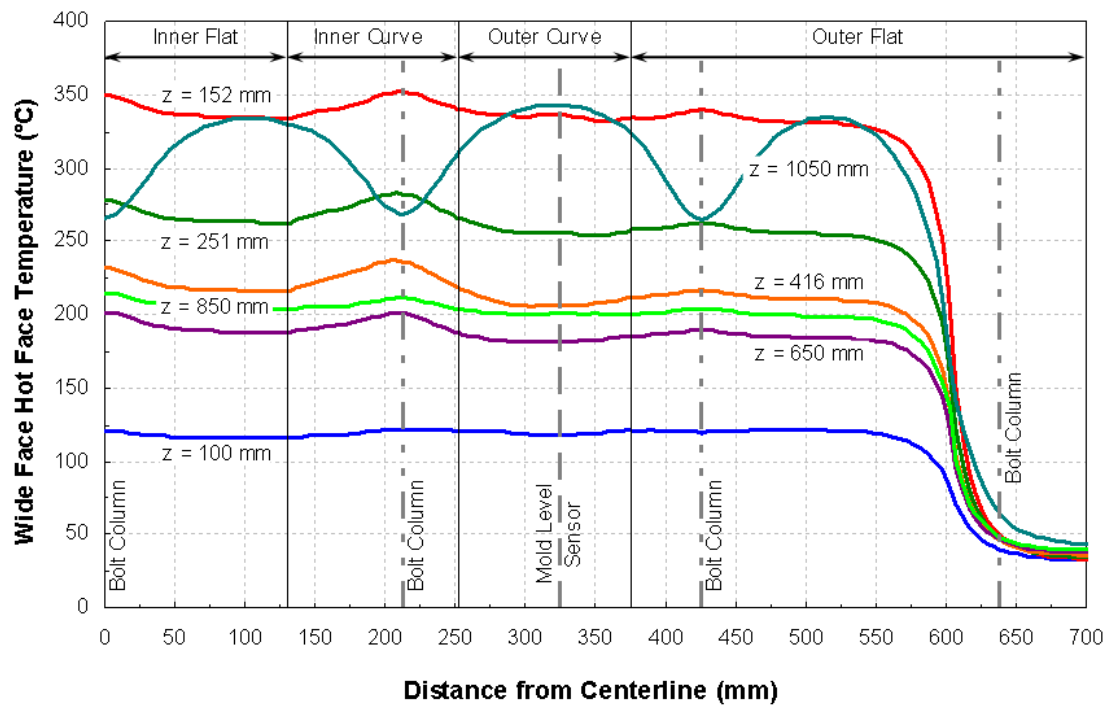
Figure 2.15 Funnel mold hot face temperature profiles around perimeter of mold
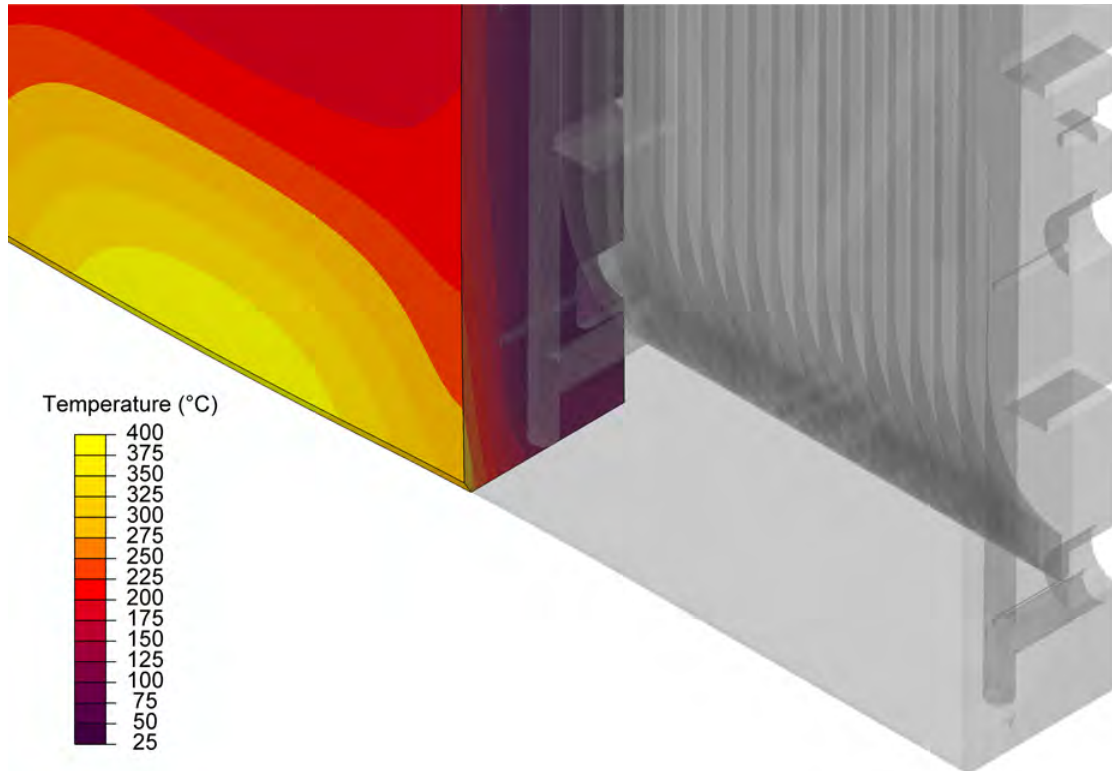
Figure 2.16 Funnel mold hot face temperaturs near mold exit
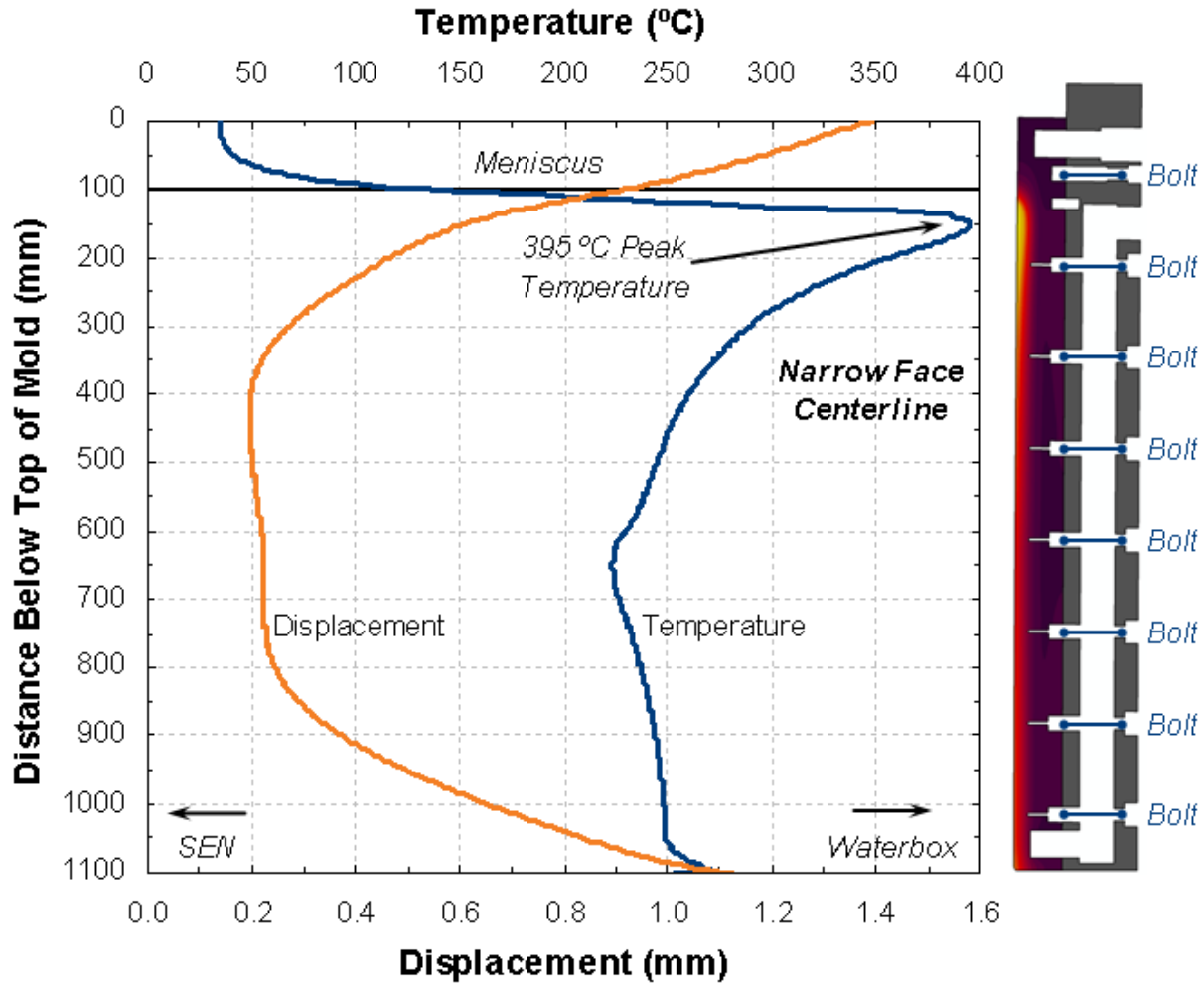
Figure 2.17 Funnel mold hot face temperature and distortion profiles for the narrow face mold

2.4.3 Thermocouple Temperature Validation

To further validate the model, the model predictions (top boxes) of thermocouple temperatures are compared against their measured values (bottom boxes) in Figure 2.14. Plant data were selected for conditions close to those modeled, except that the strand width was 1300 mm, contrasting with 1200 mm in the model. The model therefore underpredicts significantly the temperatures of the thermocouple column furthest from the centerline of the wide face, and these temperatures are not given.

The measured thermocouple temperatures were time-averaged over 30 min of steady casting and then adjusted to account for heat removal through the thermocouple wires. As discussed in Section 3.4.3, the thermocouples act like long pin-fins, and the adjustment to

24

the thermocouple temperature to account for this effect is given in Equation (3.45). The copper-constantan thermocouples used in this work with wire diameter $D_{\mathrm{TC}} = 4\,\mathrm{mm}$ and thermal conductivity $k_{\mathrm{TC}} = 212\,\mathrm{W/(m \cdot K)}$ are adjusted using a gap between the mold and thermocouple of size $d_{\mathrm{gap}} = 0.01\,\mathrm{mm}$ and thermal conductivity of $k_{\mathrm{gap}} = 1.25\,\mathrm{W/(m \cdot K)}$. The wire convection coefficient h_{wire} is taken as $5\,\mathrm{kW/(m^2 \cdot K)}$ if the thermocouple passes through water, or as $0.1\,\mathrm{kW/(m^2 \cdot K)}$ if the thermocouple is only in ambient air. The ambient temperature is taken from the CON1D model predictions of cooling water temperature if the thermocouple passes through water, or as $25\,^{\circ}\mathrm{C}$ if the thermocouple is only in ambient air. Figure 2.14 specifies with an 'A' or a 'W' which thermocouples are adjusted for air and water.

Generally, the model and measurements match fairly well, usually within $10\,^{\circ}\mathrm{C}$ (5% error). The thermocouples on the narrow faces nearest mold exit are overpredicted, but this observation is expected given that the CON1D model was calibrated for the wide face. Some of the wide face thermocouple measurements showed considerable asymmetry ($30\,^{\circ}\mathrm{C}$–$40\,^{\circ}\mathrm{C}$) between the plates on the inner and outer radius, so deviations from the modeling predictions are expected at those locations. The outer-radius wide face measurements match much better with the model predictions than the inner radius, suggesting a difference between inner- and outer-radius (the outer-radius wide face generally had the higher temperatures). The larger mismatches occur in the funnel region near the meniscus, so the shell might be losing contact with the mold more on one side than on the other.

2.5   Conclusions

This chapter provides insight into the thermal behavior of steel continuous-casting molds during steady casting, based on geometrically-accurate 3D finite-element analyses. The hot face of the mold, regardless of the shape, should maintain a uniform temperature around the perimeter to help reduce the occurrence of cracks in the mold and in the solidifying steel. The geometric accuracy of the models in this chapter reveal variations in the hot face temperature related to the spacing of the water channels, and in particular with the change in cooling related to the water channels around the columns of bolt holes in the back of the mold. Both a beam-blank mold and a funnel mold show that the hot face temperature increases near mold exit because of the change in cooling pattern, which could lead to other problems. This chapter demonstrated a method for calibrating thermocouple temperatures to account for an air gap between the tip of the thermocouple and the mold, and for heat lost along the thermocouple wires. The mold temperatures calculated in this chapter are used in other, more complicated models of the continuous casting process in the following chapters.

CHAPTER 3
Reduced-Order Model of Mold Heat Transfer[1]

3.1   Introduction

This chapter presents a reduced-order model of mold heat transfer in the continuous casting of steel. The reduced-order model itself is based on a one-dimensional solution to the heat-conduction equation, and the up-front cost of the reduced-order model is a single three-dimensional finite-element calculation of a small portion of the exact mold geometry. This three-dimensional calculation is used to calibrate the geometric parameters in the one-dimensional temperature model. Other features of the reduced-order model, namely the cooling water temperature change and thermocouple temperatures, are derived in a consistent manner with the one-dimensional solution. The reduced-order model calibration is demonstrated for four actual continuous casting molds. Combined with models of solidification and mold-metal interfacial phenomena, this accurate and efficient modeling tool can be applied to gain insights into aspects of heat transfer in the continuous casting process.

"Reduced-order modeling" is a technique that seeks to reduce the complexity of a system while robustly maintaining the relationship between inputs and outputs. After an up-front cost to develop the model, a reduced-order model (ROM) executes in a small fraction of the time of a full-order model with nearly the same accuracy. This reduction of complexity occurs by simplifying physical relationships, like linearizing or decoupling physical phenomena, or reducing the degrees of freedom of a system. Least-squares regression is the simplest form of model reduction: a large number of points are replaced by a few polynomial coefficients that define a continuum. The one- or two-equation turbulence models commonly used in computational fluid dynamics are a reduction of the complexity of the Navier–Stokes equations, though the difficulty of solving the discretized partial differential equations (PDEs) remains. Reducing the degrees of freedom in such a PDE discretization is the subject of

---

[1]Much of the work presented in this chapter has been published [31] or will appear in articles by the author and collaborators. R. J. O'Malley initially had the idea of correcting the geometric effect of the mold thermocouples, which was explored by M. M. Langeneckert [47]. J. Iwasaki later identified that additional corrections to the CON1D model were necessary, in particular to attain the correct temperature of the hot face. I. Hwang developed some computational tools that automate the calibration procedure for the mold geometry. The content of this chapter, entirely the work of the author, builds upon the work of Langeneckert and Iwasaki to create a systematic procedure for calibrating the CON1D model of mold heat transfer.

recent literature; techniques like proper-orthogonal decomposition can provide a reduced solution basis that carries most of the physics of the solution [2, 10]. Reduced-order modeling techniques have been used for approximating the transfer function in the solution of ordinary differential equations [73], circuit analysis and design [24], solid mechanics computations for real-time graphics rendering [6], fluid mechanics computations [10], and many other applications.

The back of a typical continuous slab-casting mold is shown in Figure 3.1. The mold is assembled from four single-piece slabs of a copper alloy, *e.g.*, CuBe or CuCrZr, with cooling channels machined into the back side of the slab, shown in Figure 3.1. Pressurized water flows through these channels at speeds near $10\,\mathrm{m/s}$ to remove more than $1\,\mathrm{MW}$ of power from the solidifying steel. Casting machines track the total energy removed from the solidifying steel by the mold, measured indirectly as the temperature change of the cooling water. Some molds include a thin coating layer of nickel or chromium to reduce the wearing of the "hot face," *i.e.*, the face of the mold in contact with the strand. Several bolt holes are machined into the back side of the mold for mounting the mold into its support structure and water-delivery system, collectively called the "waterbox." Molds are instrumented with thermocouples, either between the water channels or coaxially with the bolt holes, for online monitoring of the casting process. The cooling water temperature change and mold thermocouple temperatures are the key validation points for models of mold heat transfer.

Modeling heat transfer in the continuous casting process requires accurate incorporation of the mold, the solidifying strand, and the interface between them. The behavior of the material in the interface, a ceramic slag, governs the heat extraction from the strand [57, 58]. Continuous casting of steel or any other metal is a complicated process with many coupled and nonlinear phenomena, and requires advanced modeling techniques to understand what is important for the process. Most of the process phenomena are dependent upon the mold heat transfer, *e.g.*, the rate-dependent solidification shrinkage of the solid shell, the time-dependent crystallization and flow of the interfacial slag, or the the multiphase turbulent flow of the molten steel with a free surface and particle transport. Much of the previous work on these three topics makes poor assumptions about mold heat transfer because modeling these phenomena alone are challenging tasks.

The continuous casting literature has several examples of mold heat transfer models with various levels of geometric complexity. Some of the models of mold heat transfer investigate only phenomena related to mold heat transfer [11, 55, 81, 84, 97, 110], and others use the calculated thermal behavior to drive the expansion of the mold in investigations of mold distortion [33, 35, 53, 68, 69, 71, 80, 83, 98, 109, 113, 117]. Some models of the
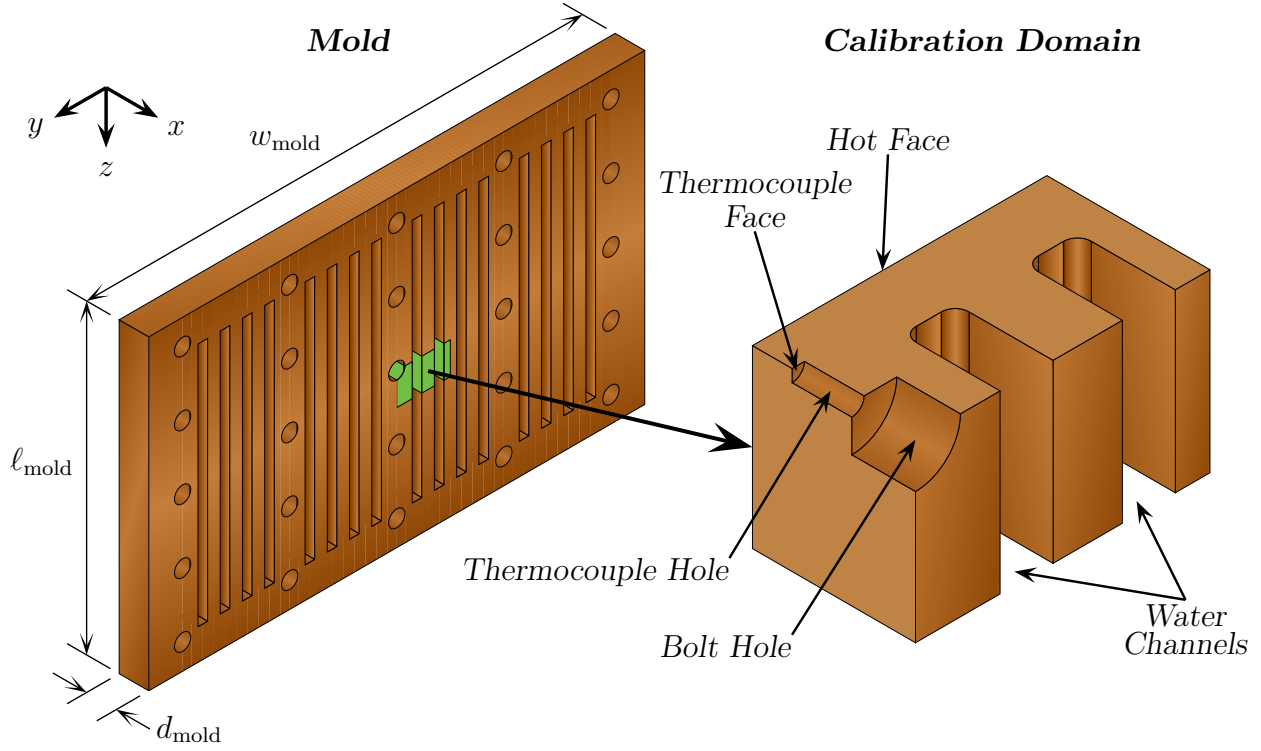
Figure 3.1   Back of a typical continuous casting mold showing the calibration domain

solidification shrinkage of the strand [27, 35, 116] and of the turbulent flow of the molten steel [18, 62, 67] have included detailed models of mold heat transfer. Some analyses are a part of an inverse model to calculate information about the heat extraction from the strand [18, 19, 22, 54, 74, 102, 108, 111, 112]. The most complicated studies have combined models of fluid flow, strand solidification and deformation, mold heat transfer, and mold distortion [38, 39, 50, 51, 63]; these studies all mention the many difficulties of converging these mutli-domain, multi-field, multi-physics models; *cf.* Chapter 5 for further discussion.

A continuous casting mold can be modeled in three dimensions, with as much geometric detail required by the modeler. Sometimes models of this complexity are necessary to explore the details of heat transfer with complicated-shaped molds [35, 39, 51, 110] and water channels [31, 33, 97], or the thermal distortion of the mold. These detailed models reveal the variation of temperature around geometric features like thermocouple holes and water channels; *cf.* Chapter 2 for examples. The mold-only heat transfer simulations, even with a fine mesh and full geometric detail [33, 35], require minutes to solve on modern computer platforms; however, interfacing and iterating the mold simulations with other models is computationally challenging. There is a need for a simple-but-accurate model of mold heat transfer for use with more complicated simulations.

The geometry of the continuous casting process allows many phenomena to be modeled reasonably well with a one-dimensional (1D) assumption, particularly away from the corners of the strand. The ROM of mold heat transfer presented in this work is a part of the process model CON1D [56], which is a 1D finite-difference model of the solidifying strand and includes simple models of solidification microscale physics and lubrication and heat transfer in the strand-mold interface. The CON1D model has been applied to several commercial casters [58, 77, 84, 86], and the mold model has evolved from a 1D heat-conduction model with several *ad hoc* corrections into the ROM presented in this work.

The reduced-order model of mold heat transfer that is presented in Section 3.3 is based on a 1D solution to the heat-conduction equation, and the up-front cost of the model is to calibrate its parameters with a single small three-dimensional (3D) finite-element model of the physical mold, which is discussed in Section 3.2. This ROM uses the physics of an analytical solution, rather than a statistical technique, to provide a robust relationship between the boundary conditions and the mold temperatures. The calibration of the ROM is discussed in Section 3.4, and then several examples are presented in Section 3.5. Section 3.6 shows calibration of the ROM is insensitive to the boundary conditions, so the calibration needs to be performed once per mold geometry.

3.2 Three-Dimensional Mold Model: Snapshot Model

Consider a small periodic and symmetric portion of the mold, shown in Figure 3.1. Analysis of this domain serves as the "snapshot" model for the reduced-order model developed in this work. The temperature in this 3D model of the mold $T_{3D}(\boldsymbol{x})$ is determined by solving the steady heat-conduction equation subject to appropriate boundary conditions, as discussed in Section 2.2. A uniform heat flux q_{hot} is supplied to the mold hot face, and energy is extracted from the water channel surfaces by a uniform convection condition with heat transfer coefficient h_{water} and sink temperature $\bar{T}_{\text{water}}$. All other faces are insulated, because of symmetry or the assumption that negligible heat flows from the back of the mold. Any other features of the mold, such as a coating layer, should be included in this snapshot model. Modern computers can solve this linear heat conduction problem in minutes or less, depending on mesh resolution.

The details of the heat transfer are computed with this small but fast and accurate model, and then the results are used to calibrate the reduced-order model of mold heat transfer presented in Section 3.3. The accurate 3D model essentially acts as a "microscale" model for the faster 1D "macroscale" model. For the calibration of the ROM, discussed in Section 3.3,

four temperatures are extracted from this small 3D model:

- the average hot face temperature, $T_{\mathrm{3D,hot}}$, which is used in calculations of the strand-mold interfacial heat transfer,
- the average water channel surface temperature, $T_{\mathrm{3D,c}}$, which is needed to calculate correctly the heat transfer coefficient of the water convection,
- the maximum water channel surface temperature, $T_{\mathrm{3D,roots}}$, which usually occurs at the channel root, is used to evaluate the risk of boiling the cooling water, and
- the average thermocouple face temperature, $T_{\mathrm{3D,TC}}$, which is an important validation point in models of mold heat transfer.

The averaging occurs over the appropriate surfaces indicated in Figure 3.1.

3.3 Reduced-Order Model of Mold Heat Transfer

This section discusses the reduced-order model of mold heat transfer in continuous casting developed in this article. The reduced-order model is based on a solution to the 1D heat-conduction equation.

3.3.1 One-Dimensional Heat Conduction Analysis

Scaling analysis [21] justifies the 1D assumption used in analyzing the mold heat transfer. The scaled steady heat-conduction equation is

$$0 = \frac{\partial^2 \theta_{\mathrm{mold}}}{\partial x^{*2}} + \left(\frac{d_{\mathrm{mold}}}{w_{\mathrm{mold}}}\right)^2 \frac{\partial^2 \theta_{\mathrm{mold}}}{\partial y^{*2}} + \left(\frac{d_{\mathrm{mold}}}{\ell_{\mathrm{mold}}}\right)^2 \frac{\partial^2 \theta_{\mathrm{mold}}}{\partial z^{*2}}, \tag{3.1}$$

where $\theta_{\mathrm{mold}} = \left(T_{\mathrm{mold}} - \bar{T}_{\mathrm{water}}\right) / \left(T_{\mathrm{mold,max}} - \bar{T}_{\mathrm{water}}\right)$ is the mold temperature T_{mold} scaled by the maximum mold temperature $T_{\mathrm{mold,max}}$ and cooling water bulk temperature $\bar{T}_{\mathrm{water}}$, and $x^* = x/d_{\mathrm{mold}}$, $y^* = y/w_{\mathrm{mold}}$, and $z^* = z/\ell_{\mathrm{mold}}$ are the coordinates scaled by the mold thickness d_{mold}, width w_{mold}, and length ℓ_{mold}. As illustrated in Figure 3.1, the aspect ratio terms in Equation (3.1) are small, *i.e.*, $d_{\mathrm{mold}}/w_{\mathrm{mold}} \ll 1$ and $d_{\mathrm{mold}}/\ell_{\mathrm{mold}} \ll 1$, so the terms that they multiply can be neglected. This analysis indicates that the conduction through the thickness of the mold, *i.e.*, in the x-direction, is the dominant mode of heat transfer. The 1D assumption is inaccurate near the liquid steel meniscus because of the large gradient of heat flux in the casting (z) direction, so a higher-order model may be necessary in this region.

The mold in the reduced-order model is envisioned as a rectangular plate with thickness d_{plate} and thermal conductivity k_{mold}, with a large number of rectangular water channels,

as shown in Figure 3.2. All water channels are identical with depth d_c, width w_c, and pitch p_c. The coating layer has thickness d_{coat} and thermal conductivity k_{coat}. Assuming that the mold copper between the water channels acts as a heat-transfer fin, the "cold face" of the mold, described in Section 3.3.2, is modeled as a convection condition with heat transfer coefficient h_{cold} and sink temperature $\bar{T}_{water}$. The mold is analyzed easily as a number of 1D thermal resistances, shown in Figure 3.3, with this treatment of the water channels.

The temperature in the mold $T_{1D}(x)$ is governed by the 1D heat-conduction equation,

$$0 = \frac{d^2 T_{1D}}{dx^2},\tag{3.2}$$

which has the general solution

$$T_{1D}(x) = c_1 x + c_2,\tag{3.3}$$

where x is the distance from the hot face, including the coating layer, and c_1 and c_2 are constants of integration. The solidifying steel supplies a heat flux $q_{hot} > 0$ to the hot face of the mold at $x = 0$, which has a normal vector of $n = -1$, or

$$-k_{coat} \left.\frac{dT_{1D}}{dx}\right|_{x=0} (-1) = -q_{hot}.\tag{3.4}$$

The interface between the coating layer and mold copper at $x = d_{coat}$ has continuous temperature,

$$T_{1D}\left(d_{coat}^-\right) = T_{1D}\left(d_{coat}^+\right),\tag{3.5}$$

and continuous heat flux,

$$-k_{coat} \left.\frac{dT_{1D}}{dx}\right|_{x=d_{coat}^-} (+1) = -k_{mold} \left.\frac{dT_{1D}}{dx}\right|_{x=d_{coat}^+} (-1).\tag{3.6}$$

The cold face at $x = d_{coat} + d_{plate}$, which has a normal vector of $n = +1$, has the convection condition

$$-k_{mold} \left.\frac{dT_{1D}}{dx}\right|_{x=d_{coat}+d_{plate}} (+1) = h_{cold} \left(T_{1D}(d_{coat} + d_{plate}) - \bar{T}_{water}\right).\tag{3.7}$$

Applying these boundary conditions gives the 1D temperature field as

$$T_{1D}(x) = \begin{cases} \bar{T}_{water} + q_{hot} \left(\dfrac{1}{h_{cold}} + \dfrac{d_{plate}}{k_{mold}} + \dfrac{d_{coat} - x}{k_{coat}}\right) & \text{if } 0 \le x \le d_{coat} \\[3mm] \bar{T}_{water} + q_{hot} \left(\dfrac{1}{h_{cold}} + \dfrac{d_{plate} + d_{coat} - x}{k_{mold}}\right) & \text{if } d_{coat} \le x \le d_{coat} + d_{plate}. \end{cases}\tag{3.8}$$

The 1D temperature solution is shown schematically in Figure 3.4.
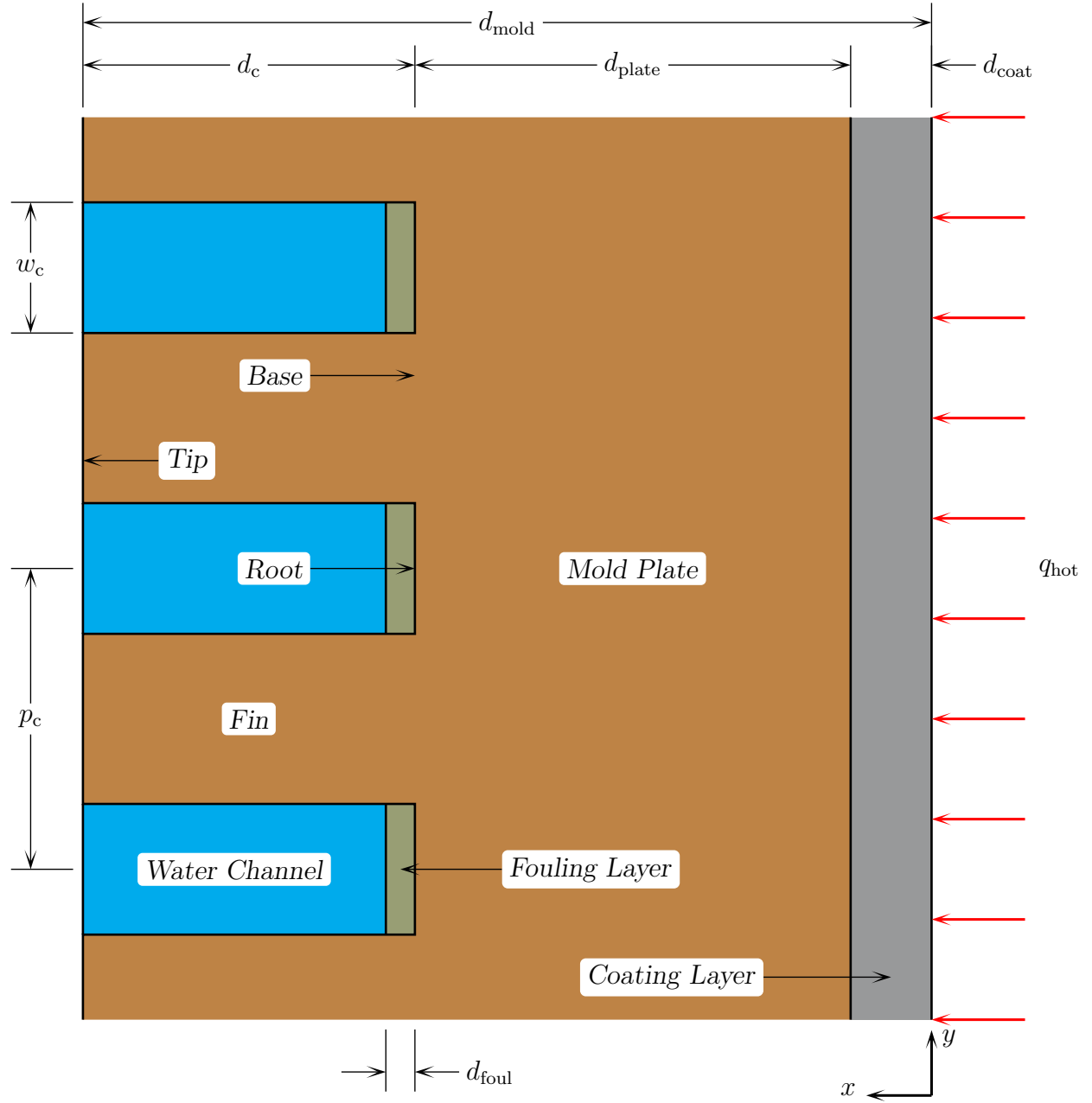
Figure 3.2 Simplified mold geometry used for developing the reduced-order model
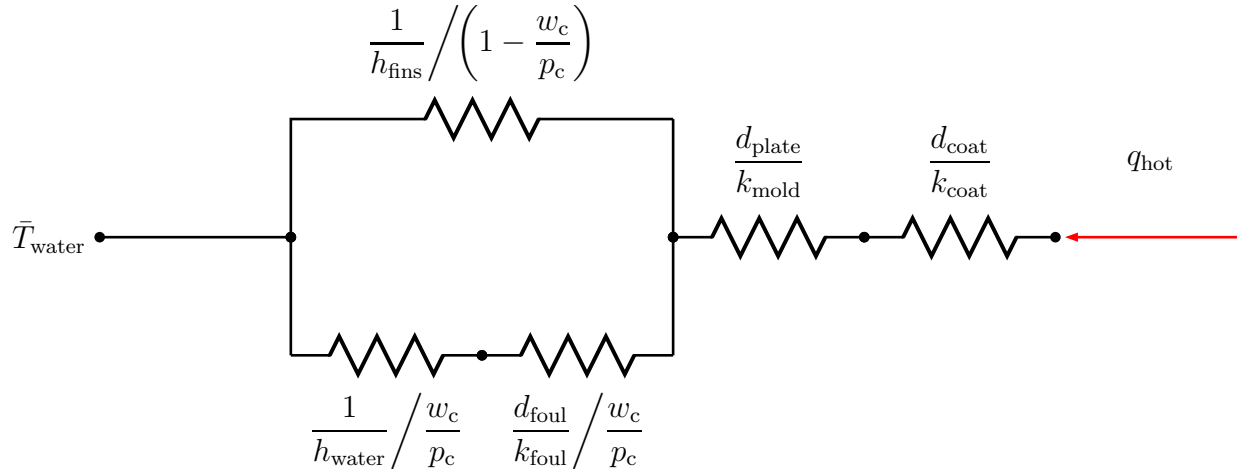
Figure 3.3 Thermal resistor model for the one-dimensional mold
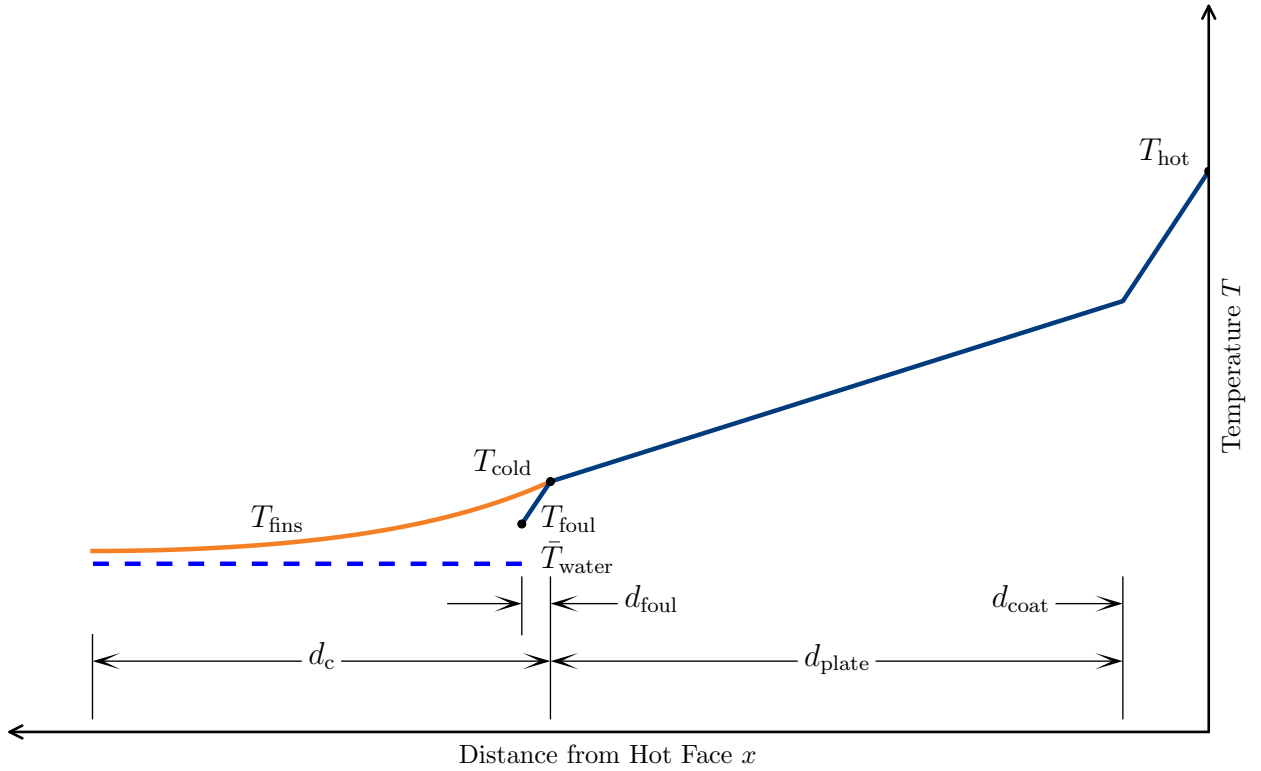
Figure 3.4 One-dimensional model of mold temperatures

33

The temperature solution, Equation (3.8), is used to find the temperature at key locations in the mold. The hot face temperature $T_{1D,\text{hot}} = T_{1D}(0)$ is

$$T_{1D,\text{hot}} = \bar{T}_{\text{water}} + q_{\text{hot}} \left(\frac{1}{h_{\text{cold}}} + \frac{d_{\text{plate}}}{k_{\text{mold}}} + \frac{d_{\text{coat}}}{k_{\text{coat}}} \right), \tag{3.9}$$

and the cold face temperature $T_{1D,\text{cold}} = T_{1D}(d_{\text{coat}} + d_{\text{plate}})$ is

$$T_{1D,\text{cold}} = \bar{T}_{\text{water}} + \frac{q_{\text{hot}}}{h_{\text{cold}}}. \tag{3.10}$$

A thermocouple with depth d_{TC} beneath the hot face has temperature $T_{1D,\text{TC}} = T_{1D}(d_{\text{TC}})$, or

$$T_{1D,\text{TC}} = \bar{T}_{\text{water}} + q_{\text{hot}} \left(\frac{1}{h_{\text{cold}}} + \frac{d_{\text{plate}} + d_{\text{coat}} - d_{\text{TC}}}{k_{\text{mold}}} \right). \tag{3.11}$$

The temperature solution also gives the heat transfer coefficient h_{mold} that can be used to model the thermal effect of the mold in other, more complicated models of the continuous casting process,

$$\frac{1}{h_{\text{mold}}} = \frac{1}{h_{\text{cold}}} + \frac{d_{\text{plate}}}{k_{\text{mold}}} + \frac{d_{\text{coat}}}{k_{\text{coat}}}, \tag{3.12}$$

with $\bar{T}_{\text{water}}$ as the sink temperature.

3.3.2 Cold Face Model

The water flowing in the cooling channels causes a nominal heat transfer coefficient of h_{water} that is modified to account for other phenomena in the water channels. The water convection coefficient h_{water} itself is calculated with a forced-internal-flow empirical correlation, such as the SLEICHER and ROUSE [89] model presented in Equation (2.7).

Heat is extracted at the cold face by convection along the roots of the channels, and by combined conduction through the bulk of and convection along the lateral surfaces of the fins. These two effects combine to provide a cold face heat transfer coefficient of

$$h_{\text{cold}} = \left(\frac{w_{\text{c}}}{p_{\text{c}}} \right) h_{\text{roots}} + \left(1 - \frac{w_{\text{c}}}{p_{\text{c}}} \right) h_{\text{fins}}, \tag{3.13}$$

where h_{roots} is the heat transfer coefficient for the root surfaces and h_{fins} is the heat transfer coefficient for the fins.

The heat transfer coefficient for the water channel roots h_{roots} is the nominal h_{water} reduced by the effects of a thin layer of fouling material, such as calcium carbonate or an organic compound, with thickness d_{foul} and thermal conductivity k_{foul} according to

$$\frac{1}{h_{\text{roots}}} = \frac{1}{h_{\text{water}}} + \frac{d_{\text{foul}}}{k_{\text{foul}}}. \tag{3.14}$$

The thickness of the fouling layer is assumed to be small compared to the channel depth, i.e., $d_{\text{foul}}/d_{\text{c}} \ll 1$, as to not affect significantly the flow of the cooling water. Additionally, as the fouling layer thickness d_{foul} increases more heat flows into the fins, causing more 2D heat transfer within the mold plate.

The mold copper between water channels is assumed to act as a rectangular fin with an insulated tip, giving a heat transfer coefficient of

$$h_{\text{fins}} = h_{\text{water}} \frac{\tanh(b)}{\sqrt{\text{Bi}_{w_{\text{fins}}}}}, \tag{3.15}$$

where the Biot number based on the fin half-width is

$$\text{Bi}_{w_{\text{fins}}} = \frac{h_{\text{water}}}{k_{\text{mold}}} \frac{p_{\text{c}} - w_{\text{c}}}{2}, \tag{3.16}$$

the Biot number based on the fin length is

$$\text{Bi}_{d_{\text{fins}}} = \frac{h_{\text{water}}}{k_{\text{mold}}} d_{\text{c}}, \tag{3.17}$$

and $b = \text{Bi}_{d_{\text{fins}}}/\sqrt{\text{Bi}_{w_{\text{fins}}}}$ is introduced for convenience. The fin tip is insulated because of the assumption that all of the energy from the steel is removed by the cooling water. Equation (3.15) was derived for a fin with uniform cross-section and material properties, and for a thin fin, i.e., $(p_{\text{c}} - w_{\text{c}})/d_{\text{c}} \ll 1$. The fin aspect ratio is approximately 1/3 in practice, so the 2D heat transfer within and at the base of the fin may be significant.

A needed quantity is the perimeter-average temperature of the water channel, T_{c}. The temperature along the length of a rectangular fin $T_{\text{fins}}(x')$ is described by

$$\frac{T_{\text{fins}} - \bar{T}_{\text{water}}}{T_{\text{base}} - \bar{T}_{\text{water}}} = \frac{1}{\cosh(b)} \cosh\left(b\left(1 - \frac{x'}{d_{\text{c}}}\right)\right), \tag{3.18}$$

where x' is the distance from the base of the fin. The perimeter-average temperature of the rectangular water channel, having two sides of length d_{c} with temperature described by Equation (3.18), one side of length w_{c} with uniform temperature $\bar{T}_{\text{water}}$, and one side of length w_{c} with uniform temperature T_{foul}, is

$$T_{\text{c}} = \frac{1}{d_{\text{c}} + w_{\text{c}}} \left(\frac{w_{\text{c}}}{2} T_{\text{foul}} + \left(\frac{w_{\text{c}}}{2} + d_{\text{c}} \right) \bar{T}_{\text{water}} + d_{\text{c}} \frac{\tanh(b)}{b} \left(T_{\text{base}} - \bar{T}_{\text{water}} \right) \right). \tag{3.19}$$

The temperature at the base of the fin is taken as the cold face temperature from Equation (3.10), i.e., $T_{\text{base}} = T_{\text{1D,cold}}$. The temperature of the surface of the fouling layer T_{foul}, computed with the circuit mathematics for the 1D heat transfer model, is

$$T_{\text{foul}} = \bar{T}_{\text{water}} + \frac{q_{\text{hot}}}{h_{\text{cold}}} \frac{h_{\text{roots}}}{h_{\text{water}}}, \tag{3.20}$$

35

which reduces to the cold face temperature $T_{\mathrm{1D,cold}}$ when $d_{\mathrm{foul}} = 0$.

Boiling in the water channels should be avoided because of the possible reduction in heat transfer and formation of fouling material. A simple evaluation of the risk of boiling is to compare the water temperature, in particular at the channel roots, against the saturation temperature of the water [31, 83]. Since the water in the mold is pressurized, the saturation temperature of water $T_{\mathrm{sat,water}}(p)$ is computed with [37]

$$T_{\mathrm{sat,water}} = 325.088 + D - \sqrt{(325.088 - D)^2 + 0.238\,556}, \tag{3.21}$$

where

$$D = \frac{1}{2} \frac{C}{\sqrt{B^2 + AC} + B} 10^3, \tag{3.22}$$

$$A = (\beta - 0.923\,517)\,(\beta - 16.1503)\,, \tag{3.23}$$

$$B = 0.583\,526\,(\beta - 0.386\,723)\,(\beta + 10.6869)\,, \tag{3.24}$$

$$C = 0.724\,213\,(\beta - 0.121\,989)\,(\beta + 4.585\,53)\,, \tag{3.25}$$

$$\beta = \sqrt[4]{p}. \tag{3.26}$$

Equation (3.21) expects the absolute pressure p in MPa and gives the saturation temperature in K. This model is valid for $0.611 \times 10^{-3}\,\mathrm{MPa} \leq p \leq 22.0\,\mathrm{MPa}$, which is satisfied in practice.

An interesting digression is to observe that the cold face heat transfer coefficient h_{cold} given in Equation (3.13), without a fouling layer and with constant h_{water}, has the maximum value of $\frac{5}{3} h_{\mathrm{water}}$ at a channel pitch of $p_{\mathrm{c}} = \frac{3}{4} \frac{k_{\mathrm{mold}}}{h_{\mathrm{water}}} \approx 9\,\mathrm{mm}$, a channel width of $w_{\mathrm{c}} = \frac{1}{4} \frac{k_{\mathrm{mold}}}{h_{\mathrm{water}}} \approx 3\,\mathrm{mm}$, and a channel depth of $d_{\mathrm{c}} = \mathrm{atanh}(\chi) \frac{1}{2} \frac{k_{\mathrm{mold}}}{h_{\mathrm{water}}} \approx 21\,\mathrm{mm}$, where $0.95 \leq \chi < 1.0$ is a tolerance on the asymptote of the hyperbolic tangent. These values of channel geometry provide an intelligent starting point for further work on optimizing mold geometry, though efficient heat extraction is but one goal of mold design. Other mold design goals may include:

- optimizing, but generally maximizing, the mold hot face temperature for best steel quality,
- minimizing the hot face temperature variation around the perimeter of the mold, across all four mold pieces, to reduce the formation of longitudinal cracks both in the steel and in the mold,
- avoiding the water boiling in the channels, as discussed above,
- minimizing the thermomechanical stress concentrations near the water channel roots to extend the mold service life,
- minimizing the hot face temperature, to avoid accelerated creep rates and reduce thermomechanical fatigue loading, to extend the mold service life,

- maximizing the mold plate thickness, to increase the mold service life and to provide a safety factor against mold cracking,

- minimizing the volume of copper of the mold, for low material cost,

- minimizing the total channel cross-sectional area, or at least the channel cross-sectional area per unit width of the mold, for low manufacturing cost, and

- maximizing the individual channel cross-sectional areas to reduce the pressure difference required to drive the water flow, for low operating cost.

Getting the steel as cold as possible as quickly as possible is not a goal of mold design. Reducing the manufacturing and operating costs of the mold are minor goals compared to producing high-quality steel. The ROM developed in this work can be used to explore some of these design issues.

3.3.3 Cooling Water Temperature Change

The temperature change of the cooling water is an important quantity in the validation of mold heat transfer models because it indirectly measures the heat removed from the steel by the mold. This section presents the calculation of the temperature change of the cooling water in the reduced-order model, in a manner that is consistent with the rest of the model.

Assuming that the water moves mostly in the axial (z) direction of the water channel with average speed $\bar{v}_{\text{water}}$, the scaled [21] steady energy equation is

$$\frac{\partial \theta_{\text{water}}}{\partial z^*} = \frac{1}{\text{Pe}_{\text{water}} \frac{D_{\text{h,c}}}{\ell_{\text{c}}}} \left(\frac{\partial^2 \theta_{\text{water}}}{\partial x^{*2}} + \frac{\partial^2 \theta_{\text{water}}}{\partial y^{*2}} + \left(\frac{D_{\text{h,c}}}{\ell_{\text{c}}} \right)^2 \frac{\partial^2 \theta_{\text{water}}}{\partial z^{*2}} \right), \qquad (3.27)$$

where $\theta_{\text{water}} = (T_{\text{water}} - T_{\text{water,min}}) / (T_{\text{water,max}} - T_{\text{water,min}})$ is the temperature of the water T_{water} scaled by the largest and smallest water temperatures in the water channel $T_{\text{water,max}}$ and $T_{\text{water,min}}$, $x^* = x/D_{\text{h,c}}$, $y^* = y/D_{\text{h,c}}$, and $z^* = z/\ell_{\text{c}}$ are the coordinates scaled by the hydraulic diameter $D_{\text{h,c}}$ and length ℓ_{c} of the water channel, $\text{Pe}_{\text{water}} = \bar{v}_{\text{water}} D_{\text{h,c}}/\alpha_{\text{water}}$ is the Péclet number of the flow in the water channel, and $\alpha_{\text{water}} = k_{\text{water}}/\rho_{\text{water}} c_{p,\text{water}}$ is the thermal diffusivity of the water. Equation (3.27) indicates that the heat conducted in the axial (z) direction is negligible relative to the heat conducted in the transverse directions because of the small aspect ratio of the channel, $i.e.$, $D_{\text{h,c}}/\ell_{\text{c}} \ll 1$. Further, since the aspect-ratio–modified Péclet number is large, $i.e.$, $\text{Pe}_{\text{water}} \frac{D_{\text{h,c}}}{\ell_{\text{c}}} \gg 1$, the heat conduction is negligible relative to the energy transported by the bulk motion of the water. Equation (3.27) then indicates that the water temperature is uniform over the entire channel, so an alternative approach must be used to analyze the temperature change of the water.
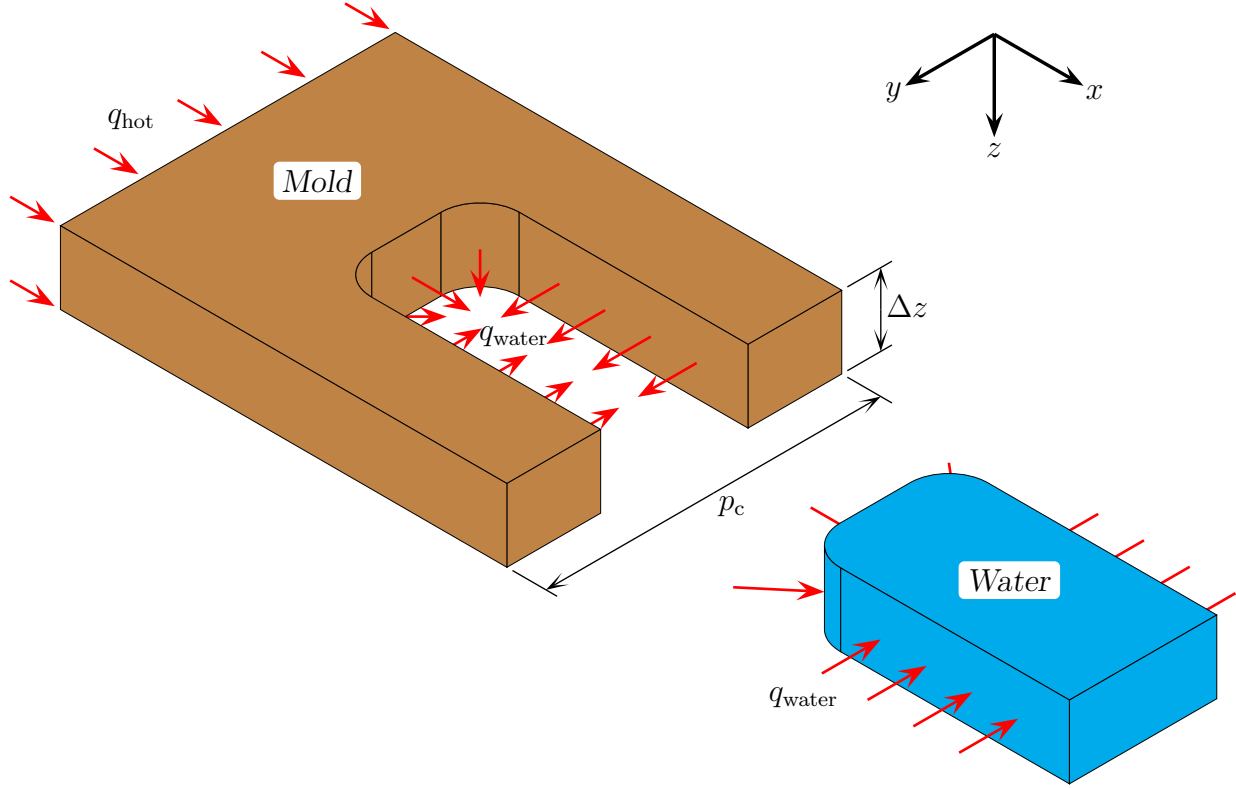
Figure 3.5 Domain for analyzing the cooling water temperature change

Consider a transverse slice with thickness $\Delta z > 0$ of a water channel and the surrounding mold, as shown in Figure 3.5. The integral form of the steady energy equation for the water, assuming no boiling, in the transverse slice is

$$\int_{V_{\text{water}}} \rho_{\text{water}} c_{p,\text{water}} v_{\text{water}} \frac{\partial T_{\text{water}}}{\partial z} \, \mathrm{d}V = - \int_{\hat{A}_{\text{c}}} -q_{\text{water}} \, \mathrm{d}A, \qquad (3.28)$$

where V_{water} is the volume of the slice of water, $\hat{A}_{\text{c}}$ is the surface area of the water channel in the slice, and $q_{\text{water}} > 0$ is the heat flux into the water. All heat supplied to the mold is assumed to be removed by the cooling water, so the integral form of the steady energy equation for the mold in the transverse slice is

$$0 = - \int_{A_{\text{hot}}} -q_{\text{hot}} \, \mathrm{d}A - \int_{\hat{A}_{\text{c}}} q_{\text{water}} \, \mathrm{d}A, \qquad (3.29)$$

where the area of the hot face in the transverse slice is $A_{\text{hot}} = p_{\text{c}} \Delta z$. If the heat flux on the hot face is uniform across the slice, then the heat input to the water is

$$\int_{\hat{A}_{\text{c}}} q_{\text{water}} \, \mathrm{d}A = q_{\text{hot}} p_{\text{c}} \Delta z \qquad (3.30)$$

38

regardless of the shape of the water channel. The hot face heat flux q_{hot} is uniform for an arbitrarily small Δz and a water channel width-to-pitch ratio $w_{\text{c}}/p_{\text{c}}$ greater than some as yet unknown value. The volume integral over the water in Equation (3.28) is avoided by defining the water bulk temperature $\bar{T}_{\text{water}}$ as the temperature that satisfies

$$\rho_{\text{water}}\left(\bar{T}_{\text{water}}\right) c_{p,\text{water}}\left(\bar{T}_{\text{water}}\right) \bar{v}_{\text{water}}\bar{T}_{\text{water}}A_{\text{c}} = \int_{A_{\text{c}}} \rho_{\text{water}}c_{p,\text{water}}v_{\text{water}}T_{\text{water}}\,\mathrm{d}A, \qquad (3.31)$$

i.e., $\bar{T}_{\text{water}}(z)$ is the internal-energy–weighted average temperature over a plane perpendicular to the flow of the water with cross-sectional area A_{c}. Equation (3.31) allows the volume integral in Equation (3.28) to be evaluated for small Δz as

$$\int_{V_{\text{water}}} \rho_{\text{water}}c_{p,\text{water}}v_{\text{water}}\frac{\partial T_{\text{water}}}{\partial z}\,\mathrm{d}V = \rho_{\text{water}}c_{p,\text{water}}\bar{v}_{\text{water}}\frac{\mathrm{d}\bar{T}_{\text{water}}}{\mathrm{d}z}A_{\text{c}}\Delta z, \qquad (3.32)$$

with ρ_{water} and $c_{p,\text{water}}$ on the right-hand side evaluated at $\bar{T}_{\text{water}}$. Combining Equations (3.28), (3.30), and (3.32) and dividing out the Δz gives the differential equation that describes the evolution of the water bulk temperature in one channel as

$$\rho_{\text{water}}c_{p,\text{water}}\bar{v}_{\text{water}}\frac{\mathrm{d}\bar{T}_{\text{water}}}{\mathrm{d}z}A_{\text{c}} = q_{\text{hot}}p_{\text{c}}. \qquad (3.33)$$

The above arguments are extended to find the temperature change of all of the cooling water in the mold. The heat flux from the steel is applied over the width of the strand w_{strand} rather than a single channel pitch. The heat leaves the mold through all water channels with total cross-sectional area $A_{\text{c,total}}$, regardless of channel shape and pitch; however, the water speed in each channel must be about the average value $\bar{v}_{\text{water}}$. The temperature evolution of the total water then is described by

$$\rho_{\text{water}}c_{p,\text{water}}\bar{v}_{\text{water}}\frac{\mathrm{d}\bar{T}_{\text{water}}}{\mathrm{d}z}A_{\text{c,total}} = q_{\text{hot}}w_{\text{strand}}. \qquad (3.34)$$

The water temperature at an arbitrary distance down the mold z is found by numerical integration of Equation (3.34),

$$\bar{T}_{\text{water}}(z) = \bar{T}_{\text{water}}(0) + \int_0^z \frac{1}{\bar{v}_{\text{water}}}\frac{w_{\text{strand}}}{A_{\text{c,total}}}\frac{q_{\text{hot}}}{\rho_{\text{water}}c_{p,\text{water}}}\,\mathrm{d}z', \qquad (3.35)$$

where $\bar{T}_{\text{water}}(0)$ is the water temperature at the top of the mold, a value measured in the plant. The temperature of the water at the bottom of the mold $\bar{T}_{\text{water}}(\ell_{\text{mold}})$ is the measurement from the plant that the reduced-order model must match as part of the heat flux calibration procedure. This calculation of water temperature change works equally well in counterflow configurations, where the cooling water flows in the direction opposite to the casting direction, but with $\bar{v}_{\text{water}} < 0$.

3.4   Reduced-Order Model Parameter Calibration

The thirteen parameters in the reduced-order model of mold heat transfer presented in Section 3.3 are the

- boundary conditions: the hot face heat flux q_{hot}, and the water heat transfer coefficient h_{water} and bulk temperature $\bar{T}_{\text{water}}$,
- material properties: the coating, mold, and fouling thermal conductivities k_{coat}, k_{mold}, and k_{foul}, and the
- geometries: the coating, mold plate, and fouling thicknesses d_{coat}, d_{plate}, and d_{foul}, the thermocouple position d_{TC}, and the water channel width w_{c}, depth d_{c}, and pitch p_{c}.

For a given problem, the non-geometric parameters, *i.e.*, the material properties and the boundary conditions are fixed parameters. Some of the geometric parameters are taken as the calibration parameters of the ROM because of the assumptions about the nature of the heat flow in the simplified model, and because these parameters allow enough leeway for the ROM to be robust with respect to changes in the non-geometric parameters, which is explored in Section 3.6. The coating and fouling layer thicknesses d_{coat} and d_{foul} are taken as fixed parameters because they are so thin that these layers act as 1D thermal resistances regardless of the complexity of the model. The five remaining geometric parameters, the mold plate thickness d_{plate}, the thermocouple depth d_{TC}, and the channel width w_{c}, depth d_{c}, and pitch p_{c}, are calibrated in this section so that the reduced-order model of the mold has the same thermal characteristics of the physical mold and can match key temperatures in the 3D model discussed in Section 3.2.

3.4.1   Water Channel Geometry

The reduced-order model water channel geometry is calibrated by appealing to physical principles. The water channels in the ROM must have the same cross-sectional area as the physical channels A_{physical}, *i.e.*,

$$w_{\text{c}} d_{\text{c}} = A_{\text{physical}}, \tag{3.36}$$

to maintain the mass flow rate of the cooling water. The water channels in the ROM also must have the same hydraulic diameter as the physical channels $D_{\text{h,physical}}$, *i.e.*,

$$2\frac{w_{\text{c}} d_{\text{c}}}{w_{\text{c}} + d_{\text{c}}} = D_{\text{h,physical}}, \tag{3.37}$$

to maintain the value of the heat transfer coefficient h_{water} from Equation (2.7). Solving Equations (3.36) and (3.37) together gives the ROM channel width w_{c} and depth d_{c} as

$$w_{\text{c}}, d_{\text{c}} = \frac{A_{\text{physical}}}{D_{\text{h,physical}}} \left(1 \pm \sqrt{1 - \frac{D_{\text{h,physical}}^2}{A_{\text{physical}}}} \right). \tag{3.38}$$

Both solutions of Equation (3.38) are real and positive if $A_{\text{physical}} \geq D_{\text{h,physical}}^2$. The aspect ratio of the physical channels determines which solution is w_{c} and which is d_{c}, subject to $w_{\text{c}} < p_{\text{c}}$. Some molds employ channels with different geometries; in this case the values of A_{physical} and $D_{\text{h,physical}}$ are taken as their respective averages over all channels in the mold.

The limitation of $A_{\text{physical}} \geq D_{\text{h,physical}}^2$ precludes molds with only circular channels. In this case, the ROM channel width is defined as the width of the square that circumscribes the circle, $w_{\text{c}} = D_{\text{physical}}$, and the depth of the channel is calculated to match the cross-sectional area, i.e., $d_{\text{c}} = \frac{\pi}{4} D_{\text{physical}}$. This approach matches the cross-sectional area but gives a hydraulic diameter of $D_{\text{h,c}} \approx 0.88 \, D_{\text{physical}}$. Taking the 1D channel width to be that of the square that inscribes the circle gives $D_{\text{h,c}} \approx 0.86 \, D_{\text{physical}}$. The previous approach [84] that used $w_{\text{c}} = \frac{2}{3} D_{\text{physical}}$ gives $D_{\text{h,c}} \approx 0.85 \, D_{\text{physical}}$. Each of these approaches over-predict the heat transfer coefficient h_{water} from Equation (2.7) by about 3%, and the larger the channel diameter the smaller the error.

The ROM channel pitch p_{c} is calibrated by requiring that the simulated and physical molds have the same amount of water flowing per unit width of the mold, i.e.,

$$\frac{A_{\text{c}}}{p_{\text{c}}} = \frac{A_{\text{c,total}}}{w_{\text{mold}}}, \tag{3.39}$$

where the ROM water channel cross-sectional area $A_{\text{c}} = w_{\text{c}} d_{\text{c}}$ is calculated with the calibrated dimensions from Equation (3.38). The mold width w_{mold} and total channel cross-sectional area $A_{\text{c,total}}$ used in this calculation should be based on regions away from the ends of the mold; ideally, this calculation is based upon the geometry of the 3D calibration domain discussed in Section 3.2. The ROM channel pitch was determined in previous work [31] from the slope of the best-fit line through the function describing the cumulative water channel cross-sectional area across the width of the mold, as shown in Figure 3.6, which is based on the example Mold D presented in Section 3.5. Equation (3.39) gives a simple but accurate, within about 3% depending on the channel geometry, approximation of this best-fit line.

3.4.2 Mold Plate Thickness

The mold plate thickness in the ROM is calibrated by forcing the temperature at specific locations in the 1D model to match the corresponding temperatures in the 3D model subject to
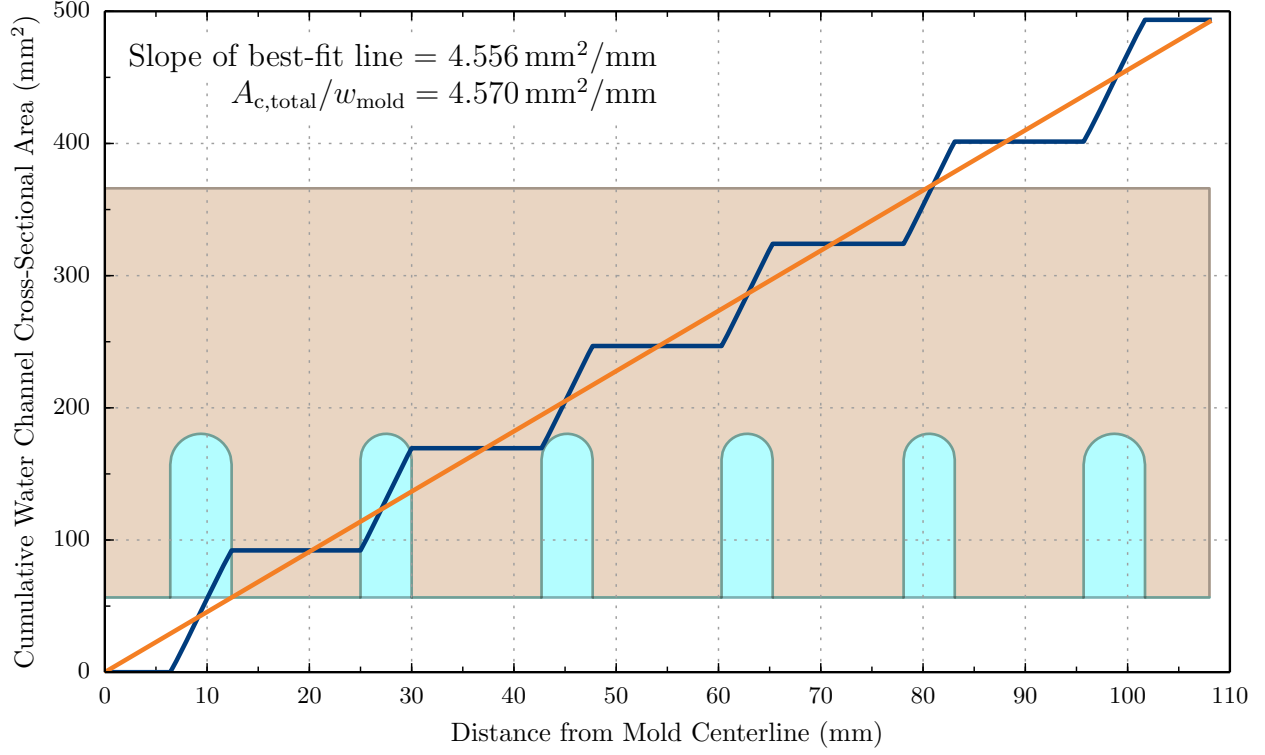
Figure 3.6 Cumulative water channel area across the Mold D calibration domain

identical boundary conditions and material properties. Before proceeding, choose reasonable values for the non-geometric model parameters $k_{\mathrm{mold}}^\diamond$, $q_{\mathrm{hot}}^\diamond$, $h_{\mathrm{water}}^\diamond$, $\bar{T}_{\mathrm{water}}^\diamond$, $d_{\mathrm{coat}}^\diamond$, $k_{\mathrm{coat}}^\diamond$, $d_{\mathrm{foul}}^\diamond$, and $k_{\mathrm{foul}}^\diamond$ to be used in both the 1D and the 3D models.

The calibrated mold plate thickness d_{plate} is found by requiring the 1D hot face temperature to be the average hot face temperature from the 3D finite-element model, *i.e.*, $T_{\mathrm{1D,hot}} = T_{\mathrm{3D,hot}}$. Manipulating the expression for the 1D hot face temperature, Equation (3.9), gives a mold plate thickness of

$$d_{\mathrm{plate}} = \frac{k_{\mathrm{mold}}^\diamond}{q_{\mathrm{hot}}^\diamond} \left(T_{\mathrm{3D,hot}} - \bar{T}_{\mathrm{water}}^\diamond \right) - k_{\mathrm{mold}}^\diamond \left(\frac{1}{h_{\mathrm{cold}}^\diamond} + \frac{d_{\mathrm{coat}}^\diamond}{k_{\mathrm{coat}}^\diamond} \right), \tag{3.40}$$

where $h_{\mathrm{cold}}^\diamond$ is calculated with Equation (3.13) using the calibrated channel geometry from Section 3.4.1. Some phenomena related to strand-mold interfacial heat transfer depend on the mold hot face temperature, and this calibrated plate thickness ensures that $T_{\mathrm{1D,hot}}$ is computed accurately.

Changing the thickness of the mold plate then requires concordant redefinition of the cold face. Two "cold face" positions are calibrated for the ROM: one for the average water channel surface temperature, d_{channels}, and one for the maximum water channel surface temperature, d_{roots}, respectively used to calculate the water heat transfer coefficient with Equation (2.7),

and to evaluate the risk of boiling with the saturation temperature, Equation (3.21). Following similar arguments as in calibrating the mold plate thickness gives

$$d_{\text{channels}} = \frac{k_{\text{mold}}^{\diamond}}{q_{\text{hot}}^{\diamond}} \left(T_{\text{3D,hot}} - T_{\text{3D,c}}\right) + d_{\text{coat}}^{\diamond} \left(1 - \frac{k_{\text{mold}}^{\diamond}}{k_{\text{coat}}^{\diamond}}\right), \tag{3.41}$$

where $T_{\text{3D,c}}$ is the average temperature of the channel surfaces in the 3D calibration domain, and

$$d_{\text{roots}} = \frac{k_{\text{mold}}^{\diamond}}{q_{\text{hot}}^{\diamond}} \left(T_{\text{3D,hot}} - T_{\text{3D,roots}}\right) + d_{\text{coat}}^{\diamond} \left(1 - \frac{k_{\text{mold}}^{\diamond}}{k_{\text{coat}}^{\diamond}}\right), \tag{3.42}$$

where $T_{\text{3D,roots}}$ is the maximum temperature of the channel roots in the 3D calibration domain. This idea of "multiple cold faces" can be extended as necessary, depending on the interests of the modeler.

3.4.3 Mold Thermocouples

The mold thermocouples in the ROM are calibrated to account for the geometric effect of the thermocouple bore, and to account for the heat lost along the long thermocouple wires. The geometric effect can be significant: the temperature from Equation (3.11) under-predicts the thermocouple temperature from the 3D model, by as much as $50\,^{\circ}\text{C}$ [47, 84], or about 25%, depending on the geometry. Following similar arguments as in calibrating the mold plate thickness, the calibrated thermocouple position d_{TC} is found by manipulating Equation (3.11) with $T_{\text{1D,TC}} = T_{\text{3D,TC}}$, giving

$$d_{\text{TC}} = \frac{k_{\text{mold}}^{\diamond}}{q_{\text{hot}}^{\diamond}} \left(T_{\text{3D,hot}} - T_{\text{3D,TC}}\right) + d_{\text{coat}}^{\diamond} \left(1 - \frac{k_{\text{mold}}^{\diamond}}{k_{\text{coat}}^{\diamond}}\right). \tag{3.43}$$

Using the result of Equation (3.43) corrects the geometric inaccuracies of the thermocouple temperature, but in practice is insufficient alone to match thermocouple measurements. Measured thermocouple temperatures often read low because of the contact resistance between the thermocouple bead and the appropriate surface on the mold. Heat also is lost through conduction and convection along the length of the thermocouple wires, especially if the wires are long and well-cooled. Assuming that the thermocouple wires behave as long circular pin-fins, the heat loss is

$$q_{\text{TC}} = \frac{k_{\text{TC}}}{D_{\text{TC}}/2} \sqrt{\frac{h_{\text{wire}} D_{\text{TC}}}{k_{\text{TC}}}} \left(T_{\text{TC}} - T_{\text{amb}}\right), \tag{3.44}$$

where D_{TC} and k_{TC} are the diameter and the thermal conductivity of the thermocouple wire, which is submersed in a fluid of temperature T_{amb} that causes a convection coefficient of h_{wire}.

The wire heat transfer coefficient h_{wire} is intended to be a tuning parameter, and should be about $5\,\text{kW}/(\text{m}^2 \cdot \text{K})$ if the ambient medium is water or about $0.1\,\text{kW}/(\text{m}^2 \cdot \text{K})$ for air. Since the heat leaving the mold through the thermocouples is small relative to the heat leaving through the water channels, this heat lost along the thermocouple wires is treated as a local adjustment to the thermocouple temperature,

$$T'_{\text{TC}} = T_{\text{TC}} + q_{\text{TC}} \frac{d_{\text{gap}}}{k_{\text{gap}}}, \tag{3.45}$$

where T_{TC} is the predicted thermocouple temperature from Equation (3.11) using the calibrated thermocouple depth d_{TC} from Equation (3.43), and d_{gap} and k_{gap} are the size and the thermal conductivity of the gap between the thermocouple and the mold copper. The thermal conductivity of the gap should be about $1.25\,\text{W}/(\text{m} \cdot \text{K})$ for a thermal paste or about $0.04\,\text{W}/(\text{m} \cdot \text{K})$ for dry air. The gap size typically is on the order of $0.01\,\text{mm}$ to $0.1\,\text{mm}$, and is used as a tuning parameter in the heat flux calibration procedure. This approach of calibrating mold thermocouple temperatures is used in Chapter 2.

3.5   Example Mold Geometries

This section presents the determination of the reduced-order model parameters for four wide face mold geometries. This work employs the commercial finite-element software ABAQUS [1] for analyzing the 3D calibration domains. Molds A and B [47] are for conventional "thick-slab" molds, Mold C [84] is for a thin-slab funnel mold, and Mold D [31] is for a thin-slab mold without a funnel. All molds do not employ coating layers. Slices through the calibration domains at the center of the thermocouple are shown in Figures 3.7 through 3.10. These figures also give the 3D model results that are necessary for the calibration calculations, and the calibrated geometries for the reduced-order models of these molds. Water channels on a symmetry plane, as on Molds A and B, have weights of 0.5 in the averaging calculations.

The severity of the adjustment to the channel geometry depends on the shapes and distribution of channels in the physical mold. The mold plate thickness and its relatives are about 10% different from the blueprint dimensions. Table 3.1 compares the temperatures from the "uncalibrated" 1D heat-transfer model of the mold using the blueprint geometry, and from the calibrated reduced-order model. The ROM matches the temperatures from the 3D model by construction, and the uncalibrated model under-predicts these temperatures by as much as 26%. The thermocouple temperatures all are significantly underpredicted by the uncalibrated model. Some molds, such as Mold D, are modeled reasonably well by the uncalibrated model.

$k_{\text{mold}}^{\diamond} = 315 \, \text{W}/(\text{m} \cdot \text{K})$

$q_{\text{hot}}^{\diamond} = 2500 \, \text{kW}/\text{m}^2$

$h_{\text{water}}^{\diamond} = 54 \, \text{kW}/(\text{m}^2 \cdot \text{K})$

$\bar{T}_{\text{water}}^{\diamond} = 35 \, ^{\circ}\text{C}$

$T_{\text{3D,hot}} = 323.8 \, ^{\circ}\text{C}$

$T_{\text{3D,TC}} = 172.0 \, ^{\circ}\text{C}$

Channel	A_{c} mm^2	$D_{\text{h,c}}$ mm	T_{c} °C	T_{roots} °C
1	56.14	7.631	71.86	107.0
2	80.0	7.619	59.20	79.79
3	80.0	7.619	60.52	80.61
4	80.0	7.619	62.50	80.70
Total	256.1			
ROM	73.18	7.623	63.52	107.0

Model	w_{c} mm	d_{c} mm	p_{c} mm	d_{plate} mm	d_{roots} mm	d_{channels} mm	d_{TC} mm
Uncalibrated ROM	16.0	5.0	22.0	30.0			24.0
Calibrated ROM	13.96	5.243	22.0	30.46	27.32	32.79	19.13

Figure 3.7 Calibration domain geometry, conditions, and results for Mold A [47]

$$k^{\diamond}_{\text{mold}} = 364 \, \text{W/(m} \cdot \text{K)}$$
$$q^{\diamond}_{\text{hot}} = 1750 \, \text{kW/m}^2$$
$$h^{\diamond}_{\text{water}} = 45 \, \text{kW/(m}^2 \cdot \text{K)}$$
$$\bar{T}^{\diamond}_{\text{water}} = 25 \, ^\circ\text{C}$$

$$T_{\text{3D,hot}} = 192.6 \, ^\circ\text{C}$$
$$T_{\text{3D,TC}} = 103.8 \, ^\circ\text{C}$$

Channel	A_{c} mm^2	$D_{\text{h,c}}$ mm	T_{c} °C	T_{roots} °C
1	105.0	8.077	44.78	72.54
2	90.0	7.826	37.93	59.84
3	90.0	7.826	38.33	60.37
4	90.0	7.826	38.35	60.40
5	90.0	7.826	37.72	60.43
Total	420.0			
ROM	93.33	7.882	39.42	72.54

Model	w_{c} mm	d_{c} mm	p_{c} mm	d_{plate} mm	d_{roots} mm	d_{channels} mm	d_{TC} mm
Uncalibrated ROM	5.0	18.0	15.0	27.0			22.0
Calibrated ROM	4.994	18.69	17.22	27.51	24.98	31.87	18.48

Figure 3.8 Calibration domain geometry, conditions, and results for Mold B [47]

$k^\diamond_{\mathrm{mold}} = 350\,\mathrm{W/(m \cdot K)}$

$q^\diamond_{\mathrm{hot}} = 3000\,\mathrm{kW/m^2}$

$h^\diamond_{\mathrm{water}} = 36\,\mathrm{kW/(m^2 \cdot K)}$

$\bar{T}^\diamond_{\mathrm{water}} = 40\,^\circ\mathrm{C}$

$T_{\mathrm{3D,hot}} = 282.5\,^\circ\mathrm{C}$

$T_{\mathrm{3D,TC}} = 179.6\,^\circ\mathrm{C}$

Channel	A_{c} mm^2	$D_{\mathrm{h,c}}$ mm	T_{c} °C	T_{roots} °C
1	78.54	10.0	91.18	124.1
2	72.32	7.642	72.04	115.9
3	72.32	7.642	63.58	109.3
4	72.32	7.642	62.85	107.4
5	72.32	7.642	62.52	106.4
6	72.32	7.642	62.37	105.9
7	72.32	7.642	62.24	105.5
8	72.32	7.642	62.20	105.5
9	72.32	7.642	62.16	105.4
10	72.32	7.642	62.17	105.3
Total	729.4			
ROM	72.94	7.878	66.33	124.1

Model	w_{c} mm	d_{c} mm	p_{c} mm	d_{plate} mm	d_{roots} mm	d_{channels} mm	d_{TC} mm
Uncalibrated ROM	5.0	14.0	10.0	21.0			15.0
Calibrated ROM	5.682	12.84	11.50	21.37	18.47	25.22	12.01

Figure 3.9 Calibration domain geometry, conditions, and results for Mold C [84]

ALL DIMENSIONS IN MM   WATER CHANNEL PITCHES REFLECT GEOMETRY AWAY FROM THERMOCOUPLE HOLE

$k^{\diamond}_{\text{mold}} = 340\,\text{W}/(\text{m}\cdot\text{K})$

$q^{\diamond}_{\text{hot}} = 2100\,\text{kW/m}^2$

$h^{\diamond}_{\text{water}} = 32.5\,\text{kW}/(\text{m}^2\cdot\text{K})$

$\bar{T}^{\diamond}_{\text{water}} = 31\,°\text{C}$

$T_{\text{3D,hot}} = 245.7\,°\text{C}$

$T_{\text{3D,TC}} = 146.7\,°\text{C}$

Channel	A_{c} mm^2	$D_{\text{h,c}}$ mm	T_{c} °C	T_{roots} °C
1	92.14	8.897	60.64	96.65
2	77.32	7.760	62.39	96.76
3	77.32	7.760	57.95	93.57
4	77.32	7.760	55.34	90.69
5	77.32	7.760	57.53	92.35
6	92.14	8.897	60.02	95.47
Total	493.5			
ROM	82.26	8.139	58.98	96.76

Model	w_{c} mm	d_{c} mm	p_{c} mm	d_{plate} mm	d_{roots} mm	d_{channels} mm	d_{TC} mm
Uncalibrated ROM	5.333	15.0	18.4	25.0			18.0
Calibrated ROM	5.647	14.57	18.0	25.75	24.12	30.24	16.03

Figure 3.10 Calibration domain geometry, conditions, and results for Mold D [31]

Table 3.1 Example mold geometry temperatures

Temperature (°C)	Mold A [47]		Mold B [47]		Mold C [84]		Mold D [31]	
	Uncalibrated	Calibrated	Uncalibrated	Calibrated	Uncalibrated	Calibrated	Uncalibrated	Calibrated
Hot face, T_{hot}	317.5	323.8	187.9	192.6	276.3	282.5	242.1	245.7
Cold face, T_{cold}	79.36		58.09		96.33		87.67	
Channel max., T_{roots}		107.0		72.54		124.1		96.76
Channel avg., T_{c}	59.55	63.52	37.65	39.42	62.30	66.33	60.32	58.98
Thermocouple, T_{TC}	127.0	172.0	82.12	103.8	147.8	179.6	130.9	146.7

3.6 Sensitivity of Mold Geometry Calibrations to Model Parameters

The calibration procedure evidently is insensitive to the non-geometric model parameters. For simplicity, take $d_{\text{coat}} = 0$ and $d_{\text{foul}} = 0$. The derivative of the one-dimensional temperature solution, Equation (3.8), with respect to the heat load is

$$\frac{\partial T_{1D}}{\partial q_{\text{hot}}} = \left(\frac{1}{h_{\text{cold}}} + \frac{L}{k_{\text{mold}}} \right) + \left(\frac{q_{\text{hot}}}{k_{\text{mold}}} \frac{\partial L}{\partial q_{\text{hot}}} \right). \tag{3.46}$$

The second term arises because of the dependence of the calibrated dimension L upon the hot face heat flux; this term must be small relative to the first term for the calibration process to be insensitive to q_{hot}, or that

$$\left| \frac{\partial L}{\partial q_{\text{hot}}} \right| \ll \frac{k_{\text{mold}}}{q_{\text{hot}} h_{\text{cold}}} + \frac{L}{q_{\text{hot}}}. \tag{3.47}$$

The conditions for insensitivity of the calibration process for the other parameters are

$$\left| \frac{\partial L}{\partial k_{\text{mold}}} \right| \ll \frac{L}{k_{\text{mold}}}, \tag{3.48}$$

$$\left| \frac{\partial L}{\partial h_{\text{water}}} \right| \ll \frac{k_{\text{mold}}}{h_{\text{cold}}^2} \left(\left(\frac{w_c}{p_c} \right) + \left(1 - \frac{w_c}{p_c} \right) \left(\frac{\tanh(b) + b \left(1 - \tanh^2(b) \right)}{2 \sqrt{\text{Bi}_{w_{\text{fins}}}}} \right) \right), \tag{3.49}$$

$$\left| \frac{\partial L}{\partial \bar{T}_{\text{water}}} \right| \ll \frac{k_{\text{mold}}}{q_{\text{hot}}}. \tag{3.50}$$

The sensitivity of the calibrated dimensions to the model parameters are evaluated with these conditions.

Consider Mold A in Section 3.5; Figure 3.11 presents the results of a numerical experiment that investigates the sensitivity of the calibrated mold plate thickness with respect to the four non-geometric parameters over a wide range of values. The other molds in Section 3.5 produce similar results. The value of d_{plate} is

- not at all sensitive to the heat load $q_{\text{hot}}^{\diamond}$: the maximum derivative with respect to $q_{\text{hot}}^{\diamond}$ is 7×10^{-10}, which is many orders of magnitude smaller than the limit predicted by Equation (3.47),
- weakly sensitive to the mold thermal conductivity $k_{\text{mold}}^{\diamond}$: and the maximum derivative with respect to $k_{\text{mold}}^{\diamond}$ is 2.5×10^{-3}, which is 5% or less of the limit predicted by Equation (3.48),
- somewhat sensitive to the water heat transfer coefficient $h_{\text{water}}^{\diamond}$ and bulk temperature $\bar{T}_{\text{water}}^{\diamond}$: the derivatives with respect to these variables are about 30% of the limits predicted by Equations (3.49) and (3.50).
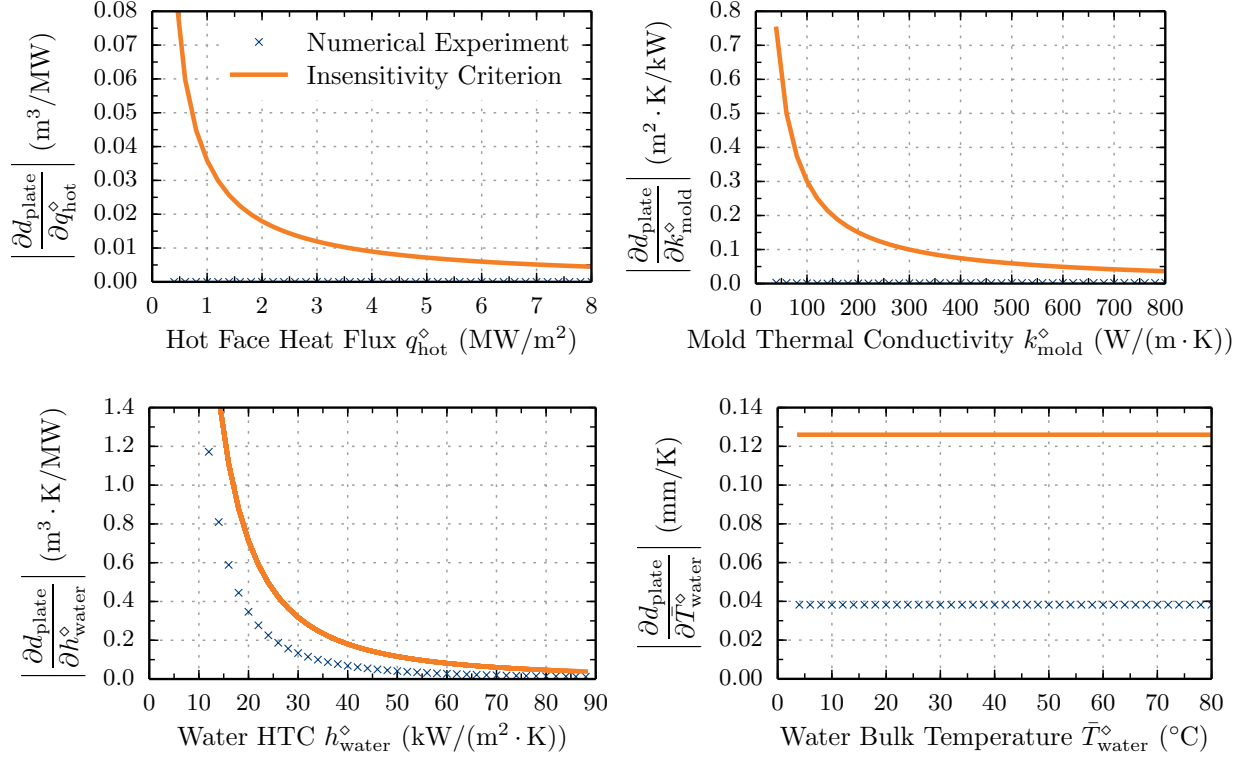
Figure 3.11   Sensitivity of calibrated d_{plate} to non-geometric ROM parameters

As $h_{\text{water}}^{\diamond}$ decreases the derivative increases, and by $h_{\text{water}}^{\diamond} = 27\,\text{kW}/(\text{m}^2\cdot\text{K})$ the derivative is 40% of the limit predicted by Equation (3.49). These lower values of h_{water} are valid and feasible predictions from Equation (2.7) at lower water speeds. Reasonable accuracy is attained from the ROM by calibrating it with values of $h_{\text{water}}^{\diamond}$ and $\bar{T}_{\text{water}}^{\diamond}$ that represent averages of their ranges encountered in the plant.

3.7   Conclusions

A reduced-order model has been developed by calibrating some of the parameters in a simple analytical solution that contains the physics of the problem. The methodology has been demonstrated specifically for mold heat transfer in continuous casting, and has created a rigorous procedure for calibrating the geometric parameters for the mold. The "blueprint" values of the mold geometry are changed by about 10% in the reduced-order model to compensate for multi-dimensional heat transfer. This approach is insensitive to the boundary conditions, so the model calibration procedure needs to be performed once per mold geometry. Once this geometric calibration is performed, other more complicated models of continuous casting can include accurate mold heat transfer with negligible computational cost.

CHAPTER 4
Steady-State Mechanical Behavior of the Mold[1]

4.1   Introduction

The thermal distortion of the continuous casting mold from room temperature to steady operating temperatures can influence the behavior of the solidifying steel strand in many ways, but likely the most important of these is the narrow-face (NF) taper. The thermo-mechanical behavior for steady casting conditions has been explored for billet molds [50, 80, 82, 83, 109, 113], conventional thick-slab molds [53, 98, 117], and thin-slab molds with [63, 68, 69] and without [68, 69] a funnel. Each mold shape has distinctive thermo-mechanical behavior, but in general, these studies have revealed the importance of the waterbox on the mechanical behavior of the system [98], and the importance of mold distortion on mold taper [80, 113], mold cracks [63, 69], and steel strand cracks [50, 83]. Experimental measurements of the mechanical behavior of molds during casting are rare; a few studies measured the wide face waterbox shape with linear displacement transducers [13, 64, 65].

Mold distortion is less severe with lower mold temperatures, such as caused by lower casting speeds [50, 80] or thinner mold plates [53, 80]. Coating layers have little influence on the mechanical behavior of the mold [53] because they are so thin. The highest temperature generally is found just below the meniscus, and operating with a metal level near a row of bolts increases inelastic deformation of the copper near the hot face [80].

Many previous mold distortion models assume elastic behavior; incorporating inelastic behavior of the mold copper is needed to predict residual stresses and residual distortion, but does not significantly affect the mold shape during operation [63]. The previous models have oversimplified the bolts and clamping, mold–mold and mold–waterbox contact, and the mold and waterbox geometry. A complete quantitative analysis of thermal distortion during operation of a continuous-casting mold, including realistic heat transfer, all of the important geometric details, proper constraints, and validation with plant measurements, has not yet been performed, and is the aim of this study.

---

[1]Much of the work presented in this chapter has been published by the author, for beam-blank molds [35] and for funnel molds [33, 34]. Beyond the content of these articles, this chapter contains an updated literature review and some details that were not included in the original publications. The measurements presented in this chapter were provided by G. Abbel, A. Chown, R. Schimmel, and H. Visser at Tata Steel.

4.2 Model Description

The mechanical behavior of the mold and waterbox pieces is governed by the quasi-static conservation of momentum,

$$\mathbf{0} = \nabla \cdot \boldsymbol{\sigma} + \boldsymbol{b}, \tag{4.1}$$

where $\boldsymbol{\sigma}$ is the Cauchy stress tensor and $\boldsymbol{b}$ is the body force density vector. The strains experienced by the mold and waterbox are small, so a linearized description of motion is adopted with total strain tensor

$$\boldsymbol{\varepsilon} = \frac{1}{2} \left(\nabla \boldsymbol{u} + \nabla \boldsymbol{u}^{\top} \right), \tag{4.2}$$

which decomposes additively into elastic and thermal parts, *i.e.*,

$$\boldsymbol{\varepsilon} = \boldsymbol{\varepsilon}^{\mathrm{el}} + \boldsymbol{\varepsilon}^{\mathrm{th}}. \tag{4.3}$$

The mold and waterbox are composed of isotropic polycrystalline copper and steel, so the stress tensor is related to the elastic strain tensor with HOOKE's law,

$$\boldsymbol{\sigma} = \mathbb{C} : \boldsymbol{\varepsilon}^{\mathrm{el}}, \tag{4.4}$$

where the components of the fourth-rank elastic stiffness tensor $\mathbb{C}$ are

$$\mathbb{C}_{ijk\ell} = \left(\kappa - \frac{2}{3}\mu \right) \delta_{ij}\delta_{k\ell} + \mu \left(\delta_{ik}\delta_{jl} + \delta_{i\ell}\delta_{kj} \right), \tag{4.5}$$

where κ and μ are the isotropic bulk and shear moduli and δ_{ij} is the KROENECKER delta. The thermal strain tensor is

$$\boldsymbol{\varepsilon}^{\mathrm{th}} = \alpha \left(T - T_{\mathrm{ref}} \right) \boldsymbol{I}, \tag{4.6}$$

where α is the isotropic coefficient of thermal expansion based on reference temperature T_{ref}, and $\boldsymbol{I}$ is the second-rank identity tensor.

Symmetry planes on the mold and waterbox have no normal displacement,

$$\boldsymbol{u} \cdot \boldsymbol{n} = 0, \tag{4.7}$$

and no tangential traction,

$$(\boldsymbol{I} - \boldsymbol{n} \otimes \boldsymbol{n}) \cdot \boldsymbol{t} = \mathbf{0}, \tag{4.8}$$

where $\boldsymbol{t} = \boldsymbol{\sigma}^{\top} \cdot \boldsymbol{n}$ is the traction vector on the surface. Contacting surfaces between the mold and waterbox or between the wide and narrow faces of the mold move together or form gaps according to nonlinear conditions. Any point on the "master" surface with normal vector $\boldsymbol{n}$

is nearest to some point on the "slave" surface, and the relative position between them is $\boldsymbol{x}_{\text{rel}}$. The normal component of this relative position, $d_{\text{gap}} = \boldsymbol{x}_{\text{rel}} \cdot \boldsymbol{n}$, is the size of the gap between the surfaces. If the surfaces are not in contact, *i.e.*, $d_{\text{gap}} > 0$, then they are free of tractions,

$$\boldsymbol{t} = \boldsymbol{0}. \tag{4.9}$$

If the surfaces are in contact, *i.e.*, $d_{\text{gap}} = 0$, then they move with a relative velocity $\boldsymbol{v}_{\text{rel}}$ that has no normal component,

$$\boldsymbol{v}_{\text{rel}} \cdot \boldsymbol{n} = 0, \tag{4.10}$$

and a tangential traction that follows the COULOMB law,

$$(\boldsymbol{I} - \boldsymbol{n} \otimes \boldsymbol{n}) \cdot \boldsymbol{t} = -\eta\,(\boldsymbol{t} \cdot \boldsymbol{n})\,\frac{\boldsymbol{v}_{\text{rel}}}{\|\boldsymbol{v}_{\text{rel}}\|_2}, \tag{4.11}$$

where η is the coefficient of friction, and the interfacial dissipation $\boldsymbol{t} \cdot \boldsymbol{v}_{\text{rel}}$ is maximum. This contact model [1] is described as "hard" because the contact pressure $p_{\text{c}} = \boldsymbol{t} \cdot \boldsymbol{n}$ follows

$$p_{\text{c}} = 0 \tag{4.12}$$

if the surfaces are not in contact, *i.e.*, $d_{\text{gap}} > 0$, and

$$d_{\text{gap}} = 0 \tag{4.13}$$

if the surfaces are in contact, *i.e.*, $p_{\text{c}} > 0$. Mechanical contact is cast as a variational problem [1] that finds the gap size d_{gap} as

$$d_{\text{gap}}\boldsymbol{n} = \boldsymbol{x}_{\text{slave}} - \boldsymbol{x}_{\text{master}} \tag{4.14}$$

subject to orthogonality with the two vectors $\hat{\boldsymbol{t}}^1$ and $\hat{\boldsymbol{t}}^2$ that are tangent to the direction of sliding, *i.e.*,

$$\hat{\boldsymbol{t}}^1 \cdot (\boldsymbol{x}_{\text{slave}} - \boldsymbol{x}_{\text{master}}) = 0 \tag{4.15}$$

$$\hat{\boldsymbol{t}}^2 \cdot (\boldsymbol{x}_{\text{slave}} - \boldsymbol{x}_{\text{master}}) = 0, \tag{4.16}$$

where $\boldsymbol{x}_{\text{master}}$ is a point constrained to lie on the master surface, *i.e.*, a finite-element face, and $\boldsymbol{x}_{\text{slave}}$ is the nearest point on the slave surface, and the tangent vectors are computed from the incremental motion across a time step. If the surfaces are in contact then the contact pressure is introduced as a LAGRANGE multiplier that enforces $d_{\text{gap}} = 0$, *i.e.*, $\Pi = p_{\text{c}}\,(\boldsymbol{x}_{\text{slave}} - \boldsymbol{x}_{\text{master}}) \cdot \boldsymbol{n}$.

The hot face of the molds are supplied the traction

$$\boldsymbol{t} = -p_{\text{f}}\boldsymbol{n}, \tag{4.17}$$

to model the effect of ferrostatic pressure, where the applied pressure p_{f} increases with distance below the top of the liquid steel according to

$$p_{\mathrm{f}} = \begin{cases} 0 & \text{if } z \leq z_{\mathrm{men}} \\ \rho_{\mathrm{steel}} g \left(z - z_{\mathrm{men}} \right) & \text{if } z_{\mathrm{men}} \leq z \end{cases}, \tag{4.18}$$

where z_{men} is the position of the meniscus below the top of the mold, ρ_{steel} is the mass density of the liquid steel, and g is the acceleration due to gravity. The traction specified by Equation (4.17) assumes that the dynamic pressure and skin friction of the molten steel have negligible effect on the behavior of the mold. Strictly, the pressure distribution described by Equation (4.18) is valid for the inside surface of the solidifying shell, but the ferrostatic pressure is assumed to transmit perfectly through the solidifying steel and slag layers to the mold hot faces. The ferrostatic pressure is applied only on the "active" hot face in contact with the strand, from the meniscus to mold exit and in between the mold pieces.

As mentioned in Section 2.2, the waterbox is thermally inert, which decouples the thermal and mechanical problems. Negligible heat is assumed to flow between the mold pieces because the distortion opens an air gap along most of their originally-mating faces, as discussed later. For the model of mold distortion, the waterbox is specified as isothermal at ambient temperature, and the mold temperature fields are taken from the work presented in Chapter 2. These temperatures drive the mechanical problem relative to an initial stress-free state at a uniform temperature of T_0, except for the mold bolts, which are described in Section 4.3.

The finite-element method is employed to solve this mechanical boundary-value problem, using the commercial software ABAQUS [1]. The molds and waterboxes are modeled with complete geometric detail, including the mold plates, water channels, bolts, bolt holes, tie-rods, and waterboxes, as discussed in Sections A.1 and A.2. Only one symmetric fourth of the assembly is modeled for computational efficiency. The domains are discretized with a mix of "fully-integrated" linear 4-node tetrahedral, 6-node wedge, and 8-node hexahedral elements (ABAQUS continuum elements C3D4, C3D6, and C3D8). Numerical experiments with these elements in similar thermo-mechanical problems [1] has shown them quite capable of matching analytical solutions, so numerical artifacts are of little concern. The ferrostatic pressure given by Equation (4.18) is applied with the user subroutine DLOAD. Mechanical contact is treated with the above-described "hard" contact algorithm within ABAQUS.

4.3 Bolt Calculations

The bolts that attach the mold to the waterbox are modeled as T3D2 truss elements, *i.e.*, axial-displacement-only finite elements. The nodes on these truss elements are attached

with a "distributing coupling constraint" to the appropriate surfaces on the molds and waterboxes, *i.e.*, the female bolt threads on the mold and the outside surface of the waterbox in contact with the bolt head, as illustrated in Figure 4.1. The distributing coupling constraint distributes the behavior of the truss node over the designated surface in an average sense such that the force and moment balances are maintained. Each simulated bolt is given a stiffness based on its length and the effective stiffness of the actual bolt and was pre-stressed according to plant practice, as discussed in this section.

The bolts are tightened to a specified torque when the mold is assembled. Following previous work [98], a torque T is converted to an axial force with

$$F_{\text{bolt}} = \frac{T}{D_{\text{bolt}}/2} \left(\frac{\pi D_{\text{bolt}} - \eta_{\text{bolt}} p_{\text{t}}}{p_{\text{t}} + \eta_{\text{bolt}} \pi D_{\text{bolt}}} \right), \tag{4.19}$$

where D_{bolt} is the basic diameter of the bolt, p_{t} is the thread pitch, and η_{bolt} is the coefficient of friction between the male and female threads. The coefficient of friction is taken as $\eta_{\text{bolt}} = 0.25$ for greased bolts and $\eta_{\text{bolt}} = 0.5$ for ungreased bolts. The bolt pre-stress is applied in the ABAQUS text input file[2] with, for example,

```
*INITIAL CONDITIONS, TYPE=STRESS
 NFBolt01.BoltBody, 167.51
```

where `NFBolt01.BoltBody` refers to the set "BoltBody" on the instance "NFBolt01" of the narrow-face bolt part, and `167.51` is the bolt pre-stress, in this case in MPa.

The weight of the mold is negligible relative to the pre-stress on the bolts, so the effect of gravity in the momentum balance, Equation (4.1), is neglected. For the funnel mold analyzed in this work, a mass density of $8900 \, \text{kg/m}^3$ gives weights of $7.23 \, \text{kN}$ and $0.527 \, \text{kN}$ for the wide and narrow faces. Uniformly distributing these loads over the appropriate number of bolts, the average shearing stress due to the mold weight is $0.569 \, \text{MPa}$ and $0.364 \, \text{MPa}$. These loads are negligible relative to the pre-stress, so the effect of gravity is neglected safely.

The mold assembly includes typically four large clamping rods, known as "pull rods" or "tie rods," that hold the assembly together and oppose the ferrostatic pressure and the thermal distortion. Due to symmetry, however, only two of these clamping rods are modeled. These rods are modeled as pre-stressed truss elements with distributing-coupling constraints, much like the mold bolts. For the funnel mold, the clamping force is controlled with packs of Belleville-washer disc springs.

The actual mold bolts have varying section properties along the length of the bolt, so the

---

[2]The ABAQUS graphical interface currently does not support initial stresses.

bolts are modeled as several springs in series, which give an effective stiffness K_{eff} of

$$\frac{1}{K_{\text{eff}}} = \sum_{i=1}^{N} \frac{1}{K_i}, \tag{4.20}$$

where each bolt has N segments, and

$$K_i = \frac{A_i E_i}{L_i} \tag{4.21}$$

is the stiffness of segment i that has cross-sectional area A_i, Young's modulus E_i, and length L_i. This calculation neglects the effect of the small geometric features of the bolts such as the fillets at the interface between segments. The springs-in-series model assumes the same force in each segment of the bolt, so the displacements of each segment add together to give the total displacement of the bolt. The stiffness of the Belleville-washer springs, of 47.1 MN/m and 44.6 MN/m for the upper and lower tie rods, are included as additional stiffnesses in the series for the tie rods.

The funnel mold analyzed in this work uses on the wide face of the mold a long bolt and a short bolt, shown in Figures 4.2 and 4.3, and on the narrow face of the mold a short bolt, shown in Figure 4.4. On the wide face, the short bolts go through a only backing plate, and the long bolts go through the backing plate and stiffener plates or the mold water. Tables 4.1, 4.2, and 4.3 give the details of calculating the effective stiffness of these three bolts.
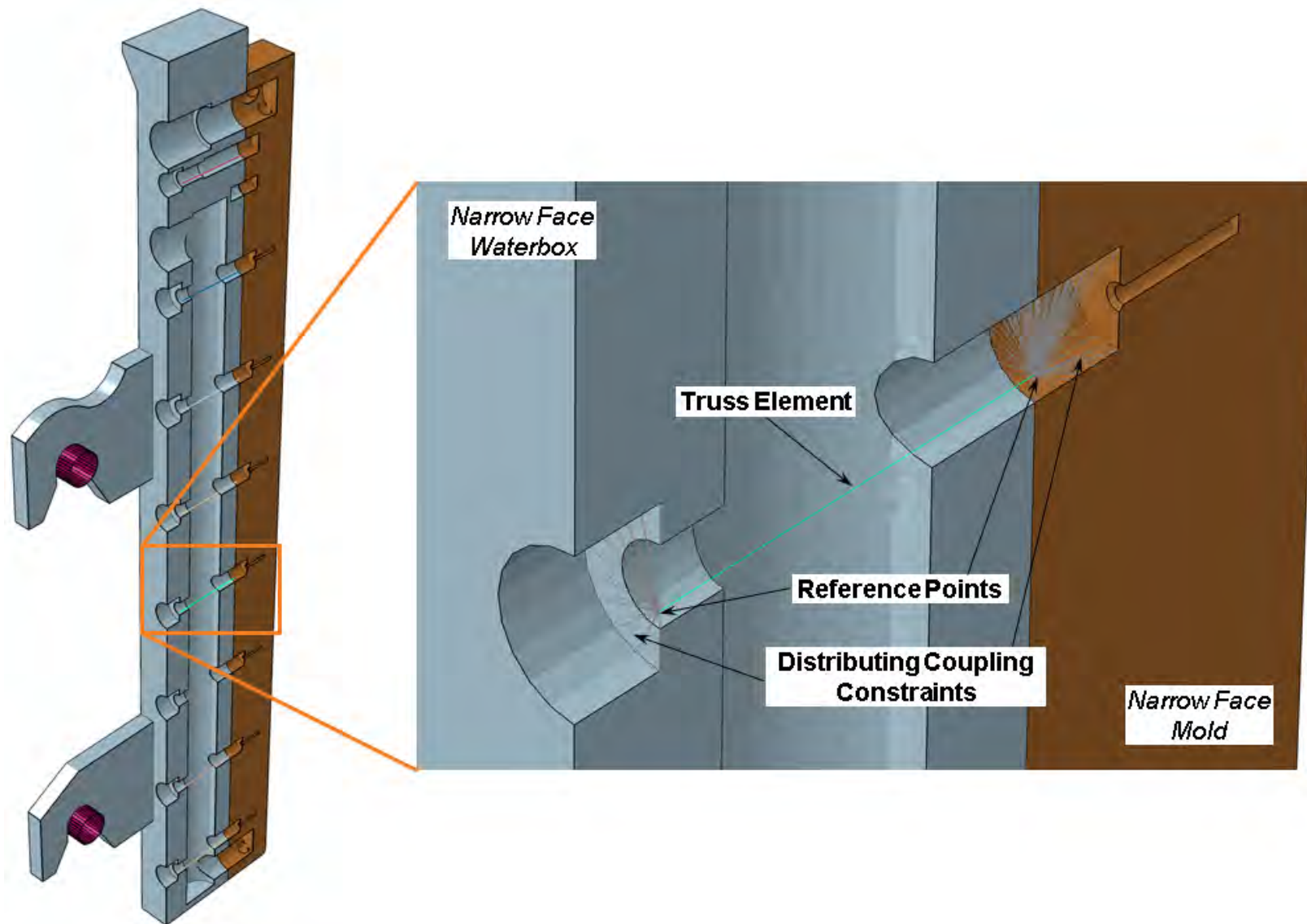
Figure 4.1 Simulated mold bolt with "distributing coupling constraint." Shown as zoom of the narrow face mold and waterbox for the funnel mold considered in this work.

ALL DIMENSIONS IN MM
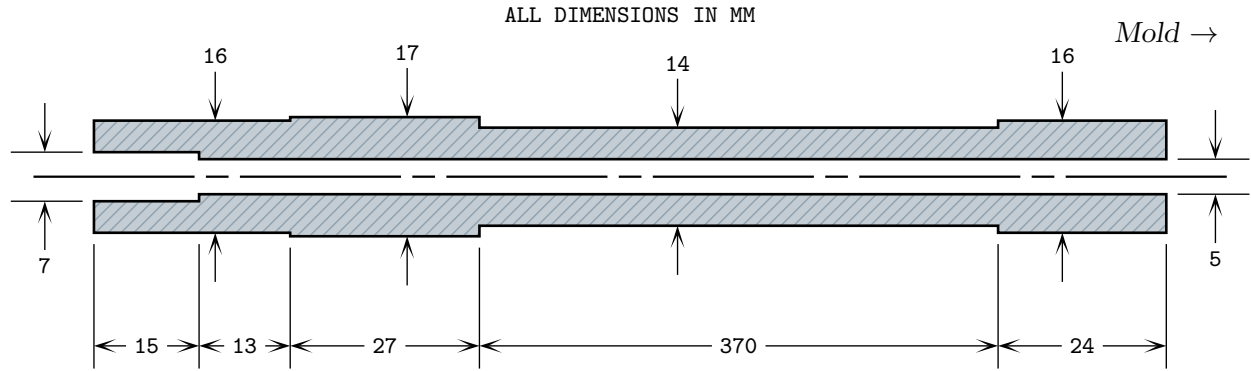
Mold →

Figure 4.2 Mold bolt: funnel mold, "WF long"

Table 4.1 Section properties for the funnel mold "WF long" mold bolt

	L	d_i	d_o	A	K
	mm	mm	mm	mm^2	MN/mm
Segment 1	15	7	16	162.58	2.168
Segment 2	13	5	16	181.43	2.791
Segment 3	27	5	17	207.3	1.5359
Segment 4	370	5	14	134.30	0.072 60
Segment 5	24	5	16	181.43	1.5119
Total	449				0.062 87
Model	400			125.53	0.062 87

ALL DIMENSIONS IN MM

17

16   16   Mold →

7

5

16   11   38   22
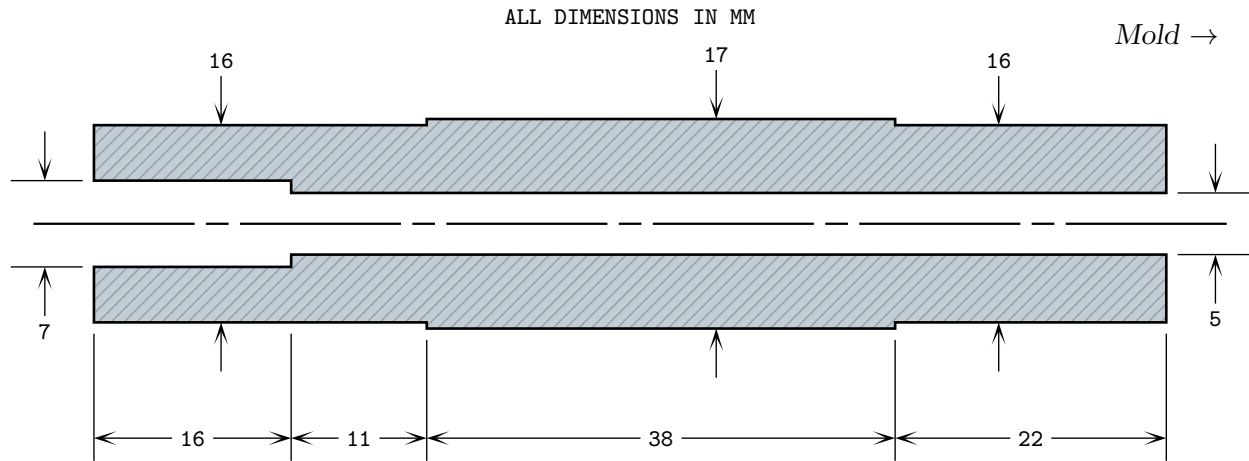
Figure 4.3 Mold bolt: funnel mold, "WF short"

Table 4.2 Section properties for the funnel mold "WF short" mold bolt

	L	d_i	d_o	A	K
	mm	mm	mm	mm^2	MN/mm
Segment 1	16	7	16	162.58	2.032
Segment 2	11	5	16	181.43	3.299
Segment 3	38	5	17	207.3	1.0913
Segment 4	22	5	16	181.43	1.6493
Total	87				0.4314
Model	35			74.27	0.4314

ALL DIMENSIONS IN MM
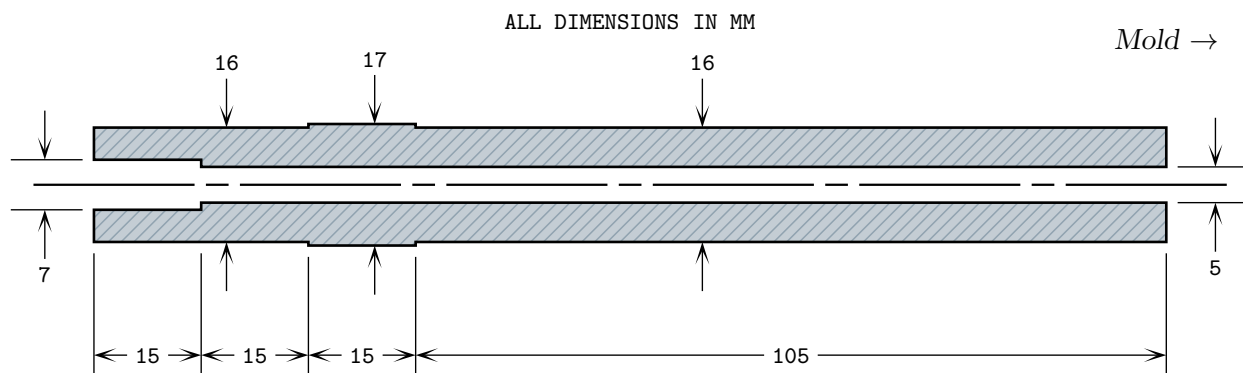
Mold →

Figure 4.4 Mold bolt: funnel mold, "NF short"

Table 4.3 Section properties for the funnel mold "NF short" mold bolt

	L	d_i	d_o	A	K
	mm	mm	mm	mm^2	MN/mm
Segment 1	15	7	16	162.58	2.168
Segment 2	15	5	16	181.43	2.419
Segment 3	15	5	17	207.3	2.765
Segment 4	105	5	16	181.43	0.3456
Total	150				0.2421
Model	90			108.01	0.2421

The bolts on the funnel mold are threaded with M16 external threads, which are fed in to a M16 internal / M22x1.5 external bushing, which then is fed into the mold, which has M22x1.5 internal threads. The bushing is neglected from the stiffness calculation of Equation (4.20). The applied torque of $T = 100 \, \text{N} \cdot \text{m}$ converts to an axial load of about $F_{\text{bolt}} = 30 \, \text{kN}$ for all bolts. The length of the simulated bolts and tie rods changes to fit in the geometry of the simulation, so the simulated area of the bolts is changed accordingly so that the effective stiffness of the bolt remains the same. The pre-stresses are applied based on this adjusted area. The upper tie rod has a simulated half-length of 520.25 mm, a pre-load of 40 kN, a stiffness of 34.8 MN/m, and a simulated area of $96.50 \, \text{mm}^2$. The lower tie rod has a simulated half-length of 520.25 mm, a pre-load of 70 kN, a stiffness of 33.4 MN/m, and a simulated area of $86.94 \, \text{mm}^2$. The calculations for the bolts in the beam-blank mold are modeled similarly: the simulated bolt lengths are 158.75 mm, 171.45 mm, and 184.15 mm.

4.4 Beam-Blank Mold

4.4.1 Model Details

The geometry of the beam-blank mold and waterbox analyzed in this work is presented in Section A.2. For the mechanical analysis, only one-fourth of the mold and waterbox are modeled, even though they do not have four-fold symmetry. Contact between the two mold pieces and two backing plates was enforced manually by iteratively applying constraint equations on contacting nodes.

4.4.2 Mold and Waterbox Distortion

The mold temperatures calculated in Section 2.3 drive the thermal distortion of the mold. Figure 4.5 presents these temperatures on the calculated distorted shape of the mold. The wide face of the mold does not distort very much because the web region of the mold is so thick and provides a large, cold region to constrain the distortion. The predicted distortions for the wide and narrow faces are shown in Figures 4.6 and 4.7. The wide face is pushed away from the steel by about 0.2 mm because of the ferrostatic pressure, and the mensicus region is bent another 0.1 mm to 0.3 mm further away from the steel because of the thermal distortion. The narrow face of the mold distorts into the usual parabolic shape [98] with about 1.5 mm depth.

On top of the casting radius, this beam-blank mold has parabolic tapers, listed in

Table 4.4, to accommodate the shrinkage of the solidifying shell. Figures 4.8 through 4.11 show the taper of the hot face, both without the mold distortion, *i.e.*, these parabolic profiles, and with the mold distortion. The distorted values are calculated with the results of the mold distortion calculation: the displacements down the mold are shifted such that the displacement at the nominal meniscus level is zero, and the results are added to the parabolic profiles. The entire field of the distorted hot face, relative to the shape of the mold at the meniscus, was converted to a 2D transient Lagrangian field for use with the multiphysics model discussed in Chapter 5.

These distortions are fractions of millimeters on top of mold dimensions on the order of 10 mm to 100 mm; however the effect on the taper can be significant, because the shrinkage of the shell is on the order of 1 mm to 10 mm. In the web region, the taper is almost doubled by mold exit, as shown in Figure 4.8. The distortion of the slanted part of the flange, shown in Figure 4.9, slightly lessens the taper, while the distortion of the tip of the flange, shown in Figure 4.10, slightly increases the taper. The distortion of the narrow face, shown in Figure 4.11, has about 0.5 mm more taper at the top 2/3 of the mold, but about 0.5 mm less taper at the bottom 1/3 of the mold.

Table 4.4   Beam-blank mold distortion simulation model properties and constants

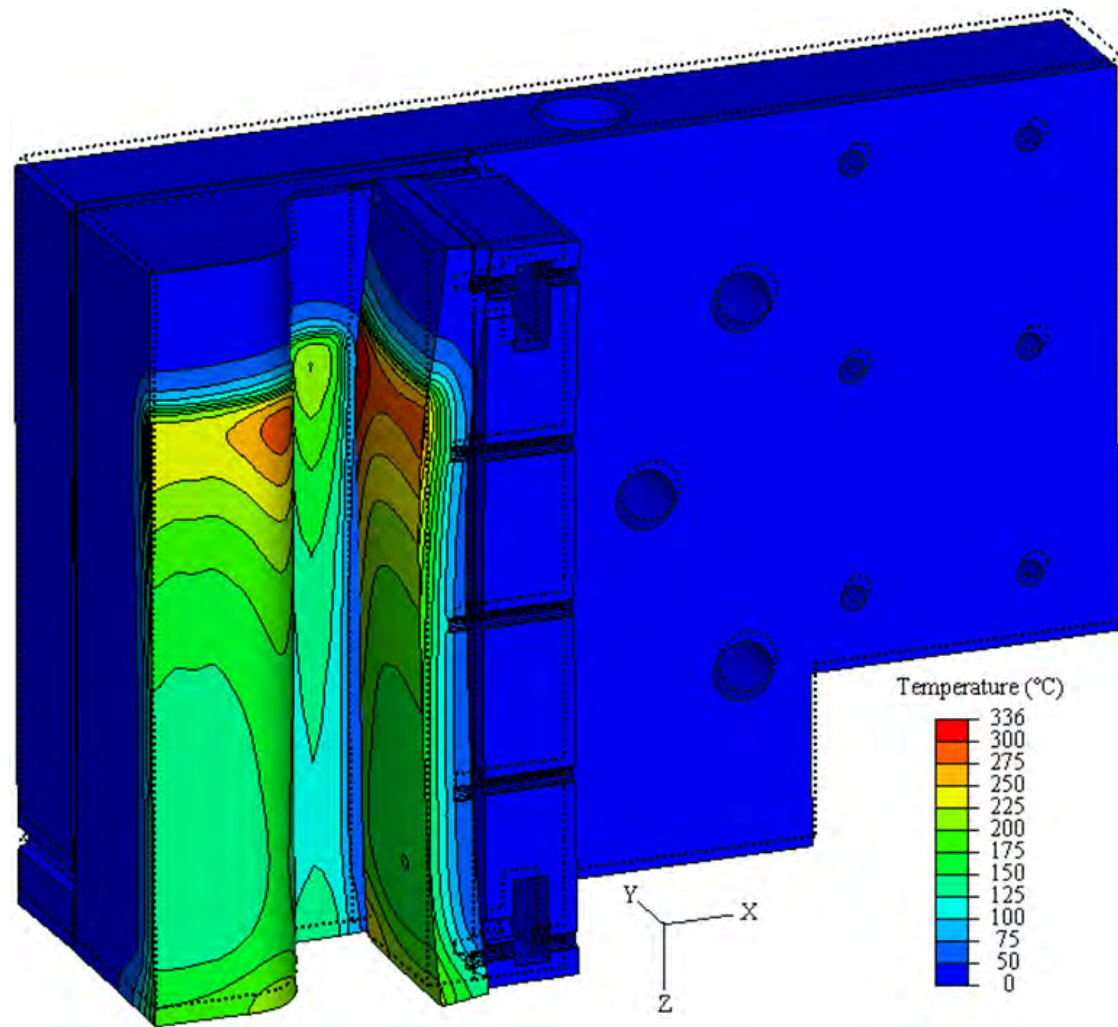| Property or Constant	Value	Unit
Strand section size, mold top	$576 \times 436 \times 93$	mm
Working mold length	660.4	mm
Total taper at flange	2.33	mm
Total taper at shoulder	-2.22	mm
Total taper at web	0.48	mm
Total taper at narrow face	3.0	mm
Casting speed	0.889	m/min
Strand initial temperature	1523.7	°C
Mold initial temperature	285.0	°C
Steel liquidus temperature	1518.70	°C
Steel solidus temperature	1471.95	°C
Cooling water temperature	34.5	°C

Figure 4.5 Hot face temperatures and distorted shape of beam-blank mold and waterbox (20 times magnified distortion)

Table 4.5 Funnel mold distortion simulation model properties and constants

Property or Constant	Value	Unit
Mold – CuCrZr alloy		
Young's modulus	117	GPa
Poisson's ratio	0.181	—
Coefficient of thermal expansion	18	$\mu m/(m \cdot K)$
Initial temperature	30	°C
Waterbox – AISI 316Ti		
Young's modulus	200	GPa
Poisson's ratio	0.299	—
Mold-mold friction coefficient	1.0	—
Mold-waterbox friction coefficient	0.5	—
Liquid steel mass density	7100	kg/m^3
Acceleration due to gravity	9.807	m/s^2
Bolt friction coefficient	0.3	—
Bolt thread pitch	1.5	mm
Bolt tightening torque	100	$N \cdot m$

4.5 Funnel Mold

4.5.1 Model Details

The geometry of the funnel mold and waterbox analyzed in this work is presented in Section A.1. The narrow face support cylinders are modeled as "analytical rigid surfaces," with mechanical contact defined between them and the appropriate surfaces on the waterbox hooks. The cylinders are constrained with zero-displacement boundary conditions to prevent rigid body motion of the narrow face. The large tie rods that hold the assembly together, the symmetry conditions on appropriate planes, and the friction between the narrow and wide faces prevent rigid body motion of the wide face. The contacting surfaces of the mold plates and between each mold plate and its waterbox are modeled with "hard" contact. The conditions for the simulation are summarized in Table 4.5.

With 4 830 081 degrees of freedom, this nonlinear mechanical model required 44.6 days to solve on an 8-core 2.66 GHz workstation with 8 GB of RAM. The large computational effort was due to both the large problem size and the iteration needed for convergence of the contact algorithm. To assist convergence, the model was marched through 10 pseudo-time steps by applying a fraction of the temperature change to steady state, converging a partial solution, and from that state applying an additional fraction of the total temperature change, until the entire temperature change was applied. Recent work on a transient mold distortion
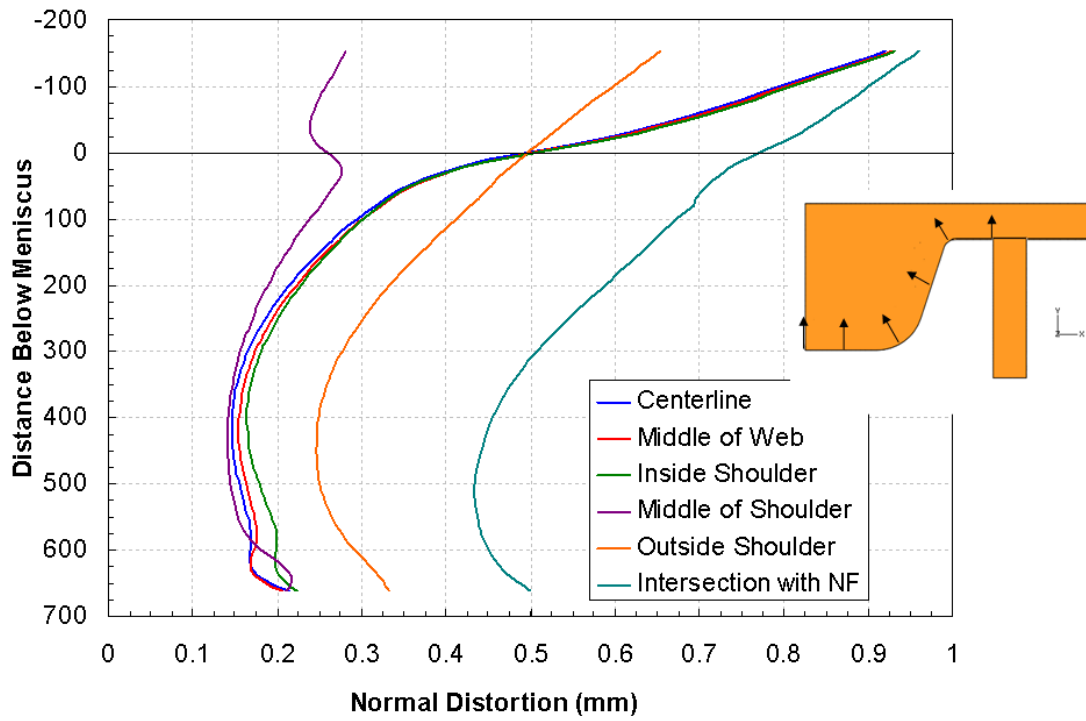
Figure 4.6   Calculated beam-blank mold distortions on the wide face
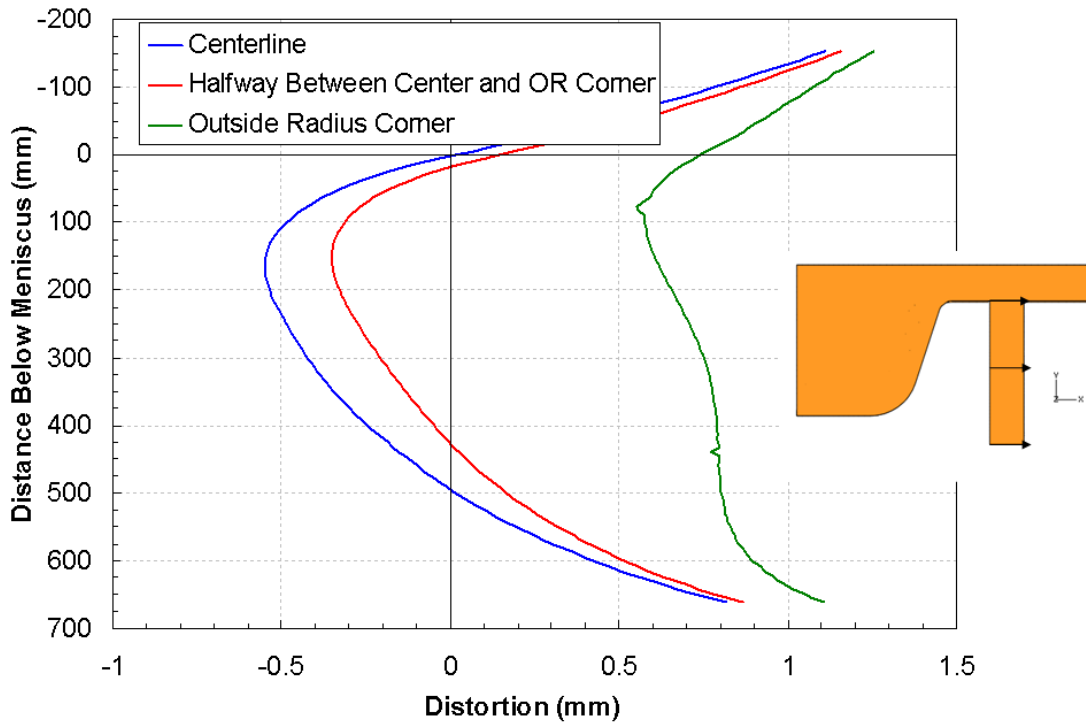
Figure 4.7   Calculated beam-blank mold distortions on the narrow face
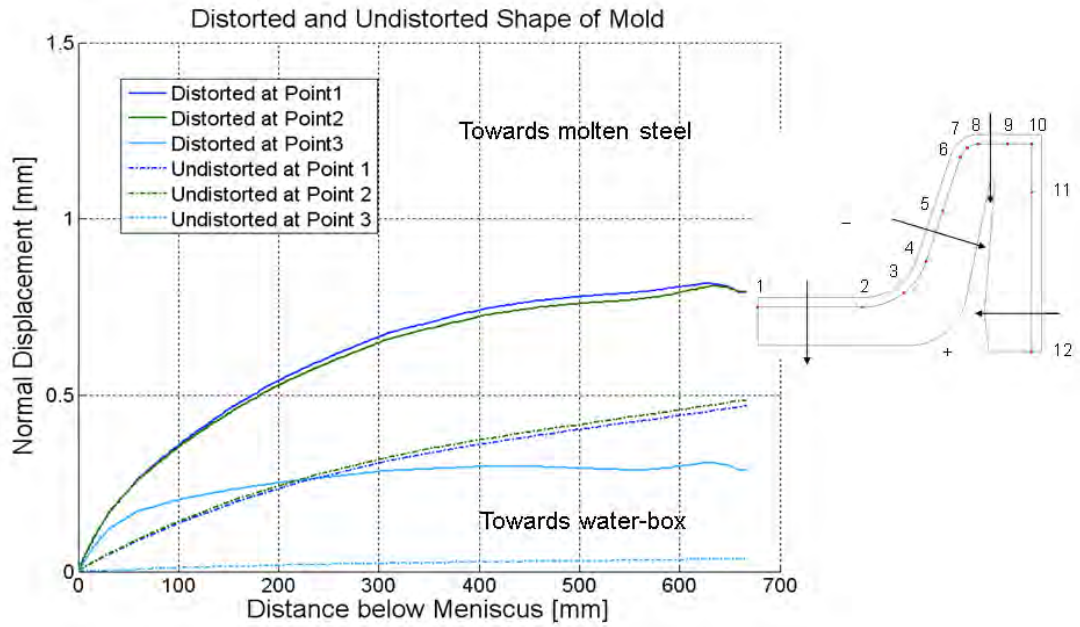
Figure 4.8   Nominal and distorted taper profiles on the beam-blank web
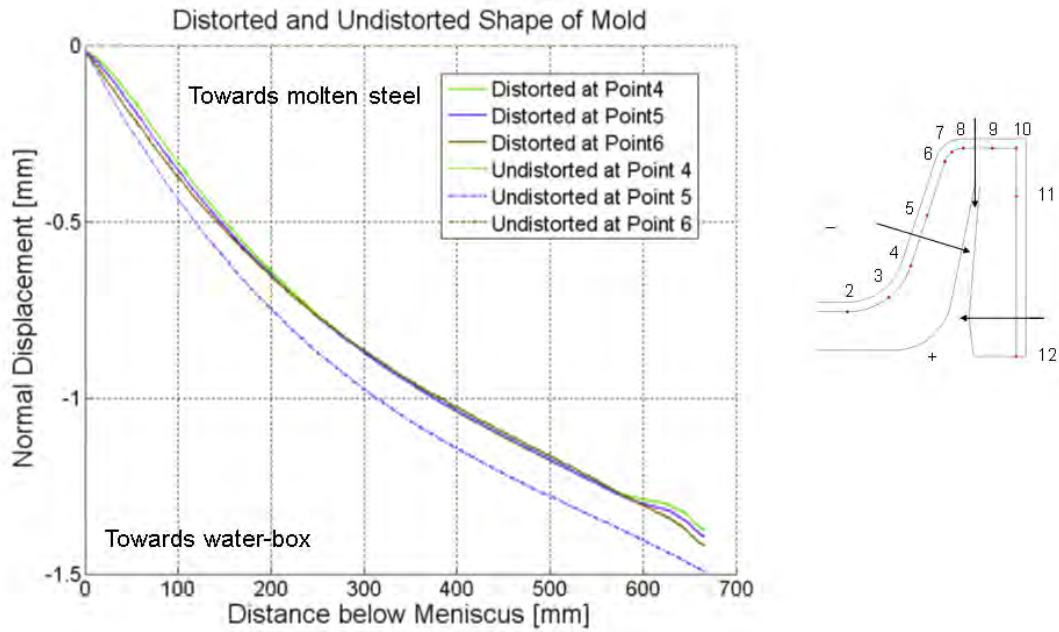
Figure 4.9   Nominal and distorted taper profiles on the beam-blank flange slant

68
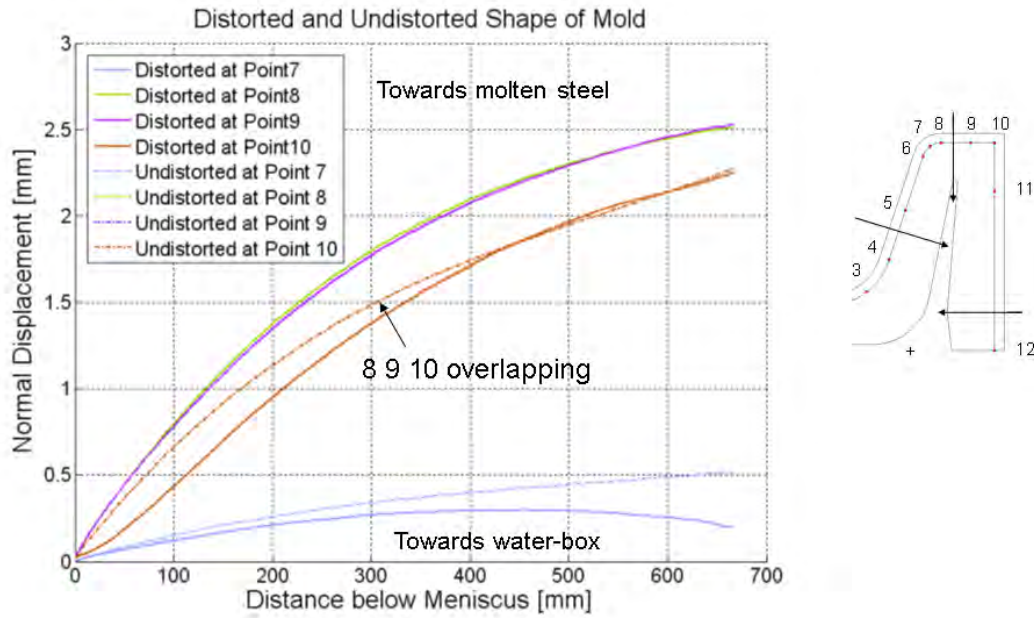
Figure 4.10 Nominal and distorted taper profiles on the beam-blank flange tip

Figure 4.11 Nominal and distorted taper profiles on the beam-blank narrow face

69

problem [34] suggests that more, smaller load steps will decrease the overall computational effort because of fewer required contact iterations.

4.5.2 Mold and Waterbox Distortion

The primary focus of this study is the distortion behavior of the mold. In addition, the practical consequences are investigated regarding possible problems of i) tensile stress overloading of the bolts, ii) bolt shearing at the mold–waterbox interface, iii) narrow face edge crushing, iv) mold taper, and v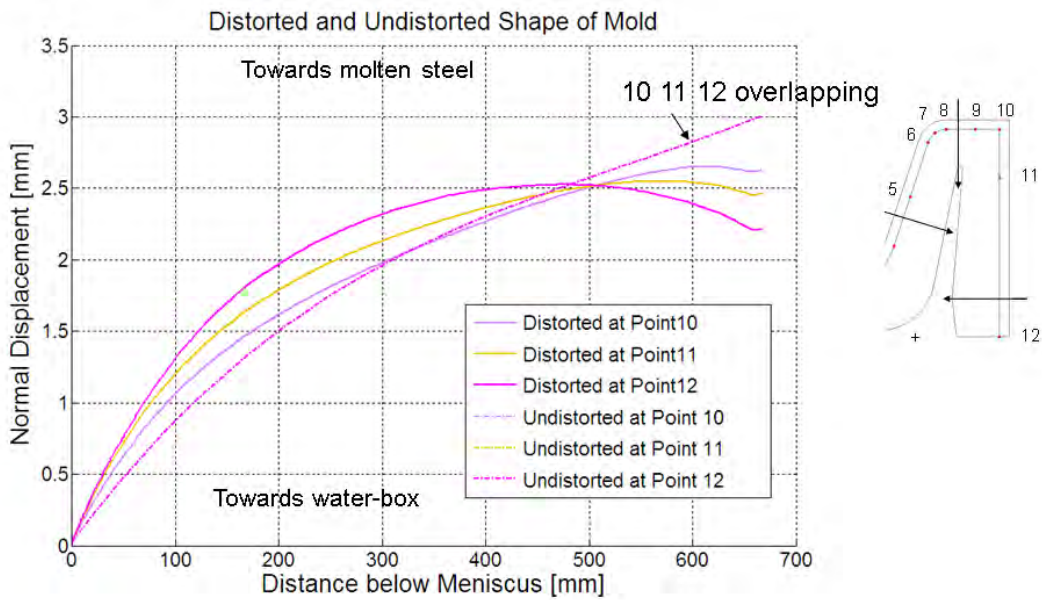) mold wear. In all results figures, increasingly positive values of displacement mean distortion further away from the molten steel, towards the mold cooling water, or further along in the casting direction.

Figures 2.17 and 4.12 show the distorted shape of the narrow-face mold plates and waterbox. Expansion of the copper hot face is constrained by the cold face and waterbox, which causes the entire assembly to bow towards the molten steel into a roughly-parabolic arc, like a bimetallic strip. This behavior of the narrow face agrees with previous work [98]. About 0.9 mm difference is predicted between the maximum, found midway down the mold, and mold exit. The parabolic distortion has a slight wobble in the middle of the mold, caused by the extra rigidity of the waterbox hooks. Distortion across the thin perimeter direction is very small.

The distortion of the wide face mold and waterbox is shown in Figures 4.13 through 4.19. In general, the thermal distortion causes the copper mold plates to bow towards the molten steel in the shape of a 'w,' both vertically and horizontally. The mold also is pushed by the molten steel due to the ferrostatic pressure, but this effect is small. More importantly, the bolts through the waterbox constrain the thermal distortion of the mold plates, especially considering the shorter, stiffer bolts. The cold edges of the mold, *i.e.*, the top edge and the edge furthest from the centerline, provide constraint against some of the expansion that the hot face experiences. The distortion is most pronounced just below the meniscus and towards mold exit, near where the surface temperatures are highest.
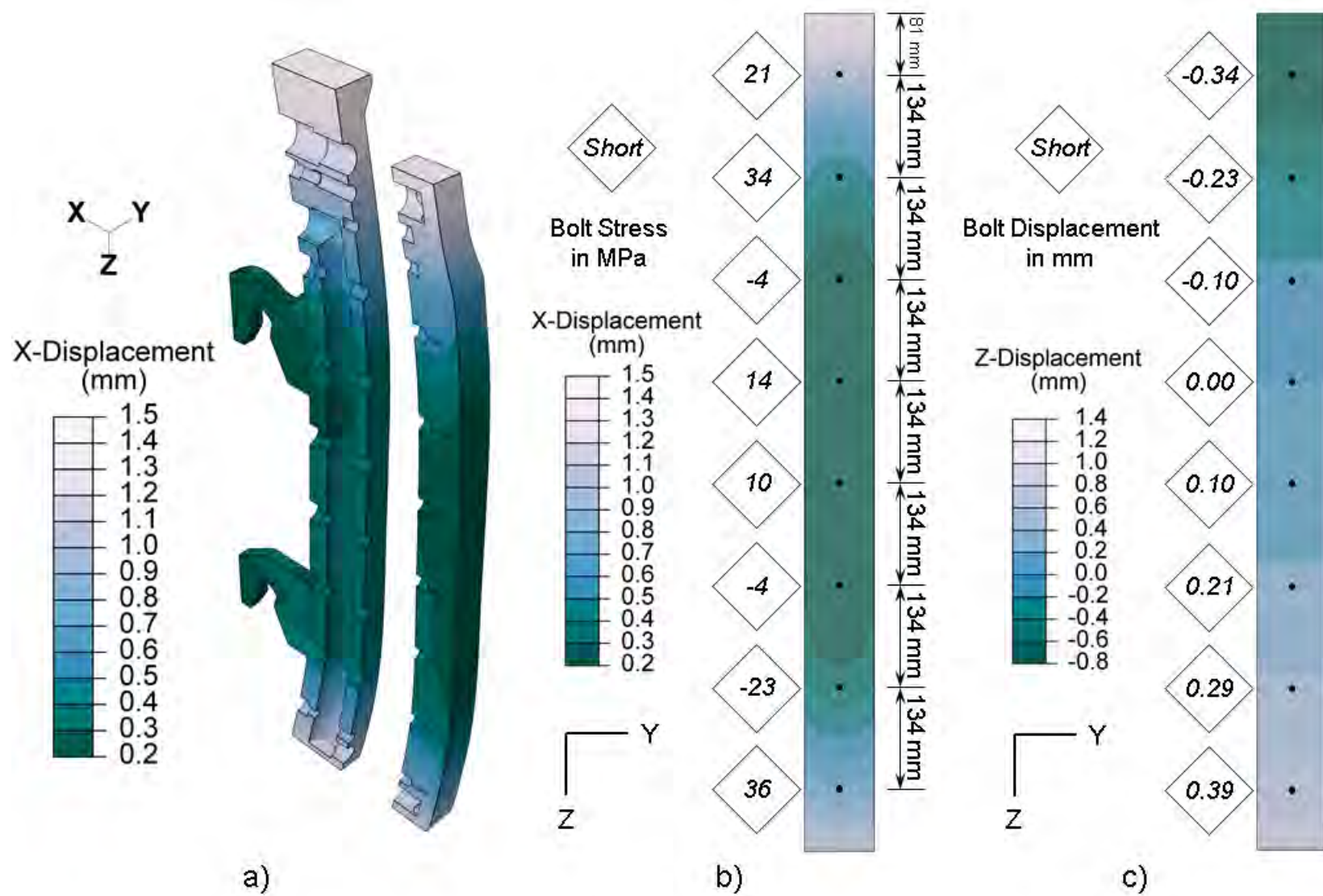
Figure 4.12 Funnel mold NF(a) mold and waterbox distortion (50 times scaled distortion), (b) hot-face displacement away from SEN and bolt stresses, and (c) hot-face and bolt displacement towards mold exit.

The central region of the wide face mold, *i.e.*, the inner flat and inner curve regions, which in conventional slab molds experiences the most distortion [98], has relatively little distortion in this mold. This effect is due to the constraint provided by the short bolts, which connect the mold plates to the hollowed-out portion of this very rigid waterbox. The most severe distortion is found just below the meniscus in the middle of the outside curve region of the funnel at the same location as the mold-level sensor channel, but this location is just a coincidence; the more relevant feature of this peak location is that it lies between two bolt columns, one of which consists only of long, compliant bolts. Comparing the bolt stiffnesses in Tables 4.1 and 4.2, the longer bolts have only about 15% of the stiffness of the shorter bolts. Except for the top two rows and bottom row of bolts, these longer bolts are attached to the mold through stiffener plates on the waterbox which offset their lower stiffness. The peaks in mold distortion occur at 325 mm from the centerline at 200 mm and 1000 mm below mold top as shown in Figures 4.14, 4.17, and 4.19, in the vicinity of the long bolts without stiffener plates. The cavities for the electromagnetic flow control system thus have significant effect on the distorted shape of the mold. In general, the mold distortion follows the bolt and waterbox stiffness more than the thermal strain in the mold.

4.5.3   Bolt and Tie Rod Tensile Stresses

The boxes in Figures 4.12b and 4.14 present the operating tensile stresses of the mold bolts for the narrow and wide faces. For the narrow face, the highest bolt stresses are found near the top and bottom of the mold, where they partially restrain the most severe copper plate distortion, as shown in Figures 2.17 and 4.12. These stresses are well below the yield strength of the bolt material. The bolts aligned with the water box hooks are calculated to operate in compression because the additional stiffness provided by the hooks generates only a small operating load, which is not enough to overcome the prestress.

In the wide face, the bolts with the highest tensile stresses are the short bolts found 425 mm from the centerline at 300 mm and 800 mm below the top of the mold. The maximum tensile stresses are over 800 MPa, and arise in the short bolts nearest to the locations of maximum distortion. Because the loading is strain-controlled and not stress-controlled, these stresses likely cause a small, permanent distortion of the steel bolts which should not present any operational problems. Figures 4.18 and 4.19 show the temperature and distortion profiles down the WF hot face at the centerline, where the distortion is relatively small, and at the middle of the outer curve region, where the distortion is most severe. Near the top and bottom of the mold, where the thermal expansion is resisted by the compliant long bolts, the
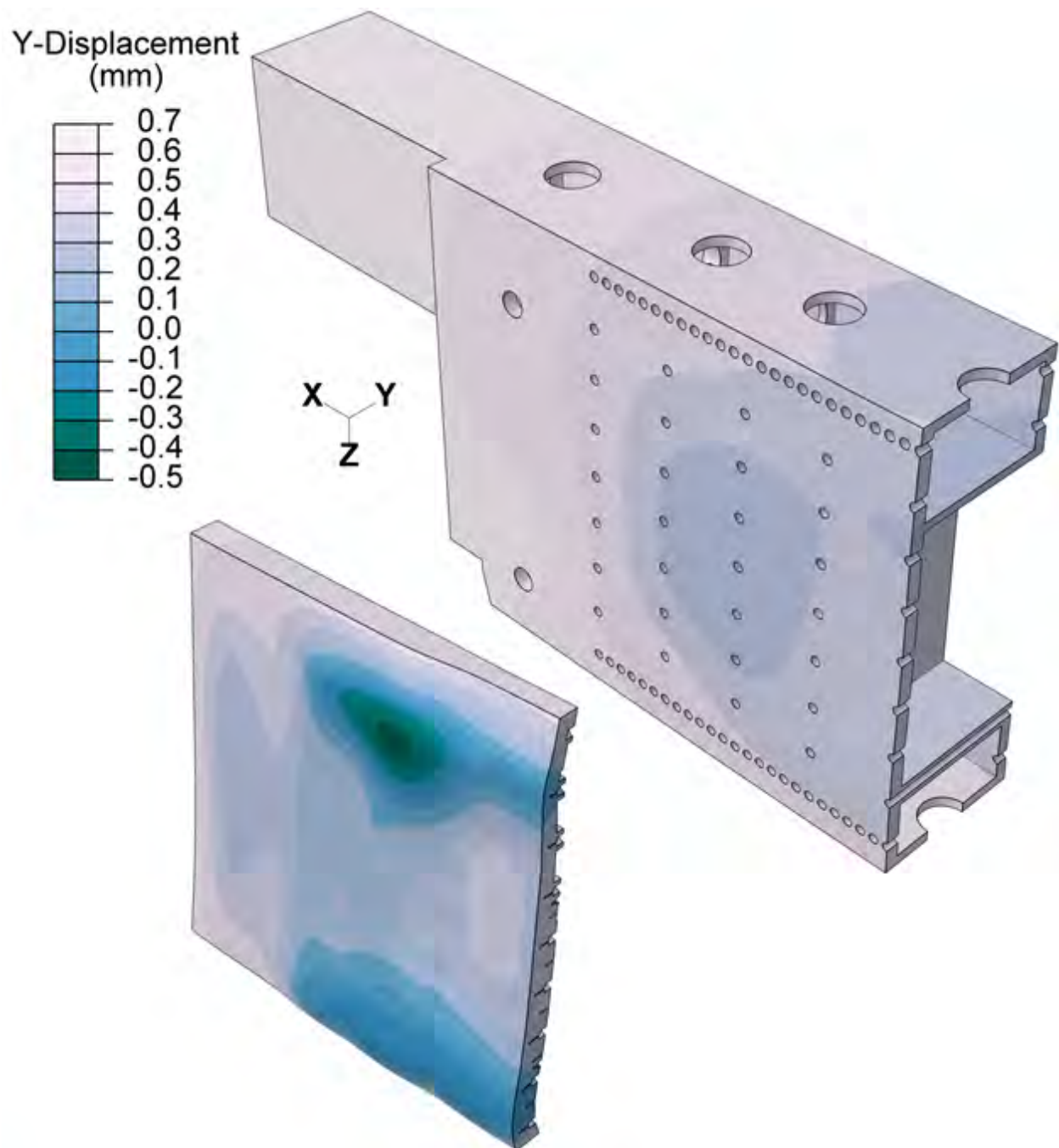
Figure 4.13 Funnel mold WF mold and waterbox distortion (50 times scaled distortion)
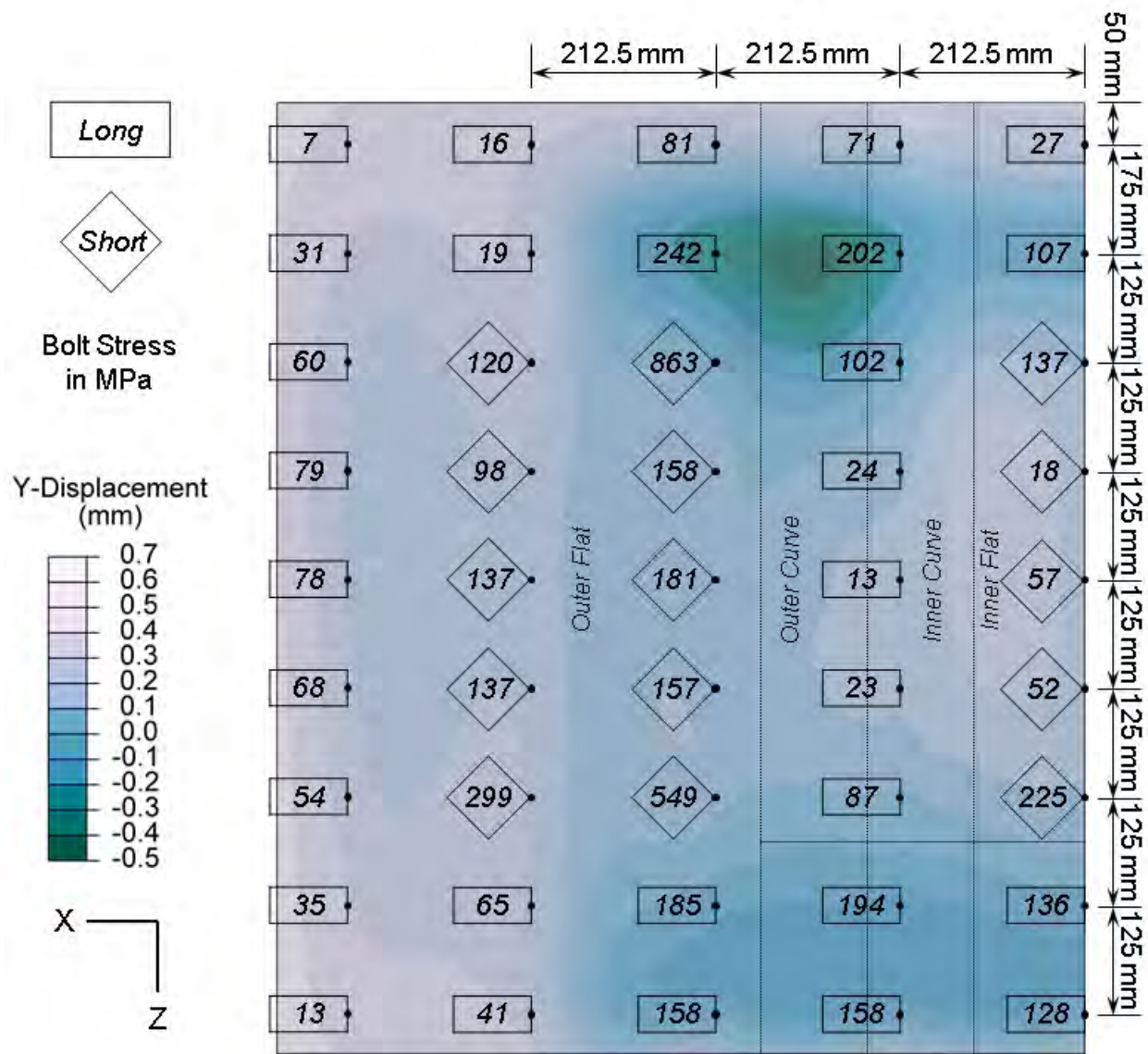
Figure 4.14 Funnel mold WF mold hot-face displacement away from the steel and bolt stresses
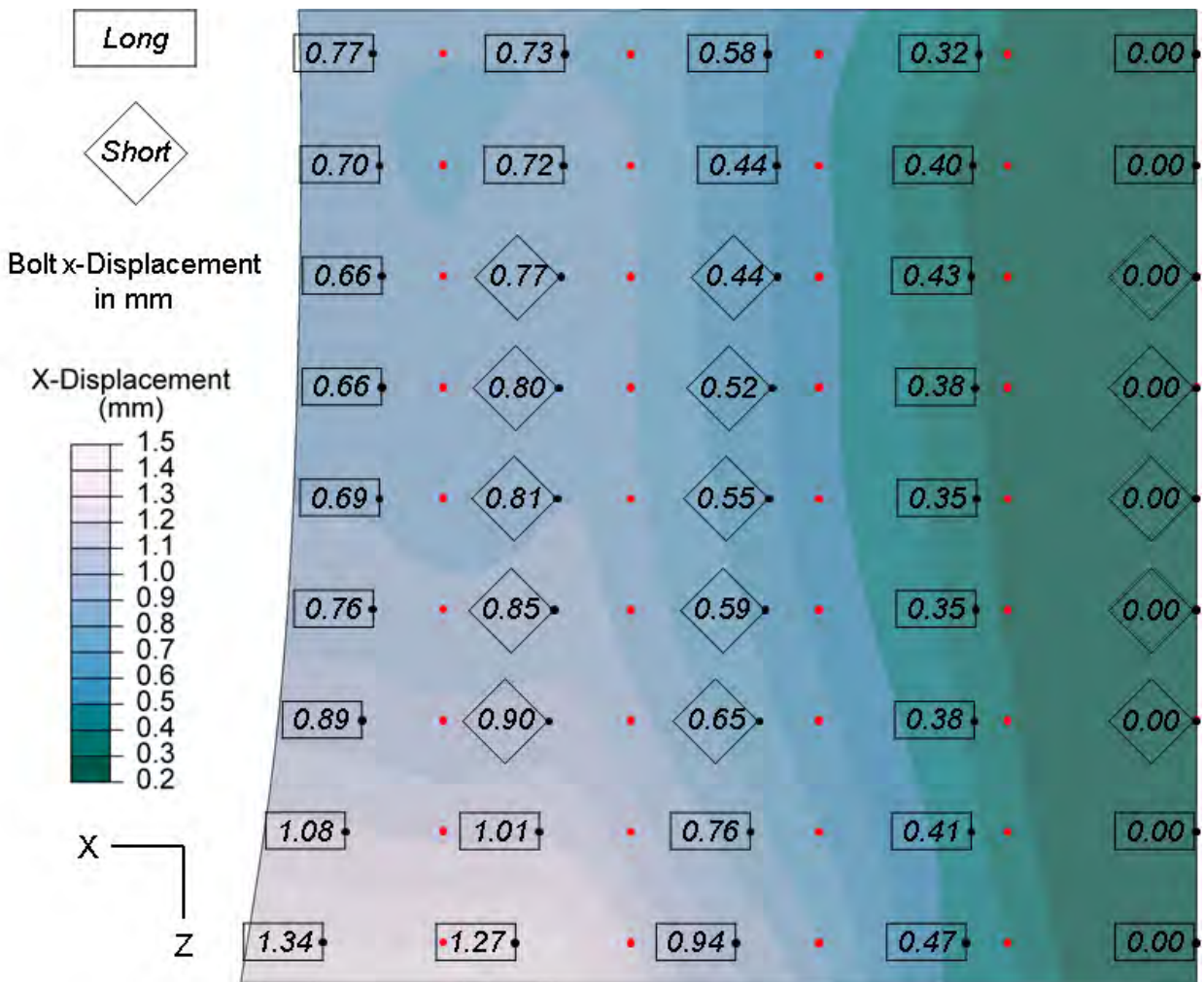
Figure 4.15 Funnel mold WF mold hot-face and bolt displacement towards narrow face (100 times scaled distortion in x-direction)
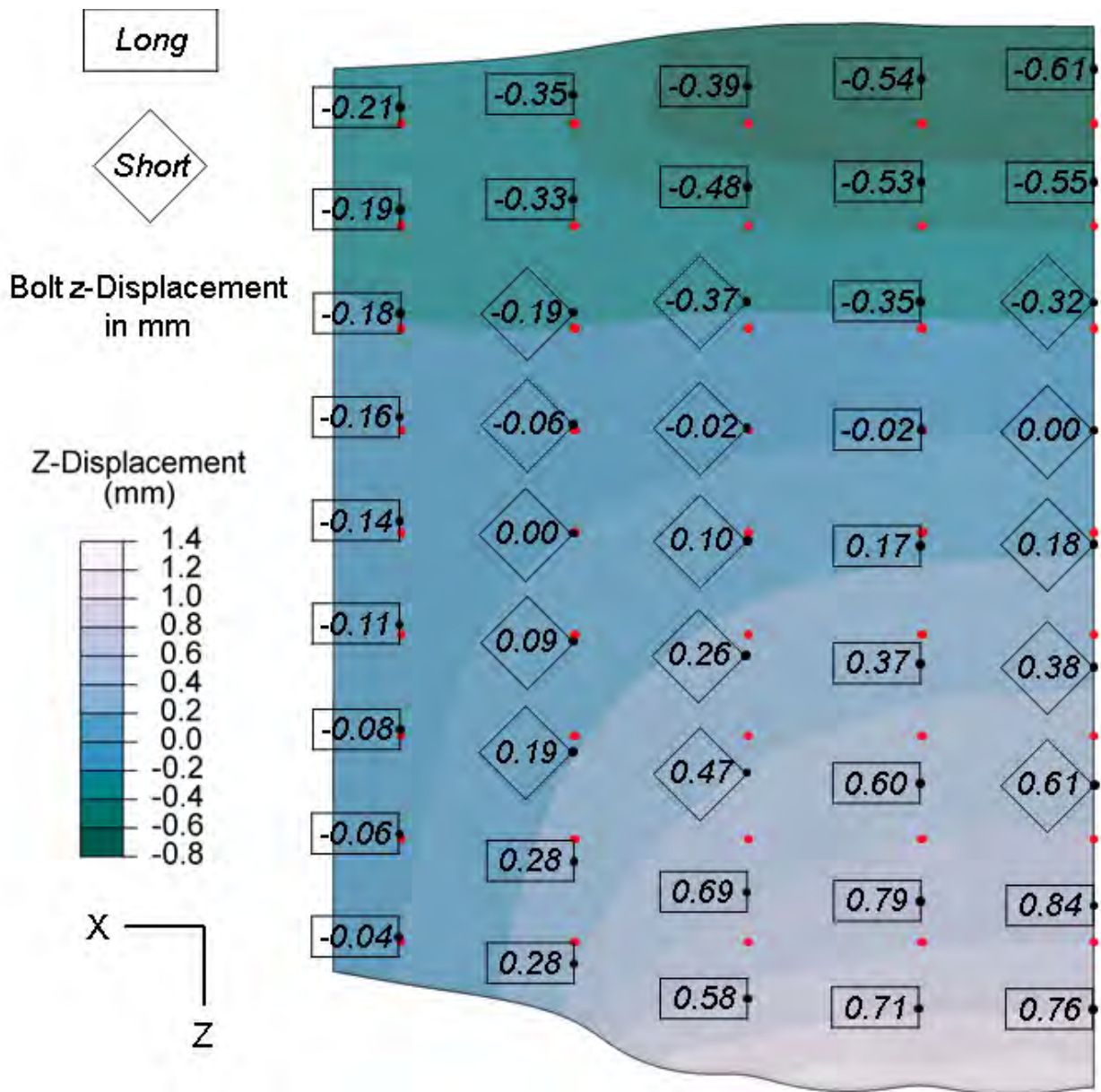
Figure 4.16 Funnel mold WF mold hot-face and bolt displacement towards mold exit (100 times scaled distortion in z-direction)
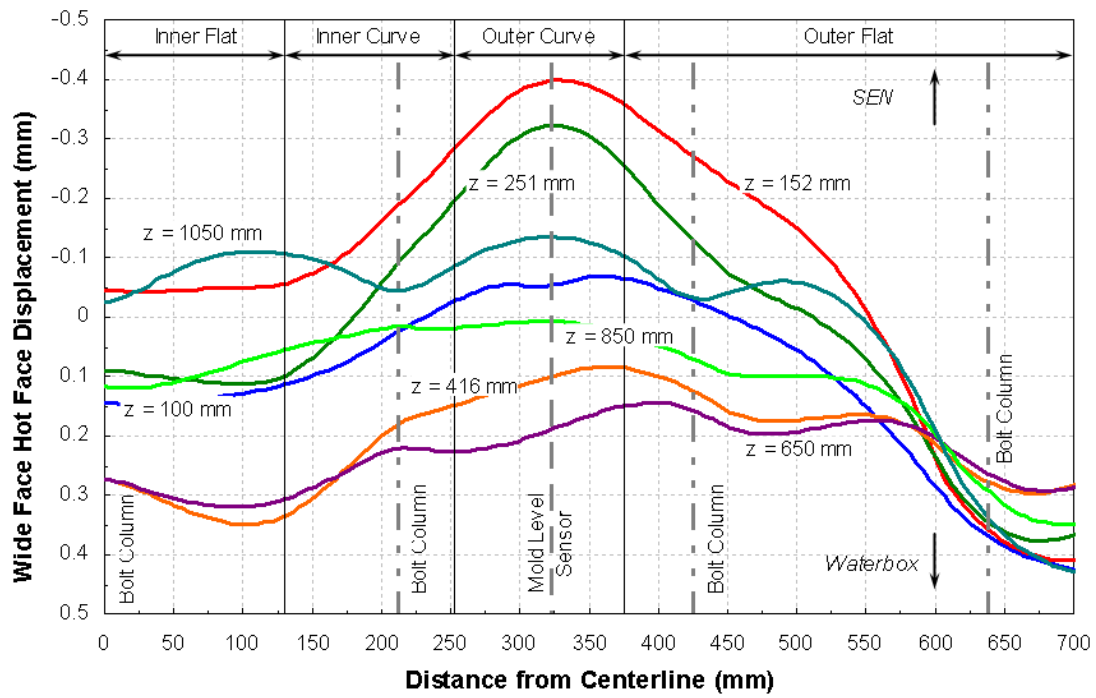
Figure 4.17   Funnel mold WF hot-face distortion profiles around the perimeter
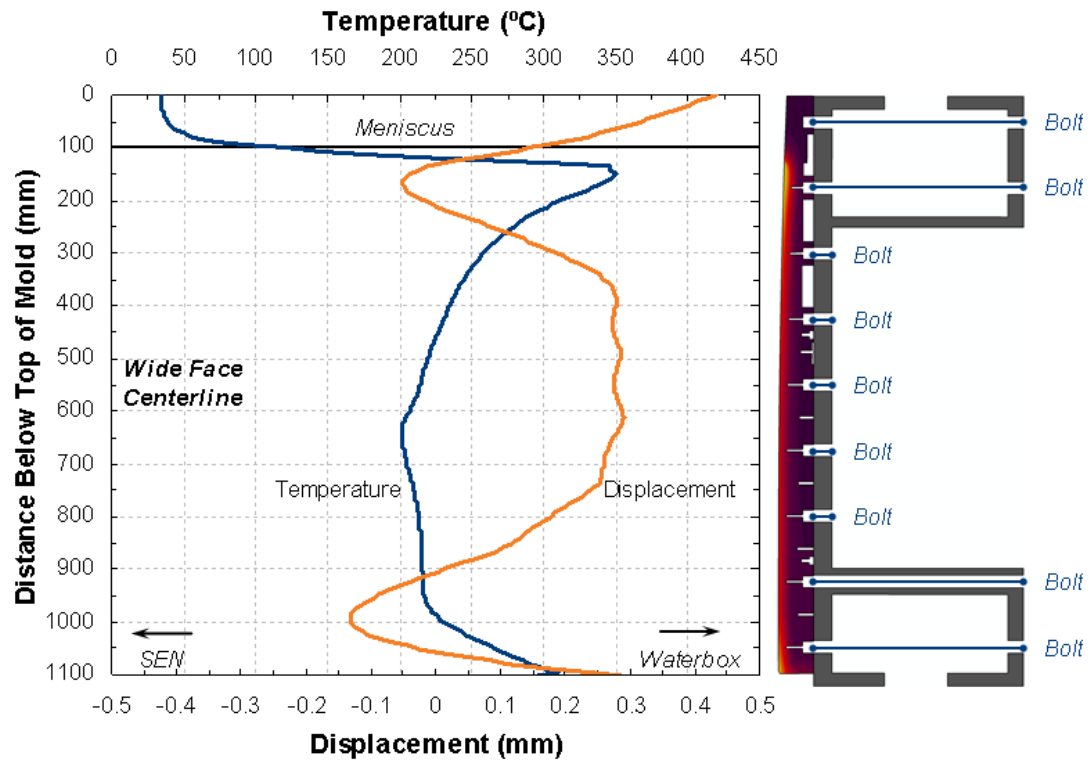
Figure 4.18   Funnel mold WF centerline hot-face temperature and distortion profiles
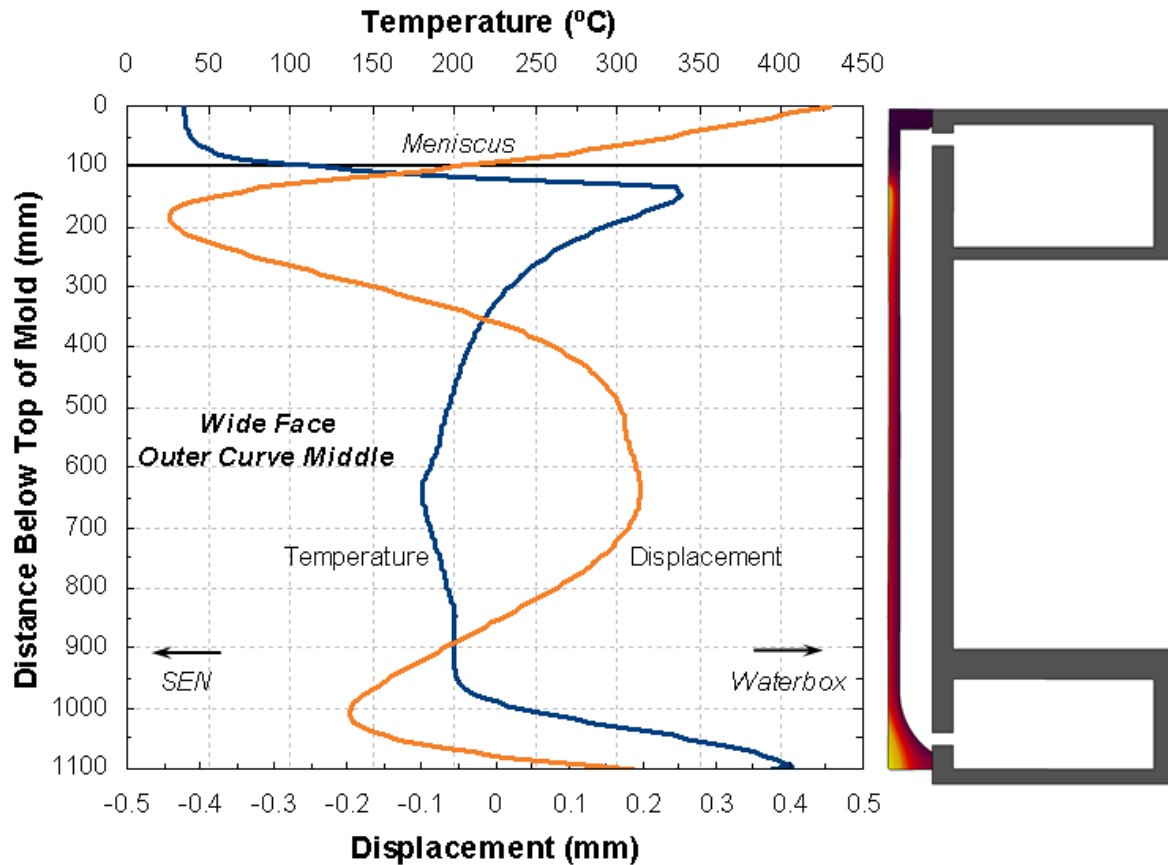
Figure 4.19 Funnel mold WF hot-face temperature and distortion profiles at the outer curve middle

hot face distorts the most and the bolts develop moderate stresses. In the middle region of the mold, the expansion is resisted by the stiff short bolts which develop high stresses, except for the column of long bolts 212.5 mm from the centerline. The variation in bolt stiffness is largely responsible for the short bolts carrying most of the load and the local increase in hot-face distortion around the longer bolts.

The model predicts the tie rod operating tensile stresses to be 151 MPa and 146 MPa for the upper and lower tie rods, which correspond to axial forces of 183 kN and 178 kN. This force exceeds what is applied in commercial practice, but should not otherwise affect the reported model predictions.

4.5.4   Mold Lateral Distortion and Bolt Shearing

If lateral distortion of the copper plates relative to the water boxes is excessive, the resulting shear forces on the bolts may cause excessive mold constraint or even bolt failure. Figure 4.12c

shows the in-plane distortion of the NF hot face, which is mainly in the casting (z-) direction, as the copper plate elongates by about $2\,$mm. There is little risk of shearing failure of the NF bolts because the bolt holes are oversized radially by $3\,$mm ($16\,$mm bolts in $22\,$mm holes) and the maximum in-plane displacements of the bolts at the mold-waterbox interface are less than $0.4\,$mm, as shown in the boxes in Figure 4.12c.

Figures 4.15 and 4.16 show contours of the in-plane distortion of the WF mold, in the directions towards the narrow face (x-) and in the casting direction respectively. The x-direction distortion is greatest at the bottom corner, while the z-direction distortion is greatest at the bottom center. This distorted shape is explained by the constraint against thermal distortion provided by the cold edges along the top and down the side of the mold. This distortion has important implications for taper practice, as discussed in Section 4.5.6. The markers in Figures 4.15 and 4.16 indicate the initial and deformed position of the bolt holes, and the boxes give the calculated bolt displacements at the mold–waterbox interface in the respective directions. The two bolts in the bottom row at $637.5\,$mm and $850\,$mm from the centerline have the highest total in-plane displacements $\sqrt{u_x^2 + u_z^2}$ of $1.30\,$mm and $1.34\,$mm. As the bolt holes on the wide face waterbox are oversized radially by $4\,$mm ($16\,$mm bolts in $24\,$mm holes), there is little risk of shearing failure of any bolts.

4.5.5   Narrow-Face Edge Crushing and Fin Formation

Excessive clamping forces combined with mold distortion is known to cause crushing of the corner of the narrow face [98]. Figure 4.20 shows the model prediction of the normal displacement of the main line of contact between the narrow and wide faces, as well as two horizontal slices through the interface that show the distorted mold shape (no scaling of the distortion) with temperature contours. The meniscus experiences a small $0.2\,$mm gap, which might entrap liquid mold flux that could solidify and cause scratching during width changes. The locations of the highest temperatures, just below the meniscus and near mold exit, are in good contact because of the higher thermal expansion and the clamping forces, while the regions in between experience a thin gap of $0.017\,$mm on average. The hash marks in Figure 4.20 indicate the positions of the rows of bolts, which are not directly responsible for the gap profile.

Combined with excessive clamping forces, the corner of the narrow faces may be crushed at the two locations of high contact pressure. If the NF mold corner heats excessively, softens, and permanently adopts to the crushed shape, then a large wedge-shaped residual gap can form at the location marked with the arrow in Figure 4.20 after the mold cools. During
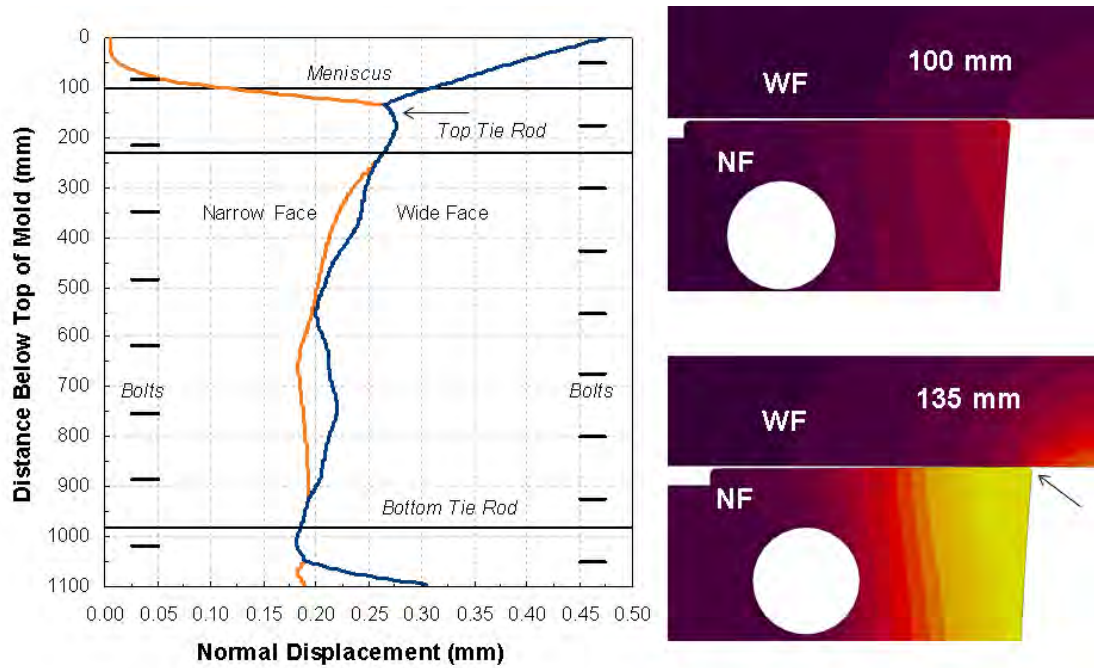
Figure 4.20 Funnel mold interfacial contact profile between mold faces

subsequent startups, this gap may fill with slag or molten steel, causing "fin" problems, and lead to sticker breakouts in extreme cases [98]. These problems were not experienced in this plant, however. The model prediction of the corner heating and contact pressure is likely overpredicted because the contact between the mold pieces allows for some cooling of the narrow face corners, which was ignored by this model.

4.5.6   Implications for Mold Taper Design

Mold distortion need not be a problem, so long as it is understood and properly accounted for when constructing the mold and designing the taper practices. The variation in the casting direction of the mold hot-face shape affects the mold taper experienced by the solidifying steel shell. The narrow face distorts about 1 mm, which is important relative to the typical NF taper of about 4 mm to 7 mm per narrow face. The wide face distorts about ±0.5 mm, which is less consequential to WF taper because ferrostatic pressure can maintain contact of the large area of unsupported shell against the WF mold.

A more important aspect of the wide-face distortion is the change in perimeter length caused by the distortion. This change is quantified by subtracting the distorted perimeter length at the meniscus from the distorted perimeter length at a given distance z down the mold. The change in perimeter length of the WF mold has contributions from the changing

80

funnel geometry, which decreases the perimeter, and the thermal distortion, which increases the perimeter. Because of this compensation provided by the thermal expansion at elevated temperatures, the total perimeter length change is smaller than what calculations at ambient temperature would show. Figure 4.21 shows the effective shape of the mold experienced by the solidifying shell moving in the casting direction (*Total*), as well as its decomposition into four components:

- the perimeter change of the wide face with the funnel geometry effect removed (*Wide Face Distortion*),
- the prevented sliding of the wide face relative to a rigid narrow face (*Interfacial Sliding*),
- the perimeter change due to the funnel geometry (*Nominal Funnel*),
- the perimeter change due to the thermally-distorted narrow face shape taken from Figure 2.17 (*Narrow Face Distortion*).

The total distortion from all four components should be considered when designing the NF taper of most clamped funnel-shaped molds, where narrow face support is insufficient to prevent mechanical backlash and gaps from allowing the narrow face to move along with the wide face expansion. In molds with rigidly-positioned narrow faces, the edge of the narrow face that contacts the wide face may slide, so the *Interfacial Sliding* effect should not be considered. During operation of the mold with slab width changes during operation, the *Interfacial Sliding* effect is determined mainly during startup, due to the heat-up from a cold mold to a hot mold. Online monitoring of the shape of the narrow face mold by inclinometers, as demonstrated in Section 4.6 is recommended to quantify these effects during casting operation, and to ensure that optimal taper is maintained.

Under conditions of ideal taper, the shape of the hot face of the distorted NF mold should match the shrinkage of the solidifying steel in the casting direction. Previous work [30, 32] has investigated the shrinkage of the solidifying shell in the funnel mold described in this work, using a 2D elastic-viscoplastic thermal-stress model. Figure 4.22 shows the shell shrinkage down the narrow face predicted in this previous work both with and without friction (0.16 static friction coefficient between the shell and mold). These two shrinkage predictions are compared in Figure 4.22 with the perimeter changes of both the cold mold and the distorted mold calculated in this work. Both mold lines in Figure 4.22 include a 1 %/m taper, which is 12 mm total for the 1200 mm strand width considered in this work. At room temperature, this taper is a straight line from the origin to 6 mm of shrinkage at 1000 mm below meniscus in Figure 4.22. Ideally, this applied taper should make the mold shape match the shell

shrinkage, and though not entirely ideal, this taper does a fairly good job when all effects are considered.

The deviation from ideal narrow-face taper is explored in Figure 4.23, which shows the difference between the mold lines and shell lines in Figure 4.22. In this figure, negative numbers mean that the shell is shrinking more than the applied narrow face taper can accommodate, so a gap tends to form between the shell and the mold on the narrow face. Positive numbers mean that the shell is pushing against the narrow-face mold wall, which would cause excessive mold wear, and other problems such as off-corner buckling of the shell and longitudinal cracks. Figure 4.23 shows that mold distortion and friction both greatly lessen the ideal narrow face taper needed to match the shell shrinkage.

4.5.7 Mold Wear

The narrow face mold wear as a function of distance down the mold $w(z)$ may be assumed to be composed of at least three phenomenological components: a constant term due to the "steady" wear of two bodies in sliding contact c_0; a linear term proportional to the ferrostatic pressure load $c_1 p_f$; and a third term due to the mismatch from ideal taper $d(z)$. These components are added together to give a crude estimate of the total narrow face wear,

$$w(z) = c_0 + c_1 \rho_{\text{steel}} g z + d(z) \,. \tag{4.22}$$

Other work on mold wear [106] proposes that the wear is proportional to the yield strength of the mold copper and the interfacial pressure, and shows the highest mold wear near the bottom of the mold.

Measurements of narrow face mold wear from the plant, shown in Figure 4.24, are consistent with taking the mismatch function $d(z)$ as the "hot mold with friction" penetration profile presented in Figure 4.23. Good match with the measurements may be observed by taking $c_0 = 0.97\,\text{mm}$ and $c_1 = 5 \times 10^{-6}\,\text{mm/Pa}$ as fitting constants. Minimum wear is observed between $200\,\text{mm}$ and $500\,\text{mm}$ below the meniscus. The higher wear towards the top and bottom of the mold agrees with the modeling prediction of two regions of locally excessive taper and corresponding high NF mold wear. The very high wear at mold exit likely is related to the combined effects of the infiltration of corrosive spray-cooling water, increased scraping by the strand at mold exit, and the softening caused by the locally high mold temperatures discussed in Section 2.4. This problem can be treated in many ways: changing the bolt pattern, changing bolt tightness or grease, stiffening the waterbox, or changing the NF taper. Further modeling work is needed to improve the mold taper for the
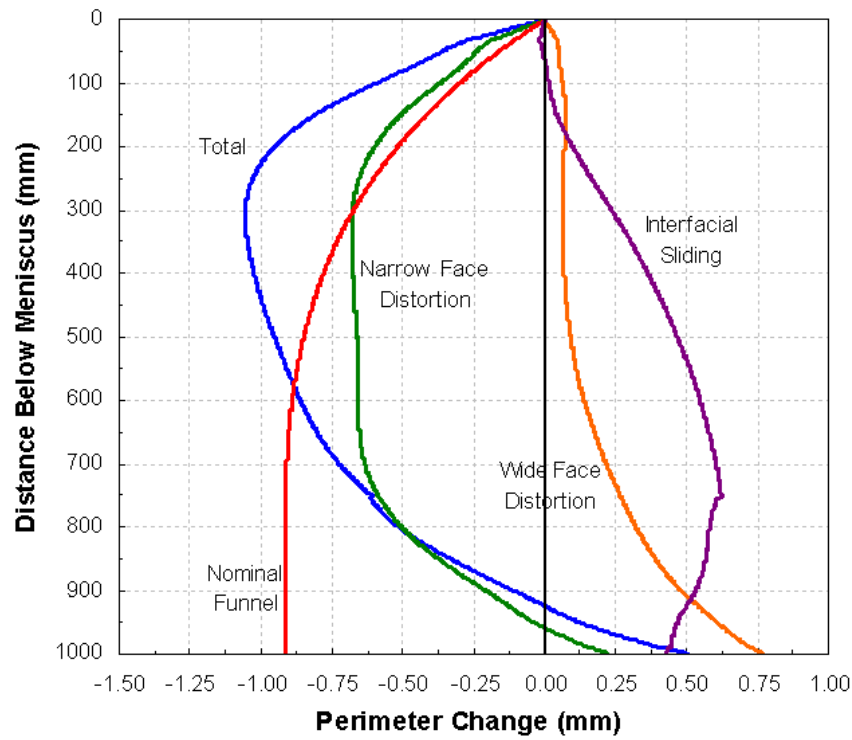
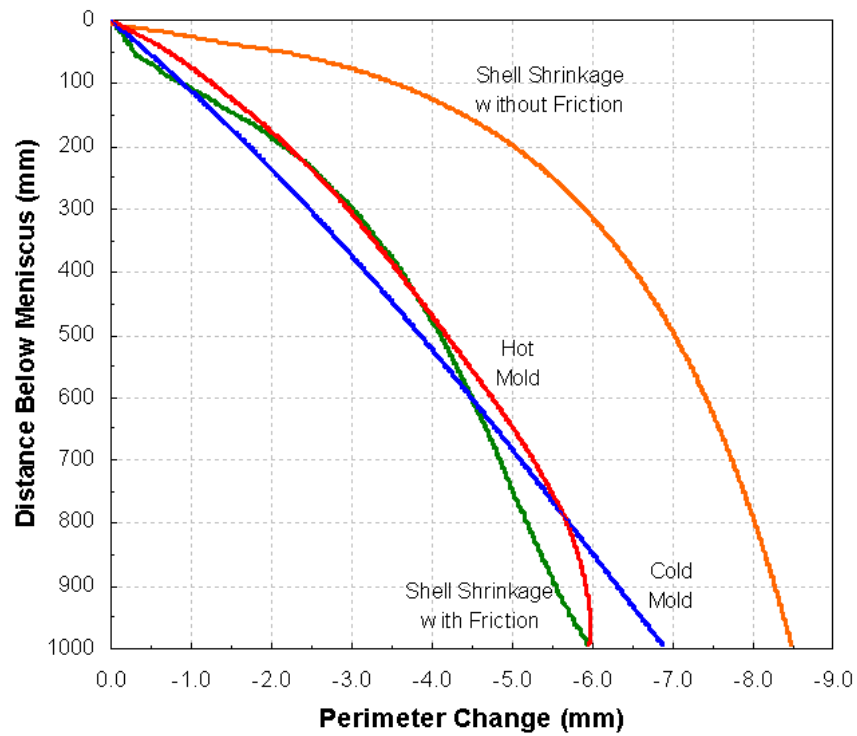**Figure 4.21** Funnel mold perimeter change due to distortion and funnel geometry

Figure 4.22 Steel shell shrinkage in a funnel mold with friction and mold distortion

83

range of operating conditions found in commercial practice.

4.6   Online Measurement of Mold Distortion and Taper

The instantaneous NF tapers were measured in real time during casting with inclinometers. Each NF waterbox was instrumented with two inclinometers, one centered at 94 mm below the top of the mold plate, and the other centered at 31 mm above the bottom of the mold plate, as shown in Figure 4.25. The inclinometers give a nominal ± 5 V signal for $\pm 3°$ angle from vertical, which is scaled to a ± 10 V signal for $\pm 6°$ angle based on the calibration certificates. The signal from the inclinometers is filtered with a first-order low-pass filter to remove the noise created by the mold oscillation.

The simulations of the mold presented in this section are compared with the inclinometer measurements. The distorted NF shape is a combination of the distortion of the mold itself, governed by its waterbox, and of the frictional contact with the wide face. The mold is assembled and clamped together while at room temperature, and as the mold heats and expands during startup, the friction between the mold faces resists some of the tendency for the NF mold to deform. The orange "Sticking NF" curve in Figure 4.26 shows the shape of the mold about 2 min after the start of mold filling, at a $v_{\text{cast}} = 3.5$ m/min steady state. This curve is calculated as the nominal taper plus *Narrow Face Distortion* plus *Interfacial Sliding* from Section 4.5.6. The model predictions of mold orientation match the inclinometer measurements to within $2'$ at the top and to within $1'$ at the bottom of the mold.

When the clamping forces are released for a strand-width change during casting, the frictional forces disappear, and the NF mold takes on a different shape, shown by the blue "Sliding NF" curves in Figures 4.26 and 4.27. This curve is calculated as the nominal taper plus *Narrow Face Distortion* from Section 4.5.6. The model predictions of mold orientation match the inclinometer measurements to less than $1'$ for both the top and bottom of the mold. The simulations show that the slope of the distorted NF mold in the middle of the mold is in good agreement with the applied taper. The taper near the top and bottom of the mold is substantially different than this nominal value, due to the important effect of mold thermal distortion.

4.7   Conclusions

This chapter provides insight into the mechanical behavior of steel continuous-casting molds during steady casting, based on a nonlinear 3D finite-element elastic stress analysis. The
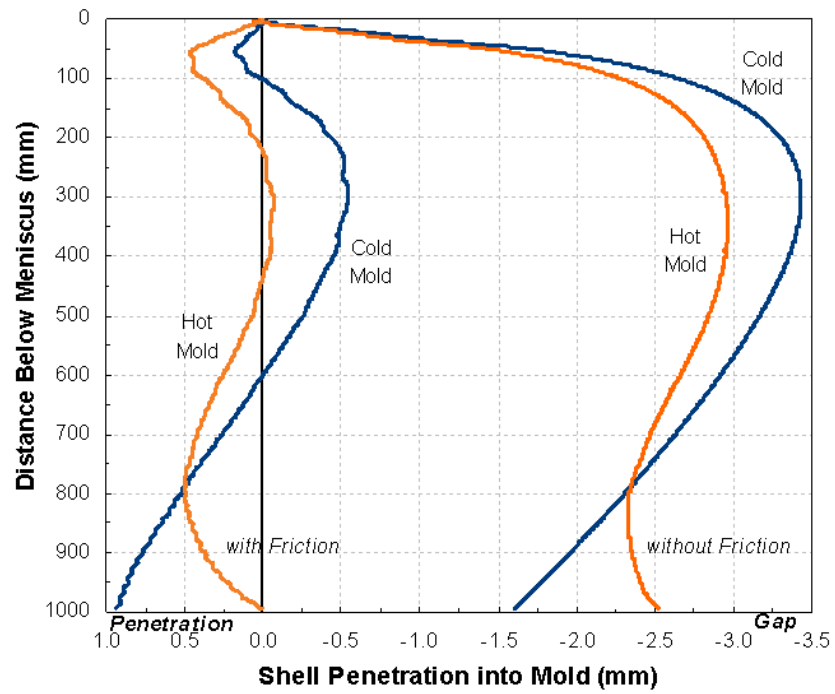
Figure 4.23 Strand-mold gap in a funnel mold with friction and mold distortion
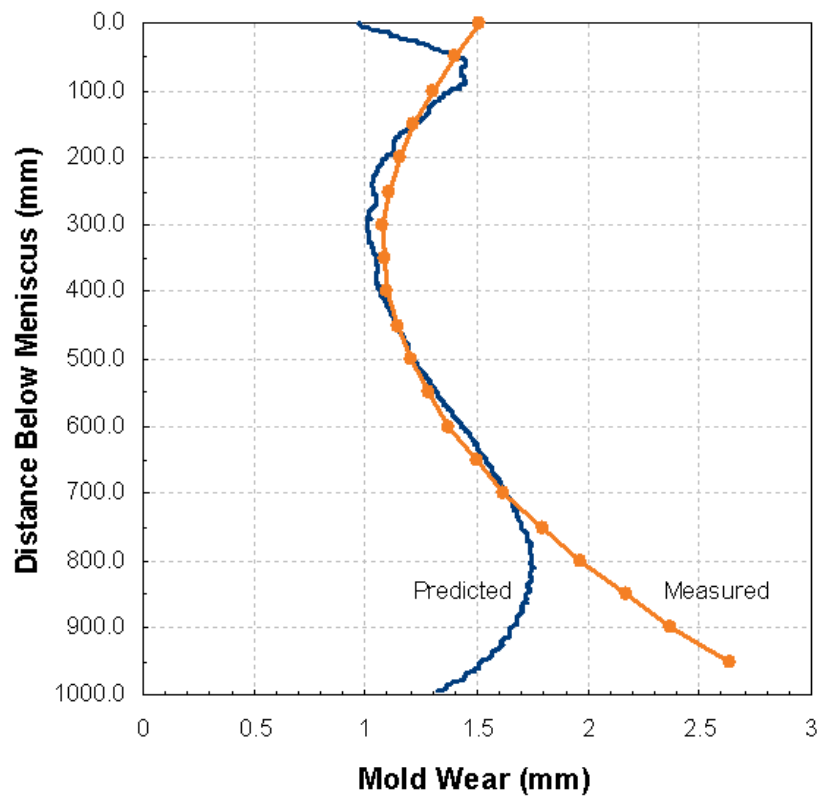
Figure 4.24 Funnel mold NF wear predictions and measurements

85
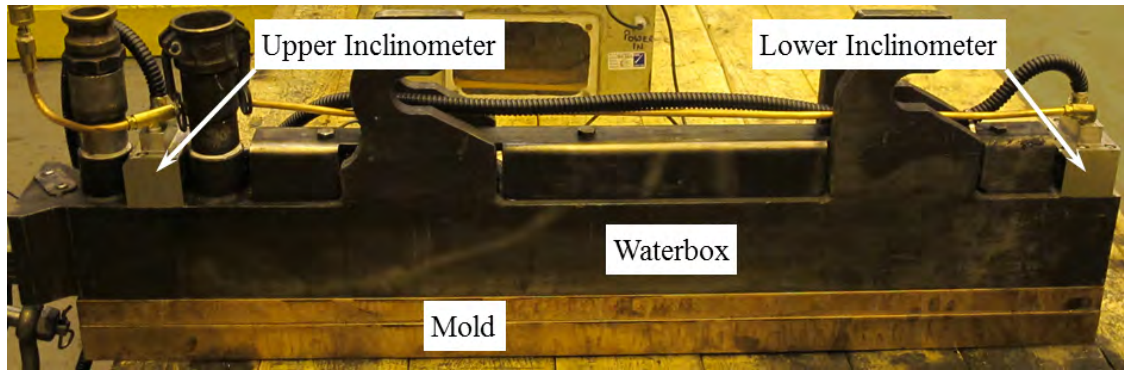
Figure 4.25 Funnel mold NF instrumented with inclinometers

model features realistic thermal boundary conditions based on plant measurements, complete geometric details of the mold plates and waterboxes, tightened bolts and tie-rods, and realistic contact with friction and ferrostatic pressure.

For beam-blank molds, the regions of of the hot face furthest from the water channel become very hot, especially at the meniscus. These hot spots are found at the "shoulder," and are alleviated with smaller and/or more water channels in the region. The mold generally bows outward, away from the steel, with a slight twisting motion. This distorted shape, calculated in 3D, has been translated into a moving-slice 2D Lagrangian database for use with the multiphysics model presented in Chapter 5.

Owing to the changes in water cooling around the mold bolts and near mold exit on the wide face, combined with widely varying bolt stiffnesses, the wide face contorts into a W shape in both the perimeter- and casting-directions. The predicted shape of the narrow face was validated with inclinometers measurements; measuring taper with inclinometers is a powerful tool for mold operation.

For both beam-blank molds and funnel molds, the narrow face distorts into a parabolic arc a few millimeters deep. These behaviors are predictable and must be accommodated when designing taper practices. The distortion of the narrow face in a funnel mold was validated with inclinometer measurements from a plant trial, and match to within a few arc-minutes.

The results of the funnel-mold distortion simulation were evaluated from an operational perspective, considering the potential for several different practical problems:

1. Mold distortion has a significant effect on mold taper. The thermal distortion of each of the mold pieces, the effect of the changing funnel geometry, and the interfacial sliding of the wide and narrow faces all contribute to the effective taper seen by the solidifying shell, each in a nonlinear fashion with distance down the mold. The thermal
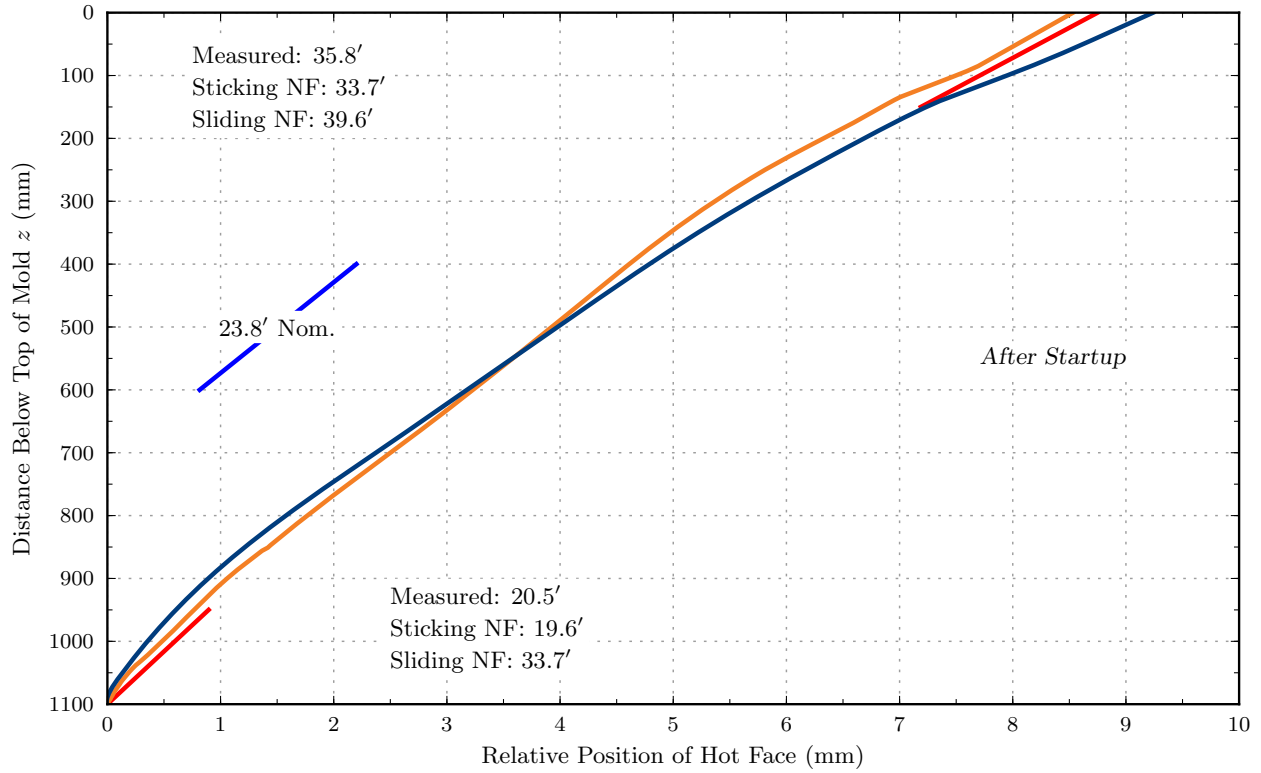
Figure 4.26   Funnel mold NF shape and inclinometer measurements after startup
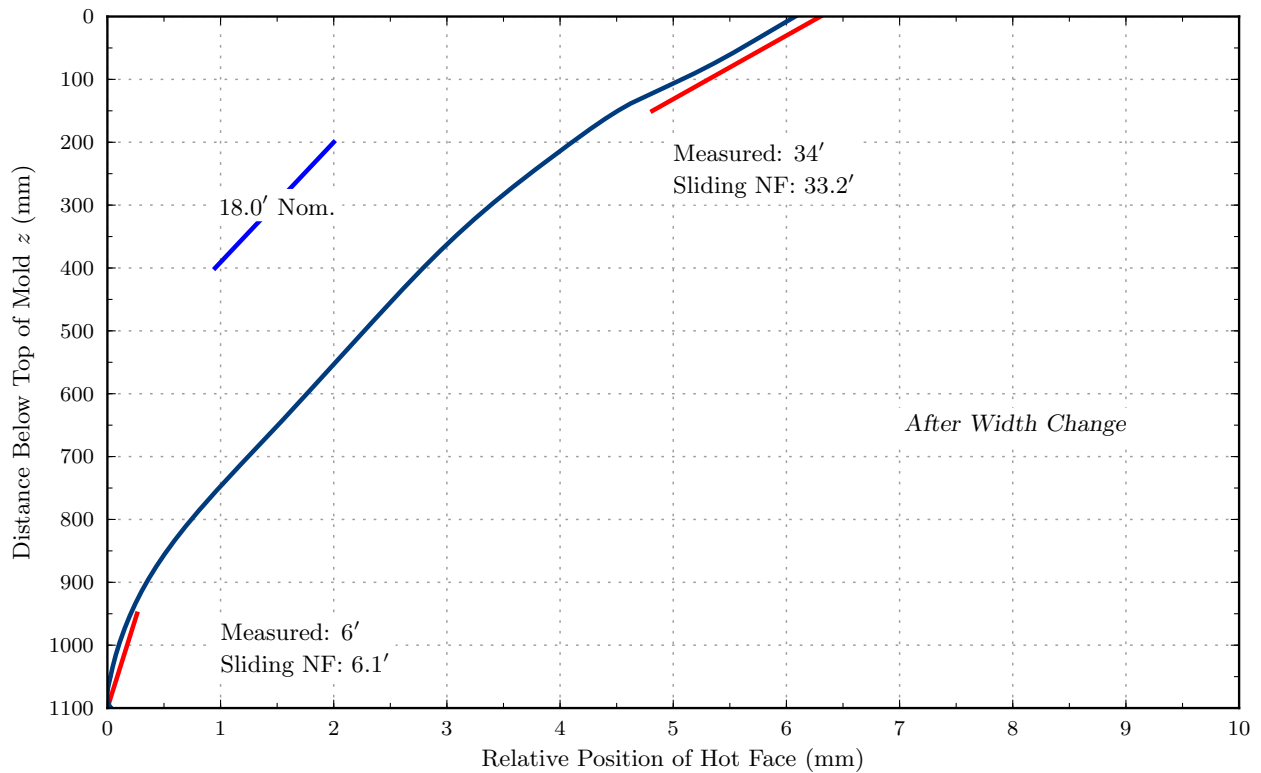
Figure 4.27   Funnel mold NF shape and inclinometer measurements after width change

expansion of the wide face works against the applied taper and the effect of the funnel, so calculations based only on room-temperature dimensions are insufficient.

2. To avoid shell buckling and cracks, the thermal distortion of the mold should be considered when designing taper practices.

3. The mold pieces are in strong contact just below meniscus and just above mold exit, where temperatures are highest. The meniscus region could experience scratching due to slag infiltration into a thin, 0.2 mm, interfacial gap. The submeniscus region could experience the "crushing" phenomenon observed in previous work unless care is taken to avoid excessive clamping forces.

4. Mold wear was estimated by superimposing the total effect of the thermal distortion of the mold and a linear 1 %/m taper on previous calculations of the shell behavior. Although this taper generally produces acceptable matching with the shell shrinkage, the shell is predicted to wear against the mold just below the meniscus and near mold exit. Plant measurements of mold wear are consistent with this prediction.

5. The mold bolts have no risk of either tensile failure or shearing failure at the mold-waterbox interfaces, owing to the bolt holes being sufficiently oversized.

CHAPTER 5
Multiphysics Model of Continuous Casting[1]

5.1   Introduction

This chapter presents a multi-physics, multi-field, multi-domain model of the continuous casting process that accounts for turbulent fluid flow, heat transfer, solidification, and mechanical distortion. The multiphysics model is demonstrated for continuous casting in the beam-blank mold presented in earlier chapters.

As the demand for better computer simulations of solidification processes increases, there is a growing need to include the effects of fluid flow into thermo-mechanical analyses. The multiphysics approach of simulating all three macroscale phenomena (i.e. fluid flow, solidification heat transfer, and mechanical distortion) simultaneously has been demonstrated in several previous works [5, 38, 51], but is very computationally demanding for realistic problems. Major difficulties stem from the inherently different coordinate descriptions and numerical techniques used in the separate models for these three fields. Fluid flow typically is performed on structured Eulerian domains using steady-state control-volume methods with iterative solution algorithms. Stress analysis typically is performed on unstructured Lagrangian domains using transient finite-element methods with direct solvers. Many different methods are used to treat heat transfer with moving solidification front(s) [101]. Further difficulties arise from the complex geometries, which require large computational meshes.

The steel continuous casting process has been analyzed with two 2D multiphysics models [38, 51] that include fluid flow, deformation of the shell and mold, and a coupled shell-mold interfacial gap. The melting of gallium was explored with these same phenomena [94]. Some researchers have decoupled the thermal-flow analysis from the deformation analysis [17, 23, 61, 66, 75, 87], but doing so neglects the important effects of the deformation, namely the behavior of the interface between the casting and the mold [92].

Alternatively, the fluid flow simulation can be decoupled from the deformation analysis

---

[1]Much of the work presented in this chapter has been published by the author [35, 39, 96] and colleagues. Beyond the content of these articles, this chapter contains an updated literature review and some details that were not included in the original publications. The modeling effort presented in this chapter is a collaborative effort between the author, S. Koric, who was responsible for the solidifying strand simulations with his new "enhanced latent heat" technique [41], and R. Liu, who was responsible for the fluid-flow simulations. The author was responsible for the mold simulations, and interfacing between the three models.

of the shell if the shape of the liquid pool can be estimated *a priori*, such as in continuous casting of steel and aluminium, or cryolite electrolysis. Simulations of such processes can readily output the "superheat flux" that delivers heat to the liquid side of the solidification front. A recent simulation [41] demonstrated that this superheat flux can be incorporated into a transient simulation of heat transfer in the solid and mushy region by enhancing the latent heat in the mush, without explicitly tracking the solidification front.

5.2   Solidifying Shell Model

The earliest work that analyzed the deformation of solidifying bodies considered a semi-infinite plate, using various semi-analytical techniques [76, 99, 103]. However, the complexity of solidification-deformation problems generally is too difficult for closed-form analytical solutions, and computational methods, typically the finite-element method, quickly became the usual method of analysis [7, 26, 44, 104]. Cylindrical geometries were able to be analyzed with numerical approaches [7, 115]. The solidifying metal has been treated as everything from elastic [99, 104] to elastic–perfect-plastic [7, 103] to elastic-viscoplastic [40, 44, 45, 52, 76, 114, 115, 118]. The literature has a few examples of other approaches for solidification-deformation problems that seem to have fallen out of use, such as the boundary-element method [29] and internal-variable inelasticity [15]. Solidifying bodies usually are modeled with a Lagrangian description of motion, but the Arbitrary Eulerian–Lagrangian (ALE) technique has been implemented as well [79].

The solidifying steel shell is modeled as a transverse Lagrangian slice that moves down through the mold at the casting speed. Many continuum mechanics texts [4, 16] may serve as general references for this finite-deformation model. The strains mostly are small during solidification deformation problems, but the capability to handle arbitrary rotations is necessary to model some parts of the shell in a continuous casting mold. The mechanical behavior of the strand is governed by the quasi-static conservation of momentum,

$$\mathbf{0} = \nabla \cdot \boldsymbol{\sigma} + \boldsymbol{b}, \tag{5.1}$$

where $\boldsymbol{\sigma}$ is the CAUCHY stress tensor and $\boldsymbol{b}$ is the body force density vector, which is neglected in this work. Following the multiplicative decomposition of the deformation gradient [46, 49], the total rate-of-deformation tensor $\boldsymbol{D}$ additively decomposes into an inelastic, thermodynamically-irreversible part $\boldsymbol{D}^{\text{ie}}$ and a thermoelastic, thermodynamically-reversible $\boldsymbol{D}^{\text{te}}$ part as

$$\boldsymbol{D} = \boldsymbol{D}^{\text{te}} + \boldsymbol{D}^{\text{ie}}. \tag{5.2}$$

90

Linearized thermo-hypoelasticity provides part of the constitutive relationship between the stress and the thermoelastic rate of deformation as

$$\boldsymbol{D}^{\text{te}} = \boldsymbol{\alpha}\dot{T} + \mathbb{C}^{-1} : \overset{\triangle}{\boldsymbol{\sigma}} \tag{5.3}$$

where $\boldsymbol{\alpha}$ is the thermal expansion tensor, $\mathbb{C}$ is the fourth-rank elastic stiffness tensor, and

$$\overset{\triangle}{\boldsymbol{\sigma}} = \dot{\boldsymbol{\sigma}} + \boldsymbol{\sigma}\boldsymbol{W} - \boldsymbol{W}\boldsymbol{\sigma} \tag{5.4}$$

is the JAUMANN stress rate, where $\boldsymbol{W}$ is the spin tensor, *i.e.*, the anti-symmetric part of the velocity gradient. The inelastic rate-of-deformation tensor requires an additional constitutive relationship $\boldsymbol{D}^{\text{ie}} = \boldsymbol{D}^{\text{ie}}(\boldsymbol{\sigma}, T, \ldots)$.

For the macroscale simulation presented in this chapter, the solidifying steel is assumed to be an isotropic polycrystalline material, so the elastic stiffness tensor is defined by HOOKE's law, Equation (4.5), and the thermal expansion tensor is $\boldsymbol{\alpha} = \alpha^{\text{E}}\boldsymbol{I}$, where

$$3\alpha^{\text{E}} = -\frac{1}{\rho}\frac{\partial\rho}{\partial T} \tag{5.5}$$

is the isotropic "differential" coefficient of thermal expansion calculated from the change of mass density ρ with temperature T. Inelastic effects are described with a BODNER [8, 9]-type "unified" function, assumed to follow "J_2 plasticity" with isotropic hardening. The inelastic rate-of-deformation tensor then is described by the PRANDTL–REUSS equations,

$$\boldsymbol{D}^{\text{ie}} = \dot{\bar{\varepsilon}}^{\text{ie}}\frac{3}{2}\frac{\boldsymbol{\sigma}'}{\bar{\sigma}}, \tag{5.6}$$

where $\bar{\sigma} = \sqrt{\frac{3}{2}\boldsymbol{\sigma}' : \boldsymbol{\sigma}'}$ is the VON MISES effective stress and

$$\boldsymbol{\sigma}' = \boldsymbol{\sigma} - p\boldsymbol{I} \tag{5.7}$$

is the deviatoric part of the CAUCHY stress tensor, where $p = \frac{1}{3}\operatorname{tr}(\boldsymbol{\sigma})$ is the pressure.

The effective inelastic strain rate $\dot{\bar{\varepsilon}}^{\text{ie}}$, a scalar, is calculated as

$$\dot{\bar{\varepsilon}}^{\text{ie}} = f_{\gamma\text{C}}\left(\bar{\sigma} - f_1\bar{\varepsilon}^{\text{ie}}\left|\bar{\varepsilon}^{\text{ie}}\right|^{f_2-1}\right)^{f_3}\exp\left(-\frac{Q}{T}\right), \tag{5.8}$$

where

$$Q = 44\,465 \tag{5.9}$$

$$f_1 = 130.5 - 5.128 \times 10^{-3}T \tag{5.10}$$

$$f_2 = -0.6289 + 1.114 \times 10^{-3}T \tag{5.11}$$

$$f_3 = 8.132 - 1.54 \times 10^{-3}T \tag{5.12}$$

$$f_{\gamma\text{C}} = 46\,550 + 71\,400C_{\text{C}} + 12\,000C_{\text{C}}^2, \tag{5.13}$$

with T and Q in K, and carbon composition C_C in wt. %, for austenite. Equation (5.8) was fit [43] to high-temperature tensile [107] and creep [93] test data. In the temperature range of austenite, f_3 evaluates to between 6.5 and 5.5, which indicates climb-assisted glide as the underlying mechanism of inelastic behavior [36]. The activation energy $Q = 370\,\mathrm{kJ/mol}$ is larger than the self-diffusion activation energy of iron $(284\,\mathrm{kJ/mol})$, which likely is a consequence of the fitting. The form of Equation (5.8) allows an algorithmic approximation [52] of kinematic hardening, where the effective stress $\bar{\sigma}$ and inelastic strain rate $\dot{\bar{\varepsilon}}^\mathrm{ie}$ are signed according to the largest direct stress component; this approach demonstrates reasonable agreement [52] with the limit cycle of some cyclic test data [93] at $1300\,°\mathrm{C}$. For δ-ferrite, the effective inelastic strain rate is calculated [118] as

$$\dot{\bar{\varepsilon}}^\mathrm{ie} = 0.1 \left| \frac{\bar{\sigma}}{f_{\delta\mathrm{C}} \left(\frac{T}{300}\right)^{-5.52} (1 + 1000\bar{\varepsilon}^\mathrm{ie})^m} \right|^n, \tag{5.14}$$

where

$$m = 0.3495 - 0.941\,56 \times 10^{-6}T \tag{5.15}$$

$$1/n = -0.061\,66 + 0.1617 \times 10^{-3}T \tag{5.16}$$

$$f_{\delta\mathrm{C}} = 13.678 \times 10^3 C_\mathrm{C}^{-0.556 \times 10^{-3}}. \tag{5.17}$$

This form of a constitutive law is not a standard fit, so the underlying mechanism cannot be exposed by the value of the stress exponent. However, Equation (5.14) does give stresses in the δ-ferrite about an order of magnitude smaller than the austenite. The biggest challenge to good constitutive models here is the lack of experimental data at elevated temperatures. In both Equations (5.8) and (5.14), the VON MISES effective stress $\bar{\sigma}$ is expected in MPa and the effective inelastic strain rate $\dot{\bar{\varepsilon}}^\mathrm{ie}$ is in $1/\mathrm{s}$. The δ-ferrite function, Equation (5.14), is used when the δ-ferrite volume fraction is greater than 10%. The effective inelastic strain is the integral of the effective inelastic strain rate, *i.e.*,

$$\bar{\varepsilon}^\mathrm{ie} = \int_0^t \dot{\bar{\varepsilon}}^\mathrm{ie} \, \mathrm{d}\tau, \tag{5.18}$$

which is used as the inelastic state variable in this work. If a material point is above a coherency temperature, then $\bar{\varepsilon}^\mathrm{ie} = 0$.

In the mechanical model of the solidifying shell, the liquid and mush are modeled as isotropic perfect-plastic solids with a low yield strength, *i.e.*,

$$\dot{\bar{\varepsilon}}^\mathrm{fl} = \frac{\bar{\sigma} - \sigma_\mathrm{Y}}{3\mu\Delta t}, \tag{5.19}$$

where $\sigma_Y = 0.01\,\text{MPa}$ is the strength of the "liquid" and μ is the shear modulus of the liquid; $\mu \Delta t$ acts like a dynamic shear viscosity of the liquid. The inelastic strain in the liquid $\dot{\bar{\varepsilon}}^{\text{fl}}$ is called "fluid strain," and does not affect the behavior of the solid, $i.e,\ \bar{\varepsilon}^{\text{fl}} \neq \bar{\varepsilon}^{\text{ie}}$, though it serves the same purpose as inelastic strain in the liquid. The strength is chosen small enough to effectively eliminate stresses in the liquid-mushy zones, but large enough to avoid computational difficulties.

The thermal behavior of the solidifying shell is governed by the conservation of energy, written for a spatial description of motion as

$$\rho \left(\frac{\partial h}{\partial t} + (\boldsymbol{v}_{\text{material}} - \boldsymbol{v}_{\text{mesh}}) \cdot \nabla h \right) = \nabla \cdot (\boldsymbol{K} \cdot \nabla T), \qquad (5.20)$$

assuming no sources and negligible viscous dissipation, where h is the temperature-dependent specific enthalpy including the latent heat of solidification, T is temperature, and $\boldsymbol{K}$ is the temperature-dependent thermal conductivity tensor. In the Lagrangian description of motion used to model the shell behavior, the computational mesh moves at the same velocity as the material, $i.e.,\ \boldsymbol{v}_{\text{mesh}} = \boldsymbol{v}_{\text{material}}$. Consistent with the above assumption of isotropy, the thermal conductivity tensor reduces to $\boldsymbol{K} = k\boldsymbol{I}$. The boundary conditions on Equation (5.20) are insulated, $i.e., -k\nabla T = 0$, because of symmetry or because the liquid-only region of the domain, discussed later, is assumed to be well-mixed, or a prescribed heat flux in the form of a convection condition, $i.e., -k\nabla T = h\,(T - T_0)$, where h is the heat-transfer coefficient and T_0 is the sink temperature.

The governing equations are solved incrementally using the finite-element method in ABAQUS [1], using an implicit stepwise-coupled algorithm [25] for the time integration of the governing equations. The constitutive laws are integrated by solving a system of ordinary differential equations at each material point using the backward-EULER method with bounded NEWTON steps [42] in the user subroutine UMAT. Each time step occurs as two sub-steps: the thermal field is integrated at fixed configuration, and then the mechanical field is integrated at adiabatic conditions, driven by the increment of thermal strain. Global NEWTON iterations continue until tolerances for both the thermal and mechanical equation systems are satisfied before proceeding to the next time step.

Temperature and phase-dependent enthalpy [28], thermal conductivity [28], thermal expansion [28], and elastic modulus [60] were calculated for 0.071 % wt. C plain carbon steel with solidus and liquidus temperatures of $T_{\text{sol}} = 1471.9\,^\circ\text{C}$ and $T_{\text{liq}} = 1518.7\,^\circ\text{C}$. The volume fractions of the liquid, delta, and austenite phases, shown in Figure 5.1, are calculated according to a linearized phase diagram [105]. Other simulation conditions are listed in Table 4.4.

The Lagrangian shell-model domain given in Figure 5.2, was discretized with $32\,874$ nodes and $63\,466$ degrees of freedom, and required $12\,409$ time steps for the complete $45\,$s simulation down the mold length. The domain is a thin "stripe" of the strand section adjacent to the mold wall that is thick enough to allow twice the expected shell thickness at mold exit to solidify, while avoiding calculation of the liquid behavior away from the mold wall. More importantly, the enclosed space which represents the internal liquid cavity is able to shrink to properly model liquid feeding of the real continuous casting process.

This 2D transient model also comprises a 3D solution at steady state. The slice begins at the top of the liquid steel pool, where the uniform initial conditions are the pouring temperature, T_{init}, zero displacement, zero strain, and zero stress. The 2D assumption is valid for the thermal analysis, owing to negligible axial conduction because of the large PÉCLET number $\text{Pe} = v_{\text{cast}}\ell_{\text{mold}}/\alpha$, where v_{cast} is the casting speed, ℓ_{mold} is the mold length, and α is the thermal thermal diffusivity [21]. The appropriate two-dimensional mechanical state is that of generalized plane strain with negligible out-of-plane bending, which has been shown capable of reproducing the complete 3D stress state [40].

5.3   Fluid Flow Model

A 3D fluid flow model of the pool of molten steel solves for the time-averaged velocity and pressure distributions in an Eulerian domain. The fluid velocities $\boldsymbol{v}$ are calculated for a divergence-free velocity field,

$$\nabla \cdot \boldsymbol{v} = 0, \tag{5.21}$$

using the momentum balance with advection terms,

$$\rho\left(\frac{\partial \boldsymbol{v}}{\partial t} + \boldsymbol{v} \cdot \nabla \boldsymbol{v}\right) = \nabla \cdot \boldsymbol{\sigma} + \boldsymbol{b}, \tag{5.22}$$

for an incompressible Newtonian fluid, which has constitutive relationship for the CAUCHY stress tensor of

$$\boldsymbol{\sigma} = C_\mu \frac{k^2}{\varepsilon}\left(\nabla \boldsymbol{v} + \nabla \boldsymbol{v}^\top\right) - p\boldsymbol{I}, \tag{5.23}$$

where p is pressure, k is the specific turbulent kinetic energy, ε is the specific turbulent dissipation rate, and $C_\mu = 0.09$ is a constant. The k and ε fields are found by solving the two additional transport equations given by the standard k-ε turbulence model [48]. Buoyancy phenomena are negligible relative to the flow inertia, as indicated by $\text{Gr}/\text{Re}^2 \approx 10^{-3}$, where Gr is the GRASHOFF number and Re is the REYNOLDS number. The temperature field is calculated from the energy equation, Equation (5.20), with no mesh velocity $\boldsymbol{v}_{\text{mesh}} = 0$ for
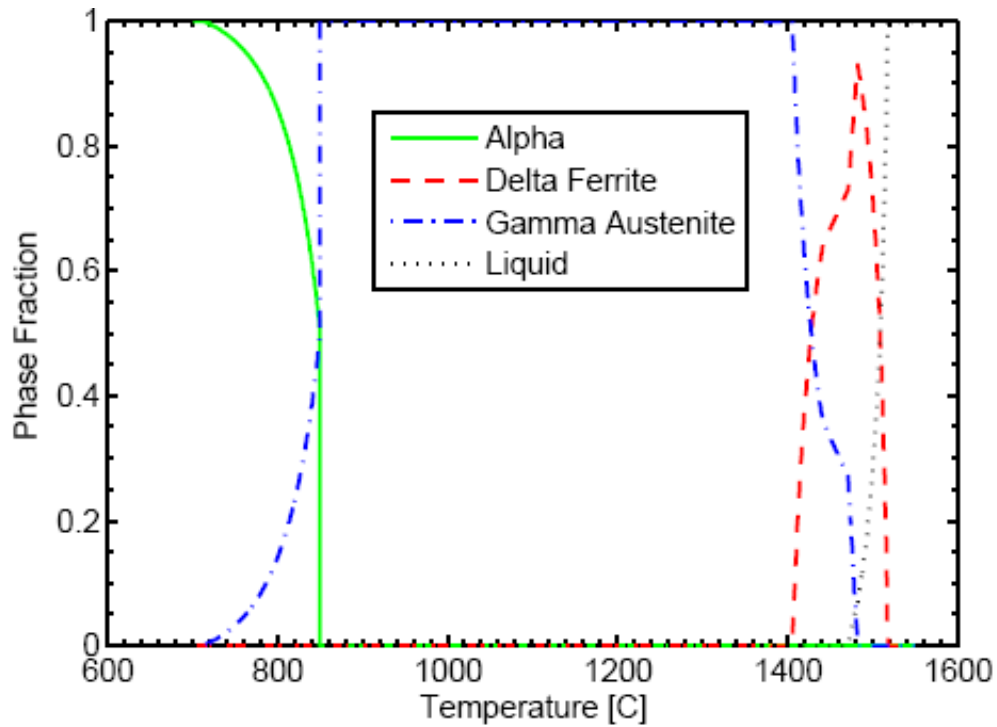
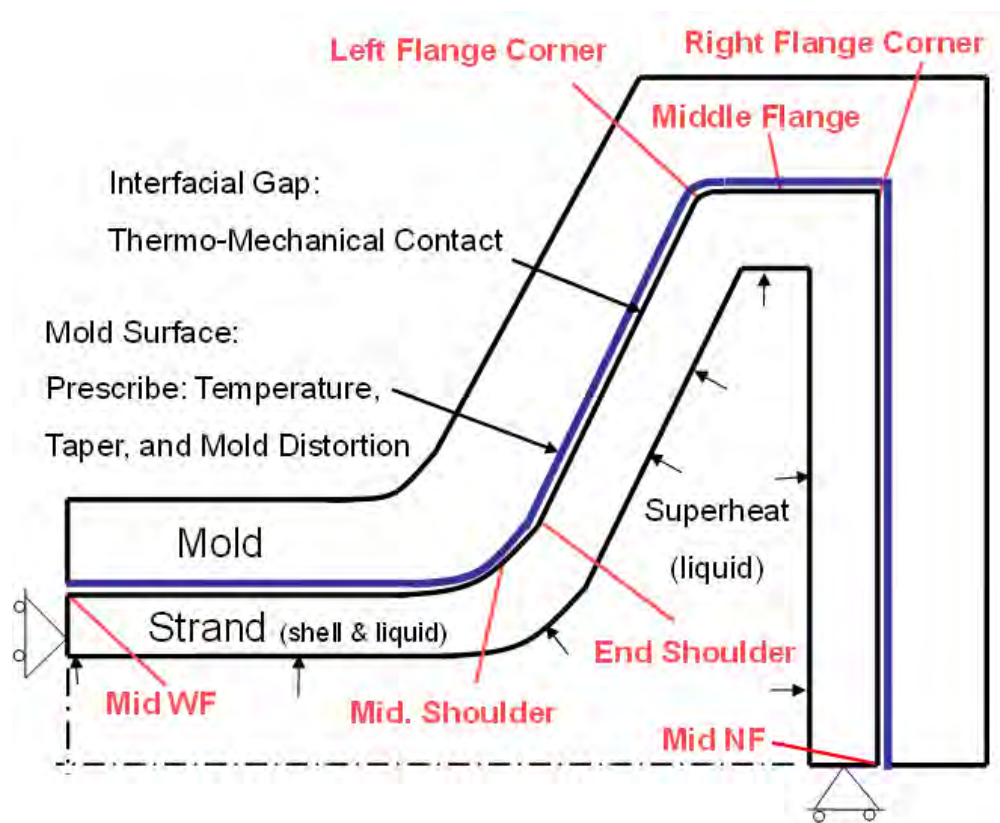**Figure 5.1**   Phase fractions for 0.071 % wt. C plain carbon steel

Figure 5.2   Shell model domain with thermo-mechanical boundary conditions

Condition	Value	Unit
Mass density	6800	kg/m^3
Kinematic shear viscosity	0.006	m^2/s
Inlet velocity	1.854	m/s
Inlet turbulent intensity	200	%
Inlet kinetic energy	0.464	J/kg
Inlet dissipation rate	2.077	J/(kg·s)
Inlet diameter	25.5	mm
Inlet area	256	mm^2
Top surface area	0.032	m^2
Outflow area	0.0215	m^2
Casting speed	0.0148	m/s

Table 5.1 Flow simulation conditions

the Eulerian description of motion. The velocity and temperature fields thus are decoupled, so the flow affects the temperature but the temperature does not affect the flow. The governing equations are discretized with the finite-volume method, and solved using the SIMPLE method and first-order upwinding for the advective terms in the governing equation. The flow problem is solved with the commercial software FLUENT [3], to give the pressure, velocity, and temperature fields at each cell in the computational domain, and the heat flux at the domain boundary surfaces.

The domain for the flow model is bounded by the symmetry planes of the mold and the position of the solidification front, defined as the liquidus temperature, extracted from the solidifying shell model described in Section 5.2. The molten steel enters the liquid pool through two pour funnels, indicated in Figure A.6, with a Reynolds number of about 54×10^3; this feature is modeled as a prescribed $\mathbf{v}$, k, and ε over an appropriate circular inlet on the top surface of the domain. The "standard" wall functions are used to model the steep velocity gradients near the solid-liquid interface. Symmetry planes are treated with the appropriate symmetry boundary conditions of no normal velocity and no tangential traction. The motion of the strand is modeled as the solid-liquid interface velocity being downward at the casting speed. To account for the solidification of the shell, the solid-liquid interface is given appropriate mass and momentum sinks [78] with a user-defined function in FLUENT.

Figure 5.3 shows the velocity and temperature distributions on the center plane and top plane, 10 mm below the free surface, calculated with the 3D thermo-fluid flow simulation of 606 720 hexahedral cells. Table 5.1 summarizes the conditions of this simulation.
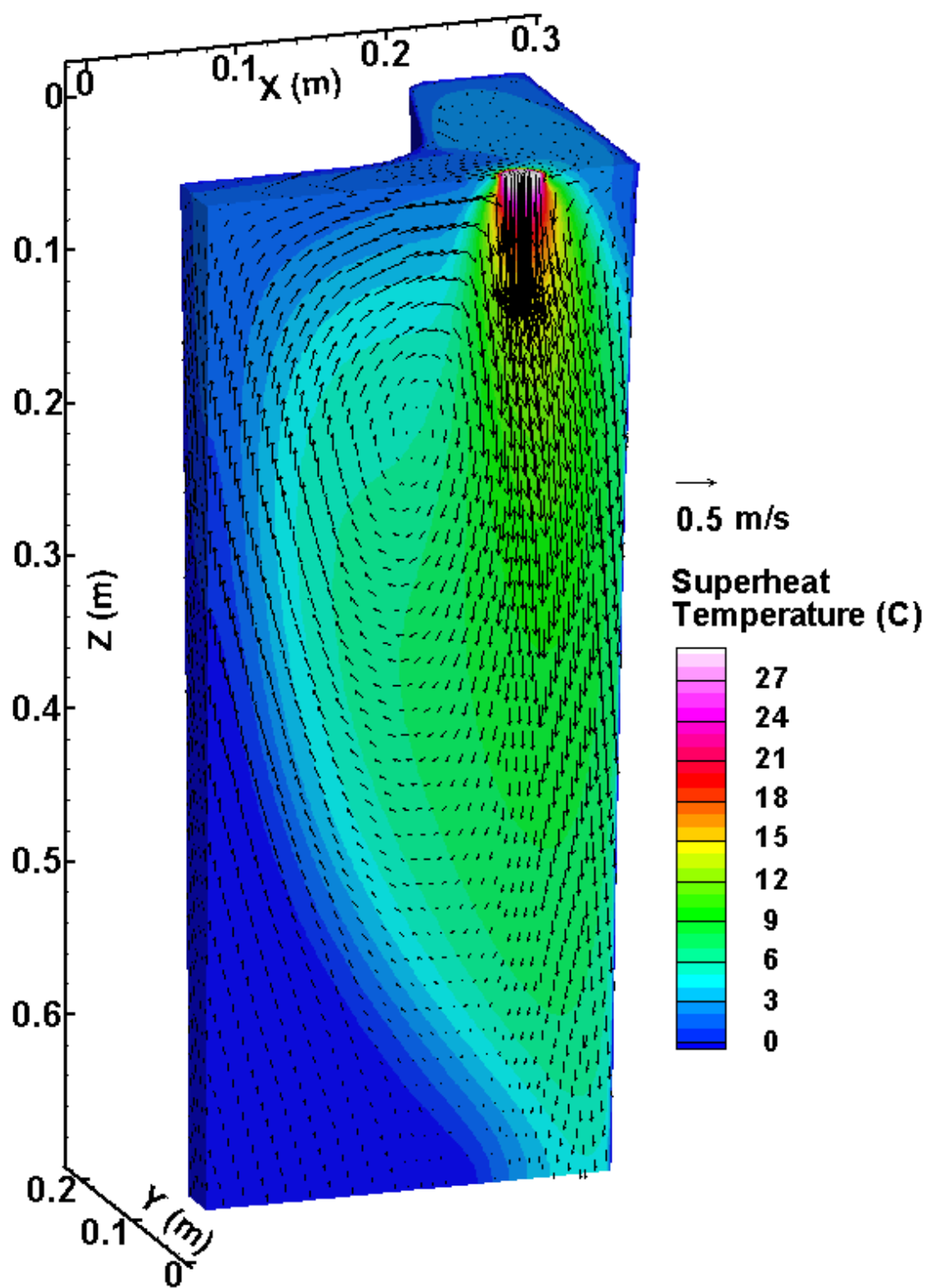
Figure 5.3 Velocity and temperature distributions in the molten steel pool

5.4   Mold Model

In this work, a 3D finite-element model of one symmetric fourth of the beam-blank mold assembly was constructed to capture the effects of mold distortion and variable mold surface temperature on the solidifying steel shell. The beam-blank mold is not symmetric across the casting radius, but this assumption was made for simplifying the demonstration of the multiphysics process model. The model mold and water box geometries include the curvature and applied taper of the hot faces, water channels, and bolt holes as described in Section A.2.

The mesh consists of 263 879 nodes and 1 077 166 tetrahedron, wedge, and hexahedron elements. The governing equations and model description are presented in Sections 2.2 and 4.2. The hot face of the mold is applied a heat flux which is extracted from the surface of the solidifying shell model described in Section 5.2. Inelastic effects are neglected because of the negligible influence on the steady operating behavior of the mold [63]. Contact between the two mold pieces and two backing plates was enforced manually by iteratively applying constraint equations on contacting nodes. The mold bolts and tie rods were simulated using linear truss elements and were appropriately pre-stressed, as described in Section 4.3.

The calculated temperature and distortion results are presented in Figure 4.5 In addition to providing insight into thermo-mechanical behavior of the mold, as discussed in Chapters 2 and 4, this model provides temperature and displacement boundary conditions for the model of the solidifying shell model discussed in Section 5.2.

5.5   Fluid/Shell Interface Treatment

Results from the fluid flow model of the liquid domain affect the solidifying shell model by the heat flux crossing the boundary, which represents the solidification front, or liquidus temperature. This "superheat flux" can be incorporated into a fixed-grid simulation of heat transfer phenomena in the mushy and solid regions by enhancing the latent heat [41] of the solidifying material. This method enables accurate decoupling of complex heat-transfer phenomena into separate simulations of the fluid flow region and the mushy and solid region. The energy boundary condition at a liquid-solid interface is the STEFAN condition [21]:

$$- \boldsymbol{q}_{\text{solid}} \cdot \boldsymbol{n}_{\text{interface}} + \boldsymbol{q}_{\text{liquid}} \cdot \boldsymbol{n}_{\text{interface}} = \rho_{\text{solid}} h_{\text{f}} \boldsymbol{v}_{\text{interface}} \cdot \boldsymbol{n}_{\text{interface}}, \tag{5.24}$$

In the model of the solidifying steel shell, the liquid region is taken as isothermal so no heat flows, $i.e.$, $\boldsymbol{q}_{\text{liquid}} = \boldsymbol{0}$. However, the $\boldsymbol{q}_{\text{liquid}}$ from the flow simulation discussed in Section 5.3, which is not zero, is modeled as an increase to the latent heat such that the STEFAN condition

in the shell model becomes

$$-\boldsymbol{q}_{\text{solid}} \cdot \boldsymbol{n}_{\text{interface}} = \rho_{\text{solid}} \left(h_{\text{f}} + \Delta h_{\text{f}} \right) \boldsymbol{v}_{\text{interface}} \cdot \boldsymbol{n}_{\text{interface}}, \qquad (5.25)$$

where the "enhanced latent heat" Δh_{f} is calculated as

$$\Delta h_{\text{f}} = \left| \frac{\boldsymbol{q}_{\text{liquid}} \cdot \boldsymbol{n}_{\text{interface}}}{\rho_{\text{solid}} \, \boldsymbol{v}_{\text{interface}} \cdot \boldsymbol{n}_{\text{interface}}} \right|. \qquad (5.26)$$

The latent heat enhancement is added to the nominal latent heat and enthalpy in Equation (5.20) with the UMATHT user subroutine in ABAQUS. Because of the limitations of ABAQUS,[2] the normal interface speed $\boldsymbol{v}_{\text{interface}} \cdot \boldsymbol{n}_{\text{interface}}$ is estimated from the local cooling rate $\dot{T}$ and temperature gradient ∇T at every time and material point near the solidification front as

$$\boldsymbol{v}_{\text{interface}} \cdot \boldsymbol{n}_{\text{interface}} = \frac{\dot{T}}{\|\nabla T\|_2} = \frac{\Delta T}{\Delta t} \frac{1}{\|\nabla T\|_2}. \qquad (5.27)$$

Equation (5.27) produces excessive and fluctuating latent heat values when the temperature increments ΔT are driven to be very small by the global NEWTON iterative procedure, particularly at early solidification times and when the superheat flux is large, such as near the pouring cup in the beam-blank mold. This issue is circumvented in this work by using an analytical solution for the interface speed when the total latent heat exceeds 40 times the nominal latent heat. The analytical solution [21] is that of the "solid-control" solidification solution with superheat. The solidification constant ϕ is determined by solving

$$c_{p,\text{s}} \left(T_{\text{liquidus}} - T_{\text{surface}} \right) = \phi \exp\!\left(\phi^2 \right) \text{erf}(\phi) \sqrt{\pi} \left(h_{\text{f}} + \frac{\boldsymbol{q}_{\text{liquid}} \cdot \boldsymbol{n}_{\text{interface}}}{\rho_{\text{solid}} \phi \sqrt{\alpha_{\text{solid}}/t}} \right) \qquad (5.28)$$

The normal interface speed then is calculated as

$$\boldsymbol{v}_{\text{interface}} \cdot \boldsymbol{n}_{\text{interface}} = \phi \sqrt{\frac{\alpha_{\text{solid}}}{t}}. \qquad (5.29)$$

This approach gives an accurate and smooth estimate of the interface speed, and performs well in both one- and two-dimensional solidification problems [41]. The additional heat delivered to the solidification front by the fluid causes the shell to solidify more slowly than without this superheat. Most most shell models in the literature use the technique of enhancing the thermal conductivity of the liquid [59] to account for the advection of the liquid, which causes the shell to solidify faster.

---

[2]The UMATHT subroutine provides only information local to an integration point, including $\dot{T}$ and ∇T. Better methods exist to calculate the interface speed that involve the temperature field across an element, but they cannot be implemented in ABAQUS.

The superheat flux $\boldsymbol{q}_{\text{liquid}} \cdot \boldsymbol{n}_{\text{interface}}$ that is calculated at the boundaries of the 3D steady Eulerian fluid flow model is converted to a function of space and time for the Lagrangian shell model. Each point on the perimeter $\boldsymbol{p}(x, y)$ around the surface of the flow model is chosen as the liquidus isotherm. These surface coordinates and the calculated superheat flux are stored in arrays of $N_{\text{perimeter}}$ points around the perimeter for each of the N_z layers of nodes below the meniscus. At a given time t in the shell model, the corresponding distance below the meniscus is $z = v_{\text{cast}}t$. The array of coordinates is searched to find the indicies i and $i+1$, where $1 \leq i \leq N_{\text{perimeter}}$, and j and $j+1$, where $1 \leq j \leq N_z$, which bound the material point in the Lagrangian shell model. The corresponding superheat fluxes at array coordinates (i, j), $(i+1, j)$, $(i, j+1)$, and $(i+1, j+1)$ then are bilinearly interpolated. The interpolation uses the standard basis functions for a quadrilateral finite element, using local coordinates $\xi = 2\left(p - p_i\right) / \left(p_{i+1} - p_i\right) - 1$ in the perimeter direction and $\eta = 2\left(z - z_j\right) / \left(z_{j+1} - z_j\right) - 1$ in the axial direction, where p is the x-coordinate for points on the wide face and is the y-coordinate for points on the narrow face.

Figure 5.4 shows a 3D view of the superheat flux distribution on the shell interface calculated from the turbulent flow model. The fluid flow causes uneven distribution of superheat fluxes that are greatest midway down the inner shoulder, and least in the flange and center of the wide face. These variations in turn cause local shell thinning and temperature changes, which affect the thermal stress behavior.

The enhancement to the latent heat described above is valid strictly at a sharp liquid-solid interface. The multiphysics model in this work uses a phase-averaged energy equation [20], so this dissonance must be reconciled. The heat flowing into a patch of the sharp interface with area A at position $\boldsymbol{x}^*$ from the liquid can be rewritten as a volumetric quantity as

$$\int_A \boldsymbol{q}_{\text{liquid}}(\boldsymbol{x}^*) \cdot \boldsymbol{n}_{\text{interface}} \, \mathrm{d}A = \int_V \boldsymbol{q}_{\text{liquid}}(\boldsymbol{x}) \cdot \boldsymbol{n}_{\text{interface}} \delta(\boldsymbol{x} - \boldsymbol{x}^*) \, \mathrm{d}V, \qquad (5.30)$$

using a property of the DIRAC delta [20]. Let ϕ_{liquid} be an "indicator function" that is unity in the liquid and zero otherwise; the gradient of this function is $\nabla \phi_{\text{liquid}} = \delta(\boldsymbol{x} - \boldsymbol{x}^*) \, \boldsymbol{n}_{\text{interface}}$. The volumetric heat flux then is

$$\int_V \boldsymbol{q}_{\text{liquid}}(\boldsymbol{x}) \cdot \boldsymbol{n}_{\text{interface}} \delta(\boldsymbol{x} - \boldsymbol{x}^*) \, \mathrm{d}V = \int_V \boldsymbol{q}_{\text{liquid}}(\boldsymbol{x}) \cdot \nabla \phi_{\text{liquid}} \, \mathrm{d}V. \qquad (5.31)$$

The multiphysics model uses volume-fraction fields f that partition unity instead of sharp indicator functions; the gradients of these functions are related by

$$\lim_{\boldsymbol{x}_{\text{liquid}} - \boldsymbol{x}_{\text{solid}} \to \boldsymbol{0}} \nabla f_{\text{liquid}} \cdot (\boldsymbol{x}_{\text{liquid}} - \boldsymbol{x}_{\text{solid}}) = \nabla \phi_{\text{liquid}} \cdot \boldsymbol{n}_{\text{interface}}, \qquad (5.32)$$

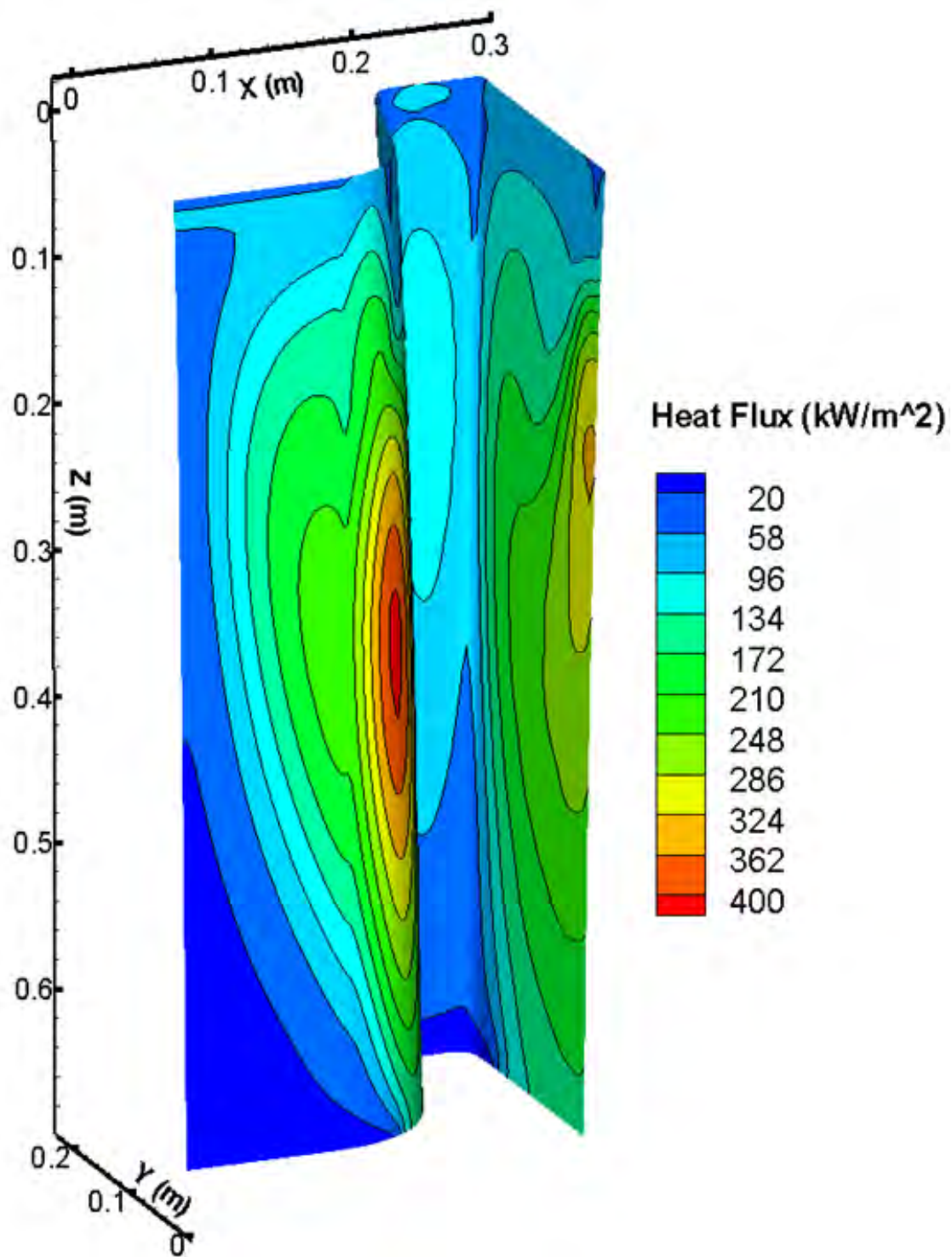**Figure 5.4** Superheat flux distribution on the liquid-solid interface

where x_liquid and x_solid are the positions of the liquidus ($f_\mathrm{liquid} = 1$) and of the solidus ($f_\mathrm{liquid} = 0$) isopleths. The finite mushy zone size introduces a length scale to the enhanced latent heat method, which must be small relative to the other major thermal length scale, the thickness of the solidified shell, for a consistent thermal model. For the first few moments after initial solidification in the continuous casting process, these two length scales are nearly equal, but eventually the length of the mushy zone is about an order of magnitude smaller than the shell thickness. For both the ultra-low-carbon grade used in the funnel mold and the low-peritectic grade used in the beam-blank mold in this work, $\ell_\mathrm{mush}/\ell_\mathrm{shell} \approx 0.1$ by mold exit. That the volumetric heat flux is proportional to ∇f_liquid indicates that the enhancement to the latent heat is applied spatially closer to the liquidus isopleth for steel, and for other materials with an effective partition coefficient less than unity, which yields an approximately consistent approach with extracting the superheat flux from the flow model at the location of the liquidus.

The effect of the ferrostatic pressure in the liquid pool is treated in the shell model as a linearly-increasing distributed load that pushes the solidifying steel shell towards the mold, as described by Equation (4.18). This boundary condition is implemented with the ABAQUS user subroutine DLOAD.

5.6   Shell/Mold Interface Treatment

Two-way thermo-mechanical coupling between the shell and mold is needed because the stress analysis depends on temperature via the thermal strains and material properties, and the heat conducted between the mold and steel strand depends strongly on the distance between the separated surfaces calculated from the mechanical solution. Heat transfer across the interfacial gap between the shell and the mold wall surfaces is defined with a resistor model that depends on the thickness of gap calculated by the mechanical model. The total heat transfer q_gap occurs along two parallel paths, one due to radiation, h_rad, and one due to conduction, h_cond, as

$$q_\mathrm{gap} = (h_\mathrm{rad} + h_\mathrm{cond})\,(T_\mathrm{shell} - T_\mathrm{mold})\,. \tag{5.33}$$

The radiation heat transfer coefficient is calculated across the transparent liquid portion of the mold slag layer as

$$h_\mathrm{rad} = \frac{\sigma_\mathrm{SB}}{\frac{1}{\varepsilon_\mathrm{shell}} + \frac{1}{\varepsilon_\mathrm{mold}} - 1}\left(T_\mathrm{shell}^2 + T_\mathrm{mold}^2\right)\left(T_\mathrm{shell} + T_\mathrm{mold}\right), \tag{5.34}$$

where $\sigma_\mathrm{SB} = 56.704\,\mathrm{nW/(m^2 \cdot K^4)}$ is the STEFAN–BOLTZMANN constant, $\varepsilon_\mathrm{shell} = \varepsilon_\mathrm{mold} = 0.8$ are the emissivities of the shell and the mold surfaces, and T_shell and T_mold are the absolute

Table 5.2 Temperature dependence of shell contact resistance [27]

T (°C)	R_{shell} (10^{-3} m^2/K)
1030	4
1150	5
1518	0.1
1530	0.05

temperatures of the shell and mold surfaces. This model of radiation assumes that the mold and shell surfaces are large, parallel planes; this assumption breaks down near corners, but calculating the correct view-factors of the radiation cavity, *i.e.*, the shell-mold interfacial gap, is not a computationally-feasible addition to this model. The conduction heat transfer coefficient depends on four resistances connected in series,

$$\frac{1}{h_{\text{cond}}} = R_{\text{mold}} + \frac{d_{\text{air}}}{k_{\text{air}}} + \frac{d_{\text{slag}}}{k_{\text{slag}}} + R_{\text{shell}}. \tag{5.35}$$

The contact resistance between the mold surface and the solidified slag film is taken as $R_{\text{mold}} = 0.4 \times 10^{-3}\,\text{m}^2/\text{W}$ [70]. The slag film thickness is taken as $d_{\text{slag}} = 0.1\,\text{mm}$ to avoid nonphysical behavior associated with very small gaps [70]. The size of the air gap is calculated from the size of the total gap between the surfaces, $d_{\text{air}} = d_{\text{gap}} - d_{\text{slag}}$. The slag and the air have thermal conductivities $k_{\text{slag}} = 1\,\text{W}/(\text{m}\cdot\text{K})$ and $k_{\text{air}} = 0.06\,\text{W}/(\text{m}\cdot\text{K})$. The contact resistance between the slag and the shell R_{shell} decreases with temperature as the shell drops below the solidifcation temperature of the mold slag [27], as listed in Table 5.2. The heat transfer coefficient of the gap, Equation (5.33), is implemented into the ABAQUS models with the GAPCON user subroutine.

Mechanical contact is treated as described in Section 4.2, with the size of the gap d_{gap} determined with the "softened" exponential contact algorithm in ABAQUS, knowing the position of the mold wall and shell surfaces $\boldsymbol{x}_{\text{mold}}(t)$ and $\boldsymbol{x}_{\text{shell}}(t)$ as

$$d_{\text{gap}}(\boldsymbol{x}, t) = \left\| \boldsymbol{x}_{\text{shell}} - \boldsymbol{x}_{\text{mold}} \right\|_2. \tag{5.36}$$

The softening of the contact is that the contact pressure $p_{\text{c}} = \boldsymbol{n} \cdot \boldsymbol{\sigma} \cdot \boldsymbol{n}$ is defined by

$$p_{\text{c}} = \begin{cases} 0 & \text{if } d_{\text{gap}} \geq d_0 \\ \frac{p_0}{\exp(1)-1} \left(\left(\frac{d_{\text{gap}}}{d_0} + 1 \right) \left(\exp\left(\frac{d_{\text{gap}}}{d_0} + 1 \right) - 1 \right) \right) & \text{if } d_{\text{gap}} < d_0 \end{cases}, \tag{5.37}$$

where $d_0 = 50\,\mu\text{m}$ is the gap size at which surfaces first are in contact, and $p_0 = 0.1\,\text{MPa}$ is the contact pressure when the surfaces are coincident. The first iteration of the shell model uses the nominal, undistorted shape of the mold. For the second iteration of the shell model,
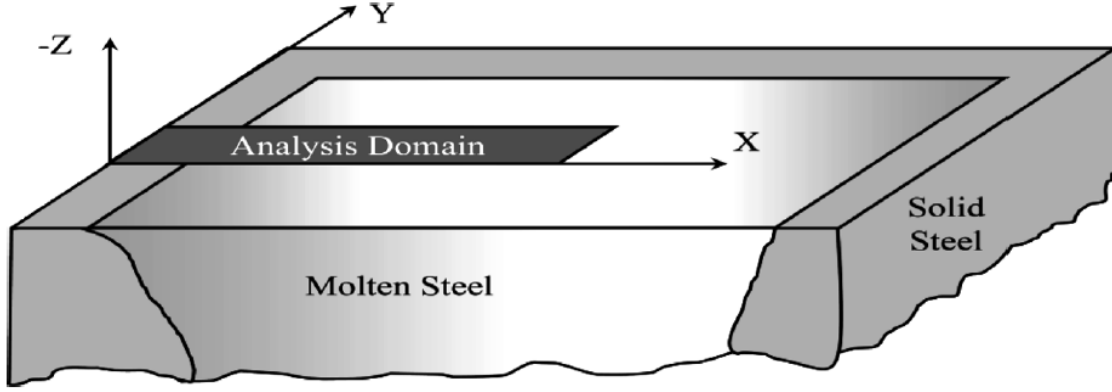
Figure 5.5 Solidifying slice for validation problem

the results of the 3D mold distortion model were post-processed to create a database of surface temperature $T_{\text{mold}}(\boldsymbol{p}, t)$ and surface position $\boldsymbol{x}_{\text{mold}}(\boldsymbol{p}, t)$ for points on the transverse perimeter of the hot face $\boldsymbol{p}$ and distance down the mold z. This database was created, using the same procedure described in Section 5.5, to turn the 3D fields into transient 2D fields for the Lagrangian shell model as a function of time below the meniscus, $t = z/v_{\text{cast}}$. A time-varying displacement is applied to each point on the hot face to re-create the distorted shape of the mold that the Lagrangian shell domain would encounter as it moves through the mold, using the ABAQUS user subroutine DISP.

5.7 Validation of the Numerical Models

The thermo-mechanical solidification model used in this work is validated with the semi-analytical solution of thermal stresses in an unconstrained solidifying plate [103]. A one-dimensional model of this test casting can produce the complete 3D stress and strain state if the condition of generalized plane strain is imposed in both the width (y) and length (z) directions [52].

The domain adopted for this problem moves with the strand in a Lagrangian frame of reference as shown in Figure 5.5. The domain consists of a thin slice through the plate thickness using 2D 4-node generalized plane strain elements, in the axial z direction, implemented in ABAQUS. The second generalized plane strain condition was imposed in the y-direction, parallel to the surface, by coupling the y-displacements of all nodes along the bottom edge of the slice domain. A fixed temperature is imposed at the left boundary, and all other boundaries are insulated.

The material in this problem has elastic–perfect-plastic constitutive behavior. The

104

yield stress drops linearly with temperature from 20 MPa at 1000 °C to zero at the solidus temperature 1494.4 °C, which was approximated by $\sigma_Y = 0.03$ MPa at the solidus temperature. A narrow mushy region, 0.1 °C, is used to approximate the single melting temperature assumed in the analytical solution. Table 5.3 summarizes the conditions of the validation problem.

Condition	Value	Unit
Thermal conductivity	33	$W \cdot K/m$
Specific heat capacity	661	$J/(kg \cdot K)$
Young's modulus in solid	40	GPa
Young's modulus in liquid	14	GPa
Poisson's ratio	0.3	–
Coefficient of linear expansion	20	$(\mu m/m)/K$
Mass density	7500	kg/m^3
Liquidus temperature	1494.45	°C
Fusion temperature (analytical)	1494.4	°C
Solidus temperature	1494.35	°C
Initial temperature, no superheat	1495	°C
Initial temperature, with superheat	1545	°C
Latent heat of fusion	272	kJ/kg
Surface temperature	1000	°C

Table 5.3 Conditions for solidifying steel in the validation problem

Figures 5.6 and 5.7 show the temperature and the stress distribution across the solidifying shell at two different solidification times. The mesh with 0.3 mm-square elements accurately matches the analytical solutions for both fields. For free-shrinking metal slabs, the surface is in compression and the solidification front is in tension because the surrounding material constrains the slab to remain planar and resists the tendency of the material to shrink [103]. More details about this model validation can be found elsewhere [30, 42, 52] including comparisons with other less-efficient integration methods and a convergence study.

The method for modeling superheat by enhancing latent heat is also tested on the same slice domain and compared with a 1D analytical solution for conduction with phase change [21]. The superheat flux is best calculated with simultaneous modeling of fluid flow; instead the initial temperature is increased by 50 °C to provide a superheat flux driven by the temperature difference between T_{init} and T_{liq}, assuming stagnant liquid. To test the enhanced latent heat method, the validation problem was first executed with the large superheat, and the heat flux at the moving solidification front during post-processing. The validation problem then was executed again with a small superheat and the enhanced latent heat method implemented in the user subroutine UMATHT, with this extracted superheat flux. Figure 5.8 shows the
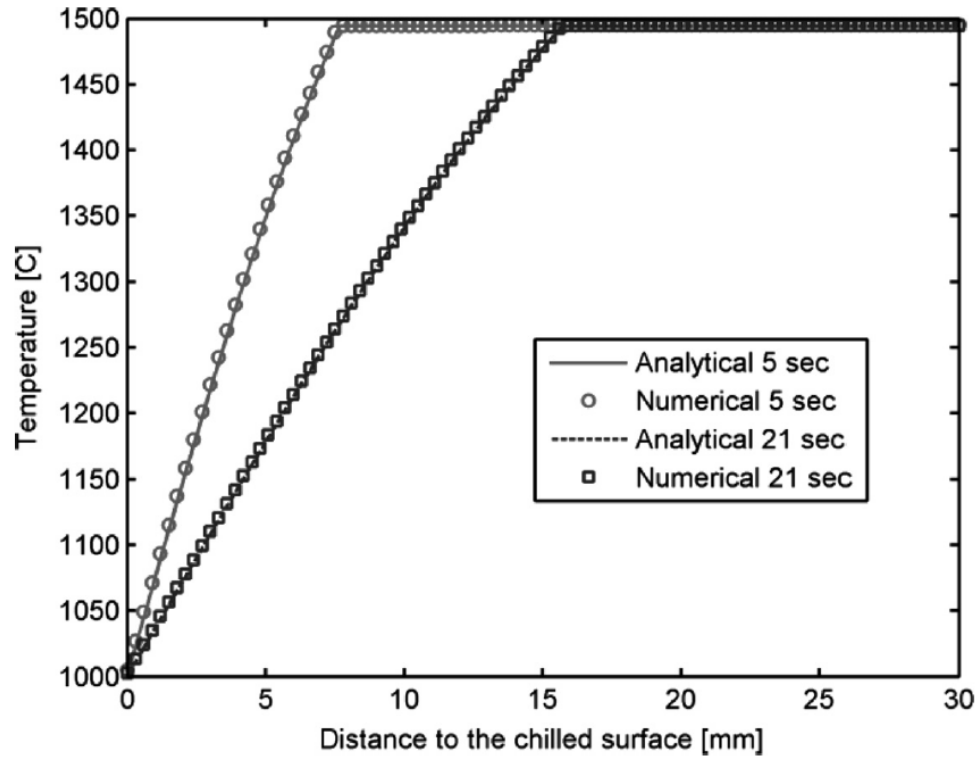
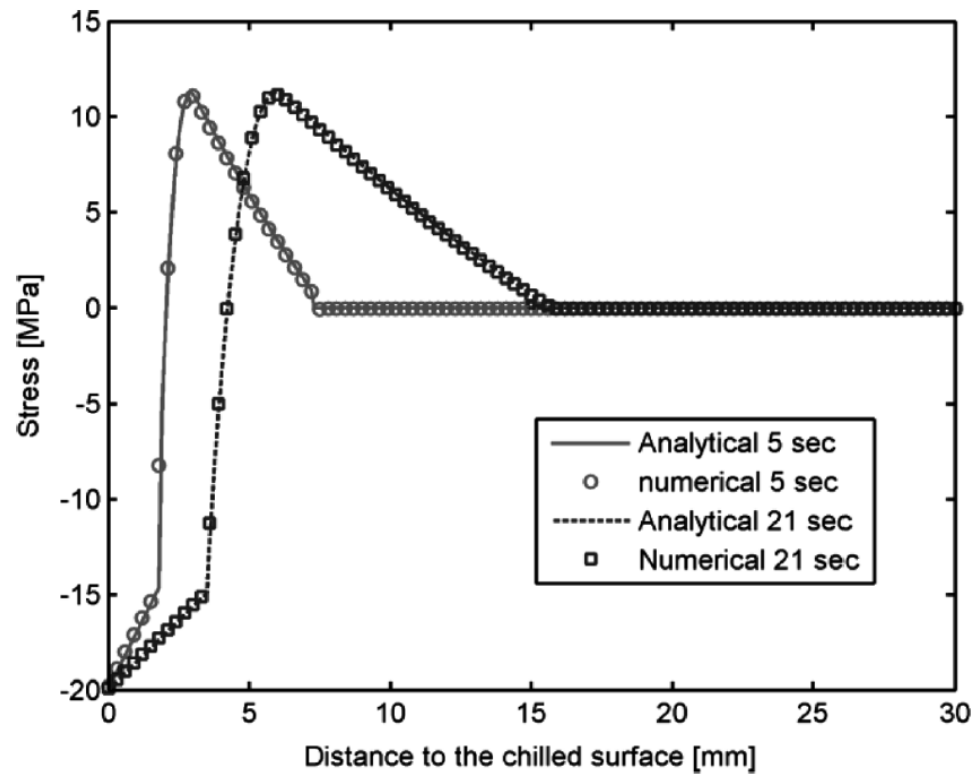**Figure 5.6** Validation problem temperature evaluation without superheat

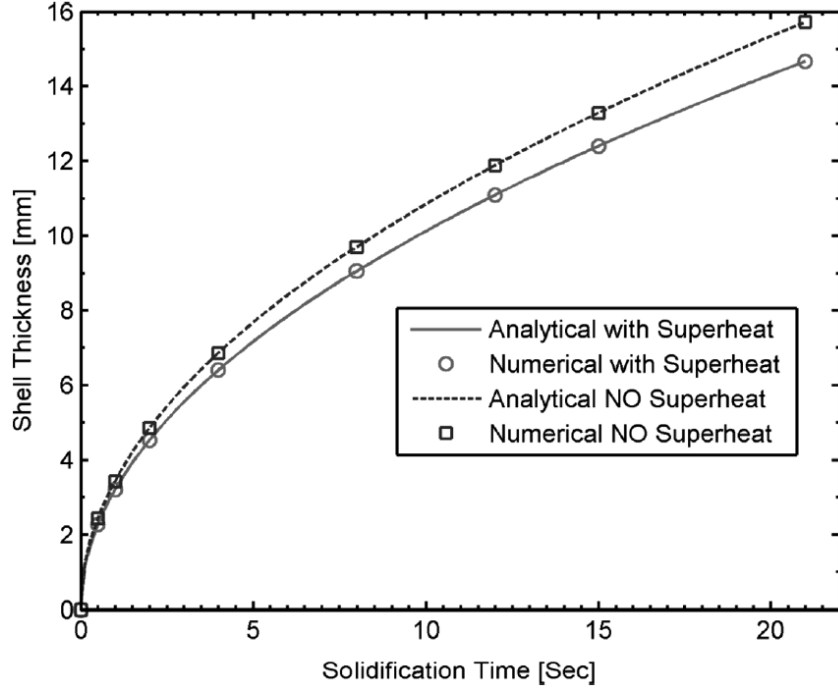**Figure 5.7** Validation problem stress evaluation without superheat

Figure 5.8   Validation problem shell growth with enhanced latent heat technique

analytical and numerical solidification front positions, with and without the 50 °C superheat; the "Numerical with Superheat" points in the plot shows that the enhanced latent heat method can accurately solve this solidification problem using the post-processed superheat flux.

5.8   Multiphysics Model of Beam-Blank Casting

The multiphysics model presented in this chapter was used to find the fluid-flow, temperature, stress, and deformation in a complex-shaped beam blank caster under realistic continuous casting conditions. Figure 5.9 is a flow chart of the solution strategy for the thermo-mechanical-fluid flow model of steel continuous casting. First, the thermo-mechanical model of the solidifying shell is simulated assuming a uniform superheat distribution driven by the temperature difference between T_{init} and T_{liq}, and artificially increasing thermal conductivity in the liquid region seven-fold. The first shell model uses a simplified thermal model of the mold, like what is presented in Chapter 3, with the nominal, undistorted shape of the mold hot face. The heat flux from the shell surface provide the boundary conditions for the thermo-mechanical model of the mold, which in turn supplies the next run of the shell model with mold temperature and thermal distortion boundary conditions. The position of

the solidification front in the shell model defines an approximate shape of the liquid pool for the fluid flow model, which is used to calculate the superheat flux distribution for the next iteration of the shell model. Finally, an improved thermo-mechanical model of solidifying shell is re-run which includes the effects of the superheat distribution and mold distortion, and completes the first iteration of the multiphysics model. Because the shell profile from the improved thermo-mechanical model has little effect on superheat results in the liquid pool, a single multiphysics iteration is sufficient to predict the shell growth accurately.

The shoulder region of the beam-blank mold has a convex shape which converges the heat flow and increases local temperature, opposite to behavior at the corners. Figures 5.10 and 5.11 show the calculated gaps at the shoulder and flange. A gap in the middle shoulder is caused by outward bending of the shell due to contact pressure from the mold onto the middle of the flange. Heat extraction from the shoulder is therefore retarded as shown in Figure 5.10, yielding a thinner shell with higher temperature. The shell pulls away from the both corners of the flange, shown in Figure 5.11, but by differing amounts; the "flange tip" corner is well-cooled by the narrow face, but the "flange corner" corner is consistently the hottest part of the surface of the shell. Figures 5.12 and 5.13 gives the temperature and gap size of several key locations around the perimeter of the hot face. The maximum and minimum principal stress contours at $457\,\text{mm}$ below meniscus are given in Figure 5.14, which show the expected compressive shell behavior at the "cold" surface and tensile stress in the hot interior near the solidification front, similar to the model validation from Figure 5.7. The tendency for the surface to be in compression and the solidification front to be in tension is mainly a consequence of the constraint provided by the surrounding material, as mentioned in Section 5.7, though other effects like the increasing strength with decreasing temperature and changes to the heat removal because of the coupled gap behavior or mold geometry affect the behavior as well. Maximum stress and strain is found in the shoulder area, which is not a surprise since the thinner shell in this region caused by gap formation leads to stress concentration. Longitudinal cracks and breakouts are often found in this same shoulder region, as revealed by plant observations [35].
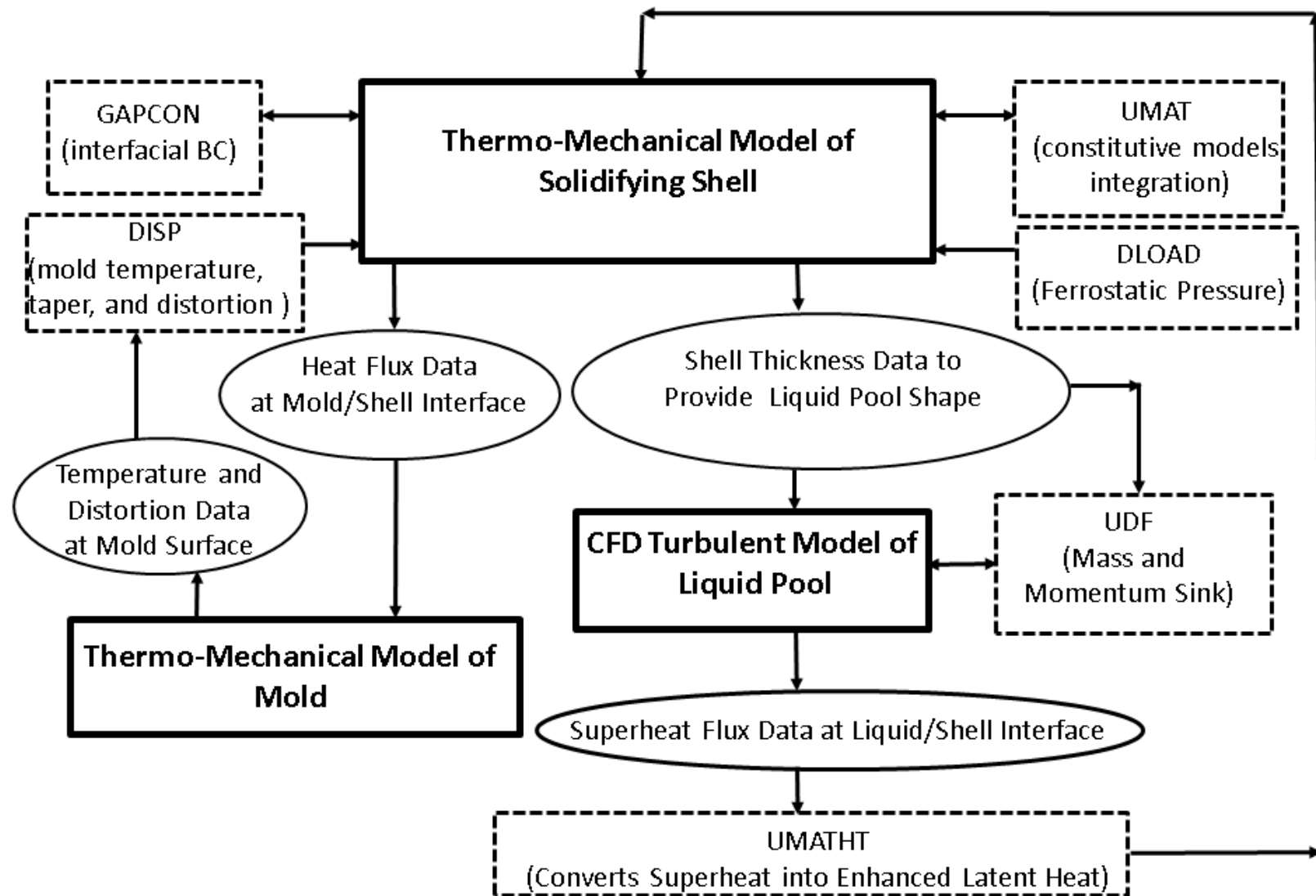
Figure 5.9   Flowchart for multiphysics solution strategy
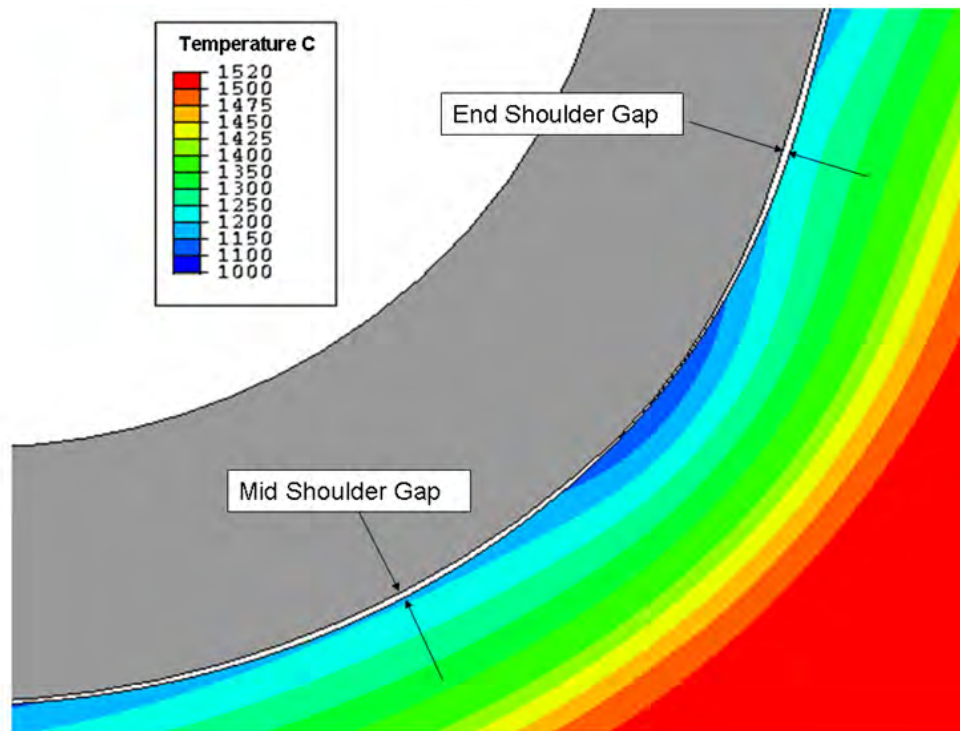
Figure 5.10   Calculated temperatures and gaps at the shoulder of the beam-blank mold
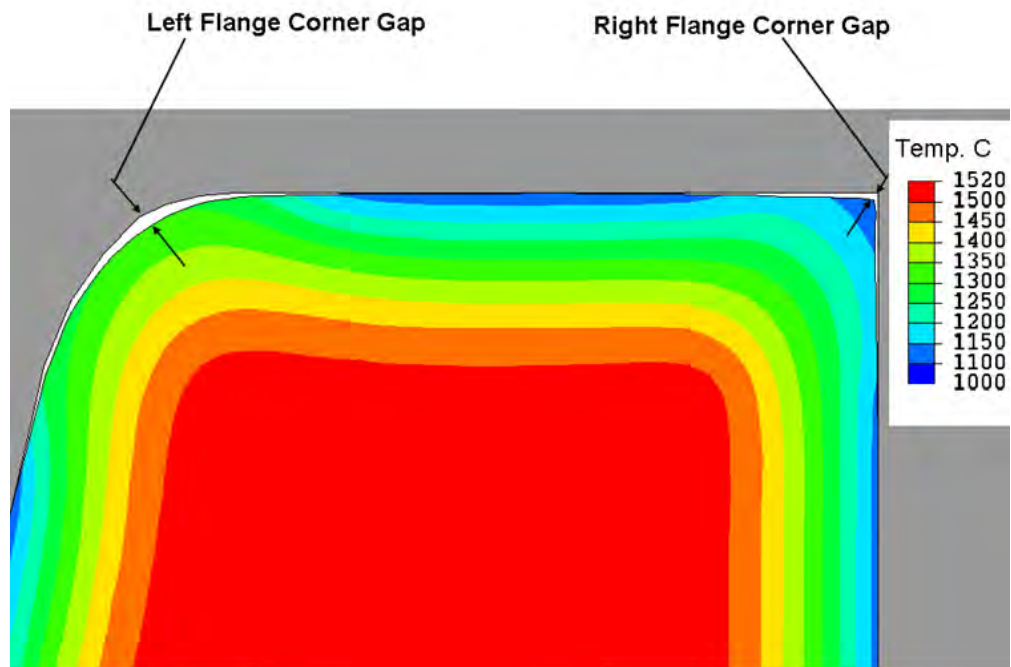
Figure 5.11   Calculated temperatures and gaps at the flange of the beam-blank mold

Figure 5.12 Calculated temperature histories of several points on the surface of the beam-blank strand

Figure 5.13 Calculated gap-size histories of several points on the surface of the beam-blank strand

(a) Maximum in-plane principal stress

(b) Minimum in-plane principal stress

Figure 5.14   Stresses in the solidifying shell at 457 mm below meniscus, in Pa

The shell thickness, defined as 90% fraction-liquid, predicted by a thermo-mechanical–only model (the first iteration) and the multiphysics model of the soldifying strand are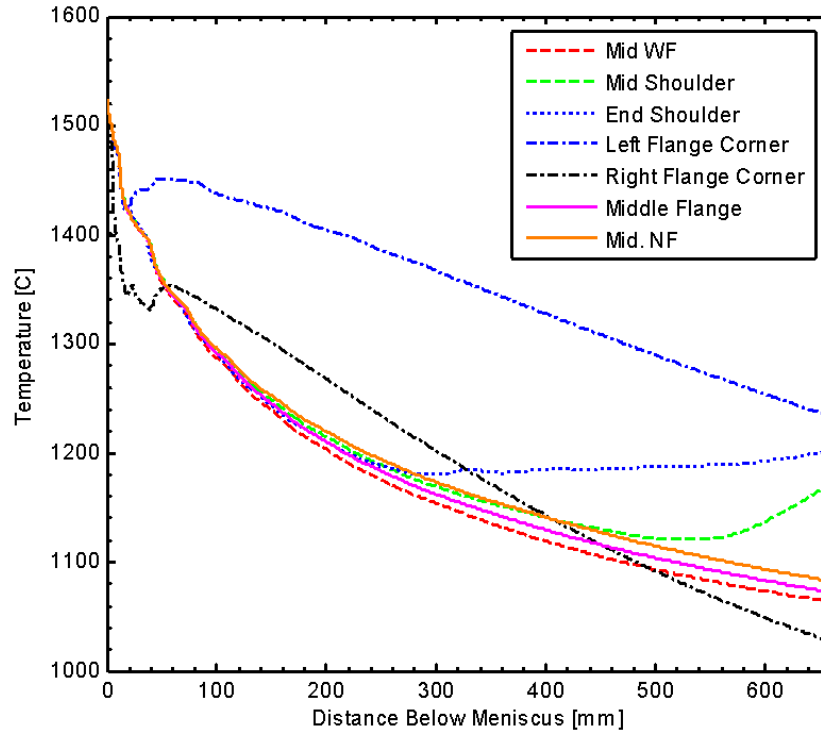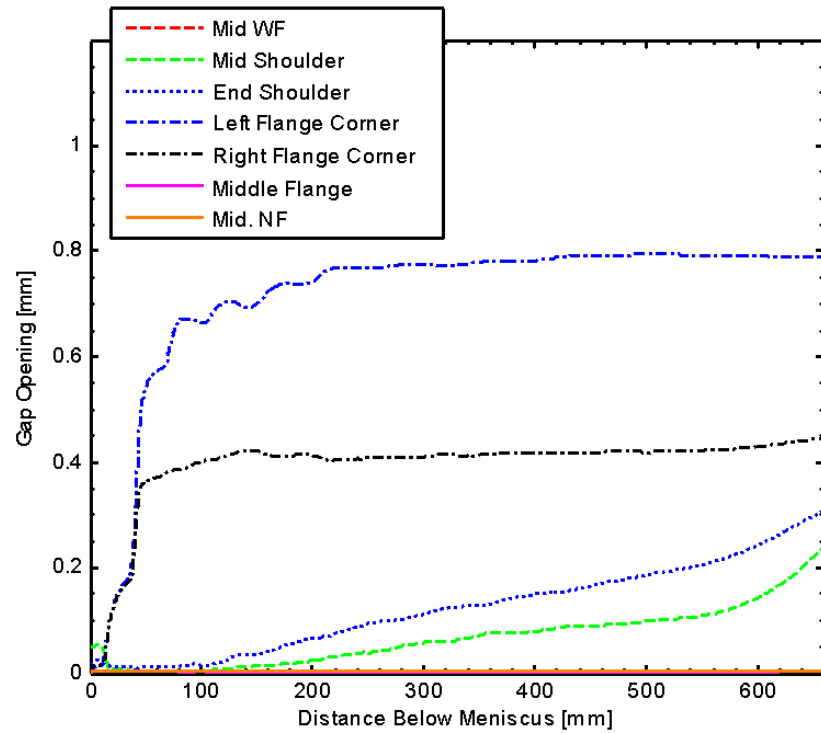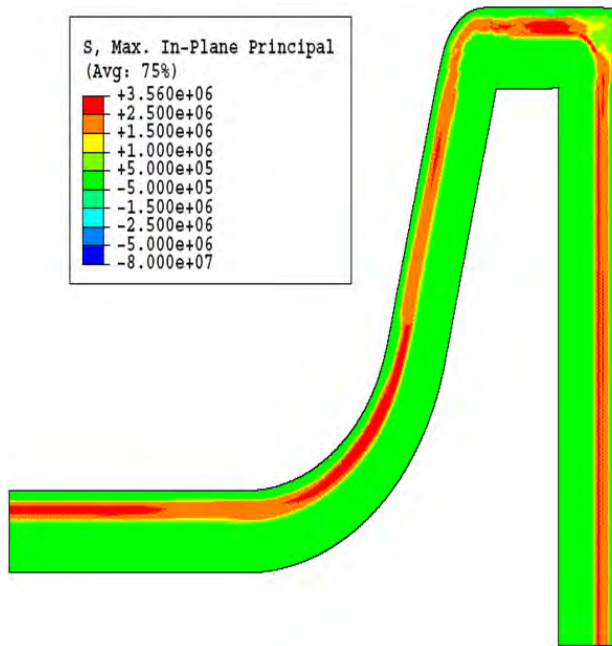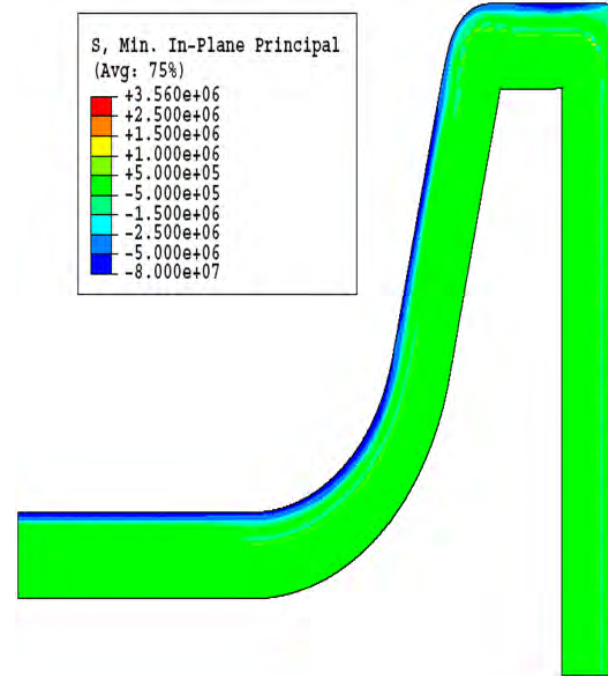 compared with measurements around the perimeter of a breakout shell [35] in Figure 5.15. The initial thermo-mechanical model with a uniform superheat distribution can only roughly match the shell thickness variations. Shell thickness variations at the corners and shoulder due to air gap formations were captured with to the interfacial heat transfer model. The variable field in the multiphysics model correctly calculates the accelerated shell growth in the middle of the web, where the liquid is the coldest, and the retarded shell growth at the corner, where the liquid is the hottest. The shell is about 4 mm thicker in the middle of the flange and 2 mm thinner at the shoulder with the multiphysics model than what it is in the thermo-mechanical–only model. The improved multiphysics model that includes the fluid flow effects matches the shell thickness measurement around the entire perimeter much more accurately. This finding illustrates the improved accuracy that is possible by including the effects of fluid flow into a thermal stress analysis of solidifying shell.

5.9   Conclusions

The model developed in this chapter enables accurate uncoupling of complicated multiphysics phenomena in continuous casting into separate simulations of the fluid flow region, the mushy zone and solid steel shell region, and the mold. Spatially and temporally non-uniform superheat fluxes, produced by turbulent fluid flow and mixing in the liquid pool, are calculated from the results of a finite-volume fluid flow model. A new latent-heat method is applied to link these results into a coupled thermo-mechanical finite-element model of the solidifying shell. The realistic effect of mold thermal distortion is incorporated through a second database and boundary condition at the shell-mold interface. The model first is validated with available analytical solutions of thermal stress, temperature, and shell growth. The model then is applied to simulate solidification in a one-quarter transverse section of a commercial beam blank caster with complex geometry, temperature dependent material properties, and realistic operating conditions. The results compare very well with in-plant measurements of the thickness of the solidifying shell.

This method illustrates an effective approach towards accurate multiphysics modeling of commercial processes. By exploiting unique features of the continuous casting of steel, individual models can be coupled together in an efficient, accurate, and robust way to achieve realistic predictions of metal solidification on the continuum scale. The key is the careful choice of the boundaries between modeling domains, and their treatment in both interface

models, such that convergence can be achieved in as little as one iteration on the macroscale. The most intimately-coupled phenomena, *i.e.*, the coupled thermal and mechanical behavior of the shell-mold interfacial gap, are modeled in the same domain and model.

Realistic prediction of shell shape, temperature, and shrinkage is just the first step in predicting the formation of defects such as porosity, segregation, and cracks, microstructure, and final properties. Much further work remains to incorporate further models of these additional phenomena into useful modeling systems, tailored for a given process like casting or welding.
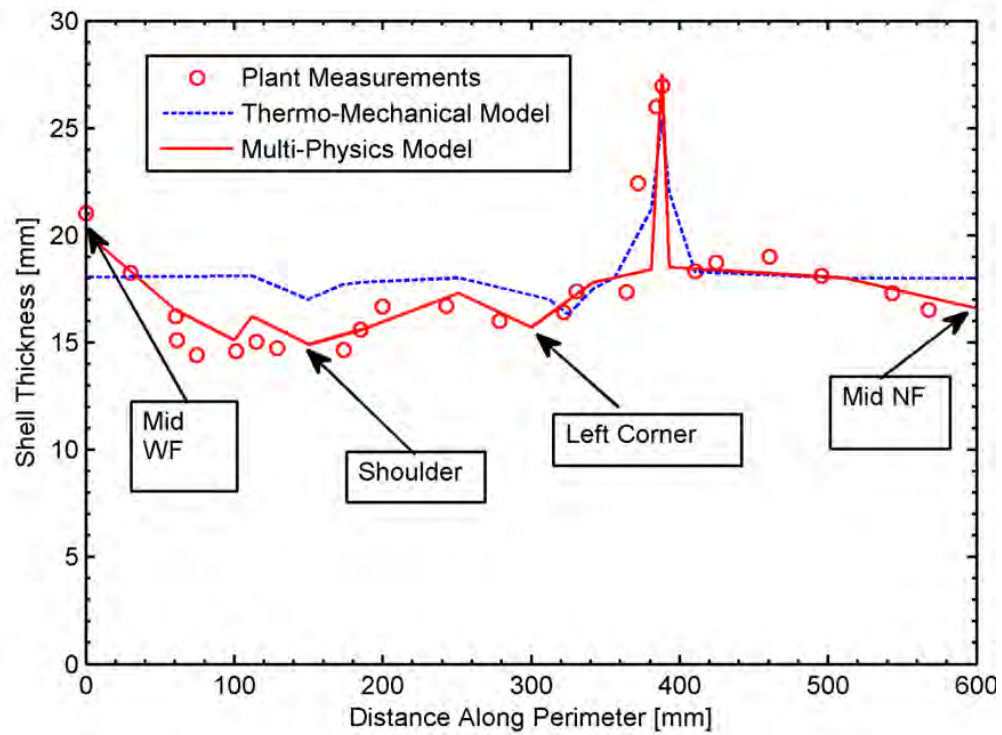
Figure 5.15 Calculated and measured shell thickness around the perimeter of beam-blank section

CHAPTER 6
Conclusions and Future Work

This work has explored some aspects of the continuous casting of steel with numerical models. The main contribution of this work is to develop a multiphysics, macroscale model of the process that simulates the coupled effects of turbulent flow and heat transport in the molten steel pool, the elastic-viscoplastic thermal shrinkage and solidification heat transfer in the solid steel shell, and the thermal distortion of the mold. This complete model of the process is possible because of the largely "one-way coupling" between the fields and domains, and appropriate techniques for interfacing between the models.

The multiphysics modeling process begins with a model of heat transfer in the solidifying shell. This first shell model must be able to match the plant-measured thermocouple temperatures and cooling water temperature change before proceeding to the remaining steps in the multiphysics procedure. This first shell model is post-processed for the heat flux from the shell into the mold, and for the position of the solidification front. These data are used to drive a elastic thermo-mechanical simulation of the mold distortion and to define the solid-liquid interface in a turbulent thermal-flow model of the liquid steel pool. The mold distortion calculation is post-processed for the temperature and distorted shape of the hot face of the mold, and the fluid flow simulation is post-processed for the heat flux entering the solid shell at the solidification front. The realistic mold hot face and the superheat flux distribution then are fed into a separate elastic-viscoplastic thermo-mechanical model of the solidifying shell, which requires special boundary conditions that represent the physics of their respective interfaces, and careful translation to change from Eulerian to Lagrangian descriptions of the fields. The multiphysics modeling approach allows each main phenomenon to be modeled accurately in a "natural" setting for each set of physics, *e.g.*, the fluid flow is simulated with an Eulerian fixed-grid approach.

To avoid the full coupling of the first shell model of the solidifying shell with the mold, the thermal effect of the mold is approximated with a one-dimensional analytical model, which results in a convection condition that represents all of the physics of the mold. The parameters in this simple analytical model related to the mold geometry first are calibrated so that this reduced-order model of mold heat transfer is able to match the temperature predictions of a small finite-element model of the exact mold geometry. Only one calibration is necessary

per mold geometry, as the method was demonstrated in Chapter 3 to be insensitive to the boundary conditions on the calibration domain. This fast and simple model of mold heat transfer is a useful tool by itself, but also provides an accurate representation of the mold in larger models of the continuous casting process, such as a model of the shell deformation, where computational effort is better spent on the physics of interest of the main model.

Only three-dimensional models with good geometric fidelity to the actual mold, such as the models presented in Chapters 2 and 4, can reveal the variations in mold temperature on the hot face and throughout the mold, particularly around the cooling channels of the mold. These variations, though small relative to the other temperatures on the hot face, can have negative consequences on the cast product, up to and including breakouts. Good geometric fidelity also is necessary when predicting the distorted shape of the mold, and the model of the mold distortion must contain the waterboxes and bolts that support and contact the molds. The simulated shape of the narrow face mold agrees very well with measurements from inclinometers on an in-service mold. The applied taper on the molds has been calculated, and measured, to change significantly because of the thermal expansion of the mold: for example, the local taper, including the effect of mold distortion, near mold exit of a funnel mold was about three times smaller than the nominal taper that was applied to the mold. Quantitative knowledge of the shape of the mold at operating temperatures is vital to properly design the taper practice and avoid defects in the cast steel.

Moreover, the uneven distribution of superheated liquid in the molten steel pool affects the behavior of the solidifying steel. This work demonstrated a technique for calculating this distribution of temperature in a flow model, and modifying the solidification boundary condition in a thermo-mechanical simulation of the shell to simulate its effect. A multiphysics model of the solidifying shell, including the effects of this uneven distribution of superheat and the distorted shape of the mold, is presented in Chapter 5, for a beam-blank mold. This particular geometry showcases the need for such a model because of the many two- and three-dimensional physical phenomena that cannot be captured with the previous approach to modeling the continuous casting process. For example, the shell growth is accelerated by about 10% in the middle of the web region of the cast section because of the much larger distance to the stream of the hot steel, and the multiphysics model is capable of matching this measured observation, while the traditional thermo-mechanical model is not. The prediction of the multiphysics model matches measurements of the varying thickness of a breakout shell all the way around the perimeter of the mold.

The multiphysics modeling approach demonstrated in this work has redefined the state of the art of continuous casting process modeling. Creating a model of a process neces-

sarily involves making assumptions about the behavior of the process to create a feasible computational model, and for most of continuous casting these assumptions are reasonable. Sometimes these assumptions prevent the model from calculating correct behavior, such as remelting of the shell under a submerged molten steel jet, or with the complicated geometry of a beam blank mold. However, these problems are no longer an issue with the modeling framework developed in this work. This comprehensive macroscale view of the process has been demonstrated to accurately match many different measurements from the plant, and can be extended in future work to include microscale effects and to investigate defect formation from a more fundamental perspective. For example, conditions of a typical segment of the strand calculated in the multiphysics model can be used as boundary conditions on microscale studies of defect formation.

APPENDIX A
Mold Geometry

Continuous casting molds are shaped to cast:

- billets and blooms, which are square sections with rounded corners
- rounds, which are circular sections
- rectangular slabs, ranging from 50 mm–90 mm "thin" slabs to 250 mm "thick" slabs
- "beam-blanks" which are a dogbone section, and
- strips, in the range of a few millimeters thick, though this variant of continuous casting is still under development.

The tendency of the steel industry over the last few years has been to move to near-net-shape castings, such as thin-slab and beam-blank, for among other reasons to reduce rolling costs. Some thin-slab casters include a gentle funnel cut into the hot face of the molds to allow space for the SEN to fit between the mold plates. This work covers a thin-slab funnel mold and a beam-blank mold, and this appendix outlines the geometry of these mold sections.

A.1   Funnel Mold

The funnel mold and its waterbox considered in this work are shown in Figures A.1 through A.5. One symmetric fourth of the mold is considered for computational efficiency, though the waterbox is not symmetrical. Other asymmetric effects, like variations in bolt tightening or mold alignment, and the mold geometry changes to accommodate the the mold-level sensor on one side, are expected to be small. This mold has no coating layers. Except for the top row, each bolt is instrumented with a thermocouple set 20 mm from the hot face.

The funnel opening on the wide face decreases from 136.8 mm at mold top to 106 mm at mold exit. The funnel has an "inner flat" region in the center, which transitions to an "outer flat" region near the narrow faces by means of two tangent circles of equal radius but opposite curvature, as shown in Figure A.1. Further detail of funnel mold geometry is given in Chapter 2 of Reference 30. The wide face water channels are 5 mm wide by 15 mm deep, cut with a ball-end mill, and set 20 mm from the hot face with 10 mm spacing in banks of 18, as shown in Figure A.2. The inlets and outlets of the water channels curve away from
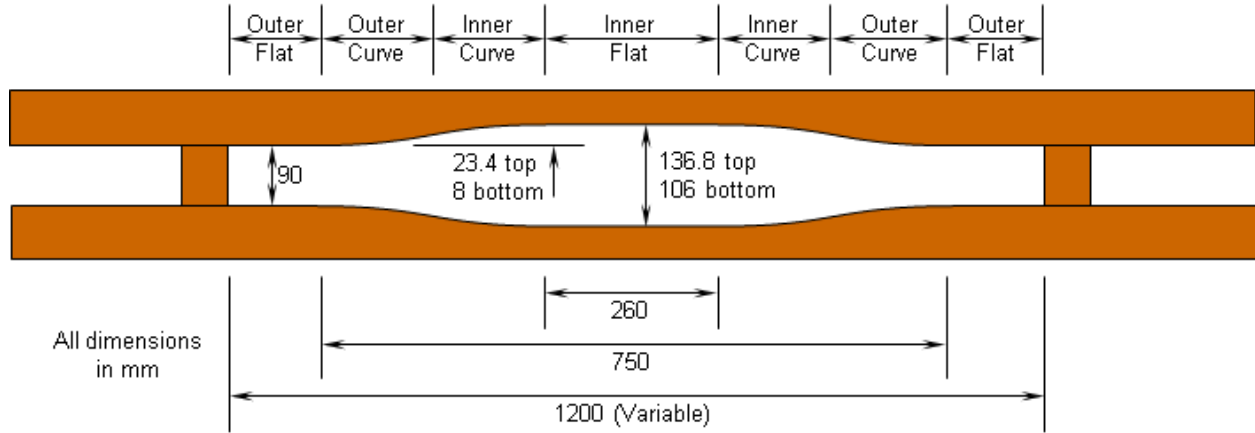
Figure A.1 Funnel mold WF mold geometry

the hot face to meet the waterbox. Each wide face has a rectangular array of 81 bolts spaced 125 mm apart in the casting direction and 212.5 mm apart in the horizontal direction. The cooling passages next to each bolt hole are a pair of 10 mm-diameter tubes. There are 18 channels and 2 tubes between bolt columns. Three water channels are cut into one wider channel, centered at 323.75 mm from the centerline, for about half the length of the mold, to accommodate a mold level sensor. The wide face waterbox, shown in Figure A.3, is built from 20 mm-, 30 mm-, and 50 mm-thick plates, and includes large 587.5 mm-by-650 mm cavities to accommodate an electromagnetic flow control system.

The narrow face mold plate is 72 mm thick and its waterbox is 110 mm thick with a 50 mm bore for the water flow, as shown in Figure A.4. Each narrow face copper plate is cooled by four

Figure A.2 Funnel mold WF water channel geometry

14 mm diameter cylindrical water tubes. The hot face of the narrow face is curved slightly concave towards the molten steel to ensure that any bulking of the strand during soft reduction below the mold is outward. Each narrow face is attached with a column of bolts with 134 mm spacing to a waterbox that is suspended by large hooks on two support cylinders. These two support cylinders are dynamically positioned to adjust mold width and taper.

120

Figure A.3 Funnel mold WF mold and waterbox geometry
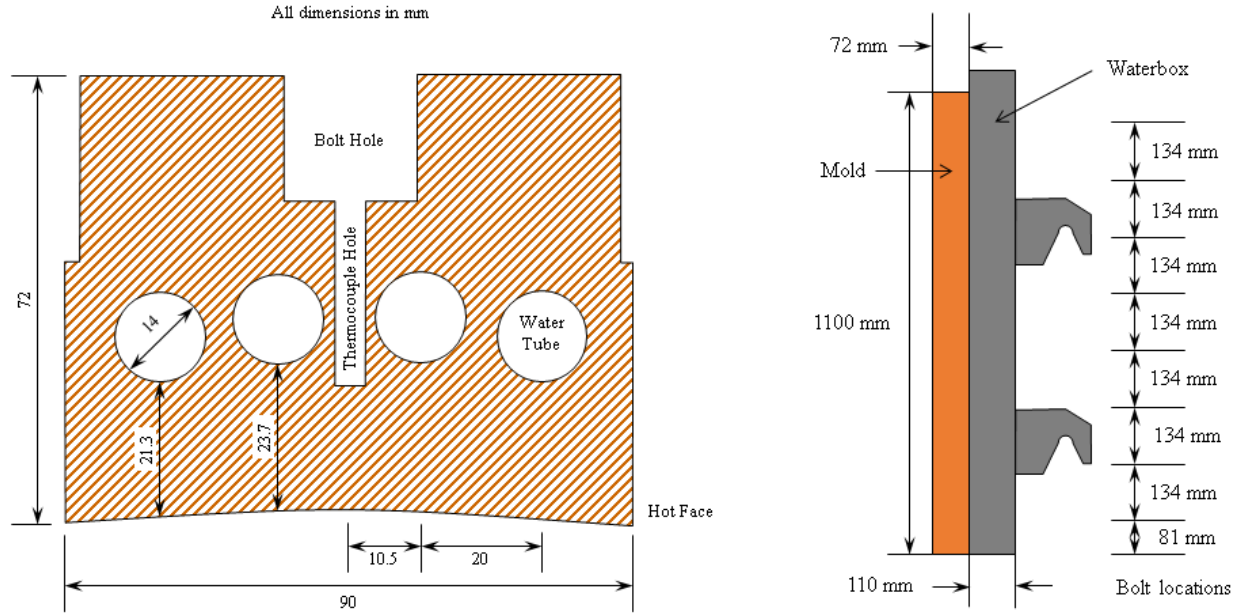
Figure A.4 Funnel mold NF mold and waterbox geometry

The finite-element mesh used in the funnel-mold simulations is shown in Figure A.5. As listed in Table A.1, this multi-part mesh consists of 1.36 million nodes and 5.15 million elements. The mold and waterbox were modeled with very good geometric accuracy, including the water channels and bolt holes. The mold bolts are approximated as truss elements, as discussed in Section 4.3. Further details are given in the body of this document.

Table A.1 Funnel mold simulation mesh details

Part	Nodes	Elements
Wide Face Mold Plate	855 235	4 223 072
Wide Face Waterbox	185 534	190 457
Wide Face Bolts	90	45
Tie Rods	4	2
Narrow Face Mold Plate	233 931	495 566
Narrow Face Waterbox	83 269	239 604
Narrow Face Bolts	16	8
Total	1 358 079	5 148 754
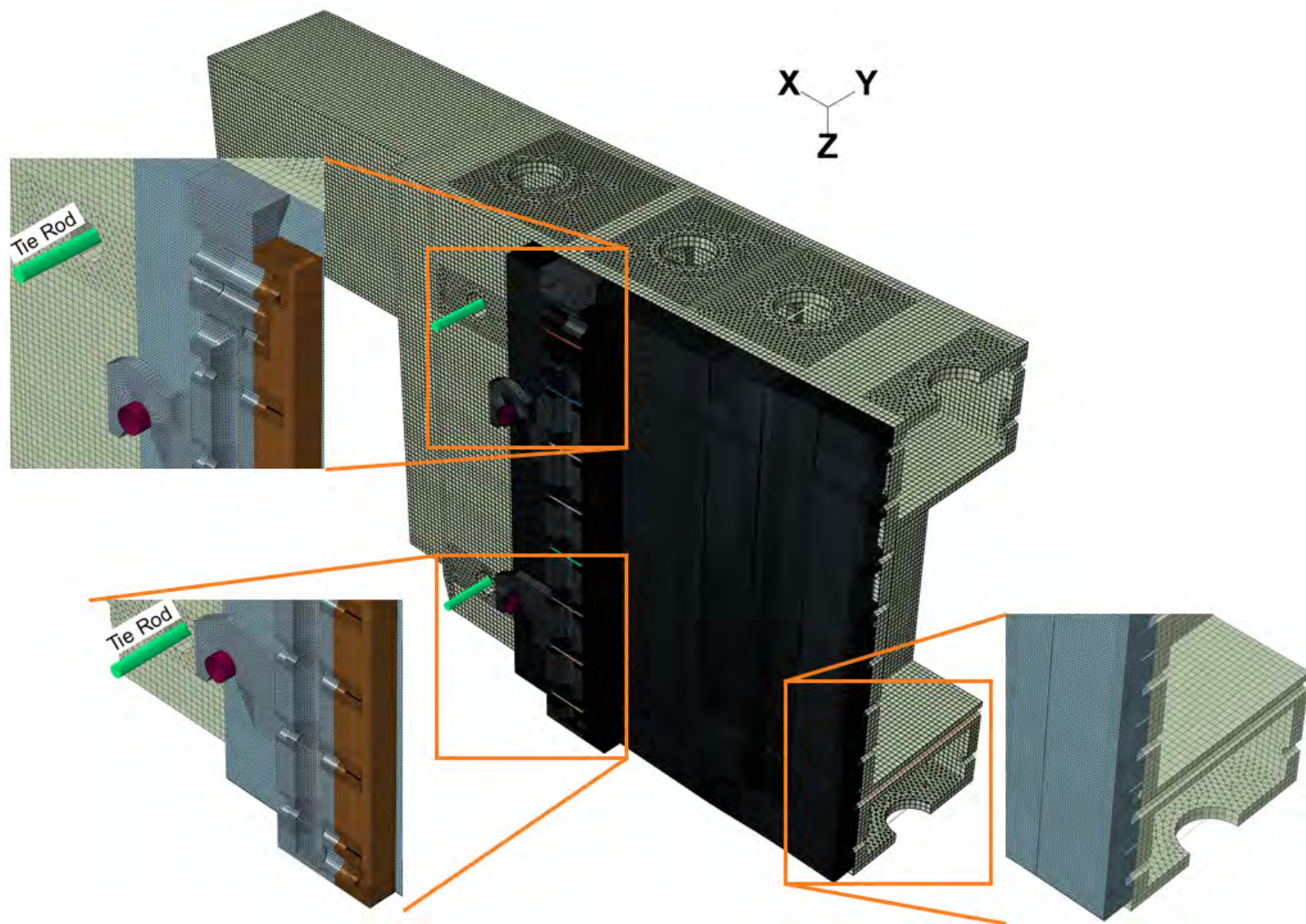
Figure A.5 Funnel mold and waterbox mesh

A.2   Beam-Blank Mold

The beam-blank mold and its waterbox considered in this work are shown in Figures A.6 through A.8. Two versions of the beam-blank mold geometry were considered: one with half-symmetry and one with quarter-symmetry, though the waterbox is not symmetrical. Other asymmetric effects, like variations in bolt tightening or mold alignment, are expected to be small. This mold has no coating layers.

The beam-blank profile shown in Figure A.6 is 576 mm wide, and has a 436 mm-wide flange and a 93 mm-thick web. The mold has various ball-end–milled water channels around the perimeter of the bottoms of the flanges, and several large cooling tubes around the web and tops of the flanges. The cooling tubes all have internal "restrictor rods" to increase the speed of the cooling water. A slice through the middle of the web is shown in Figure A.7, which identifies the mold thicknesses at various points down the length of the mold. Figure A.7 also shows the locations of several thermocouples that were instrumented in this mold for the model validation discussed in Section 2.3.

The quarter-symmetry finite-element mesh used in the beam-blank-mold simulations is shown in Figure A.8. This multi-part mesh consists of 264 thousand nodes and 1.08 million elements. The mold and waterbox were modeled with very good geometric accuracy, including the casting radius of the hot face, the water channels, and the bolt holes. The mold bolts are approximated as truss elements, as discussed in Section 4.3. Further details are given in the body of this document.
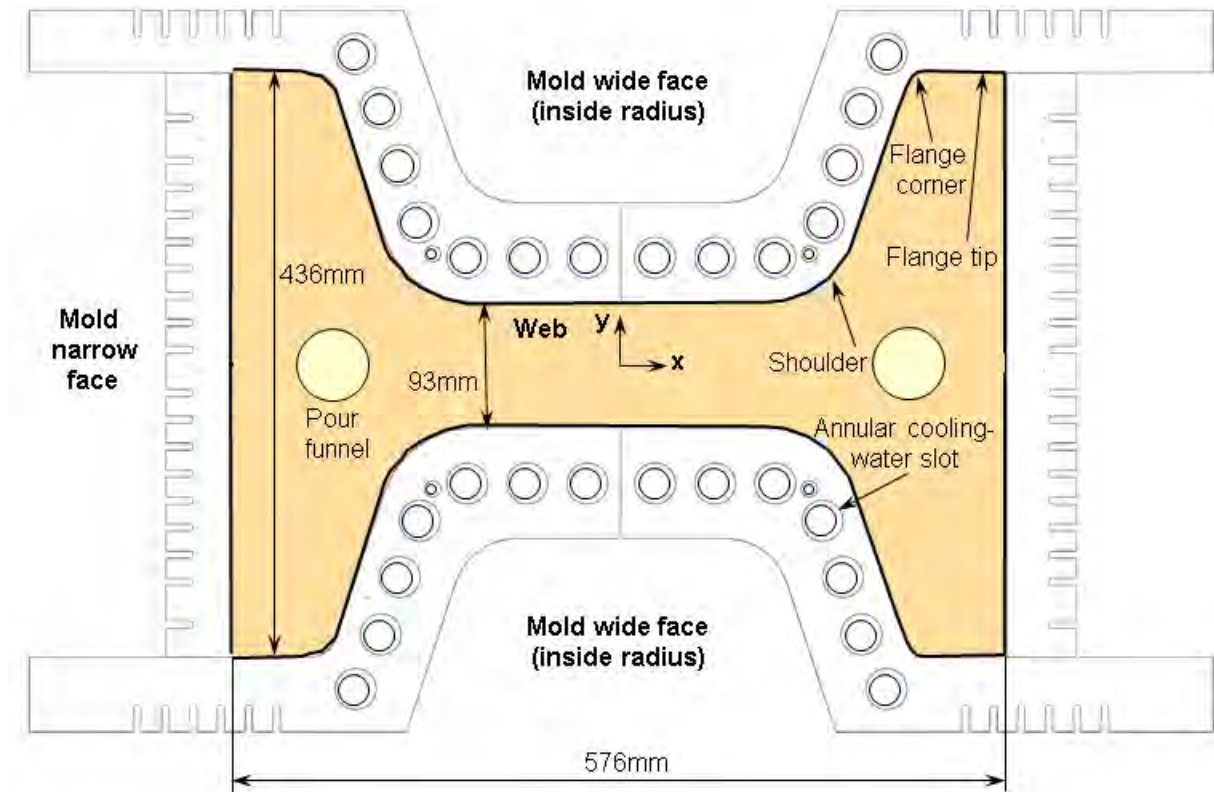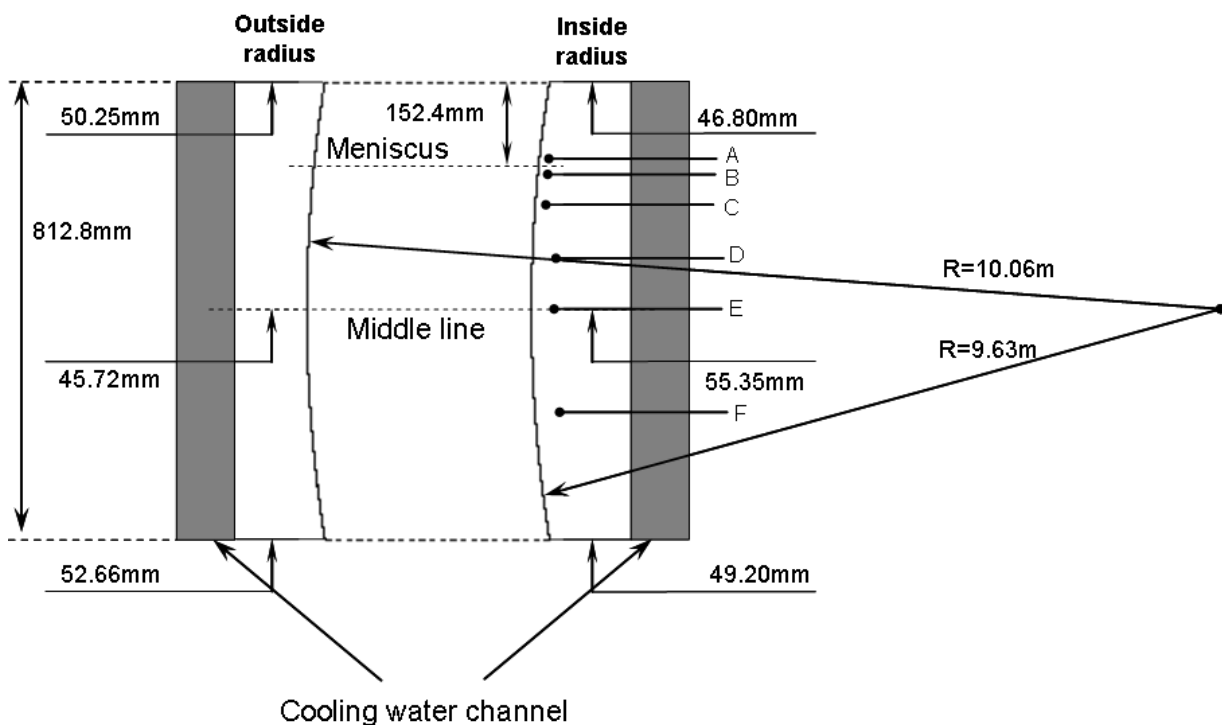
Figure A.6   Beam-blank mold geometry, top view

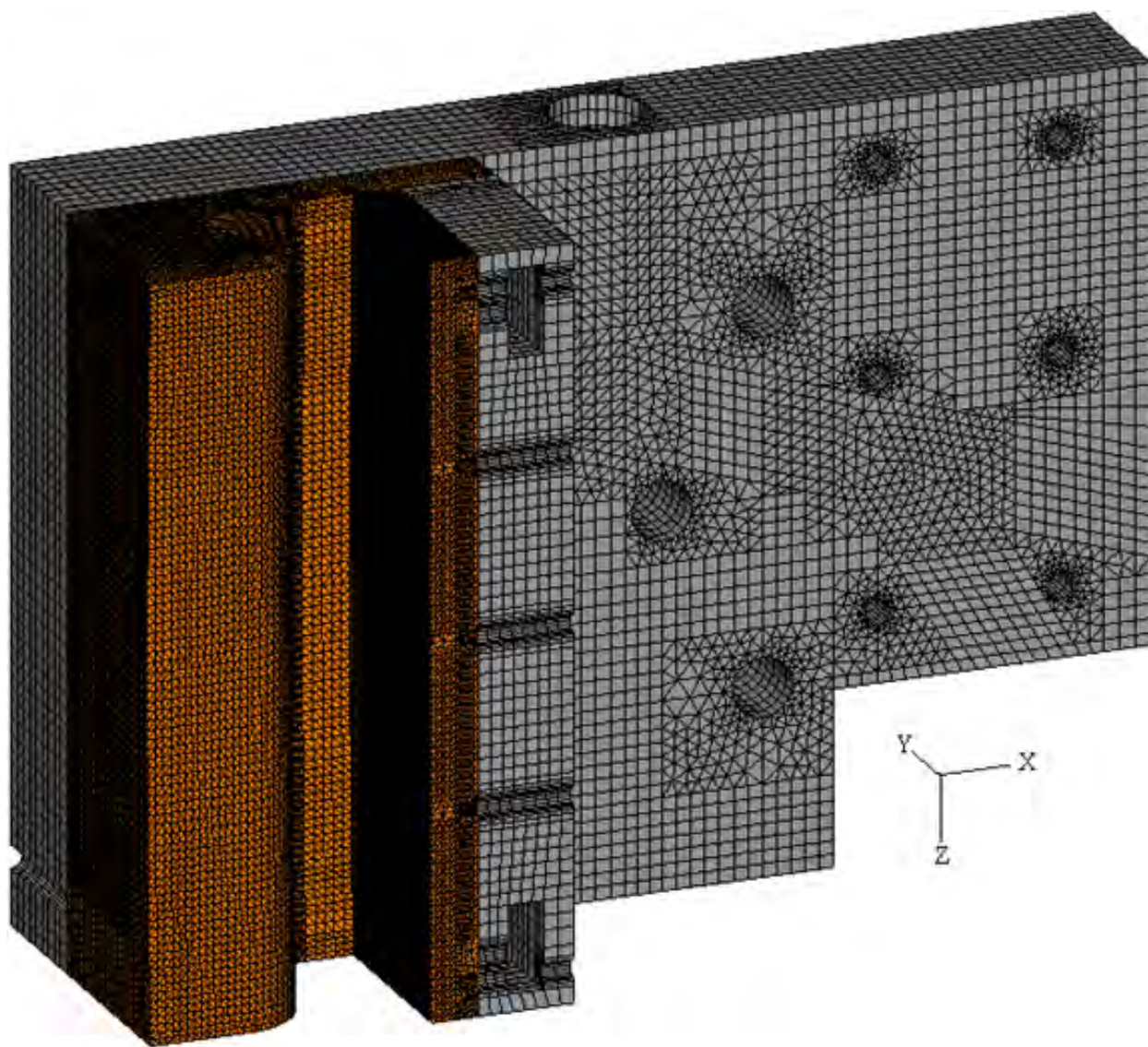**Figure A.7**   Beam-blank mold geometry, slice through WF centerline

Figure A.8   Beam-blank mold and waterbox mesh

APPENDIX B

The Eigenvalues and Eigenvectors of a 3×3 Matrix[1]

Eigenvalue problems permeate engineering and science, so the ability to calculate efficiently both the eigenvalues and eigenvectors of a matrix is important. Calculating the principal stresses and strains, and their principal directions, is an example of an eigen-problem related to the deformation analysis work in Chapter 5. Three-dimensional problems take a special place in this class of problems because of the nature of the physical world. This appendix presents a method to calculate efficiently and accurately the eigenvalues and eigenvectors of an arbitrary 3×3 real matrix. An explicit, algebraic expression for the eigenvectors is presented.

B.1   Introduction

Consider an arbitrary 3×3 matrix $\boldsymbol{A}$ with real-valued components A_{ij},

$$\begin{bmatrix} \boldsymbol{A} \end{bmatrix} = \begin{bmatrix} A_{11} & A_{12} & A_{13} \\ A_{21} & A_{22} & A_{23} \\ A_{31} & A_{32} & A_{33} \end{bmatrix}. \tag{B.1}$$

The statement of the (right) eigen-problem is to find the scalar-vector pair λ, $\boldsymbol{x}$ such that the action of the matrix $\boldsymbol{A}$ upon the vector $\boldsymbol{x}$ is the same as scaling the vector by λ, *i.e.*,

$$\boldsymbol{A}\boldsymbol{x} = \lambda\boldsymbol{x}, \tag{B.2}$$

and λ is called an eigenvalue and $\boldsymbol{x}$ is its associated eigenvector. Non-trivial solutions to Equation (B.2), *i.e.*, $\boldsymbol{x} \neq \boldsymbol{0}$, are found by requiring that

$$0 = \det(\boldsymbol{A} - \lambda\boldsymbol{I}), \tag{B.3}$$

where $\det(\cdot)$ is the matrix determinant operator and $\boldsymbol{I}$ is the identity matrix. Expanding Equation (B.3) provides the characteristic equation of the matrix,

$$0 = -\lambda^3 + I_1\lambda^2 - I_2\lambda + I_3, \tag{B.4}$$

---

[1]The content of this chapter was created entirely by the author, independent of other coauthors, including his advisor. This work will soon be submitted for publication.

where the principal invariants I_1, I_2, and I_3 are

$$I_1 = A_{11} + A_{22} + A_{33}, \tag{B.5a}$$

$$I_2 = A_{22}A_{33} + A_{33}A_{11} + A_{11}A_{22} - A_{23}A_{32} - A_{31}A_{13} - A_{12}A_{21}, \tag{B.5b}$$

$$I_3 = A_{11}A_{22}A_{33} + A_{23}A_{31}A_{12} + A_{32}A_{13}A_{21} - A_{11}A_{23}A_{32} - A_{22}A_{31}A_{13} - A_{33}A_{12}A_{21}. \tag{B.5c}$$

Re-casting the characteristic equation, Equation (B.4), in terms of the deviatoric principal invariants of $\boldsymbol{A}$ simplifies the problem at hand. The deviatoric part $\boldsymbol{A}'$ of the matrix $\boldsymbol{A}$ is

$$\boldsymbol{A}' = \boldsymbol{A} - p\boldsymbol{I}, \tag{B.6}$$

where, borrowing the language from the stress tensors, the quantity

$$p = \frac{1}{3}I_1 \tag{B.7}$$

is the "pressure." The principal invariants of $\boldsymbol{A}'$ are expressible in terms of the principal invariants of $\boldsymbol{A}$ as

$$J_1 = 0 \tag{B.8a}$$

$$J_2 = 3p^2 - I_2 \tag{B.8b}$$

$$J_3 = I_3 + p\left(2p^2 - I_2\right). \tag{B.8c}$$

A few arithmetical operations are saved,[2] however, by computing the deviatoric invariants directly from the components of the matrix $\boldsymbol{A}$, *i.e.*,

$$J_1 = 0, \tag{B.9a}$$

$$J_2 = \frac{1}{6}\left((A_{22} - A_{33})^2 + (A_{33} - A_{11})^2 + (A_{11} - A_{22})^2\right) \\ + A_{23}A_{32} + A_{31}A_{13} + A_{12}A_{21}, \tag{B.9b}$$

$$J_3 = (A_{11} - p)(A_{22} - p)(A_{33} - p) + A_{23}A_{31}A_{12} + A_{32}A_{13}A_{21} \\ - (A_{11} - p)A_{23}A_{32} - (A_{22} - p)A_{31}A_{13} - (A_{33} - p)A_{12}A_{21}. \tag{B.9c}$$

The substitution $\lambda = \ell + p$ into the characteristic equation of $\boldsymbol{A}$, Equation (B.4), gives

$$0 = -\ell^3 + J_2\ell + J_3, \tag{B.10}$$

---

[2] As a side note, J_2 can be computed with one less addition, multiplication and division than Equation (B.9b) using

$$J_2 = (A_{11} - p)^2 - (A_{22} - p)(A_{33} - p) + A_{23}A_{32} + A_{31}A_{13} + A_{12}A_{21},$$

or with cyclic permutations of the A_{11}, A_{22}, and A_{33} terms. However, these expressions are more prone to problems with round-off errors than Equation (B.9b), to the point where J_2 can be negative for symmetric matrices. Robustness should be favored over the small increase in execution speed.

i.e., the characteristic equation of $\boldsymbol{A}'$. Without the quadratic term, Equation (B.10) is in some sense easier to solve than Equation (B.4) for finding the eignevalues, as discussed in Section B.2.

B.2 Calculating the Eigenvalues

The characteristic equation of a 3×3 matrix is a cubic equation, whose solution dates back to the sixteenth-century Italian mathematicians DEL FERRO, TARTAGLIA, and CARDANO [12]. The closed-form algebraic solution for the eigenvalues λ provided by the cubic formula necessarily involves complex arithmetic, which is inconvenient when all eigenvalues are real. The eigenvalues of $\boldsymbol{A}$ are computed as

$$\lambda_1 = p + 2a \tag{B.11a}$$

$$\lambda_2 = p - a - j\sqrt{3}b \tag{B.11b}$$

$$\lambda_3 = p - a + j\sqrt{3}b, \tag{B.11c}$$

where

$$2a = c + d \tag{B.12a}$$

$$2b = c - d \tag{B.12b}$$

$$c^3 = K_3 + \sqrt{K_3^2 - K_2^3} \tag{B.12c}$$

$$d^3 = K_3 - \sqrt{K_3^2 - K_2^3} \tag{B.12d}$$

$$3K_2 = J_2 \tag{B.12e}$$

$$2K_3 = J_3, \tag{B.12f}$$

and $j = \sqrt{-1}$ is the imaginary unit. An alternative approach, due to VIÉTE [100], exploits the trigonometric identity

$$\cos(3\theta) = 4\cos^3(\theta) - 3\cos(\theta), \tag{B.13}$$

which, with the substitution $u = \cos(\theta)$, gives the cubic equation

$$0 = -u^3 + \frac{3}{4}u + \frac{1}{4}\cos(3\theta). \tag{B.14}$$

Now, let $u = m\ell$, so that Equation (B.14) is written as

$$0 = -\ell^3 + \frac{3}{4}\frac{1}{m^2}\ell + \frac{1}{4}\frac{1}{m^3}\cos(3\theta), \tag{B.15}$$

129

which is identical to the deviatoric characteristic equation, Equation (B.10), if $J_2 = 3/\left(4m^2\right)$ and $J_3 = \cos(3\theta)/\left(4m^3\right)$. Thus $1/m = 2\sqrt{K_2}$ and the angle θ is calculated by

$$\theta = \frac{1}{3}\arccos(k), \tag{B.16}$$

where $k = K_3/K_2^{3/2}$. The angle θ is known as the LODE angle in some mechanics applications, and is an invariant quantity. The roots of Equation (B.14) are $u = \cos(\theta)$, $u = \cos(\theta - 2\pi/3)$, and $u = \cos(\theta + 2\pi/3)$, which allows the eigenvalues of $\boldsymbol{A}$ to be determined as

$$\lambda_1 = p + 2\sqrt{K_2}\cos(\theta) \tag{B.17a}$$

$$\lambda_2 = p + 2\sqrt{K_2}\cos(\theta - 2\pi/3) \tag{B.17b}$$

$$\lambda_3 = p + 2\sqrt{K_2}\cos(\theta + 2\pi/3). \tag{B.17c}$$

SMITH [90] evidently introduced engineers to the trigonometric approach for the eigenvalues of a 3×3 matrix, but avoided discussing the numerical issues that arise in the approach.

Equation (B.16) identifies that $\boldsymbol{A}$ has real eigenvalues when $-1 \leq k \leq +1$, or $K_3^2 \leq K_2^3$. The case of $J_2 < 0$ is not considered here. Examining Equations (B.17) reveals that $\boldsymbol{A}$ has one distinct real eigenvalue $\lambda = p$ only when $K_2 = 0$, regardless of the behavior of k. The matrix $\boldsymbol{A}$ has two distinct real eigenvalues when $\theta = n\pi/3$ for any integer n, which is possible only when $k = +1$, or $\theta = 0$, and when $k = -1$, or $\theta = \pi/3$. The characteristic equation has a polynomial discriminant of zero when $k = \pm 1$, which corresponds to $K_2^3 = K_3^2$. Otherwise, the eigenvalues are real and distinct, or are real and a complex-conjugate pair[3].

If $K_2 \neq 0$, then Equation (B.17) gives the natural scaling for the eigenvalues as

$$\Lambda_i = \frac{\lambda_i - p}{2\sqrt{K_2}}, \tag{B.18}$$

where $i = 1, 2, 3$, and $-1 \leq \Lambda_i \leq +1$ when the eigenvalues are real. In terms of these scaled eigenvalues, the polynomial to solve is

$$0 = -4\Lambda^3 + 3\Lambda + k, \tag{B.19}$$

which is no easier to solve than the deviatoric characteristic equation, Equation (B.10), but it does have advantageous properties when moving to a computer, namely that for real eigenvalues the equation evaluates to values between -1 and $+1$. Indeed, introducing the scaled matrix

$$\boldsymbol{D} = \frac{1}{2\sqrt{K_2}}\boldsymbol{A}' \tag{B.20}$$

---

[3]The case of $J_2 < 0$ produces eigenvalues that are real and a complex-conjugate pair, but involves more complex arithmetic.

alleviates some of the numerical difficulties of the eigenvalue problem. Note that for the matrix $\boldsymbol{D}$, the invariants are $J_2 = \frac{3}{4}$ and $J_3 = \frac{1}{4}k$, where k is calculated for the matrix $\boldsymbol{A}$ as described above; calculating k from the scaled matrix is less subject to numerical cancellation errors.

Using the trigonometric identities $2\cos(x \pm 2\pi/3) = -\cos(x) \mp \sqrt{3}\sin(x)$, the eigenvalues are written[4] as

$$\Lambda_1 = \cos(\theta) \tag{B.21a}$$
$$2\Lambda_2 = -\cos(\theta) + \sqrt{3}\sin(\theta) \tag{B.21b}$$
$$2\Lambda_3 = -\cos(\theta) - \sqrt{3}\sin(\theta), \tag{B.21c}$$

which saves one evaluation of a trigonometric function. The arccosine function extended over the entire real line is

$$\arccos(x) = \begin{cases} \pi - j\operatorname{arcosh}(-x) & \text{if } x \leq -1 \\ \arccos(x) & \text{if } -1 \leq x \leq +1 \\ j\operatorname{arcosh}(x) & \text{if } +1 \leq x \end{cases} \tag{B.22}$$

and using the identities $\sin(x + jy) = \sin(x)\cosh(y) + j\cos(x)\sinh(y)$ and $\cos(x + jy) = \cos(x)\cosh(y) - j\sin(x)\sinh(y)$, for $k \leq -1$, the eigenvalues are

$$2\Lambda_1 = \cosh(\theta') - j\sqrt{3}\sinh(\theta') \tag{B.23a}$$
$$2\Lambda_2 = \cosh(\theta') + j\sqrt{3}\sinh(\theta') \tag{B.23b}$$
$$\Lambda_3 = -\cosh(\theta'), \tag{B.23c}$$

with $\theta' = -\frac{1}{3}\operatorname{arcosh}(-k)$, and for $-1 \leq k \leq +1$, the eigenvalues are

$$\Lambda_1 = \cos(\theta') \tag{B.24a}$$
$$2\Lambda_2 = -\cos(\theta') + \sqrt{3}\sin(\theta') \tag{B.24b}$$
$$2\Lambda_3 = -\cos(\theta') - \sqrt{3}\sin(\theta'), \tag{B.24c}$$

with $\theta' = \frac{1}{3}\arccos(k)$, and for $+1 \leq k$, the eigenvalues are

$$\Lambda_1 = \cosh(\theta') \tag{B.25a}$$
$$2\Lambda_2 = -\cosh(\theta') + j\sqrt{3}\sinh(\theta') \tag{B.25b}$$
$$2\Lambda_3 = -\cosh(\theta') - j\sqrt{3}\sinh(\theta'). \tag{B.25c}$$

with $\theta' = \frac{1}{3}\operatorname{arcosh}(k)$. Figure B.1 shows a plot of Equations (B.23), (B.24), and (B.25). Note that Figure B.1 reveals that $\lambda_1 \geq \lambda_2 \geq \lambda_3$ always holds, so no effort need be expended on sorting the computed eigenvalues.

---

[4]Equation (B.21) shows that evidently, $a = \sqrt{K_2}\cos(\theta)$ and $b = j\sqrt{K_2}\sin(\theta)$ in the cubic formula, Equation (B.11).
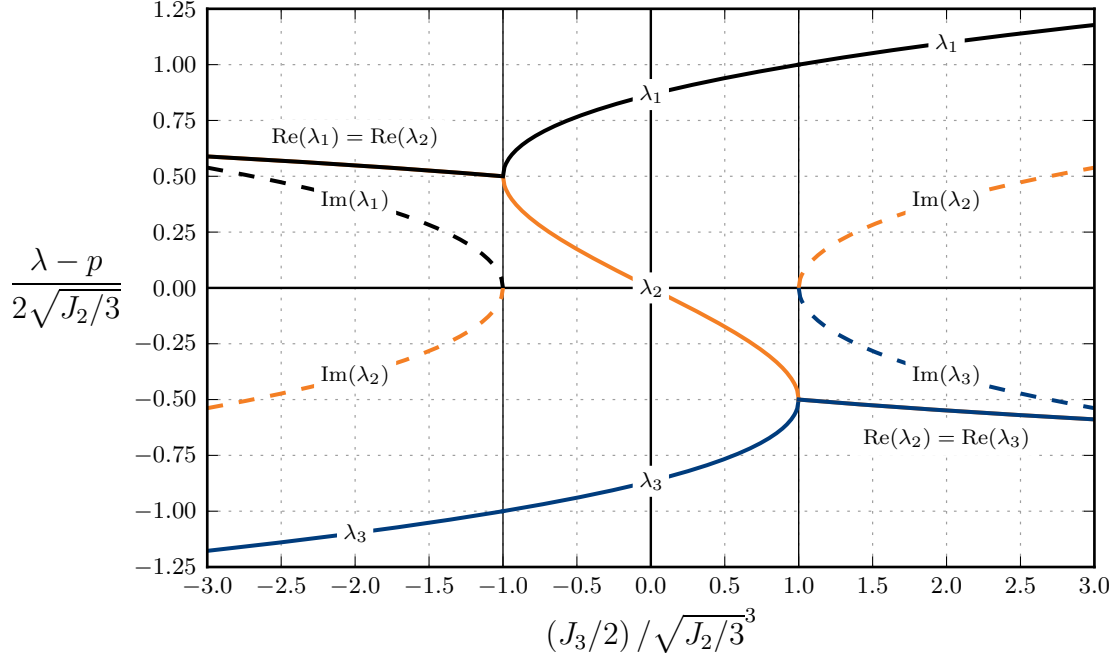
Figure B.1 The eigenvalues of a 3×3 matrix

Sufficiently far away from the cases of repeated eigenvalues, *i.e*, $k = \pm 1$, Equations (B.23), (B.24), and (B.25) are adequate for use in computer implementation [90]. However, algorithms should be designed around the difficult ranges of input. Consider now the case of all real eigenvalues; as pointed out by SIMO and HUGHES [88, p. 244], the arccosine function is ill-conditioned near the cases of repeated eigenvalues, and exploiting the trigonometric identity

$$\arccos(x) = \begin{cases} \arctan\left(\sqrt{\frac{1}{x^2} - 1}\right) & \text{if } x > 0 \\ \frac{\pi}{2} & \text{if } x = 0 \\ \pi - \arctan\left(\sqrt{\frac{1}{x^2} - 1}\right) & \text{if } x < 0 \end{cases} \tag{B.26}$$

somewhat helps to alleviate the issue. SCHERZINGER and DOHRMANN [85] demonstrated that as $|k| \to 1$, the eigenvalues computed from the trigonometric functions are accurate to about $\sqrt{\epsilon_{\text{mach}}}$, where ϵ_{mach} is machine epsilon. SCHERZINGER and DOHRMANN [85] then proposed a method to find the eigenvalues and eigenvectors at the same time, which first finds the "most distinct" eigenvalue, *i.e.*, λ_1 if $k > 0$ and λ_3 if $k < 0$, transforms the matrix to a basis where the eigenvector corresponding to the "most distinct" eigenvalue is one of the basis vectors, and then solves accurately the quadratic equation for the other eigenvalues in the transformed basis. Their method demonstrates accuracy on the order of machine precision, but at the cost of larger execution time than other non-iterative methods for solving the eigenproblem.

132

As far as the author has been able to determine, the accuracy of the SCHERZINGER and DOHRMANN [85] approach is paralleled only by well-conditioned iterative algorithms,[5] though these come at the cost of algorithmic overhead. The best alternative that the author could produce is documented below.

Consider solving the scaled characteristic equation, Equation (B.19), using NEWTON iterations. Initial iteration values are found by first expanding Equation (B.19) about Λ_0 to second order,

$$- \left(12\Lambda_0\right)\Lambda^2 + \left(12\Lambda_0^2 + 3\right)\Lambda + \left(-4\Lambda_0^3 + k\right) = 0, \tag{B.27}$$

and then taking Λ_0 as -1, $-1/2$, 0, $+1/2$, and $+1$, to create several approximations of the cubic equation,

$$0 = -12\Lambda^2 - 15\Lambda - 4 - k \tag{B.28a}$$

$$0 = -6\Lambda^2 - 6\Lambda - 1/2 - k \tag{B.28b}$$

$$0 = -3\Lambda - k \tag{B.28c}$$

$$0 = 6\Lambda^2 - 6\Lambda + 1/2 - k \tag{B.28d}$$

$$0 = 12\Lambda^2 - 15\Lambda + 4 - k. \tag{B.28e}$$

The approximations are used in their appropriate ranges, broken around values of k that give good approximations to the original cubic, as shown in Figure B.2, to provide initial iteration values for the scaled eigenvalues,

$$^{0}\Lambda_1 = \begin{cases} \frac{1}{2}\left(1 + \sqrt{\frac{2}{3}\left(1+k\right)}\right) & \text{if } k < -1/2 \\ \frac{5}{8}\left(1 + \sqrt{\frac{16}{75}\left(1+k\right) - \frac{1}{15}}\right) & \text{if } -1/2 \le k \end{cases} \tag{B.29a}$$

$$^{0}\Lambda_2 = \begin{cases} \frac{1}{2}\left(1 - \sqrt{\frac{2}{3}\left(1+k\right)}\right) & \text{if } k < -2/3 \\ -k/3 & \text{if } -2/3 \le k \le +2/3 \\ -\frac{1}{2}\left(1 - \sqrt{\frac{2}{3}\left(1-k\right)}\right) & \text{if } +2/3 < k \end{cases} \tag{B.29b}$$

$$^{0}\Lambda_3 = \begin{cases} -\frac{5}{8}\left(1 + \sqrt{\frac{16}{75}\left(1-k\right) - \frac{1}{15}}\right) & \text{if } k \le +1/2 \\ -\frac{1}{2}\left(1 + \sqrt{\frac{2}{3}\left(1-k\right)}\right) & \text{if } +1/2 < k \end{cases}. \tag{B.29c}$$

Equations (B.29) are written to avoid the usual cancellation problem with the quadratic formula, but still suffer from cancellation under the radical. This cancellation under the radical is the limit to high accuracy in this approach.

The NEWTON method update is

$$^{i+1}\Lambda = {}^{i}\Lambda + \delta\Lambda, \tag{B.30}$$

---

[5]For example, DSYEV in the LAPACK library.
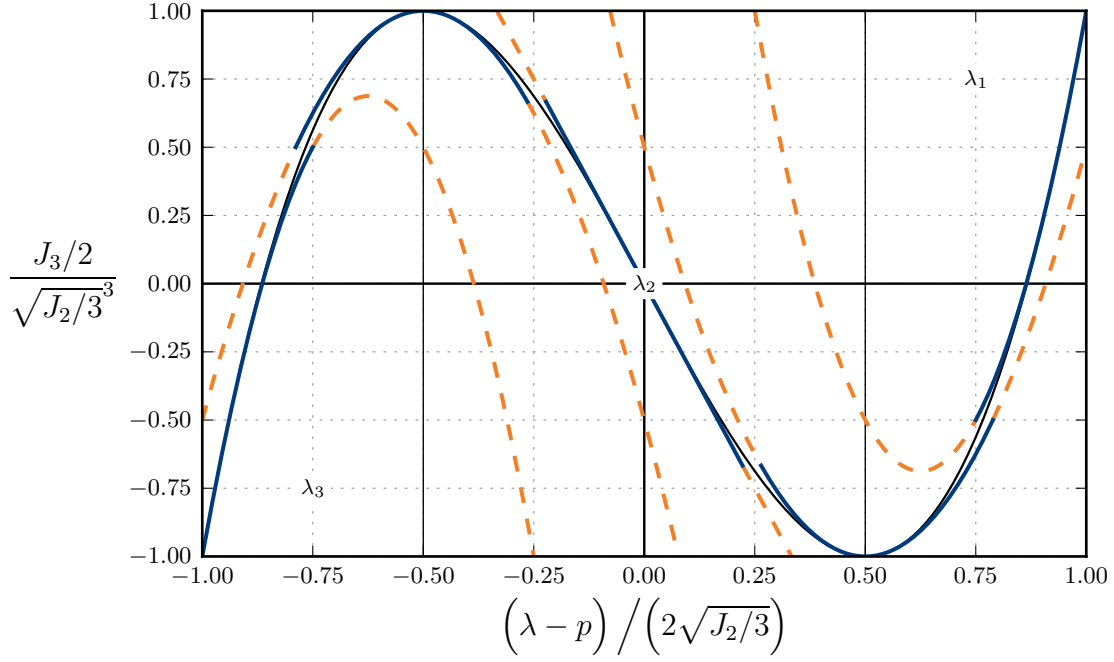
Figure B.2 Second-order approximations of the scaled cubic equation

where the standard correction is

$$\delta\Lambda = -\frac{f(^i\Lambda)}{f'(^i\Lambda)}. \tag{B.31}$$

The function f, the scaled cubic equation, admits the factorization

$$f(\Lambda) = -(2\Lambda + 1)^2 (\Lambda - 1) - (1 - k) \tag{B.32}$$

for use when $k > 0$, and the factorization

$$f(\Lambda) = -(2\Lambda - 1)^2 (\Lambda + 1) + (1 + k) \tag{B.33}$$

for use when $k < 0$, to help control cancellation and round-off errors. The derivative of the function is

$$f'(\Lambda) = -3(2\Lambda - 1)(2\Lambda + 1). \tag{B.34}$$

The correction is decomposed into partial fractions as

$$\delta\Lambda = -\frac{1}{6}\left(\left(2\Lambda - \frac{k+1}{2\Lambda - 1}\right) + \frac{k-1}{2\Lambda + 1}\right) \tag{B.35}$$

if $k > 0$, and as

$$\delta\Lambda = -\frac{1}{6}\left(\left(2\Lambda + \frac{k-1}{2\Lambda + 1}\right) - \frac{k+1}{2\Lambda - 1}\right) \tag{B.36}$$

if $k < 0$, coded exactly as parenthesized, to help control cancellation and round-off errors.

134

The NEWTON method for this problem, given initial values from Equations (B.29), converges to better than $3\epsilon_{\text{mach}}$ in five or less iterations away from the region of two distinct eigenvalues. Curiously, this approach maintains accuracy of about $3\epsilon_{\text{mach}}$ for three nearly repeated eigenvalues. For matrices with nearly two distinct eigenvalues, the accuracy is no better than $\sqrt{\epsilon_{\text{mach}}}$. The following techniques were explored:

1. NEWTON iterations, as described above,
2. deflating the cubic polynomial to a quadratic polynomial and solving analytically,
3. deflating the cubic polynomial to a quadratic polynomial and solving the eigenvalue problem for the companion matrix,
4. NEWTON iterations for multiple roots $(\delta\Lambda = ff'/\left((f')^2 - ff''\right))$, for both the cubic and the quadratic equations
5. MAEHLY–NEWTON iterations,
6. using KAHAN summation with the NEWTON iterations, for both the cubic and the quadratic equations.

B.3 Calculating the Eigenvectors

The eigenvector $\boldsymbol{x}$ associated with the eigenvalue λ is found by solving the equations

$$A_{11}x_1 + A_{12}x_2 + A_{13}x_3 = \lambda x_1 \tag{B.37a}$$

$$A_{21}x_1 + A_{22}x_2 + A_{23}x_3 = \lambda x_2 \tag{B.37b}$$

$$A_{31}x_1 + A_{32}x_2 + A_{33}x_3 = \lambda x_3. \tag{B.37c}$$

However, explicitly trying to solve this system of equations yields only the zero vector. The issue is that the system of equations is homogeneous, which allows as a solution either the zero vector or an arbitrary scaling of some particular vector, *i.e.*, the eigenvector. Since the vector has some amount of arbitrariness, take x_1 as unity and then solve for x_2 and x_3 as

$$x_2 = \frac{-\left((A_{33} - \lambda)A_{21} - A_{23}A_{31}\right)}{(A_{33} - \lambda)(A_{22} - \lambda) - A_{23}A_{32}} \tag{B.38a}$$

$$x_2 = \frac{-\left((A_{33} - \lambda)A_{31} - A_{32}A_{21}\right)}{(A_{33} - \lambda)(A_{22} - \lambda) - A_{23}A_{32}}. \tag{B.38b}$$

The denominator of x_2 and x_3 are the same, and since the eigenvector has arbitrary magnitude anyway, scale it by this denominator to give

$$x_1 = (A_{33} - \lambda)(A_{22} - \lambda) - A_{23}A_{32} \tag{B.39a}$$

$$x_2 = -((A_{33} - \lambda)A_{21} - A_{23}A_{31}) \tag{B.39b}$$

$$x_3 = -((A_{22} - \lambda)A_{31} - A_{32}A_{21}), \tag{B.39c}$$

which gives an explicit expression for the eigenvector. Equation (B.39) was known as early as 1829 by CAUCHY [14, Eqs. 44 and 45] for a symmetric matrix, but this simple result seems to have been largely forgotten, likely because matrix theory was then in its infancy.

In practice, Equation (B.39) is not robust. Consider a diagonal matrix with two distinct eigenvalues; Equation (B.39) gives the zero vector for two of the three eigenvalues. Nine eigenvectors are found using this approach: each of the three components set to unity have three pairs of equations to use to find the other two components. The nine vectors produced by this method all have the same direction vector, and after scaling by the denominators, only three are algebraically distinct. These three vectors are Equation (B.39),

$$x_1 = -((A_{33} - \lambda)A_{12} - A_{13}A_{32}) \tag{B.40a}$$

$$x_2 = (A_{33} - \lambda)(A_{11} - \lambda) - A_{31}A_{13} \tag{B.40b}$$

$$x_3 = -((A_{11} - \lambda)A_{32} - A_{31}A_{12}), \tag{B.40c}$$

and

$$x_1 = -((A_{22} - \lambda)A_{13} - A_{12}A_{23}) \tag{B.41a}$$

$$x_2 = -((A_{11} - \lambda)A_{23} - A_{21}A_{13}) \tag{B.41b}$$

$$x_3 = (A_{22} - \lambda)(A_{11} - \lambda) - A_{12}A_{21}, \tag{B.41c}$$

all of which are identical up to a multiplicative constant. The robust expression is created by adding together Equations (B.39), (B.40), and (B.41), again, since these all have the same direction but arbitrary magnitude, giving

$$\begin{aligned} x_1 = &\lambda(\lambda - I_1) + \lambda(A_{11} + A_{12} + A_{13}) \\ &+ (A_{22}A_{33} - A_{32}A_{23}) + (A_{32}A_{13} - A_{12}A_{33}) + (A_{12}A_{23} - A_{22}A_{13}) \end{aligned} \tag{B.42a}$$

$$\begin{aligned} x_2 = &\lambda(\lambda - I_1) + \lambda(A_{21} + A_{22} + A_{33}) \\ &+ (A_{23}A_{31} - A_{33}A_{21}) + (A_{33}A_{11} - A_{31}A_{13}) + (A_{13}A_{21} - A_{23}A_{11}) \end{aligned} \tag{B.42b}$$

$$\begin{aligned} x_3 = &\lambda(\lambda - I_1) + \lambda(A_{31} + A_{32} + A_{33}) \\ &+ (A_{21}A_{32} - A_{31}A_{22}) + (A_{31}A_{12} - A_{11}A_{32}) + (A_{11}A_{22} - A_{12}A_{21}) \end{aligned} \tag{B.42c}$$

The components of the eigenvectors given in Equations (B.39), (B.40), and (B.41) are the determinants of the nine possible minors of the matrix $\boldsymbol{A} - \lambda \boldsymbol{I}$. Also, evidently, Equation (B.42) is

$$\boldsymbol{x} = \left(\lambda \left(\lambda - I_1 \right) \boldsymbol{I} + \lambda \boldsymbol{A} + I_3 \boldsymbol{A}^{-1} \right) \begin{Bmatrix} 1 \\ 1 \\ 1 \end{Bmatrix} . \tag{B.43}$$

Note that the inverse of $\boldsymbol{A}$ is not calculated explicitly; $I_3 \boldsymbol{A}^{-1}$ is the transpose of the adjugate matrix of $\boldsymbol{A}$. The CAYLEY–HAMILTON theorem is used to rewrite the coefficient in Equation (B.43) as $\left(\lambda \left(\lambda - I_1 \right) + I_2 \right) \boldsymbol{I} + \left(\lambda - I_1 \right) \boldsymbol{A} + \boldsymbol{A}^2$, which then allows use of the characteristic equation to rewrite the coefficient as $\left(I_3 / \lambda \right) \boldsymbol{I} + \left(\lambda - I_1 \right) \boldsymbol{A} + \boldsymbol{A}^2$. Since $I_1 = \lambda_1 + \lambda_2 + \lambda_3$ and $I_3 = \lambda_1 \lambda_2 \lambda_3$, the eigenvector associated with λ_1 is

$$\boldsymbol{x}_1 = \boldsymbol{C}_1 \begin{Bmatrix} 1 \\ 1 \\ 1 \end{Bmatrix} , \tag{B.44}$$

where

$$\boldsymbol{C}_1 = \lambda_2 \lambda_3 \boldsymbol{I} - \left(\lambda_2 + \lambda_3 \right) \boldsymbol{A} + \boldsymbol{A}^2 \tag{B.45}$$

and appropriately permuted for the other two eigenvectors. Equation (B.44) involves fewer arithmetic operations than does Equation (B.43).

References

[1] *ABAQUS 6.11 User Manuals.* Dassault Simulia, 2011.

[2] D. Amsallem, M. J. Zahr, and C. Farhat. Nonlinear model order reduction based on local reduced-order bases. *International Journal for Numerical Methods in Engineering*, 92(10):891–916, 2012.

[3] ANSYS Inc., Canonsburg, PA. *ANSYS FLUENT 14 Theory Guide*, 2011.

[4] R. J. Asaro and V. A. Lubarda. *Mechanics of Solids and Materials.* Cambridge University Press, 2006.

[5] C. Bailey, P. Chow, M. Cross, Y. Fryer, and K. Pericleous. Multiphysics modelling of the metals casting process. *Proceedings of the Royal Society of London A*, 452:459–486, 1996.

[6] J. Barbič and D. L. James. Real-time subspace integration for St. Venant–Kirchhoff deformable models. *ACM Transactions on Graphics*, 24(3):982–990, 2005.

[7] H. G. Baumann and G. Schäfer. Beitrag zur Berechnung der Kontraktion von Stahl während seiner Erstarrung. *Archiv für das Eisenhüttenwesen*, 41(12):1111–1115, 1970.

[8] S. R. Bodner and Y. Partom. A large deformation elastic-viscoplastic analysis of a thick-walled spherical shell. *Journal of Applied Mechanics*, 39(3):751–757, 1972.

[9] S. R. Bodner and Y. Partom. Constitutive equations for elastic-viscoplastic strain-hardening materials. *Journal of Applied Mechanics*, 42(2):385–389, 1975.

[10] J. Burkardt, M. Gunzburger, and H.-C. Lee. POD and CVT-based reduced-order modeling of Navier–Stokes flows. *Computer Methods in Applied Mechanics and Engineering*, 196(1-3):337–355, 2006.

[11] J. E. Camporredondo, A. H. Castillejos, F. A. Acosta, E. P. Gutiérrez, and M. A. Herrera. Analysis of thin-slab casting by the compact-strip process: Part I. heat extraction and solidification. *Metallurgical and Materials Transactions B*, 35(3):541–560, 2004.

[12] H. Cardano. *Artis Magnæ, Sive de Regulis Algebraicis Liber Unus.* 1545.

[13] G. Carlsson, B. Brolund, and R. Nystrom. Measurement of mould distortion and mould heat flux in industrial casters. *Journées Sidérurgiques ATS*, 10, 1989.

[14] A.-L. Cauchy. Sur l'équation à l'aide de laquelle on détermine les inégalités séculaires des mouvements des planètes. In *Exercices de mathématiques*, volume 4, pages 140–160. De Bure frères, Paris, 1829. Reprinted in *Œuvres Série* 2, vol. 9, pages 174–195.

[15] D. Celentano, S. Oller, and E. Oñate. A coupled thermomechanical model for the solidification of cast metals. *International Journal of Solids and Structures*, 33:647–673, 1996.

[16] P. Chadwick. *Continuum Mechanics: Concise Theory and Problems.* George Allen & Unwin Ltd., London, 1976.

[17] A. Chatterjee and V. Prasad. A full 3-dimenisonal adaptive finite volume scheme for transport and phase-change processes, part I: Formulation and validation. *Numerical Heat Transfer A*, 37:801–821, 2000.

[18] R. Chen, H. F. Shen, and B. C. Liu. Numerical simulation of fluid flow and solidification in continuous slab casting mould based on inverse heat transfer calculation. *Ironmaking and Steelmaking*, 38(7):546–551, 2011.

[19] C. Chow, I. V. Samarasekera, B. N. Walker, and G. Lockhart. High speed continuous casting of steel billets: Part 2: Mould heat transfer and mould design. *Ironmaking and Steelmaking*, 29(1):61–69, 2002.

[20] J. A. Dantzig and M. Rappaz. *Solidification.* Ecole Polytechnique Fédérale de Lausanne Press, 2009.

[21] J. A. Dantzig and C. L. Tucker. *Modeling in Materials Processing.* Cambridge University Press, 2001.

[22] V. K. de Barcellos, C. R. F. Ferreira, C. A. dos Santos, and J. A. Spim. Analysis of metal mould heat transfer coefficients during continuous casting of steel. *Ironmaking and Steelmaking*, 37(1):47–56, 2010.

[23] C. del Borello and E. Lacoste. Numerical simulation of the liquid flow into a porous medium with phase change: Application to metal composites processing. *Numerical Heat Transfer A*, 44:723–741, 2003.

[24] P. Feldmann and R. W. Freund. Efficient linear circuit analysis by Padé approximation via the Lanczos process. *IEEE Transactions on Computer-Aided Design of Integrated Circuits and Systems*, 14(5):639–649, 1995.

[25] C. A. Felippa and K. C. Park. Staggered transient analysis procedures for coupled mechanical systems: Formulation. *Computer Methods in Applied Mechanics and Engineering*, 24:61–111, 1980.

[26] A. Grill, K. Sorimachi, and J. K. Brimacombe. Heat flow, gap formation and break-outs in the continuous casting of steel slabs. *Metallurgical Transactions B*, 7(2):177–189, 1976.

[27] H. N. Han, J.-E. Lee, T.-J. Yeo, Y. M. Won, K.-H. Kim, K. H. Oh, and J.-K. Yoon. A finite element model for 2-dimensional slice of cast strand. *ISIJ International*, 39(5):445–454, 1999.

[28] K. Harste. *Investigation of the Shrinkage and the Origin of Mechanical Tension during the Solidification and Successive Cooling of Cylindrical Bars of Fe-C Alloys*. PhD thesis, Technical University of Clausthal, 1989.

[29] M. Heinlein, S. Mukherjee, and O. Richmond. A boundary element method analysis of temperature fields and stresses during solidification. *Acta Mechanica*, 59(1–2):59–81, 1986.

[30] L. C. Hibbeler. Thermo-mechanical behavior during steel continuous casting in funnel molds. Master's thesis, The University of Illinois at Urbana–Champaign, 2009.

[31] L. C. Hibbeler, M. M. Langeneckert, J. Iwasaki, I. Hwang, B. G. Thomas, and R. J. O'Malley. Calibration of thermal models of steel continuous casting molds. *Iron and Steel Technology*, 10(9):199–210, 2013.

[32] L. C. Hibbeler, B. G. Thomas, B. Santillana, A. Hamoen, and A. Kamperman. Longitudinal face crack prediction with thermo-mechanical models of thin slabs in funnel moulds. *La Metallurgia Italiana*, (2):1–10, 2009.

[33] L. C. Hibbeler, B. G. Thomas, R. C. Schimmel, and G. Abbel. The thermal distortion of a funnel mold. *Metallurgical and Materials Transactions B*, 43(5):1156–1172, 2012.

[34] L. C. Hibbeler, B. G. Thomas, R. C. Schimmel, and H. H. Visser. Simulation and online measurement of narrow face mold distortion in thin slab casting. In *Proceedings of the 8th European Continuous Casting*, 2014.

[35] L. C. Hibbeler, K. Xu, B. G. Thomas, S. Koric, and C. Spangler. Thermomechanical modeling of beam blank casting. *Iron and Steel Technology*, 6(7):60–73, 2009.

[36] W. F. Hosford. *Mechanical Behavior of Materials*. Cambridge University Press, 2005.

[37] Revised release on the IAPWS industrial formulation 1997 for the thermodynamic properties of water and steam. Technical report, The International Association for the Properties of Water and Steam, 2007.

[38] J. E. Kelly, K. P. Michalek, T. G. OConnor, B. G. Thomas, and J. A. Dantzig. Initial development of thermal and stress fields in continuously cast steel billets. *Metallurgical Transactions A*, 19(10):2589–2602, 1988.

[39] S. Koric, L. C. Hibbeler, R. Liu, and B. G. Thomas. Multiphysics model of metal solidification on the continuum level. *Numerical Heat Transfer B*, 58(6):371–392, 2010.

[40] S. Koric, L. C. Hibbeler, and B. G. Thomas. Explicit coupled thermo-mechanical finite element model of steel solidification. *International Journal of Numerical Methods in Engineering*, 78:1–31, 2009.

[41] S. Koric and B. G. Thomas nad V. R. Voller. Enhanced latent heat method to incorporate superheat effects into fixed-grid multiphysics simulations. *Numerical Heat Transfer B*, 57:396–413, 2010.

[42] S. Koric and B. G. Thomas. Efficient thermo-mechanical model for solidification processes. *International Journal for Numerical Methods in Engineering*, 66:1955–1989, 2006.

[43] P. F. Kozlowski, B. G. Thomas, J. A. Azzi, and H. Wang. Simple constitutive equations for steel at high temperature. *Metallurgical and Materials Transactions A*, 23:903–918, 1992.

[44] J. O. Kristiansson. Thermal stresses in the early stage of solidification of steel. *Journal of Thermal Stresses*, 5(3–4):315–330, 1982.

[45] J. O. Kristiansson. Thermomechanical behavior of the solidifying shell within continuous casting billet molds- a numerical approach. *Journal of Thermal Stresses*, 7:209–226, 1984.

[46] E. Kröner. Allgemeine Kontinuumstheorie der Versetzungen und Eigenspannungen. *Archive for Rational Mechanics and Analysis*, 4(1):273–334, 1959.

[47] M. M. Langeneckert. Influence of mold geometry on heat transfer, thermocouple and mold temperatures in the continuous casting of steel slabs. Master's thesis, The University of Illinois at Urbana–Champaign, 2001.

[48] B. E. Launder and D. B. Spalding. The numerical computation of turbulent flows. *Computer Methods in Applied Mechanics and Engineering*, 3:269–289, 1974.

[49] E. H. Lee. Elastic-plastic deformation at finite strain. *Journal of Applied Mechanics*, 36(1):1–6, 1969.

[50] J.-E. Lee, H. N. Han, K. H. Oh, and J.-K. Yoon. A fully coupled analysis of fluid flow, heat transfer and stress in continuous round billet casting. *ISIJ International*, 39(5):435–444, 1999.

[51] J.-E. Lee, T.-J. Yeo, K. H. Oh, J.-K. Yoon, and U.-S. Yoon. Prediction of cracks in continuously cast steel beam blank through fully coupled analysis of fluid flow, heat transfer, and deformation behavior of a solidifying shell. *Metallurgical and Materials Transactions A*, 31(1):225–237, 2000.

[52] C. Li and B. G. Thomas. Thermomechanical finite-element model of shell behavior in continuous casting of steel. *Metallurgical and Materials Transactions B*, 35(6):1151–1172, 2004.

[53] X. Liu and M. Zhu. Finite element analysis of thermal and mechanical behavior in a slab continuous casting mold. *ISIJ International*, 46(11):1652–1659, 2006.

[54] R. B. Mahapatra, J. K. Brimacombe, I. V. Samarasekera, N. Walker, E. A. Paterson, and J. D. Young. Mold behavior and its influence on quality in the continuous casting of steel slabs: Part I. Industrial trials, mold temperature measurements, and mathematical modeling. *Metallurgical Transactions B*, 22(6):861–874, 1991.

[55] X. Meng and M. Zhu. Thermal behavior of hot copper plates for slab continuous casting mold with high casting speed. *ISIJ International*, 49(9):1356–1361, 2009.

[56] Y. Meng and B. G. Thomas. Heat-transfer and solidification model of continuous slab casting: CON1D. *Metallurgical and Materials Transactions B*, 34(5):685–705, 2003.

[57] Y. Meng and B. G. Thomas. Modeling transient slag-layer phenomena in the shell/mold gap in continuous casting of steel. *Metallurgical and Materials Transactions B*, 34(5):707–725, 2003.

[58] Y. Meng and B. G. Thomas. Simulation of microstructure and behavior of interfacial mold slag layers in continuous casting of steel. *ISIJ International*, 46(5):660–669, 2006.

[59] E. A. Mizikar. Mathematical heat transfer model for solidification of continuously cast steel slabs. *Transactions of the Metallurgical Society of AIME*, 239:1747–1753, 1967.

[60] H. Mizukami, K. Murakami, and Y. Miyashita. Elastic modulus of steels at high temperature. *Journal of the Iron and Steel Institute of Japan*, 63(146):S–652, 1977.

[61] A. N. O. Moraga, D. C. Ramirez, M. J. Godoy, and P. D. Ticchione. Study of convection non-newtonian alloy solidification in moulds by the PSIMPLER/finite-volume method. *Numerical Heat Transfer B*, 57:936–953, 2010.

[62] H. Nam, H.-S. Park, and J. K. Yoon. Numerical analysis of fluid flow and heat transfer in the funnel type mold of a thin slab caster. *ISIJ International*, 40(9):886–892, 2000.

[63] T. G. O'Connor and J. A. Dantzig. Modeling the thin-slab continuous-casting mold. *Metallurgical and Materials Transactions B*, 25(3):443–457, 1994.

[64] M. R. Ozgu. Mold and strand guide instrumentation for continuous slab casters. In *Proceedings of the 13th Process Technology Division Conference*, 1995.

[65] M. R. Ozgu. Continuous caster instrumentation: State-of-the-art review. *Canadian Metallurgical Quarterly*, 35(3):199–223, 1996.

[66] R. Pardeshi, A. K. Singh, and P. Dutta. Modeling of solidification processes in rotary electromagnetic stirrer. *Numerical Heat Transfer A*, 55:42–57, 2009.

[67] H.-S. Park, H. Nam, and J. K. Yoon. Numerical analysis of fluid flow and heat transfer in the parallel type mold of a thin slab caster. *ISIJ International*, 41(9):974–980, 2001.

[68] J. K. Park, I. V. Samarasekera, B. G. Thomas, and U. S. Yoon. Thermal and mechanical behavior of copper molds during thin-slab casting (I): Plant trial and mathematical modeling. *Metallurgical and Materials Transactions B*, 33(3):425–436, 2002.

[69] J. K. Park, I. V. Samarasekera, B. G. Thomas, and U. S. Yoon. Thermal and mechanical behavior of copper molds during thin-slab casting (II): Mold crack formation. *Metallurgical and Materials Transactions B*, 33(3):437–449, 2002.

[70] J. K. Park, B. G. Thomas, and I. V. Samarasekera. Analysis of thermomechanical be-

haviour in billet casting with different mould corner radii. *Ironmaking and Steelmaking*, 29(5):359–375, 2002.

[71] X. Peng, J. Zhou, and Y. Qin. Improvement of the temperature distribution in continuous casting moulds through the rearrangement of the cooling water slots. *Journal of Materials Processing Technology*, 167(2–3):508–514, 2005.

[72] B. Petrus, K. Zheng, X. Zhou, B. G. Thomas, and J. Bentsman. Real-time, model-based spray-cooling control system for steel continuous casting. *Metallurgical and Materials Transactions B*, 42(1):87–103, 2011.

[73] L. T. Pillage and R. A. Rohrer. Asymptotic waveform evaluation for timing analysis. *IEEE Transactions on Computer-Aided Design of Integrated Circuits and Systems*, 9(4):352–366, 1990.

[74] C. A. M. Pinheiro, I. V. Samarasekera, J. K. Brimacombe, and B. N. Walker. Mould heat transfer and continuously cast billet quality with mould flux lubrication: Part 1: Mould heat transfer. *Ironmaking and Steelmaking*, 27(1):37–54, 2000.

[75] M. Pokorny, C. Monroe, C. Beckermann, L. Bichler, and C. Ravindran. Prediction of hot tear formation in magnesium alloy permanent mold casting. *International Journal of Metalcasting*, 2(4):41–53.

[76] O. Richmond and R. H. Tien. Theory of thermal stresses and air-gap formation during the early stages of solidification in a rectangular mold. *Journal of the Mechanics and Physics of Solids*, 19(5):273–284, 1971.

[77] M. R. Ridolfi, B. G. Thomas, G. Li, and U. D. Foglia. The optimization of mold taper for the Ilva-Dalmine round bloom caster. *Revue de Métallurgie*, 91(4):609–620, 1994.

[78] B. Rietow. Fluid velocity simulation and measurement in thin slab casting. Master's thesis, The University of Illinois at Urbana–Champaign, 2007.

[79] J. M. Risso, A. E. Huespe, and A. Cardona. Thermal stress evaluation in the steel continuous casting process. *International Journal for Numerical Methods in Engineering*, 65(9):1355–1377, 2006.

[80] I. V. Samarasekera, D. L. Anderson, and J. K. Brimacombe. The thermal distortion of continuous-casting billet molds. *Metallurgical Transactions B*, 13(1):91–104, 1982.

[81] I. V. Samarasekera and J. K. Brimacombe. The thermal field in continuous-casting moulds. *Canadian Metallurgical Quarterly*, 18(3):251–266, 1979.

[82] I. V. Samarasekera and J. K. Brimacombe. *Ironmaking and Steelmaking*, 9:1–15, 1982.

[83] I. V. Samarasekera and J. K. Brimacombe. The influence of mold behavior on the production of continuously cast steel billets. *Metallurgical Transactions B*, 13(1):105–116, 1982.

[84] B. Santillana, L. C. Hibbeler, B. G. Thomas, A. Hamoen, A. Kamperman, and W. van der Knoop. Heat transfer in funnel-mould casting: Effect of plate thickness. *ISIJ International*, 48(10):1380–1388, 2008.

[85] W. M. Scherzinger and C. R Dohrmann. A robust algorithm for finding the eigenvalues and eigenvectors of 3×3 symmetric matrices. *Computer Methods in Applied Mechanics and Engineering*, 197:4007–4015, 2008.

[86] J. Sengupta, M. K. Trinh, D. Currey, and B. G. Thomas. Utilization of CON1D at ArcelorMittal Dofasco's no. 2 continuous caster for crater end determination. In *Proceedings of AISTech*, 2009.

[87] M. R. Shamsi and S. K. Ajmani. Three dimensional turbulent fluid flow and heat transfer mathematical model for the analysis of a continuous slab caster. *ISIJ International*, 47:433–442, 2008.

[88] J. C. Simo and T. J. R. Hughes. *Computational Inelasticity*. Springer, New York, 1998.

[89] C. A. Sleicher and M. W. Rouse. A convenient correlation for heat transfer to constant and variable property fluids in turbulent pipe flow. *International Journal of Heat and Mass Transfer*, 18(5):677–683, 1975.

[90] O. K. Smith. Eigenvalues of a symmetric 3×3 matrix. *Communications of the ACM*, 4(4):168, 1961.

[91] *Steel Statistical Yearbook 2011*. World Steel Association, 2011.

[92] D. Sun and S. V. Garimella. Numerical and experimental investigation of solidification shrinkage. *Numerical Heat Transfer B*, 52:145–162, 2007.

[93] T. Suzuki, K. H. Tacke, K. Wunnenberg, and K. Schwerdtfeger. Creep properties of steel at continuous casting temperatures. *Ironmaking and Steelmaking*, 15:90–100, 1988.

[94] A. Teskeredzic, I. Demirdzic, and S. Muzaferija. Numerical method for heat transfer, fluid flow, and stress analysis in phase-change problems. *Numerical Heat Transfer B*, 42:437–459, 2002.

[95] B. G. Thomas, J. Jiang, and D. Lorento. Optimization of water channel design in beam-blank molds. In *Proceedings of the 5th European Continuous Casting Conference*, pages 139–147, 2005.

[96] B. G. Thomas, S. Koric, L. C. Hibbeler, and R. Liu. Multiphysics model of continuous casting of steel beam-blanks. In *Proceedings of the 4th International Conference on Modeling and Simulation of Metallurgical Processes in Steelmaking*, 2011.

[97] B. G. Thomas, M. Langeneckert, L. Castellá, M. Dziuba, G. di Gresia, and W. Balante. Optimisation of narrow face water slot design for Siderar slab casting mould. *Ironmaking and Steelmaking*, 30(3):235–239, 2003.

144

[98] B. G. Thomas, G. Li, A. Moitra, and D. Habing. Analysis of thermal and mechanical behavior of copper molds during continuous casting of steel slabs. *Iron and Steelmaker*, 25(10):125–143, 1998.

[99] R. H. Tien and V. Koump. Thermal stresses during solidification on basis of elastic model. *Journal of Applied Mechanics*, 36(4):763–767, 1969.

[100] F. Viéte. *De Aequationum Recognitione et Emendatione*. J. Laquehan, Paris, 1615.

[101] V. R. Voller. An overview of numerical methods for solving phase-change problems. *Advances in Numerical Heat Transfer*, 1(9):341–380, 1997.

[102] X. Wang, L. Tang, X. Zang, and M. Yao. Mold transient heat transfer behavior based on measurement and inverse analysis of slab continuous casting. *Journal of Materials Processing Technology*, 212(9):1811–1818, 2012.

[103] J. H. Weiner and B. A. Boley. Elasto-plastic thermal stresses in a solidifying body. *Journal of the Mechanics and Physics of Solids*, 11(3):145–154, 1963.

[104] J. R. Williams, R. W. Lewis, and K. Morgan. An elasto-viscoplastic thermal stress model with applications to the continuous casting of metals. *International Journal for Numerical Methods in Engineering*, 14(1):1–9, 1979.

[105] Y. M. Won and B. G. Thomas. Simple model of microsegregation during solidification of steels. *Metallurgical and Materials Transactions A*, 32:1755–1767, 2001.

[106] Y. M. Won, T.-J. Yeo, K. H.n Oh, J.-K. Park, J. Choi, and C. H. Yim. Analysis of mold wear during continuous casting of slab. *ISIJ International*, 38(1):53–62, 1998.

[107] P. J. Wray. Effect of carbon content on the plastic flow of plain carbon steels at elevated temperatures. *Metallurgical Transactions A*, 13:125–134, 1982.

[108] Y. Xie, H. Yu, X. Ruan, B. Wang, and Y. Ma. Fe numerical simulation of mould temperature field during the continuous casting of steel. *International Journal of Advanced Manufacturing Technology*, 30(7–8):645–651, 2006.

[109] Y.-M. Xie and S.-R. Yin. Three-dimensional thermal stress analysis of the mould during high-speed casting of steel. *Journal of Strain Analysis for Engineering Design*, 43(7):565–568, 2008.

[110] H. L. Xu, G. H. Wen, W. Sun, K. Z. Wang, B. Yan, and W. Luo. Thermal behaviour of moulds with different water channels and their influence on quality in continuous casting of beam blanks. *Ironmaking and Steelmaking*, 37(5):380–386, 2010.

[111] M. Yao, H. Yin, and D. Fang. Real-time analysis on non-uniform heat transfer and solidification in mould of continuous casting round billets. *ISIJ International*, 44(10):1696–1704, 2004.

[112] H. Yin, M. Yao, and D. Fang. 3-D inverse problem continuous model for thermal

behavior of mould process based on the temperature measurements in plant trial. *ISIJ International*, 46(4):539–545, 2006.

[113] H. Yin, M. Yao, H. Zhan, and D. Fang. 3D stress model with friction in and of mould for round billet continuous casting. *ISIJ International*, 46(4):546–552, 2006.

[114] N. Zabaras, Y. Ruan, and O. Richmond. Front tracking thermomechanical model for hypoelastic-viscoplastic behavior in a solidifying body. *Computer Methods in Applied Mechanics and Engineering*, 81(3):333–364, 1990.

[115] N. Zabaras, Y. Ruan, and O. Richmond. On the calculation of deformations and stresses during axially symmetric solidification. *Journal of Applied Mechanics*, 58(4):865–871, 1991.

[116] D. Zhang, S. Lei, S. Zeng, and H. Shen. Thermo-mechanical modeling in continuous slab casting mould and its application. *ISIJ International*, 54(2):336–341, 2014.

[117] J. Zhou, X. Peng, and Y. Qin. A coupled thermalmechanical analysis of a mold-billet system during continuous casting. *International Journal of Advanced Manufacturing Technology*, 42(5–6):421–428, 2009.

[118] H. Zhu. *Coupled Thermal-Mechanical Finite-Element Model with Application to Initial Solidification*. PhD thesis, University of Illinois at Urbana–Champaign, 1993.